



HAL
open science

Biomass-based hydrochars for hard-carbon for Na-ion batteries

Julie Michel

► **To cite this version:**

Julie Michel. Biomass-based hydrochars for hard-carbon for Na-ion batteries. Material chemistry. Université Grenoble Alpes [2020-..], 2023. English. NNT : 2023GRALI114 . tel-04525124

HAL Id: tel-04525124

<https://theses.hal.science/tel-04525124v1>

Submitted on 28 Mar 2024

HAL is a multi-disciplinary open access archive for the deposit and dissemination of scientific research documents, whether they are published or not. The documents may come from teaching and research institutions in France or abroad, or from public or private research centers.

L'archive ouverte pluridisciplinaire **HAL**, est destinée au dépôt et à la diffusion de documents scientifiques de niveau recherche, publiés ou non, émanant des établissements d'enseignement et de recherche français ou étrangers, des laboratoires publics ou privés.

THÈSE

Pour obtenir le grade de

DOCTEUR DE L'UNIVERSITÉ GRENOBLE ALPES

École doctorale : I-MEP2 - Ingénierie - Matériaux, Mécanique, Environnement, Energétique, Procédés, Production

Spécialité : 2MGE - Matériaux, Mécanique, Génie civil, Electrochimie

Unité de recherche : CEA Grenoble / LITEN

Hydrochars à base de biomasse pour la production de carbone dur pour les accumulateurs Na-ion

Biomass-based hydrochars for hard-carbon for Na-ion batteries

Présentée par :

Julie MICHEL

Direction de thèse :

Loic SIMONIN
INGENIEUR HDR, Université Grenoble Alpes

Directeur de thèse

Capucine DUPONT
ASSOCIATE PROFESSOR, IHE

Co-encadrante de thèse

Rapporteurs :

Rosa PALACIN
FULL PROFESSOR, Institut de Ciència de Materials

Frederik RONSSE
ASSOCIATE PROFESSOR, Universiteit Gent

Thèse soutenue publiquement le **20 novembre 2023**, devant le jury composé de :

Loic SIMONIN
INGENIEUR HDR, CEA centre de Grenoble

Directeur de thèse

Philippe AZAIS
DIRECTEUR DE RECHERCHE, CEA centre de Grenoble

Président

Cécile ROSSIGNOL
MAITRESSE DE CONFERENCES HDR, Université Grenoble Alpes

Examinatrice

Kentaro UMEKI
FULL PROFESSOR, Lulea Tekniska Universitet

Examineur

Rosa PALACIN
FULL PROFESSOR, Institut de Ciència de Materials

Rapporteuse

Frederik RONSSE
ASSOCIATE PROFESSOR, Universiteit Gent

Rapporteur

Invités :

John Abou-Rjeily
INGENIEUR DOCTEUR, Tiamat

Camélia Ghimbeu
DIRECTRICE DE RECHERCHE, CNRS Mulhouse



S'il n'y a pas de solution, alors il n'y a pas de problème.

Devise Shadock, Jacques Roussel

Table of contents

Introduction – Context & objectives.....	7
Chapter 1 – State of the art.....	9
1. Na-ion batteries electrode materials.....	9
1.1. Positive electrode.....	10
1.2. Negative electrode.....	11
1.3. Hard carbon as negative electrode.....	12
2. Biomass conversion to biochar.....	22
2.1. Biomass specificities.....	22
2.2. Pyrolysis.....	25
2.3. Hydrothermal carbonisation.....	26
3. Biomass-based hard carbon for Na-ion batteries.....	31
3.1. Feedstock influence.....	31
3.2. HTC pre-treatment for hard carbon synthesis.....	33
Conclusions.....	35
Chapter 2 – Materials & methods.....	43
1. Raw biomass.....	43
2. Biochar & hard carbon synthesis.....	44
2.1. Hydrothermal carbonisation.....	44
2.2. Low temperature pyrolysis.....	45
2.3. High temperature pyrolysis.....	45
3. Chemical composition of the materials.....	46
3.1. Moisture content.....	46
3.2. C, H, N, S, O contents.....	46
3.3. Ash content.....	47
3.4. Inorganic contents by ICP-OES.....	47
3.5. Inorganics by UV-visible spectrophotometry.....	48
3.6. Macromolecules.....	50
3.7. Total organic and inorganic carbon, total nitrogen.....	51
3.8. Gas composition.....	51
3.9. Yield definitions and calculations.....	51

3.10. Elemental balance calculations	52
4. Physicochemical properties.....	53
4.1. Structure by XRD	53
4.2. Structure defects by Raman spectroscopy.....	54
4.3. Surface characterisation.....	54
5. Electrochemical tests	55
5.1. Battery assembly.....	55
5.2. Galvanostatic tests.....	56
Chapter 3 – Hydrothermal carbonisation operational condition influence on the hard carbon properties	59
1. Experimental campaign settlement	59
2. HTC pre-treatment	61
2.1. Raw biomass composition.....	61
2.2. Operational condition influence	62
2.3. Genera influence.....	64
3. Driftwood-based hard carbons and their properties	67
3.1. Operational conditions influence	67
3.2. Genera influence.....	70
Conclusions	74
Chapter 4 – Influence of the feedstock on the electrochemical performances	75
1. Selection of the feedstock and conditions	75
2. Raw biomass composition	76
2.1. Organic composition	76
2.2. Inorganic composition	77
2.3. Macromolecule content.....	79
2.4. Structure	80
3. Hydrochar composition	82
3.1. Organic composition	82
3.1. Inorganic composition	83
3.2. Structure	92
4. Hard carbons.....	95
4.1. Chemical composition	95
4.2. Structure	97
4.3. Surface area and morphology	100

4.4. Electrochemical performances	107
Conclusions	117
Chapter 5 – Fate of inorganics during hydrothermal carbonisation and its influence on the hard carbon properties	119
1. Experimental campaign settlement	119
2. Fate of inorganics during HTC	121
2.1. Raw biomass compositions	121
2.2. Organic elemental distribution between the different phases	125
2.3. Ash content in the solids	127
2.4. Inorganic elemental distribution between the different phases	128
2.5. Influence on the hydrochar structure	135
3. Impact on the hard carbon properties	137
3.1. Hard carbon compositions	137
3.2. Electrochemical performances	144
Conclusions	149
Chapter 6 – Hydrothermal carbonisation vs. pyrolysis as pre-treatment in biomass based hard carbon synthesis for negative electrode in Na ion battery: comparison of the two processes	151
1. Experimental campaign settlement	151
2. Influence on the biochar	153
2.1. Raw biomass composition	153
2.2. Biochars organic composition	153
2.1. Biochars inorganic composition	154
2.2. Structure	156
3. Influence on the hard carbon properties	159
3.1. Composition of the hard carbons	159
3.2. Structure of the hard carbons	159
3.3. Surface area	164
3.4. Electrochemistry	166
Conclusions	170
General conclusion – Conclusions & outlooks	171
References	173
Abstract	186

Introduction

Context & objectives

Li-ion batteries are the most suitable technology for energy storage which makes them the most widely used for electronic devices, intermittent energy storage and transportation. Yet, lithium availability on Earth is limited in quantity and poorly distributed [1], [2]. Moreover Li-ion battery materials need other critical elements, such as Co, Ni, Cu and F. Replacing these elements becomes a real challenge. Contrary to lithium, sodium is abundant and well spread around the world. Also, it presents a similar reactivity to lithium. Furthermore, sodium battery mechanism enables to replace copper current collector by aluminium [2]. Hence, Na system has become an attractive alternative technology to Li-ion and has been heavily investigated in the last 10 years [3]. The differences between the two systems are summarized in **Table 1**.

Table 1: Differences between lithium and sodium battery. Critical elements are in red.

	Li-ion	Na-ion
Low availability elements	Li, Co, Ni, Cu, F	Fe, Mn, F
Negative electrode	Graphite (natural)	Hard carbon
Current collector	Cu	Al
Performances	+++	++
Price	€€€	€

Although rather similar, Li- and Na-ion mechanisms bear significant differences, so that the materials must be adapted to each ion. Graphite is the main material used as negative electrode in commercial Li-ion batteries, however the difference of reactivity between Li and Na makes it a poor material for sodium battery [4], [5].

As graphite is not suitable for Na insertion, hard carbon is widely used in Na-ion batteries. Hard carbon is a non-graphitizable disordered carbon material. It is the most promising material as negative electrode, as it presents the best compromise between high capacity and low voltage against Na⁺/Na. Hard carbon is produced from complex molecules, such as heteroatom-rich polymers and organic macromolecules [2]. These precursors are generally expensive and produced from fossil resources. To reduce its cost and environmental impact, it is possible to obtain it from waste biomass. Many studies report a direct or two-steps pyrolysis of dry biomass [6]–[10], but few deal with wet biomasses, which are potentially cheap and underlooked carbon resource because of their high moisture content (>60 %). Hence, this high moisture makes very difficult regular pyrolysis and generally requires a drying step. From this point of view, hydrothermal carbonisation (HTC) appears as a good method to carbonize this type of biomasses. HTC is an autoperpressurized thermal treatment in which the sample is immersed in water. With this method there is no need in drying the biomass before processing. Furthermore, inorganics – which are a known obstacle to the electrochemical properties of hard-carbon [11] – tend to leach in the liquid phase in the process.

The objective of this work is to determine the influence of the HTC conditions, the feedstock properties, and the inorganic leaching on the hydrochar and hard carbon properties as well as the electrochemical performances in Na-ion batteries.

To do so, this work will focus on the HTC pre-treatment of wet biomass. First the impact the HTC operating conditions on the resulting hard carbon will be studied. Secondly, the impact of different feedstock properties will be investigated. Particularly, we will consider the inorganics behaviour during each step, and how they interact with the carbon matrix, as they are known to be a key factor for electrochemical behaviour. This study will try to deeply understand the role these elements play in the whole hard carbon synthesis process. This thesis is organised as follows:

Chapter 1 presents general aspects and provides a state of the art about Na-ion batteries. It describes the biomass-based hard carbon, and focuses on the HTC process. Finally, it explains the main motivations of this study.

Chapter 2 summarises the materials and methods used through this study.

Chapter 3 focuses on the preparation of hard carbon from river driftwoods. We investigate the impact of the HTC conditions on the structure of the resulting hard carbon. To determine the pre-treatment experimental conditions, a panel of residence times and temperatures are studied to settle a protocol. It set the basis for the further investigations. The study reported in this chapter has been published in in Journal of Environmental Chemical Engineering in 2021 [12].

Chapter 4 investigates the impact of the feedstock's composition on the resulting hard carbon. It covers a wide range of raw materials, with 11 biomasses from various compositions. The materials are characterised after each step, providing a follow-up of the whole process.

Chapter 5 focuses on the reactions occurring during the HTC, and especially on the inorganic behaviours at different temperatures. The influence on the physicochemical properties of both the hydrochars and hard carbons are investigated, which enables to deduce mechanisms during both thermal steps. This work is the object of a scientific article submitted to Biomass Conversion and Biorefinery.

Chapter 6 evaluates how the HTC impacts the hard carbon by comparing HTC with a low-temperature pyrolysis on the same materials. Both biochars are then annealed on the same conditions and assemblies in half cell.

At last, a general conclusion presents the main highlights of this thesis, as well as future perspective to better understand the reactions that occurs during each step and possible improvements to the model system.

This work have been carried out at CEA Grenoble in France, and UNESCO-IHE Delft in the Netherlands, in the frame of the NAIMA project. This project has received funding from the European Union's Horizon 2020 research and innovation programme under grant agreement No 875629.

Chapter 1

State of the art

This chapter lays the foundations for this study, describing the notions, materials, and processes that are used from biomass to hard carbons for sodium batteries. It presents the advances in the subject so far and opens the reflection for the studies presented in the following chapters.

1. Na-ion batteries electrode materials

A Na-ion battery is composed of a positive electrode, a negative electrode, and in between an electrolyte. Ions are going to intercalate in one or the other electrode depending on the state of the cell, as shown in **Figure 1**. When the battery delivers energy – during the discharge – an oxidation occurs at the negative electrode: an electron goes out when a sodium ion is released and migrates to the positive electrode through the electrolyte, where a reduction happens. In charge, the reactions are the opposite: reduction at the negative electrode and oxidation at the positive one. Different mechanisms can occur at the electrodes: intercalation – where Na^+ are reversibly intercalated without major structure phase transition –, alloy formation – where the sodium reacts directly with a metal to form an alloy –, and conversion – where the ion insertion leads to a structural change, such as amorphous phase formation [13].

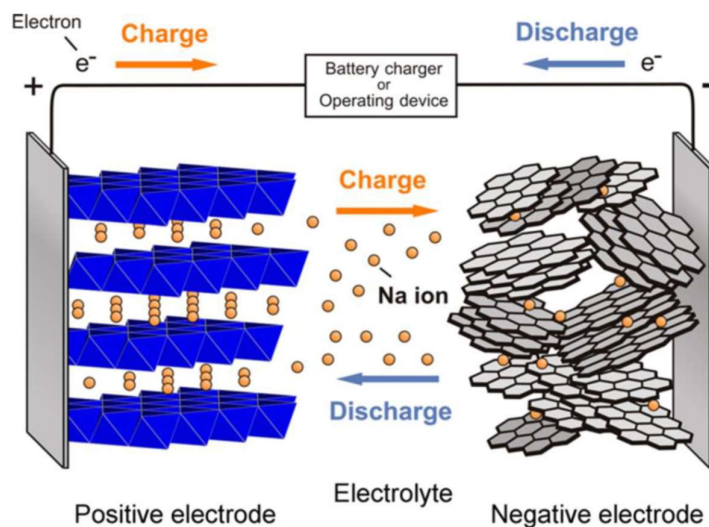


Figure 1: Sodium-ion battery principle, from [14].

1.1. Positive electrode

As the positive electrode, four main categories of materials are usually used, each with their properties. The materials from the four kinds are represented according to their capacity and voltage in **Figure 2** and described below.

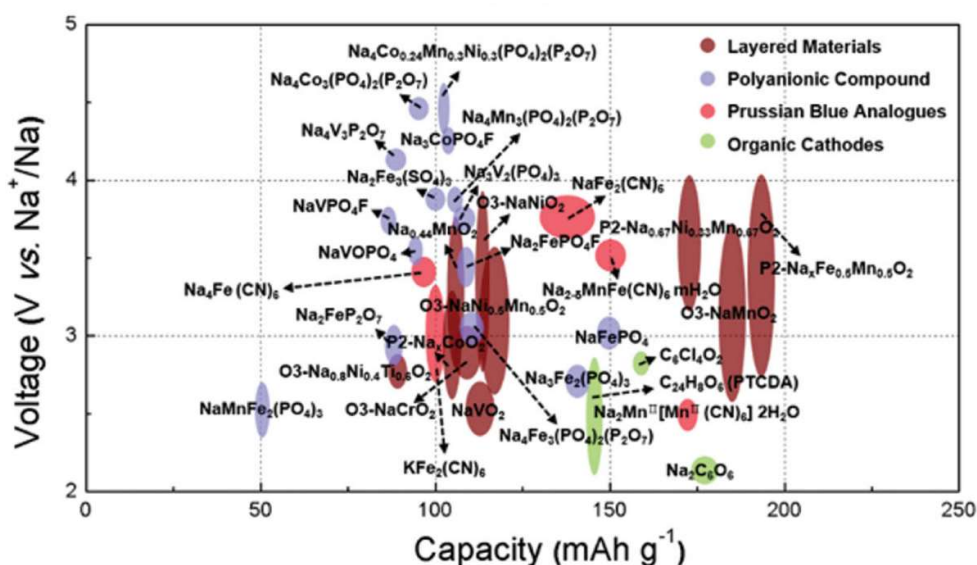


Figure 2: Voltage–capacity plots of representative positive electrode materials for Na-ion batteries, from [3].

Layered oxides are the most investigated materials because of their high theoretical capacity and relatively simple synthetic process [3]. Their structure is a succession of octahedral MO_2 pattern layers with Na^+ ions in between, leading to the Na_xMO_2 general formula. These materials are known for their phase transitions during cycling that are unfavourable for the cycling performance in general. Suppressing phase transitions is the key to improve the cycling stability of layered oxides in sodium batteries [15].

Due to their structural diversity and stability, polyanionic compounds are an essential category of positive electrode. The groups the most used are phosphates $(PO_4)^{3-}$, pyrophosphates $(P_2O_7)^{4-}$, fluorophosphates and sulfates $(SO_4)^{2-}$. They offer a many formula possibilities and a structural stability at high potential vs Na^+/Na due to the strong covalent bond in the anion [16], [17].

Prussian blues $A_xMM'(CN)_6$ have a cubic structure that allows a reversible insertion/disinsertion of alkaline ions due to the open framework and favourable interstitial sites. Different materials with Ni, Cu, Fe, Mn, Co, and Zn were investigated, they provide good performances but the toxicity of KCN during the synthesis is an obstacle to their development [3].

At last, organic compounds are the last category of positive electrode in Na-ion battery because of their abundance, safety, environmental friendliness, and high theoretical capacity. The storage mechanism is between the C=O bond and the alkali ion [3].

1.2. Negative electrode

Different categories of negative electrodes have been investigated depending on their sodation mechanism: insertion where Na^+ ions are reversibly intercalated without major structure phase transition, alloy formation, and conversion. The materials are described below, and the capacity-voltage stability is represented in **Figure 3**.

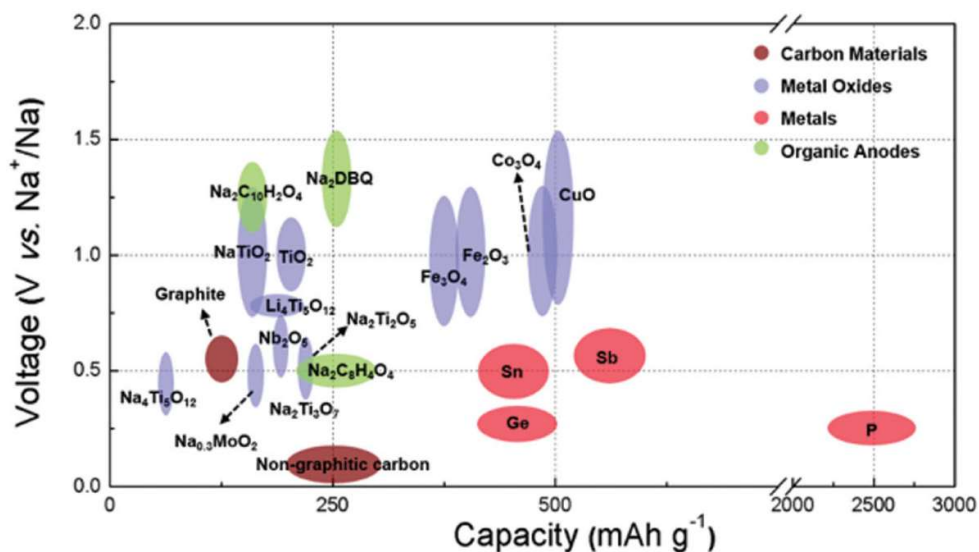


Figure 3: Voltage–capacity plots of representative negative electrode materials for Na-ion batteries, adapted from [3].

Metal oxides are widely investigated with various metal due to their good safety, high volumetric energy density and their appropriate sodium storage potentials [18]. Many works on TiO_2 with different phases lead to good capacity and cyclability through an insertion mechanism, while other metal such as Fe_2O_3 , Fe_3O_4 , Mn_3O_4 , or NiCo_2O_4 exhibit very high specific capacities but through a conversion mechanism.

Intermetallic compounds store the sodium through alloying reactions. They have been investigated because of their high theoretical capacity and low Na storage potential. Different materials Sn-, Sb-, P-, Si-, and Ge-based were studied, with different composition such as $\text{Na}_{15}\text{Sn}_4$, NaSn_3 , Na_3P , NaSi or NaGe . Unfortunately, despite the good theoretical performances, the volume expansion that occurs through cycling negatively impacts the cyclability.

Organic materials are suitable for negative electrodes for the same reasons as positive ones. Disodium terephthalate ($\text{Na}_2\text{C}_8\text{H}_4\text{O}_4$), coronoic acid disodium salt (CADS), polymeric Schiff-based functional ($\text{R}_1\text{HC} = \text{NR}_2$) groups and other groups were investigated, leading to promising good capacities [19].

Carbon materials are the last category used as negative electrode, represented in **Figure 4** with their structures. Graphite is the main material used in commercial Li-ion batteries; therefore the difference in reactivity between Li and Na makes it a poor material for sodium batteries. While Li ions can insert with a specific capacity of 372 mAh.g^{-1} at 0.1 V vs Li^+/Li , sodium intercalation in graphite is very low with a theoretical capacity of 35 mAh.g^{-1} [5], because of the instability of the sodium-graphite intercalation

compound [4]. Instead of graphite, hard carbon is the most promising material for Na-ion batteries with good cyclability and capacity. It is composed of graphene layers, but when graphite is really organised, hard carbon is not: it has pores, defects, abundant sodium storage sites and a stable structure. It is the most promising negative electrode material and will be described in the next part.

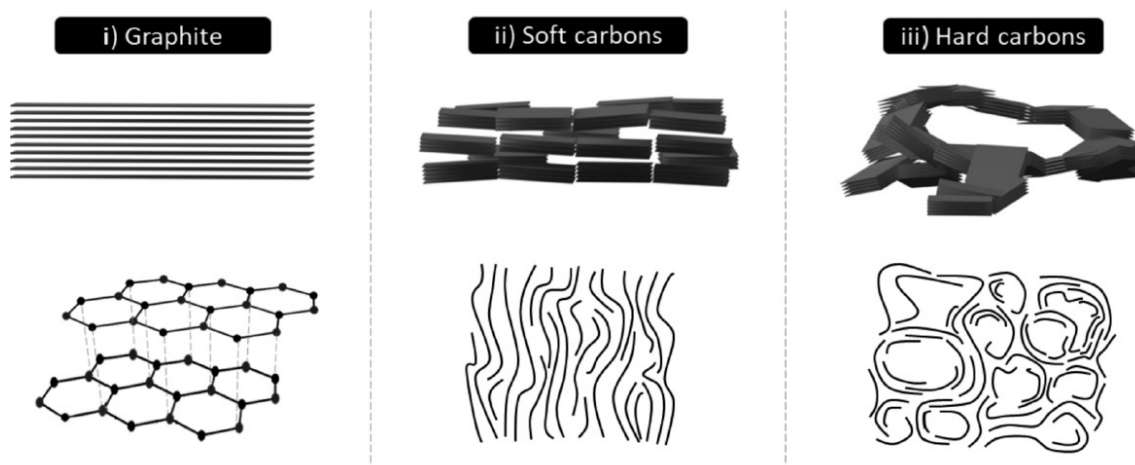


Figure 4: Organisation of graphene layers in carbon materials [20].

1.3. Hard carbon as negative electrode

1.3.1. Structure

Hard carbon is a non-graphitizable carbon material, which will not graphitize even at very high temperatures of about 3000 °C. This property comes from the highly cross-linked raw material that prevents the graphitic structure from happening [21]. Instead of “hard”, it can also be referred to as “non-graphitizable” or “disordered” but should not be called “amorphous”: by definition, it implies localized π electrons that hard carbon lacks [22]. Different models have been established to determine the hard carbon structure in the last century, as represented in **Figure 5**. Those models are all based on graphene layer assembly. Thereby, Warren first proposed it in 1941 [23] as randomly oriented graphitic nanodomains. Franklin then updated it in 1951 [24] and added amorphous domains that link the organized area, leading to micropore formation that prevents graphitization. Ban proposed later in 1975 [25] a model consisting of an interlaced network of curved graphitic nanoribbons. However this model could not explain why the material was not graphitizable despite the graphene layers’ mobility above 2500 °C. Further investigations implying transmission electron microscopy showed that the graphene layers were curved, leading to a model similar to Harris’ in 1997 [26]; a fragmented fullerenes-like structure not fully aligned, creating micropores [21], [22], [27]. Twenty years later, Dou *et al.* [22] proposed a different explanation for these observations. They deduced the structure is not random graphene layers but graphite-like with many defects. Despite these new observations, the hard carbon organisation is still not precisely defined. Nowadays, the one used is the “house of cards” model described by Dahn in 1999 [28], which considers the structure as “a mixture of pseudo-graphitic micro-crystallites (sp^2 -hybridized, turbostratic staked graphene layers) and amorphous regions (sp^3 -hybridized) along with nanovoids (nanopores)” [21].

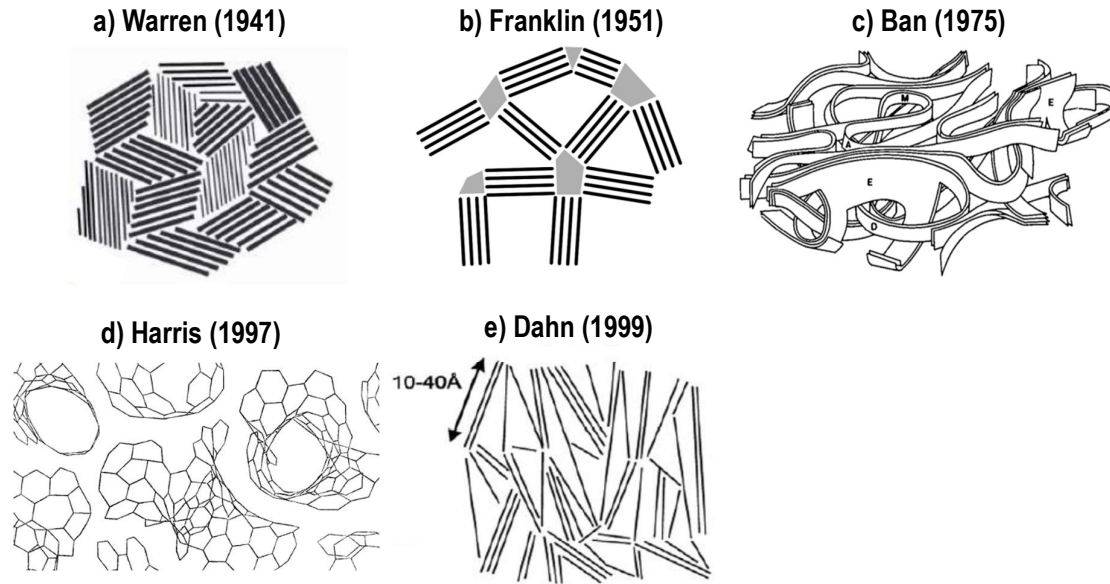


Figure 5: Evolution of hard carbon structure representation, adapted from [21] and [27] from the original works of [23]–[26], [28].

The **global morphology** at the macroscale is still similar to the raw material, which means it can be spherical, fibrous, plant cell-shaped... depending on the precursor [29]. At a smaller scale, the **crystalline and amorphous areas** from the “house of cards” model show different properties. Crystalline parts are described as 40 Å long and composed of 2 to 3 graphene layers [28], but this model is still discussed for smaller but more organised areas [22]. TEM observations highlight these organized and regular areas, and allow seeing parallel curved planes, as shown in **Figure 6**. To complete these observations, XRD gives information on the **lattice**, with two broad peaks, consequence of the diffraction of the X-rays of the basal graphene planes (002) and perpendicular to them (100). The broadness of the peak is related to the disorder of the material, while the (002) peak gives the average distance between the layers d_{002} and the thickness of the domain L_c ; the (100) peak is related to the width of the domain L_a [21]. Hard carbon’s d_{002} is between 3.6 to 4.0 Å while graphite’s is 3.35 Å [29]. This value is used to characterise the level of graphitisation of the material.

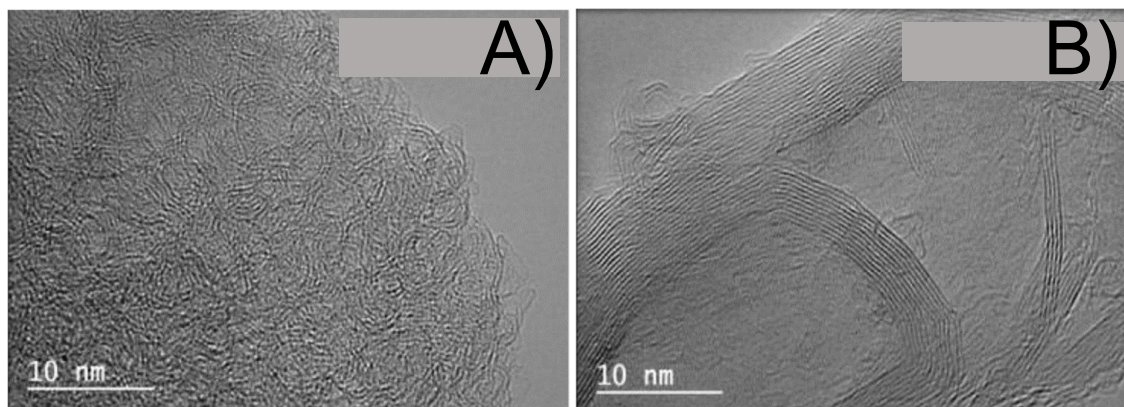


Figure 6: TEM picture of hard carbon from washed **A)** asparagus peel and **B)** grape waste synthesised on the same conditions, adapted from [30]. The image on the left shows small-range organisation, while bigger organised areas, made of more and longer sheets on the right.



Even if the global morphology remains the one of the raw material, the **surface area** and inside **porosities** are peculiarities of each material, respectively called open and closed porosity. Both are important for sodium ions storage, which, at the same time, intercalate between the layers, fill the pore, and are adsorbed at the surface [13], [29]. These different mechanisms and their conditions are described in 1.3.5. Surface area and open porosity are usually measured by gas adsorption. N₂ adsorption is the most common technique, but CO₂ molecules are smaller and gives bigger surface areas, which highlights the important number of ultramicropores (pore size <0.7 nm) [31]. Nevertheless, no matter which one, gas can only be adsorbed where it has access: it gives limited information on the material. In order to complete the analysis, SAXS is used to study the closed porosity and together, they give a very good understanding of the material both inside and outside. SAXS uses the same principle as XRD, an X-ray beam that diffuses in the material, diffracts, and is collected for processing. The angle range observed is different, which gives information at different scales. A proper fitting of the curves can also give the pore volume [21].

The **chemistry surface** is also essential. It is mainly composed of oxygen functions, in particular hydroxyl –OH, carboxyl –COOH, and ether –R–O–R–, but can also contain heteroatoms such as N, S and P [21]. X-ray photoelectron spectroscopy (XPS) allows to obtain information, both quantitative and qualitative at the surface of the material. It consists of measuring the emitted energy after excitation by X-ray. Each atom has a specific bonding energy, which allows identifying and quantifying the elements. Another method to quantify oxygen groups is by thermal programmed desorption mass spectroscopy (TPD-MS). Each function is decomposed at a specific range of temperature, releasing CO, CO₂, H₂O or H₂, the analysis of these gas allows to determine the surface chemistry.

Even if the graphene-layered structure is established, there are a non-negligible number of **defects** in the structure at the atomic scale, depending on the synthesis parameters and the precursor. Thus, there are vacancies, edges and defective sites in the structure. The crystalline area, supposedly composed of 2D sp²-hybridized hexagonal carbon rings, has, in fact, some pentagonal and heptagonal defective sites. Depending on the method or model, a few hexagonal units are aligned before an irregularity [29]. In order

to characterize these defects, Raman spectroscopy is widely used to complement XRD. Depending on the electronic state of a sample, an induced laser beam is scattered differently; it is collected and processed to give quantitative information on this interaction (such as frequency, vibration symmetry...) [32]. For hard carbon, it results in two broad peaks corresponding to the in-plane vibration of sp^2 carbon, called the G band, and to the disorder in these six-fold aromatic rings, called the D band. It is easier to relate to D band to sp^3 carbon because its intensity depends on the structure defects, when in fact, it corresponds to the π states of sp^2 vibrations located near sp^3 carbon. The ratio of the intensities of the peaks I_D/I_G or I_G/I_D estimates the number of defects [21], [22], [33], yet it is not quantitative. Indeed, some sp^2 carbons are also present in amorphous domains, and defects due to micropores are not detected by this technique [21], [22]. In order to complete Raman information, TPD-MS quantifies the amount of defects including micropores, by measuring the active surface area correlated to the surface, like stacking faults, single and multiple vacancies and dislocations [21]. This technique is yet not very common and requires a specific set-up.

Table 2: Comparison between graphite and hard carbon properties. The value are ranges; it has to be kept in mind that hard carbon does not describe one specific material but a category. Adapted from [21], [27], [29].

	Graphite	Hard carbon
Organisation of the graphene layers		
d_{002}	3.35 Å	3.6 - 4.0 Å
I_D/I_G	0.05	0.5 - 2.5
Surface functionalisation	-	-OH, -COOH, -R-O-R-

1.3.2. Synthesis and mechanisms

Hard carbon is synthesized by pyrolysis above 1000°C from highly cross-linked materials such as raw biomass, synthetic polymer and biopolymers [21]. Pyrolysis takes place under inert atmosphere; the material is decomposed and three phases result: the hard carbon, tars and gas. However, the mechanisms are not fully understood yet and are still under investigation. A significant fraction of O and N remains in the solid until 1000 °C, which is finally removed as gas. The gas is composed of combustibles such as H_2 , CO, CO_2 and CH_4 from small molecule degradation; and condensable gas [34]. These gases might also react with the carbon matrix itself through Boudouard reaction: $C + CO_2 \rightarrow 2 CO$, releasing another reactive gas and increasing the decomposition of the material [35]. The global morphology of the raw material is maintained: the carbons have some mobility that organises as graphene layers at high temperatures, but the material's cross-linking prevents from a total organisation of the layers. By opposition, if the linking between the layers is weak, the mobility of the layers at high temperature will create a more structured material with a smaller interlayer space and less pores, but also with more defects [29], [33]. The different mechanisms and structure depending on the temperatures is illustrated in **Figure 7**.

The inorganic behaviour is strongly dependent of the temperature and feedstock. It is admitted that part of alkali and alkaline earth metals are removed in high proportion at temperatures higher than 1000 °C [36], [37]. They are found in lignocellulosic biomass mainly as water-soluble or ion-exchangeable compounds [38], which are available for volatilisation. However, their release is partial [36], [37]. Heavy metals are usually thought to be kept in the final structure, however Lane *et al.* [39] worked on trace elements on microalgae through several thermal treatments including pyrolysis and observed an important volatilisation of Zn, Pb and Sb from algae from 700 to 1000 °C. They also studied the leaching in water of these elements on the raw algae and resulting material; they observed that most of the elements in the final biochar do not leach, unlike in the feedstock.

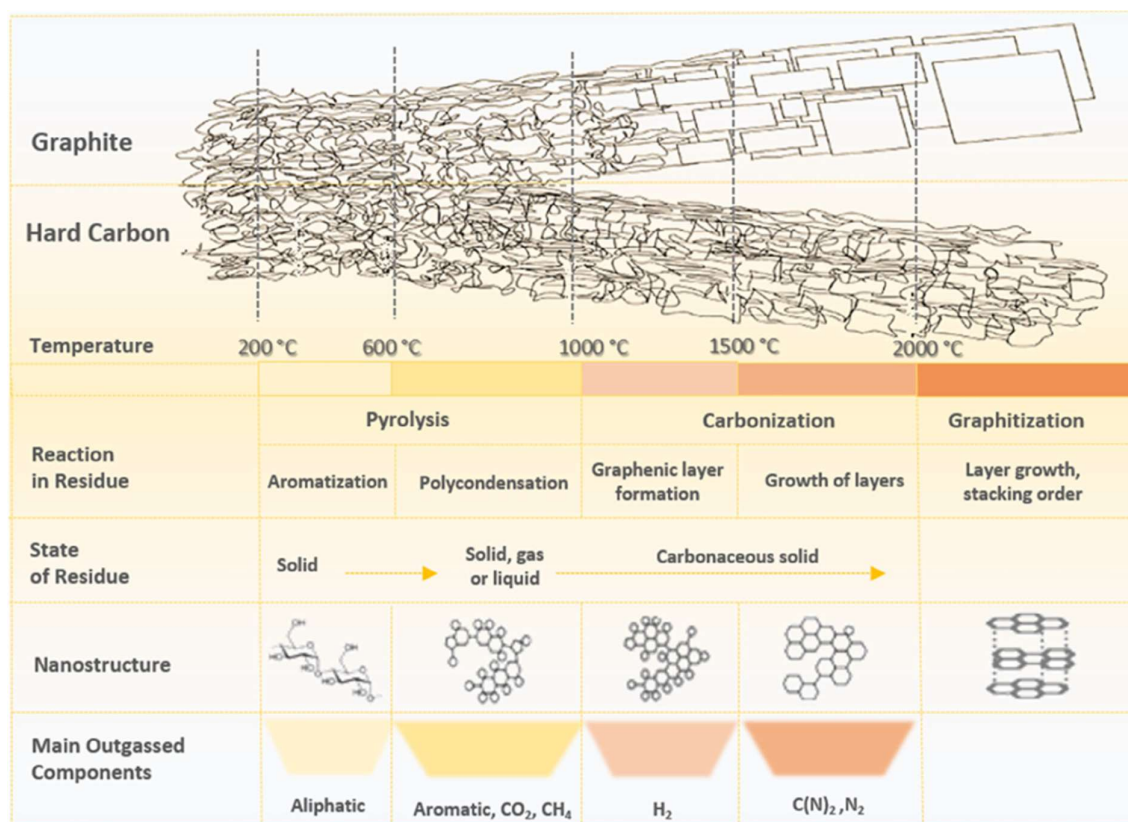


Figure 7: Hard-carbon formation scheme as a function of temperature. The circles in the polymeric-structure schemes represent moieties like functional groups and side chains. From [22].

1.3.3. Operating conditions influence

The operating conditions have a major effect on the hard carbon properties. The temperature is one of the most studied parameters: its increase gives a more organized structure. The graphene layers are closer and the pores are bigger [31], [40]. With the increase of the temperature, there is a decrease of the interlayer distance d_{002} . This observation was seen in many studies dealing with a wide range of temperatures, at least from 1000 to 1600 °C from cellulose [41], peanut shell [42], mangosteen shell [7], *Spartina Alterniflora* [6], date palm pulp and seeds [43]. Simone *et al.* [41] highlighted the d_{002} reducing from 4.2 to 3.8 Å from 700 to 1600 °C on their cellulose-based hard carbons. They also reported the increase of the organisation, completing their observations by TEM: below 1150 °C, graphene layers

seem independent, whereas above this temperature, small-scale graphitisation begins with the alignment of 4 to 5 graphene sheets until reaching 10 nm crystalline domains at 1400 °C, and finally at 1600 °C even larger organised areas. Similar observations were reported by Hasegawa *et al.* [44]. However, this continuous decrease of d_{002} is not always observed: Gomez-Martin *et al.* [9], by working with olive stones, highlighted a bell-shaped correlation: the interlayer space increases until 1400 °C and decreases at higher temperature.

The reorganisation of the layers with the temperature also impacts the porosity of the material. Hasegawa *et al.* [44] worked on temperatures from 800 to 3000 °C on resorcinol-formaldehyde gel and highlighted a major difference between 1200 and 1600 °C: the specific surface area drops from 620 m²/g to 3.8 m²/g. Simone *et al.* [41] also mentioned that the specific surface area of their cellulose-based materials decreases until 1150 °C, then stabilises around 10 m².g⁻¹ at higher temperatures. Furthermore, they reported an increase of the structure defect I_D/I_G : before 1150 °C, the graphene layers are independent, and defects appear only with the increase of organisation. This observation is also reported by Gomez-Martin *et al.* (2019). However, this observation was via N₂ adsorption: it allows to measure only open pores bigger than 0.7 nm due to the large size of the gas molecule and slow diffusion kinetic on hard carbons [45]. Furthermore, the small values are close to the limit of detection of the technique, which does not allow to conclude properly on the study [31]. To go through this problem, Matei Ghimbeu *et al.* [31] and Beda *et al.* [45] recommend completing the studies with CO₂ adsorption: since the smaller molecule size allows to reach ultramicropores below 0.7 nm. Unfortunately, CO₂ cannot be used alone for mesopores (2-50 nm) [46]. Moreover, SAXS accesses the closed porosity in order to have a complete overall of the porosity. Buiel *et al.* [47] highlighted a correlation between the closed porosity and the pyrolysis temperature: working with dewatered sucrose between 900 and 1400 °C, they found a reduction of the number of pores despite an increase of their volume, resulting from their merge, as well as the increase of closed porosity. It appears that above 1300 °C, close pores are dominant.

Fewer studies deal with the residence time, even if it also has an impact on the resulting hard carbon. Wang *et al.* [7] worked on mangosteen shells from 0.5 to 5 h, and reported a similar tendency: the longer the reaction time, the smaller the d_{002} and the higher the I_D/I_G .

The heating rate is also an impact factor on the structure. Xiao *et al.* [48] studied its influence on sucrose at 1300 °C between 0.5 and 5 °C.min⁻¹, which is a common range for hard carbon synthesis. They highlighted that a low rate leads to a material with less BET surface, smaller pores, and bigger organised domains with slightly smaller d_{002} and fewer defects. A slow rate allows the gas produced to fully evacuate the material that results a closed porosity. Zhen *et al.* [49] worked on a fast heating rate between 300 to 500 °C.min⁻¹ when the usual rate is a few degrees per minute only, from sucrose at 900, 1100 and 1300 °C for 5 min. The observations they deduced were similar to standard heating rates: the increase of temperature decreases the d_{002} , the BET surface, the I_D/I_G and the O content. By comparison with a blank synthesized at a usual rate of 5 °C.min⁻¹ at 1100 °C for 3 h, the resulting material has a slightly higher d_{002} , I_D/I_G and O content than its homolog at 1100 °C at 300 °C/min, however the BET surface was more than 5 times higher.

At last, the gas atmosphere was also investigated. Marino *et al.* [50] worked on almond shell pyrolysis under Ar, N₂ and Ar/H₂ atmosphere at 1000 °C after a biomass acidic wash. They observed similar d_{002} and defect ratios, whereas the surface area were 21, 185 and 252 m².g⁻¹ under Ar, N₂ and Ar/H₂ respectively, which highlight the great impact of the atmosphere. The authors suggested that the method used was unsuitable for covering the whole materials' porosity: they used N₂ adsorption to measure the surface area, but it can't access the micro- and ultramicroporosity as explained in 1.3.1. It implies Ar favours smaller pores than N₂ and reduces the surface area. Furthermore, the flow of the gas also play a role on the porosity: Irisarri *et al.* [33] worked from sugar at 1100 °C under Ar flow from 200 to 1000 cm³.min⁻¹, they observed an important decrease of the surface area, from 670 to 11 m².g⁻¹ from the slowest to fastest rate respectively. According to their study, a higher gas flow prevents the released gas – mostly CO₂ – from react with the material responsible for porosity development.

The influence of the different parameters on the resulting hard carbon properties discussed above is summarised in **Table 3**.

Table 3: Summarize of the influence of the process on hard carbon properties from the discussion above. *nd* stands for no data.

	Graphitisation	Porosity	Pores size	Surface area	Defects	O groups
Temperature	+++	Open: - Closed: ++	-	--	--	-
Time	+	nd	nd	nd	-	nd
Heating rate	-	Open: + Closed: -	-	-	-	-
Gas flow	nd	+	--	--	nd	nd

1.3.4. Electrochemical behaviour

In order to evaluate the performances of a materials, two parameters are mainly used in literature: the specific capacity and the initial coulombic efficiency. It is common knowledge that the specific capacity of Li⁺ in graphite is 372 mAh.g⁻¹; such values are the goal to obtain with Na⁺ in hard carbon as well. The ratio between the de-insertion capacity and insertion is called the **coulombic efficiency**, it is a key parameter to judge the viability of the battery: if the reactions are not reversible, then the life span of the battery is drastically reduced. The aimed coulombic efficiency is 100 % for each cycle to keep the best performances all along the cycling. A cell is at its end of life after losing 20% of its initial capacity [13]. During the first discharge of the cell (Na⁺ insertion), irreversible reactions happen with the material and the electrolyte to form a more or less thin layer at its surface called the solid electrolyte interface (SEI). The degradation of the electrolyte occurs in every cell [51], when the energy of the high occupied and low unoccupied molecular orbital (HOMO, LUMO) are respectively below and above the anode potential. A stable and homogeneous SEI protects the electrode from more electrolyte degradation, otherwise it leads to a continuous capacity loss [13] and a lower **initial coulombic efficiency (ICE)**. The higher the ICE, the higher the battery's energy density [52].

Even if the sodium insertion (sodation) mechanism is not fully understood, the hard carbon physico-chemical properties have already proved to have a major impact on the Na⁺ insertion and de-insertion. First of all, the degree of graphitization is a key parameter. To evaluate it, the interlayer space d_{002} is crucial. Cao *et al.*, while working on the sodium insertion mechanism, evaluated the critical minimum space between the layers. They calculated that at least 0.37 nm is required [53]. It is coherent with experimental observations [11]. Moreover, defects on the lattice allow sodium ions to be reversibly stored. Their influence is still discussed, mainly about the mechanism that will be described in the next part, and thus, the electrochemical behaviour regarding the defects of heteroatoms or structural [27], [31].

As its name suggests, the SEI is created in contact at the interface between the electrode and the electrolyte. As a result, a higher specific area of the hard carbon leads to a lower ICE [22], [54], [55]. A low surface area is then required. The SEI is not the only factor dependent on the surface. Many authors highlighted that a large specific area leads to a poor low-potential capacity and a decrease in the cycling behaviour [54], although it also allows electrolyte percolation which is needed for a high power capability [27]. From this point of view, a good comprehension of the SSA is required.

An overview of the hard carbon synthesis conditions, properties and electrochemical performances is presented in part 3. of this chapter.

1.3.5. Insertion mechanism

It is well admitted that the electrochemical profile of charge/discharge is composed of two areas, so-called the “slope” region and the “plateau” region, as described in **Figure 8A**). The difference in capacity between the charge and discharge curves is related to the irreversible reactions that occur, like SEI formation, as described before. Sodium can be stored at different places in the hard carbon: at its surface and in the defects by adsorption, between the graphene layers by intercalation, or in the pores by filling as it is represented in **Figure 8B**). However, what happens at the nanometric scale during the cycling split the scientific community. Depending on the method and hard carbon used, opposite mechanisms were deduced that highlights the lack of knowledge and the need of further investigations. The different mechanisms are presented in **Figure 9** and described below.

The first mechanism proposed, called the insertion-filling model, was presented by Stevens and Dahn in the early 2000s [28], [56]. They worked on carbon materials with different structures, porosities, crystallinities and compositions and compared both lithium and sodium intercalation, characterised by in situ XRD. They observed an increase of the d_{002} with the voltage and concluded on a two-step mechanism. They attributed the potential decrease to the slop area to the cation intercalation and the adsorption-like mechanism in the nanopores to the low voltage plateau.

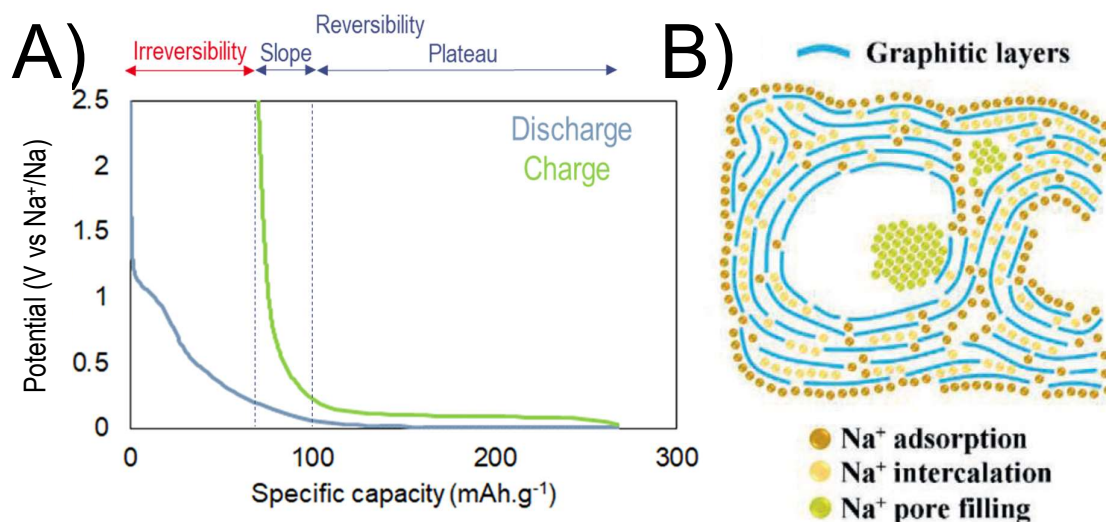


Figure 8: A) Typical hard carbon first cycle reduction – oxidation pattern and B) Schematic illustrations of Na⁺ storage in hard carbon [29].

Nevertheless, other studies showed different results leading to the opposite conclusion: Cao *et al.* [53] worked on hollow carbon nanowires and assembled half cells both with sodium and lithium electrolyte. The discharge-charge profile of the cell with Li electrolyte does not exhibit a plateau area at the opposite of the Na electrolyte. As mentioned in section 1.3.4, Na⁺ almost do not insert between the graphene layers, which discredits the insertion filling model. Instead, the authors proposed the adsorption-insertion model, where the slope is attributed to the Na⁺ adsorption and the plateau to its intercalation. Bommier *et al.* [57] went further in this interpretation; they measured an increase of the sodium diffusion coefficient at the end of the plateau, on their sucrose-derived hard carbon with different turbostatic areas. They attributed this behaviour to the surface pore filling. The sodation would then be in three stages: the adsorption in the slope area, the intercalation at the beginning of the plateau, and a small contribution of pore filling at the end of the plateau. A four stage model was even deduced by Alvin *et al.* [58]: they observed an additional pore-filling zone at the beginning of the plateau. The slope, similarly to the adsorption-insertion and the three-stage models, is attributed to the sodium adsorption at the surface and defects of the hard carbon. The beginning and the end of the plateau are attributed to the pore-filling, and its middle to the sodium insertion.

Different authors have investigated and admitted all these mechanisms, revealing how complex the sodation is. Sun *et al.* [10] reported different mechanisms depending on the hard carbon structure: they worked on ginko leaves they pyrolysed from 600 to 2500 °C for 2 h. The resulting materials covered a large panel of properties, particularly on the d_{002} , as explained in section 1.3.3. They observed different mechanisms depending on the interlayer distance: above 4 Å; the space is big enough to allow “pseudo-adsorption” of the sodium ion, while between 3.6 and 4.0 Å the mechanism is insertion. No insertion nor other mechanism below 3.6 Å. Regarding the attribution of the different mechanisms to the charge profile, they described a model similar to Cao *et al.*, with the plateau linked to the insertion; and

the slope to the adsorption at the surface, edges and defects, as well as the pseudo-adsorption between the spaced graphene layers. They called their model the extended adsorption-insertion model.

One last model was reported in 2016 by Zhang *et al.* [59]. They worked on carbon nanofibres obtained from 650 to 2800 °C, they followed the first discharge of the half cell in situ, and observed no d_{002} change during the cycling that the Na^+ insertion should induce: they discredited this mechanism. Instead, they observed an increase of the plateau with the decrease of the material's porosity. Hence, they described the adsorption-filling model: the slope was attributed to the sodium adsorption, similarly to most models, but the plateau to the pore filling.

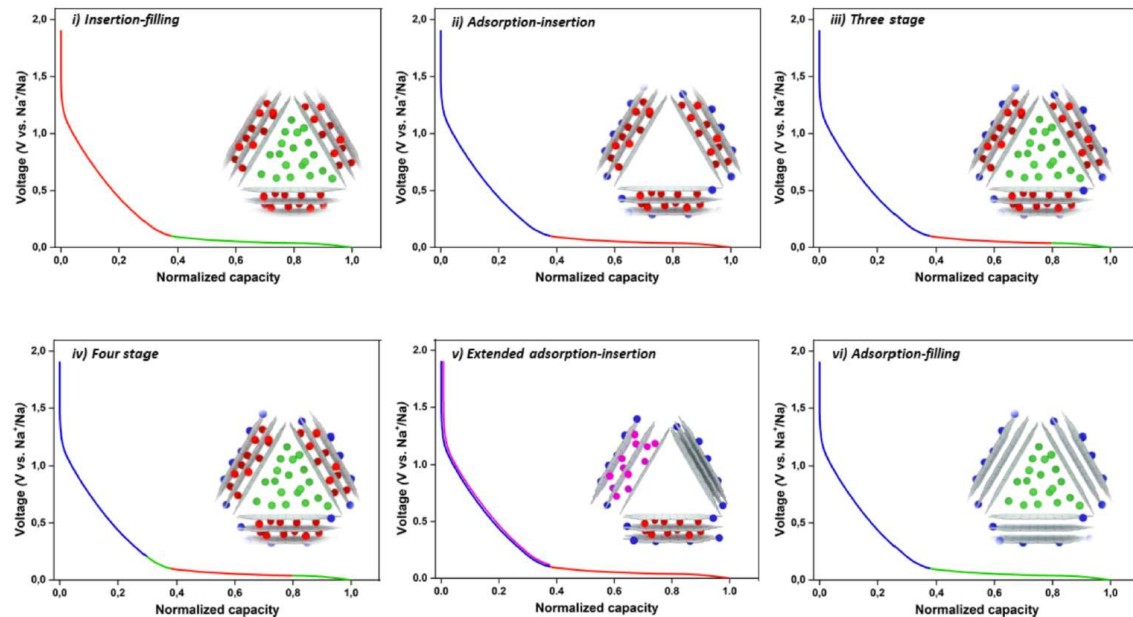


Figure 9: Representation of the different sodium storage mechanisms, from [20].

Therefore, the sodation mechanism is still not fully understood and requires more investigation. Here, six models were presented, but more were reported depending on the material. Indeed, it seems agreed by almost all models that the slope is due to the sodium adsorption at the surface, edges, and defects of the materials, while the plateau area cause is still confused. However, it appears that the sodation mechanism is highly dependent on the structure of the hard carbon, as highlights Sun *et al.* when they described their extended adsorption-insertion model. Over time, many authors investigated the mechanism and used various techniques on a wide range of materials; all the presented models have been validated by other authors despite them all being different [13], [29], [31], [60]–[63]. It highlights the importance the hard carbon has on the mechanism and hence the performances.

To better predict the final cell capacities, it is then important to control the properties as the interlayer space, the porosity or defects, since it directly impacts the sodation. As explained in the **Introduction**, using waste biomass as raw material for hard carbon production is a promising valorisation. It is then essential to determine the feedstock's impact on the resulting material, design its physico-chemical properties to provide the best performances. These two aspects are detailed on the following parts: first,

generalities about biomass are presented with a promising valorisation thermal treatment: hydrothermal carbonisation. The impact this pre-treatment has on the material is described. Second, a scope of the biomass-based hard carbon is reported with the influence the raw material has on its final properties, followed by the influence of the HTC pre-treatment on the cell performances.

2. Biomass conversion to biochar

2.1. Biomass specificities

As explained earlier, the most promising material for negative material is hard carbon. It can come from fossil resources or renewable. Biomass represents an important amount of carbon and interest molecules produced yearly, and most of the time it is underexploited. By characterisation its amounts and composition, it is possible to re-use waste matter and optimise process to reduce environmental impact at the same time as costs. They are described below.

2.1.1. Definition and amount

Biomass was defined by Vassilev *et al.* [64] as: “Biomass is contemporaneous (non-fossil) and complex biogenic organic–inorganic solid product generated by natural and anthropogenic (technogenic) processes, and comprises: (1) natural constituents originated from growing land- and water-based vegetation via photosynthesis or generated via animal and human food digestion; and (2) technogenic products derived via processing of the above natural constituents.”. According to them, it can be divided in 6 varieties:

1. Wood and woody biomass: everything that is wood related: stems, branches, foliage, bark, chips...
2. Herbaceous and agricultural biomass: annual or perennial, grass, flowers, straws, fruits, shell, seeds...
3. Aquatic biomass: algae, macro/microalgae, water plants...
4. Animal and human biomass wastes: bones, meat, manure...
5. Contaminated biomass and industrial biomass waste: municipal solid waste, sewage sludge, demolition wood...
6. Biomass mixtures: blends from the other varieties

According to Bar-on *et al.* [65], there are about 550 Gt of carbon on Earth, where 80 % are plants. To determine the quantity of biomass produced and available is a challenge, as highlighted by Becerra-Pérez *et al.* [66]: it is complicated to have an accurate amount since the numbers are assumptions depending on the condition of the study and the location. However, Bentsen *et al.* [67] estimated the global production per year of 3.7 billion tons of agricultural residues. At the same time, the European Commission reported around 1 billion tons of agricultural biomass per year in Europe, where 46 % are residues [68], which are commonly under valorised and considered as waste. Instead of disposing of them, they represent an essential input for high-value products, and they can be used for platform molecules or high added value

products. To that end, it is necessary to know their composition to valorise them the best, which is described below.

2.1.2. Composition

Biomass is organic matter, composed mainly of C, H and O. It also contains N, S and inorganic elements, such as Ca, K, P, Si, usually gathered as ash. However, the composition is highly dependent on where the biomass is collected, the biomass type, which part of the biomass is selected, and when it is sampled. It is even more accurate for contaminated and industrial waste, which regroups very wide materials. A summary of the main components among the different biomass varieties is detailed below.

2.1.2.1. Moisture

It has to be kept in mind that every biomass contains water. The term “wet biomass” is used for moisture contents higher than 60 % by opposition of the “dry biomass” for lower contents. The intrinsic moisture is naturally present in the material, while extrinsic moisture depends on the weather and the environment.

On a wet basis, terrestrial plants are composed of 10 to 70 % of water, while algae range usually between 70 to 90 % [69]. Studies reported moisture contents ranging from 30 to 60 % for wood bark only, or 25 to 55 % for sawdust [70]. These large ranges for similar feedstock highlight the heterogeneity among the biomasses.

Because the amount of water in the material is highly dependent on external factors, such as the weather, temperature and storage conditions, the composition of the different components described below are usually expressed on a dry basis, meaning without taking any moisture in consideration in the material composition by drying it first.

2.1.2.2. Macromolecules

Plants are composed mainly of 3 macromolecules: cellulose, hemicellulose and lignin, which gives them the name of lignocellulosic biomass. Cellulose, the most abundant polymer on Earth, represents 35 to 50 % of the plant cell wall. This glucose polymer can form crystalline zones by stable hydrogen bonds, which can have a crystallinity of 50 to 90 %, linked together by amorphous zones [71]. Hemicellulose represents 20 to 30 % of the plant. This polysaccharide is composed of hexose and pentose units, mainly xylose, arabinose, mannose, galactose and glucose, with a composition that varies depending on the feedstock [72]–[74]. At last, lignin represents 15 to 25 % and is the only abundant aromatic polymer on Earth. It is composed of monolignol units, with three main units of p-coumaryl alcohol (H), coniferyl alcohol (G) and sinapyl alcohol (S). It forms a rigid structure, protecting the polysaccharides from microbial attacks [74], [75]. While cellulose structure is very well known and is organised as microfibril assembly, the hemicellulose structure is more complex: the polymer chains are shorter and branched. Lignin structure is not well known and is still investigated [76], [77]. Interestingly, cellulose can be described as a 1D polymer, hemicellulose as 2D and lignin 3D. The three polymers are closely linked together by hemicellulose, due to acetylation of free hydroxyl groups, creating highly hydrophilic areas [74]. Lignocellulosic structure is shown in **Figure 10** below.

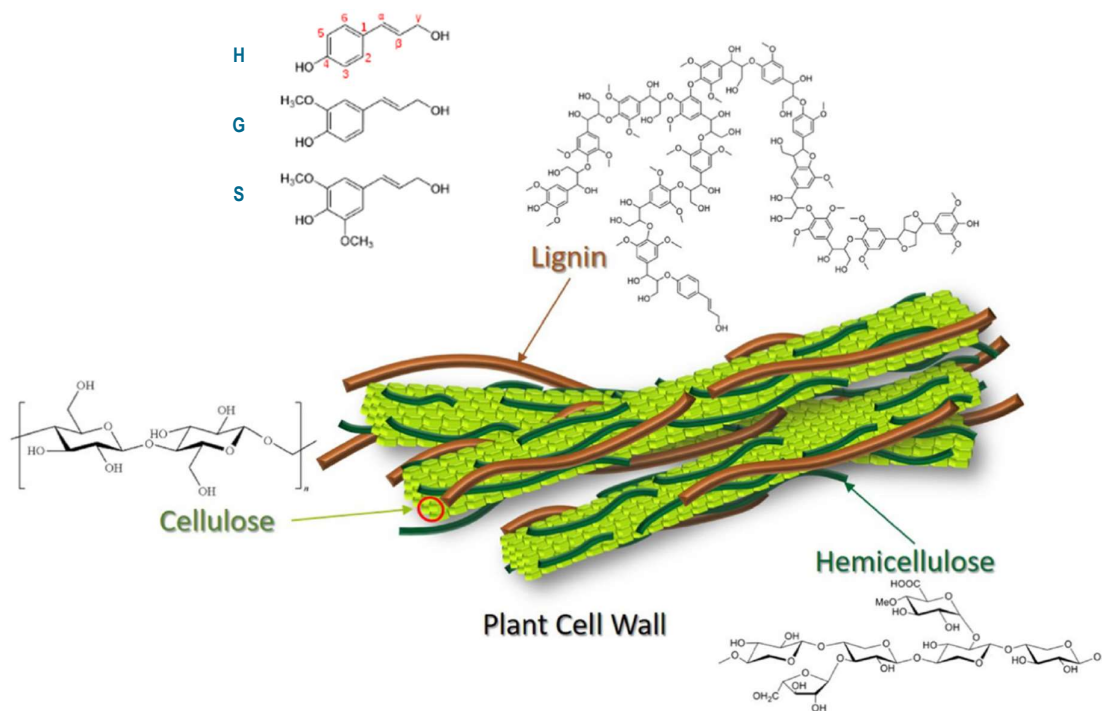


Figure 10: Lignocellulosic biomass structure, adapted from [78]

Their proportions depend on the feedstock, each of them giving different properties to the material. Vassilev *et al.* [79] regrouped more than 93 lignocellulosic biomass from different studies to determine tendencies among their compositions, based on these three components only (without taking into consideration extractives and ash). Wood stems and agricultural residues appeared to be richer in cellulose, with no tendency between hemicellulose and lignin. Conversely, most wood barks, twigs, leaves and some grass are richer in hemicellulose. At last, lignin seems to be in higher quantity in shells, husks and some bark. As already mentioned, it gives rigidity to the cells; it is indeed coherent to have higher contents in woods and shells than leaves or stalks. Algae also contain polysaccharides; they can be composed of half of carbohydrates but contain only a few percent of lignin [80].

Manure may contain cellulose or lignin, depending on the animal forage. It is indeed known that these molecules are not degraded during digestion; good quality forage contains low amounts of lignin and indigestible fibers [81].

2.1.2.3. Extractives

“Extractive” describes any molecule extracted in hot water or organic solvent, such as polyphenol, proteins, lipids, or saccharides. Their proportion and nature is highly feedstock dependant, as well of the extracting method used.

Lignocellulosic biomasses contain a minor proportion of extractives, usually from 0 to 15 % [82]. Vassilev *et al.* [79] listed the main common ones: saccharides, proteins, hydrocarbons, oils, aromatics, lipids, fats, starches, phenols, waxes, and inorganic compounds. In lower proportions, they also contain chlorophyll,

resins, terpenes, terpenoids, acetyls, uronic acids, organic acids, sterols, and glycosides; and may also contain small amounts of minor organic components such as alkaloids, gums, mucilages, dyes, saponins, tannins, or flavonoids. Herbaceous and agricultural residues are usually richer in extractives than woody products [79]. Algae are known to contain high lipid contents, and may also be rich in protein or carbohydrate [69].

Manure is usually rich in nitrogen, like ammonia [81], or phosphorus species [83], commonly used as compost for soil amendment due to their mobility.

2.1.2.4. Ash and inorganics

Ash regroups any inorganic compound, small molecule like oxide, phosphate, or silicate, and any other compound that does not burn after calcination. Some of the ash can also be extracted by water or solvent, and can be considered both ash and extractive.

Many inorganic species are reported in lignocellulosic biomass. However, their nature and content depend on the plant. According to Vassilev *et al.* and their critical review already mentioned [79], there are some trends among the different lignocellulosic biomass categories: woody products usually have more Ca, followed by Si, K, Mg, Al and P in this order; while grass and straws are richer in Si, K and Ca in this order, followed by P, Mg and Al for grass and Mg, P and Al for straws. Other agricultural residues, such as husks or shells, are usually richer in K, Si, Ca, P, Mg and Al in this order. Even among the different part of the same biomass, their compositions vary: for instance, wood bark is known to concentrate the inorganics by contrast with the stem part that is very low in ash. The quantity also highly vary between the kind of plant: fast-growing and annual crop are richer in moisture, inorganics and elements such as Ca, Cl, K, Mg, N, Na, P and S. These elements are known to move through the material and be exchanged with its environment [69].

Manure is rich in P, as already mentioned in the previous part. They also contain K and Si species, however, the ash contents depend on the animal, their forage, and the bedding. Only on dairy manure, Reeves and Van Kessel [84] reported from 99 samples ash contents ranging from 8 to 52 wdb%, highlighting the heterogeneity among the same animal.

Sewage sludge is reported to contain Si, P, K, Ca, S, Cl and Na [85], as well as various heavy metals [86], [87], in proportion depending on their origin. They usually contain P, which is usually recovered [88]. While some elements are present from the start, others come from their treatment. For instance, Fe and Al sulphates are used as flocculants for P removal [88], [89].

2.2. Pyrolysis

Pyrolysis was briefly described in 1.3.2 for hard carbon synthesis. However, it is usually used at lower temperatures, from 300 to 600 °C, to provide a carbonaceous material with an important amount of O, N and H. This solid is called pyrochar, it is also reported as biochar despite this term refers to any charcoal produced from biomass but does not specify its synthesis method. It is indeed one of the most used thermal treatments and is often compared with the others. Three phases result from pyrolysis: the pyrochar, tars

and gas. Their proportion is strongly dependent of the operating conditions, especially the heating rate and temperature [90].

The mechanisms are not fully understood yet and greatly depends on the starting material. Most of the studies investigated lignocellulosic biomass, described below and summarised **Figure 11**. Below 120 °C, drying occurs. Polysaccharides start to degrade at about 150 and 200 °C to depolymerize and recondense, by solid-solid reaction mainly, which results smaller molecules. They are themselves degraded themselves into even smaller molecules [91], and then volatised with the increase of temperature. Unlike the other macromolecules, lignin suffers glass transition before decomposition [92]. During the reaction, gases are released: combustibles such as as H₂, CO, CO₂ and CH₄ from small molecule degradation, and condensable gas [34]. At 450 °C, all the macromolecules are degraded, and the pyrochar is composed of degradation and condensation products.

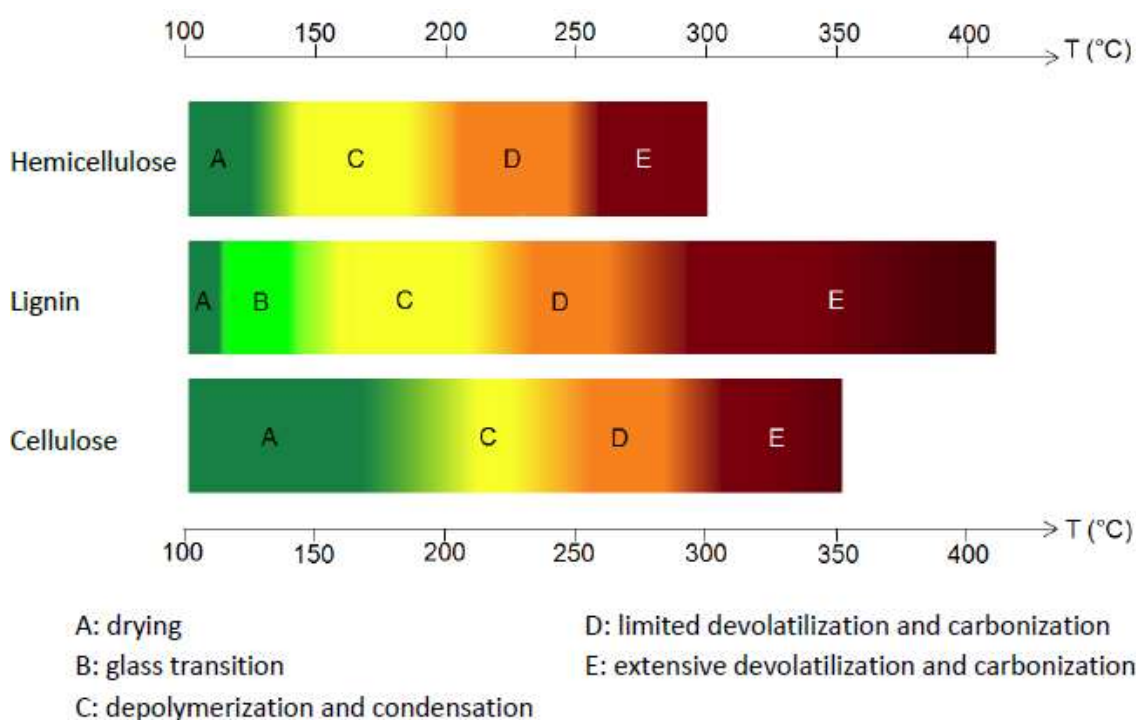


Figure 11: Thermal stability of hemicellulose, lignin and cellulose. Adapted by [90] from [92].

2.3. Hydrothermal carbonisation

Hydrothermal carbonisation is a heating treatment where the sample is immersed in water in a sealed reactor. Thus, the temperature can reach higher temperatures than 100 °C, leading to an increasing pressure, between 10 to 50 bar. The process occurs under the subcritical region. In these conditions, water's hydrogen bonds are weaker, enhancing the dissociation of water into acidic hydronium ions (H₃O⁺) and basic hydroxide ions (OH⁻). Acid-catalysed reactions can thus occur without adding acid [93]. They are usually performed at temperatures between 180 and 250 °C, for 30 min to 24 h. At the end of the process, three phases result: the solid part, the hydrochar, usually the main product; the liquid phase

composed of aqueous small molecules, mainly organic acids, furfurals and phenols [94]; and a minor gas fraction, which is mostly CO₂ but can also contain small amounts of CO, H₂ and CH₄ [93].

2.3.1. Reaction mechanisms

The mechanisms are not fully understood and are still investigated. Many studies try to clarify them, depending on the operational conditions and the origin of the biomass [95], [96]. These are summarized in **Figure 12**. It is established that there are two kinds of reactions: solid-solid reaction; and solid-liquid with the aqueous intermediates released during the process using different pathways depending on the experimental conditions and feedstock. Water molecules are removed from the biomass matrix by dehydration, reducing the amount of H and O [97]. Ester and ether bonds are cleaved by hydrolysis, which transforms cellulose and hemicellulose into monomers, mostly glucose and other C₆ and C₅ sugars. Yet, due to its inorganic and short branched chains between its various carbohydrate units, hemicellulose is easier to degrade: it is fully hydrolysed at 180 °C. Cellulose requires higher temperatures about 220 – 250 °C, while lignin is more stable and difficult to hydrolysed [95]. C₆ carbohydrates are then degraded in 5-(hydroxymethyl) furfural (HMF) and C₅ to furfural, which are then degraded into acids, such as levulinic acid, formic acid, and dihydroxyacetone. Decarboxylation occurs above 150 °C, during which carboxyl and carbonyl groups form respectively CO₂ and CO. The amount of CO₂ produced let think that also degradation product, more likely formic acid, is also a source of CO₂. A hypothesis is that water acts as an oxidizing agent in hard conditions. Polymerization also occurs during HTC with the highly reactive compounds that are formed. The last reported mechanism is aromatization. Carbohydrates – products of polysaccharide hydrolysis – can form aromatic structures in HTC conditions, increasing their reactivity. This mechanism is enhanced by alkaline conditions [95], [97].

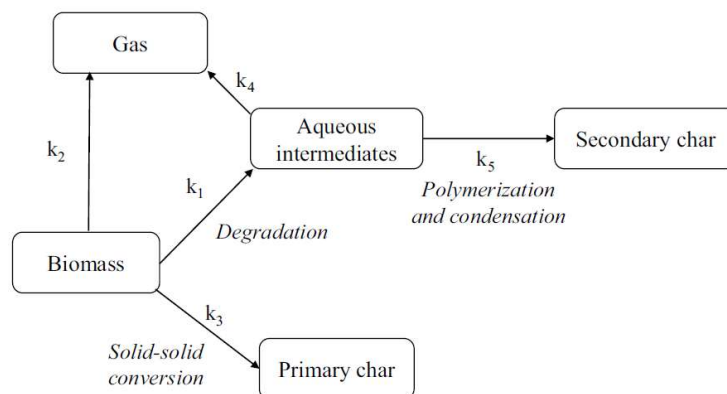


Figure 12: Simplified HTC reaction pathway, from [98]

A primary char is formed by dehydration of the biomass and solid-solid reactions; then the degradation products in the liquid phase react together with the solid to form a secondary char. The solid part is called hydrochar, despite some authors refer this term for the primary char only, while the secondary is called humins [97].

2.3.2. Process parameter influence

The different parameters are discussed in this part, and the influence of each is summarised in **Table 2**. Only a few studies deal with the heating and cooling rate, and the stirring. It will not be discussed in that part.

Table 4: Operational parameter influence on hydrochar properties adapted from [93] and completed with the analysis below. + means increasing the parameter increases the value, - it reduces it. nd stands for no data.

	Solid yield*	Surface area	Porosity	H/C	O/C	Inorganics
Temperature	-	+	+	-	-	+
Residence time	-	+	+	-	-	+
Feedwater pH	nd	-	-	+	+	nd
Substrate concentration	+	nd	nd	+	+	nd
Heating rate	-	nd	nd	+	+	nd

* Solid yield refers to the mass ratio of the hydrochar and the initial biomass.

2.3.2.1. Temperature

As already mentioned, parameters have a major influence on the yield and structure of the hydrochar. Studies lead between 150 and 280 °C on various feedstock, such as tomato peels [99], dairy manure [100], or miscanthus [101] observed similar influence of the temperature on the final product. Because the temperature directly impacts the hydrolysis level of the material and, therefore, the degradation of intermediary products, it is one of the most influential parameters. Under subcritical conditions, radical-free reactions occur, leading to polymerisation and condensation mechanisms [97]. Since the mechanisms that occur with the heat are bond-breaking, the solid fraction resulting decreases, as well as the H/C and O/C ratios, which results in a denser and carbon-rich material. Some authors describe a pyrolysis-like process when the temperature is not high enough to break bonds, a solid-solid reaction [93]. One has to keep in mind that the hydrochar still has an important amount of H and O, about <10 % for H and 10-40 % for O. C content is also affected during the process, which is highlighted by CO₂ production [99] and the organic composition of the liquid. Hence, the higher the temperature, the lower the solid yield, but the hydrochar is more carbon rich.

Moreover, the temperature has an impact on the inorganics. It is known that under the reaction conditions, alkali and alkaline earth metals leach into the liquid phase, contrary to heavy metals that stay in the hydrochar as oxide [102]. K and Na are widely solubilised under HTC conditions [103], and a majority of Ca, Mg and P as well [104]. However, Smith *et al.* [105] highlighted that some elements, Ca, P and Mg, tend to end in the liquid phase at 200 °C but reincorporate the solid at 250 °C. This trend was also reported by Reza *et al.* [104] on four other lignocellulosic biomass between 200 and 260 °C. They attributed this phenomenon to the reaction between these elements and the degradation products at such temperature. Unfortunately, they only work on short residence time of 0 and 1 h, which cannot conclude on longer time.

2.3.2.2. Residence time

The first mechanisms that occur are hydrolysis and solubilisation, which lead to solid yield decreasing. A longer time allows polymerisation and aromatisation reactions, which contribute to microsphere formation at the surface of the hydrochar. Smith and Ross [106] determined that between 1 and 4 h are required to fully hydrolyse miscanthus at 250 °C and allow almost complete polymerisation and aromatisation reactions. These mechanisms contribute to microsphere formation at the surface of the hydrochar. Gao *et al.* [107] described this mesoporous structure with a sponge-like morphology as the hydrolysed polysaccharides transformation. They also reported the size of the microsphere increases with the reaction time. However it has a limit: after 24 h no more changes were noticed [95].

As already mentioned above, HTC is known to leach K, Na, Mg, Ca and P during the reaction, however with the increase of the reaction time, P, S and Ca were reported to reincorporate in the char [93], [96], [106], [107].

2.3.2.3. Solid-liquid ratio (substrate concentration)

The two parameters with the highest impact on the product are temperature and residence time. Yet, reactions are also influenced by other factors. By increasing the solid/liquid ratio, the solid yield also tends to increase. It was explained by biomass monomers that are more concentrated, which favour the chance of polymerization [97]. However, too high substrate concentration prevents its hydrolysis, which influences the reaction intermediates and thus the char itself [93].

This observation was made on municipal waste [94], but no influence on hydrochar composition and thermal properties was reported. According to this work, this factor is significant for energy yield, for energy applications.

2.3.2.4. Feedwater pH

As already mentioned, organic acids are produced during the reaction, leading to a pH decrease. They allow reactions to happen, and HTC process is considered autocatalytic. However, some studies report catalysis with alkali or acids, added in the reactor, to enhance the ionic strength. High concentrated acid and base were reported to accelerate the cellulose dissolution, and enhance the carbonisation by favouring dehydration. Lignin degradation is more impacted at higher pH than cellulose and hemicellulose. Also, structure is impacted by the acidity: low pH leads to more porous material and enhances micropore formation [93].

2.3.3. Feedstock influence

As mentioned in part 2.1, biomass is a broad category that regroups any carbon material, including plants, as much as sludge and industrial effluents. Their compositions, structure and properties are very different, leading to different hydrochars summarized in **Table 5**.

Table 5: Feedstock influence on hydrochar properties (adapted from the discussion below [93], [96], [108], [109]). + means increasing the parameter increases the value, - it reduces it, and = it has no impact. nd stands for no data.

	Solid yield*	Surface area	Porosity, microsphere	H/C	O/C
Lignin	-	+	nd	nd	nd
Polysaccharides		+	+	nd	nd
Inorganics	+/-	nd	nd	nd	nd
Ca	-	nd	+	nd	nd
Na, Mg, K, Ca	-	nd	nd	nd	nd
Heavy metals	+	nd	nd	nd	nd

* Solid yield refers to the mass ratio of the hydrochar and the initial biomass.

2.3.3.1. Macromolecules

Most studies dealt with lignocellulosic materials and linked the macromolecule compositions to the hydrochar properties. As described in 2.3.1, hemicelluloses are easier to hydrolyse at the opposite of lignin, hence higher lignin content leads to a higher solid yield, the mass ratio between the hydrochar and raw material [96]. However, the three biopolymers are mixed together and interact with each other. In fact, lignin is reported to hinder polysaccharides' hydrolysis [95]. To understand the interactions between each and figure out the mechanisms during HTC, Rodriguez Correa *et al.* [96] analysed 3 biomasses of 3 ways: each biopolymer separately, mixed together in a synthetic biomass and the original one. They highlighted the strong interaction between each: the solid yield is much lower with the synthetic biomass than the original one, from 10 to 50 %. It was attributed to the shielded effect of lignin on the other components. However, it has to be kept in mind that the extracted macromolecules and the ones in the biomass are not exactly the same.

Also, lignin tends to be degraded as aromatic and reactive monomers favouring secondary char production and decreasing the liquid pH. The hydrochar is then more porous [93], [96], [108]. In another hand, Rodriguez Correa *et al.* [96] reported the importance of the biomacromolecule composition, on three agricultural wastes; wheat straw, pine bark and macauba nut shell. They conclude a higher carbohydrate content enhances microsphere formation from secondary char formation, leading to a higher surface area. The structure is more similar to raw biomass at low temperatures because of the low degradation of the material [93]. Carbohydrates in other biomass such as sewage sludge or industrial wastes have the same impact on the microstructure [109].

2.3.3.2. Ash content and inorganic composition

The ash also influences the yield: some inorganics leach in the liquid phase while others stay in the solid depending on their water solubility. So, K, Ca, P and Na are dissolved in the liquid, when Al, Fe, and heavy metals [96], [102], [105]. However as mentioned in 2.3.2.2, when the time increases, P, S and Ca were reported to reincorporate the char [93], [96], [106], [107]. Furthermore, many studies [106], [107], [110] highlighted the catalytic effect of Ca on the porous morphology of the char, and Chen *et al.* [110] also linked it to Ca²⁺ concentration: low concentration leads to fewer and bigger pores. Calcium ions were also reported to favour gas production instead of solid [96].

Some components in biomass can be crystalline, such as quartz or oxide. With the degradation of the raw biomass amorphous structure, their crystallinity can increase [108].

3. Biomass-based hard carbon for Na-ion batteries

As already described in 1.3, hard carbon can be synthesised from biomass, biopolymer or synthetic polymers. However this part will only treat biomass materials. As detailed in 1.3, to achieve good performances, a material with a low degree of graphitization, with defects and microporous is recommended for Na-ion applications.

3.1. Feedstock influence

Studies led on biomass focus mainly on woody products (such as wood and bark residues [111]) and herbaceous residue (straws [111], fruit shells and peels [40], [55], [112], [113]). As explained in this chapter, these biomasses are convenient because of their low price, large availability and low moisture content compared to wet biomass that requires a drying step before the carbonisation. This last point avoids an important energy-consuming step, however it is possible to use wet biomass as well after removing the water from the material as shown in studies lead on algae [114], [115]. Some of the many works performed on biomass are summarised in **Table 7**, at the end of this chapter, and the feedstock composition influence on the resulting hard carbon are summarised in **Table 6**.

It has been highlighted that O and S seem to prevent graphitisation [24], [116], unlike high H content that seems to lead to a more organised material. Furthermore, Wu *et al.* [42] worked on lignocellulose materials and tried to determine the influence on each macromolecule by working with them separately and mixed in a real biomass, similarly to the work of Rodriguez Correa *et al.* [96] described in 2.3.3 on HTC. They determined that lignin aromatic rings lead to a more compact material, while the crystallinity of the cellulose gives a more organised material. They recommend that a high cellulose/lignin ratio should lead to a high-performance hard carbon in Na-ion batteries. It also appears that lignin tends to lower surface area. Hemicellulose was also reported by Feng *et al.* [117] to increase the material's graphitisation. They linked the early decomposition of the macromolecule to the increase of order. However, despite this decrease of d_{002} , it does not seem to be the major parameter that influences the properties: Saavedra [11] reported no significant difference between grass-derived materials, rich in hemicelluloses, and wood and agricultural residue-derived materials.

A major parameter on the final material's physico-chemical properties is the ash content. Inorganics catalyse local graphitisation in the resulting hard carbons, as observed in biomass-based hard carbons [30], [118]. Saavedra *et al.* [118] tried to link the feedstock ash composition to the electrochemical performances by working on 25 different woody, grass and agricultural precursors carbonised under the same two-step pyrolysis at 450 and 1400 °C. They observed the low volatilisation of inorganics, which remains in the resulting hard carbon as SiC for wood and grass materials, and as Na and Ca oxide and sulfur for agricultural residues. They highlighted a higher specific surface area for material with higher ash

contents, especially Si-rich that could be explained by the SiC whiskers formation at the surface. They went further by observing both the plateau and slope capacity during the charge of their half-cells. Higher ash content – especially Si – and lower C contents were linked to poorer charge capacities and lower plateau capacity. Interestingly, it seems that Ca negatively impacts the performances only in the presence of Si: the author deduced a local synergic graphitisation effect. They were able to obtain hard carbon with high ICE between 76 to 87 % and reversible capacities between 260 to 314 mAh.g⁻¹ at 37.2 mA.g⁻¹ for woody products and agricultural residues, while grass precursors showed lower performances between 70 to 74 % and 225 to 271 mAh.g⁻¹ for the ICE and reversible capacity respectively. It appears the raw composition has no major impact on the discharge.

Table 6: Summarize of the influence of the feedstock on hard carbon properties. + means increasing the parameter increases the value, - it reduces it, and = it has no impact. nd stands for no data.

	d₀₀₂	Surface area	Pores size	Defects
Lignin	-	-	nd	++
Cellulose	+	+	-	nd
Hemicellulose	=	+	-	=
O, S	-	nd	nd	+
K, Ca, Si	- - -	+	nd	+

In order to control the resulting hard carbon properties, many pre-treatments and post-treatments have been investigated. The most common is washing to remove the inorganics. They can be performed in acid, base or organic solvent, before or after the pyrolysis. In order to determine if the inorganics have an impact only during the synthesis or also during the cycling, Beda *et al.* [30] worked on electrodes from acid-washed hard carbon and compared them with pristine. They worked on three food waste materials; asparagus peel, grape pomace and potato peels; and pyrolysed them at 1400 °C. They washed the hard carbon with HCl (18.5 %) and compared the pristine and acid-washed materials. Most of the inorganics were removed, lowering the d₀₀₂ and increasing the porosity. However, for one of their materials, the grape pomace, inorganics were trapped in the structure due to the local graphitisation they induced. They also highlighted the interaction between the inorganics and oxygen, the washing resulting in decreasing defects and surface chemistry. To go further in their analysis, they also washed of their materials in water before annealing instead of an acidic post-treatment. They observed similar d₀₀₂ and defects to the acid-washed material, however, the surface chemistry and area were largely lower.

Washing is the most common treatment, however it is not the only one. KOH activation gives a higher surface area composed of more and smaller pores, which tend to increase the Na-ion battery performances [113], as long as the structure is not too damaged by concentrated base [29]. Adamson *et al.* [55] worked on both basic then acidic treatment, and observed the same behaviour. Acidic pre-treatment are reported to reduce the inorganic impurities, which tend to increase the structural order of the hard carbon [29], [30].

Many authors use HTC as pre-treatment of their pyrolysis: it has the advantage of increasing the yield, and controlling the resulting material's morphology. It is described in the next section.

3.2. HTC pre-treatment for hard carbon synthesis

The combination of HTC and pyrolysis is widely used for hard carbon production from biomass waste, as try to summarise **Table 8** at the end of this chapter. HTC is usually performed during important residence time, usually longer than 10 h, to favour a stable and spherical morphology and temperature around 180 to 200 °C to decompose the macromolecules, as explained in part **2.2**. Few studies use lower temperatures lower than 180 °C; it is then not considered as HTC. However, the authors also use temperatures in the HTC range that make them suitable for our investigation.

To understand the HTC temperature impact on the resulting hard carbon, Cong *et al.* [119] carbonised corn stalks from 100 to 180 °C for 12 h before pyrolysing them at 1000 °C for 1 h. They highlighted the loss of inorganic compounds and the increase of thermal stability in the hydrochars, leading to hard carbon with homogenous d_{002} of 4 Å, and I_G/I_D increasing from 0.92 to 0.70 for respectively the materials obtained from HTC at 100 and 160 °C. However, they reported a collapse of carbon sheets and the disappearance of porosity structures at higher temperatures. They compared the materials with an untreated hard carbon; the d_{002} was similar, however a higher I_G/I_D of 0.59 and lower surface area of 3.95 m².g⁻¹ (compared to 9.24 m².g⁻¹ for the 160 °C-hydrochar), leading to lower performances. While the ICEs of the pre-treated hard carbons were comprised between 60 and 65 %, the pristine material only exhibits 58 %, with a reversible capacity of 233 mAh.g⁻¹ compared to the 160 °C-hard carbon, reaching 268 mAh.g⁻¹ at 60 mA.g⁻¹. Hence, it seems that at least 160 °C is required during the pre-treatment to provide satisfying hard carbon.

Zheng *et al.* [120] similarly worked on the HTC temperature impact, however, they also acid-washed their hydrochar before the pyrolysis, which made their study not only on the HTC impact. They used holly leaves that they carbonised at 140, 160, 180 and 200 °C before a 3M HCl wash; and the final pyrolysis at 800 °C. Again, the first temperatures are too low to be considered HTC. The materials were compared with hard carbon without the HTC step, but still with the acid-wash. Their material obtain from holly leaves after HTC at 180 °C had nanopores twice bigger than the untreated material, favourable to Na⁺ ion storage and providing better performances.

Instead of the first step optimisation, Wang *et al.* [121] worked on reed straws pyrolysed from 900 to 1500 °C, after an HTC step at 200 °C for 24 h. Similarly to what was described in part **1.3.3**, the increase of the annealing temperature reduces the interlayer distance from 4.0 to 3.8 Å and the I_G/I_D increased from 0.54 to 0.72, revealing the increase of graphitisation. The surface area dropped significantly from 325 to 23 m².g⁻¹, as well as the pore size. The best performances were obtained at 1300 °C, providing 372 mAh.g⁻¹ at 25 mA.g⁻¹ with a high ICE of 77 %. Gao *et al.* [122] worked on the same range of temperature on navel orange peels, however, they added more pre-treatment steps: first, an HTC at 180 °C for 6 h was performed, followed by a pre-carbonisation at 240 °C for 18 h and at last an acid-wash in 1M HCl for 6 h. They still observed the same trend: the higher the temperature, the lower the d_{002} ,

defects and surface area. Their best material was also obtained at 1300 °C, providing 337 mAh.g⁻¹ at 25 mA.g⁻¹ with a high ICE of 63 %.

Yan *et al.* [123] also worked on the pyrolysis temperature from oatmeal between 300 to 900 °C. These temperatures are too low to obtain hard carbon, nevertheless they provide N-rich materials. HTC pre-treatment was performed at 200 °C for 12 h to form microspheres. The resulting materials gave low ICE lower than 40 %, despite an interesting reversible capacity of 320 mAh.g⁻¹ at 50 mA.g⁻¹ from the material obtained at 500 °C.

Some authors add a few drops of H₂SO₄ to catalyse the reaction [112], [124]. Others proceed the reaction directly in acid: Wang *et al.* [125] performed their HTC in diluted H₂SO₄, while Wang and Su [126] carried out in 1M HCl and Cao *et al.* [127] on 10 % HNO₃. Basic conditions are also possible: to stronger the pre-treatment and remove lignin and hemicellulose from the rambutan peels they used, Arie *et al.* [40] proceeded the HTC in 1M NaOH at 200 °C for 20 h. A pyrolysis between 800 and 1200 °C followed on the resulting hydrochars. Despite this basic conditions, the trend among the resulting hard carbon was similar to the studies described above, as well as in part 1.3: increasing the temperature leads to a more organised and porous material, but with smaller pores and fewer defects. Their best material was obtained at 1000 °C, where usually higher temperature around 1400 – 1500 °C is recommended for direct pyrolysis.

It is also possible to add compounds in the HTC feedwater to impact the chemistry or surface of the material: Yang *et al.* [54] used salt-assisted HTC to reduce the pore size, while Demir *et al.* [112] incorporated SnO₂ particles to functionalize the final product.

At last, HTC pre-treatment also reduces the carbon emissions of the hard carbon synthesis process. Lui *et al.* [128] studied the life cycle assessment of two cellulose-based hard carbon: through direct pyrolysis at 1000 and 1300 °C, and after HTC for 12 h at 200 °C. Due to the higher yield and the best performances of the material obtained after HTC, its gas emissions are lower than the direct carbonisation, despite the additional step. By taking into consideration the electricity, water and inert atmosphere of each step for their scenarios at 1300 °C, they calculated the global warming production of 4.07 and 4.61 kg CO₂ – eq for the HTC pre-treated and direct pyrolysed hard carbon respectively, which is also lower than the 5.82 kg CO₂ – eq of commercial graphite.

Despite all these studies toward HTC pre-treatments, they usually focus on the hard carbon's physicochemical properties only, without considering its chemical composition nor the hydrochar's. The specific morphology, as well as the inorganic wash, induced by the process should provide promising materials, the lack of knowledge about the hard carbon composition should be filled.

Conclusions

Sodium-ion batteries are a major stake in future energies to replace Li-ion technology, because of the availability of the components. Nevertheless, lithium batteries are still cheaper and more efficient than sodium, which makes Na-ion unsuitable to fully replace Li-ion yet. Further investigations on the electrodes are required to reduce the cost and increase the performances. The more promising material for negative electrode is hard carbon, which is still very expensive nowadays. To reduce its cost, biomass wastes are very promising precursors.

Hard carbon has been investigated from various feedstock over time, and a link between the pyrolysis condition and the hard carbon structure has been highlighted. HTC pre-treatment has been proven to enhance the cell performances. However, the lack of knowledge regarding the mechanisms during the reaction, and in particular toward the inorganics, prevents for optimisation of the process. Most of the time, only structural properties are investigated, creating a gap in the composition of the final and intermediate product. As it has been explained in this chapter, the compositions of the raw and final products impact the electrochemical performances, mainly on the graphene interlayer distance which is a key factor in the sodation mechanism. Characterising the leaching during the HTC and its limit might help to choose biomass to provide suitable hard carbon for sodium battery application. It opens two axes of reflection:

- How does the HTC impact the hard carbon composition? What is the inorganic behaviours during the HTC, and how they impact the sodium battery performances?
- What wet biomass can be suitable for such application? Is HTC improving the electrochemical properties of the resulting hard carbon, and what are the limits and improvements toward the choice of biomass?

These two questions lead the further investigations presented in the following chapters. First, it is primordial to determine the operational conditions of the HTC. This aspect is investigated on the following chapter.

Table 7: Various works lead on biomass-based hard carbon for sodium batteries. Here are presented only half cells.

Feedstock	Pre- and post-treatment	Pyrolysis temperature (°C)	Electrolyte	Formulation	Current density (mA.g ⁻¹)	C _{rev} (mA.g ⁻¹)	ICE (%)	SSA N ₂ (m ² /g)	d ₀₀₂ (Å)	I _b /I _c	ref		
Date pulp		800	NaPF ₆ EC:DEC	97-3 HC-PANa	25				207	67	225.9	3.82	2.42
		1000							223	71	103	3.85	1.89
		1200							264	81	66.5	3.83	1.79
		1300							295	87	38.6	3.79	1.71
		1400							300	88	33.3	3.76	1.58
Date seed		800	NaPF ₆ EC:DEC	97-3 HC-PANa	25				215	72	115.6	4.01	2.3
		1000							242	78	15.6	3.86	2.15
		1200							260	85	35.1	3.84	2.02
		1300							277	88	26.7	3.76	1.73
		1400							274	88	34.7	3.71	1.69
Sugarcane bagasse		750	NaClO ₄ EC:DEC 1:1	70-20-10 HC-PVDF- carbon black	30				256	60	8	3.81	1.33
		850							268	65	5		1.15
		950							290	70	3		0.86
		1050							274	71	2	3.74	0.75
Apple waste		750	NaClO ₄ EC:DEC 1:1	70-20-10 HC-PVDF- carbon black	30				264	56		3.91	1.33
		850							267	60		3.89	0.75
		950							288	64		3.86	1.15
		1050							280	68		3.82	0.86
Beechwood	Pre-treatment: pyrolysis 450 °C	1000	NaPF ₆ EC:DMC 1:1, 1.5 FEC	80-10-10 HC-PVDF- carbon black	37.2				282	78	16	0.399	3.41
		1200							309	79	6	0.3881	2.41
		1400							200	82	4.8	0.3754	2.01
Miscanthus	Pre-treatment: pyrolysis 450 °C	1000	NaPF ₆ EC:DMC 1:1, 1.5 FEC	80-10-10 HC-PVDF- carbon black	37.2				256	75	11		3.63
		1200							243	72	8		2.48
		1400							255	75	12		2.18
Pine	Pre-treatment: pyrolysis 450 °C	1000	NaPF ₆ EC:DMC 1:1, 1.5 FEC	80-10-10 HC-PVDF- carbon black	37.2				290	80	141	0.3786	2.28
		1200							304	80	3.8	0.3868	2.23
		1400							315	82	5	0.3759	2.04
Wheat straw	Pre-treatment: pyrolysis 450 °C	1000	NaPF ₆ EC:DMC 1:1, + 1.5 % FEC	80-10-10 HC-PVDF- carbon black	37.2				190	65	10.5		2.14
		1200							194	65	22		2.52
		1400							298	70	42		1.8

Ochard apple	1400				226	70	5	3.64	
Pine forest residues	1400				299	82	5	3.76	
SRC-Willow	1400				291	82	3	3.68	
SRF-Poplar	1400				274	75	11	3.68	
Vineyard	1400				265	74	5	3.76	
Pine	1400				315	84	5	3.83	
Beechwood	1400				298	84	4.8	3.75	
Ashwood	1400				260	88	6.7	3.67	
Scot pine bark	1400				302	80	7	3.92	
Miscanthus	1400				255	74	12	3.86	
Wheat Straw-1	1400		NaPF ₆	80-10-10	200	60	42	3.76	
Wheat Straw-2	1400	Pre-treatment: pyrolysis 450 °C	EC:DMC	HC-PVDF-	232	61	73	3.79	[118]
Reed canary grass	1400		1:1, +	carbon	244	70	52	3.77	
Triticale	1400		1.5 % FEC	black	242	64	50	3.73	
Rice husk	1400				170	48	97	3.77	
Bagasse	1400				284	76	19	3.74	
Corn husk	1400				280	76	14	3.6	
Switchgrass	1400				262	72	16	3.69	
Grape seed cake	1400				263	79	7	3.69	
Sunflower seed	1400				298	79	6	3.71	
Corn cob	1400				293	78	8	3.74	
Walnut shell	1400				311	82	0	3.79	
Papaya seed	1400				256	71	10	3.77	
Coconut husk	1400				291	76	14	3.78	
Tamarind seed	1400				277	82	2	3.66	
	600				187.2	37		4,08	2.63
	800				325	52		4,05	2.50
	1000				400	53		4,02	2.22
	1200				400	57	242	4,01	2.08
Ginko leaves	1300	1M NaClO ₄ in EC:DC + 5 % FEC	90-10 HC, PVDF	30	393	56		0,385	1.69
	1400				350	58		0,382	1.56
	1500				267.2	49		0,372	1.54
	1700				200	51		0,361	1.32
	2000				120	38		0,335	0.35
	2500				125.5	42	16	0,335	0.11

Argan Shell		1300						2.6				
Carbon dots		1200						549.8				
Corn cob		1300						3.7				
Cotton		1300						38				
GPC		600			14	21		10.9	3.8	1.24		
GPC-AC	Post-treatment: Washing with NaOH + citric acid to introduce CO surface groups	600			107	31		6.5	3.8	1.22		
GPC-AC-U	Washing with NaOH + citric acid + urea + 2nd pyrolysis 600°C	600	1M NaClO ₄ in EC:DC + 5 % FEC	90-10 HC, PVDF	30	176	41	9.7	3.8	1.39	[131]	
GPC-AC-M	Washing with NaOH + citric acid + melamine + 2nd pyrolysis 600°C	600				99	38	3.2	3.8	1.26		
Lychee seeds		500						6.61				
Sucrose		1100						8.5				
Sucrose		1100						7				
Sucrose + Graphene oxides		1100						137				
Sugar		1100						70				
Wood		1100										
Shaddock peel	Post-treatment: HCl washing	800 1000 1200 1400	1M NaClO ₄ in EC:DEC 1:1	80-10-10 HC, PVDF, carbon black	30	262.8 314.5 430.5 359.7	68.2 63 67.7 69.2	25.5 68.6 82.8 39	3.92 3.82 3.8 3.76		[132]	
Mangosteen shell		800 900 1000 1100 1200 1300 1400 1500	1M NaClO ₄ in EC:PC 1:1	80-10-10 HC, polyacrylic acid sodium, carbon black	20	70 220 280 330	22 26 55 64 70 74 80 83	539.4 358.8 216.7 126.6 101.5 81.5 38.8 8.9	3.84 3.8 3.78 3.74 3.72 3.71 3.69 3.67	2.03 1.97 1.87 1.76 1.71 1.67 1.60 1.50		[7]
Chicken manure	Pre-treatment: water wash + acetone + pyrolysis 600°C 4h + NaOH 4M 6h stirring then digestion HCl 2M	1300				40			3.71		[133]	
Spartina alterniflora	Pre-treatment: Dry (150°C-4h)+pre-carbonization (600°C-20min) Post-treatment: wash: KOH, HCl, EtOH	1000 1200 1400 1600	1M NaClO ₄ in EC:PC 1:1	90-5-5 HC, CMC, carbon black	20	212 265 231 163	63 67 62 70	20.6 415.8 13.9 7.9	3.72 3.67 3.62 3.55	3.38 2.61 2.14 1.68		[6]

Olive stones		800				240		189.5	3.67	3.63	
		1000				235		64.8	3.73	3.76	
		1200	0.3M NaPF ₆ in PC + 2% FEC	90-5-5 HC, CMC, carbon black	20	280		48.7	3.77	3.58	[9]
		1400				291		4.1	3.8	2.47	
		1600				244		3.6	3.78	2.49	
	2000				105		6.8	3.72	1.97		
Chlorella vulgaris (algae)		850	1M NaClO ₄ in EC:DEC 1:1	80-10-10 HC-PVDF- carbon black	20	91			3.4		[115]
		1000			20	220			3.7		
Pinecone		500				149	39.7	393	4.21	2.70	
		800				110	33.3	557	4.17	3.03	
		850				205	67.1	400	4.13	3.03	
		900	Pre-treatment: pyrolysis 500°C + wash KOH 3M, 60°C, 3h	90-10 HC-CMC	30	287	77.6	395	4.07	2.94	[8]
		1000				301	83.5	239	4.02	2.70	
		1200				324	84.4	75	3.91	2.17	
		1400				370	85.4	40	3.81	1.89	
	1600				346	83.5	4	3.75	1.67		

Abbreviations electrolytes: EC: ethylene carbonate, DEC: diethyl carbonate, PC: propylene carbonate, DMC: dimethyl carbonate, FEC: fluoroethylene carbonate

Abbreviations formulations: HC: hard carbon, PVDF: PolyVinylidene DiFluoride, CMC: sodium carboxymethyl cellulose

Table 8: Various works lead on biomass-based hard carbon for sodium batteries with an HTC pretreatment. Here are presented only half cells.

Feedstock	Pre- and post-treatment	HTC conditions (T, t, S/L)	Pyrolysis temperature (°C)	electrolyte	Formulation	Current density (mA.g ⁻¹)	C _{rev} (mAg.g ⁻¹)	ICE (%)	SSA N ₂ (m ² /g)	d ₀₀₂ (Å)	I _b /I _G	ref
Rambutan peel	Pre-treatment: washing, water	200°C, 20h, 3% in NaOH 1M	800	1M NaPF ₆ in PC	80-10-10 HC, CMC, carbon black	30	169	51.8	198	3.87	0.92	[40]
			1000									
			1200									
Reed straw		200°C, 24h, 3%	900	1M NaClO ₄ in EC:DMC 1:1	85-10-3-2 HC-carbon black-CMC-SB R	25	160	49.2	325.2 7	4.03	1.85	[121]
			1100									
			1300									
			1500									
Apricot shell	Pre-treatment: SnO ₂ -functionalised apricot shells	200°C, 40h, 5.5% +2 drops of H ₂ SO ₄	500	1M NaClO ₄ in EC:PC	80-10-10 HC-carbon black-PVDF		130	38			0.95	[112]
			750									
			1000									
			500									
Cellulose		200 °C, 12 h, 4%	1000	1 M NaClO ₄ in EC:DMC 1:1	95-5 HC-sodium alginate (in water)	30	178	50			1.34	[134]
			1300									
			1500									
Dairy waste	Pre-treatment: wash waster post-treatment: wash water + EtOH	180°C, 12h	600	1M NaClO ₄ in EC:PC 1:1	80-10-10 HC-PVDF- carbon black	125	171	125		3.7	0.71	[135]
			800									
			1000									
Lotus leaves	wash EtOH	180, 10h, in 1M HCl	1000	1M NaClO ₄ in PC:DEC 1:1	80-10-10 HC-dimethylfor mamide-carbon black	50	259	67	365.5	3.72	1.03	[126]
Peanut skin	activation KOH 1:1 of the hydrochar (before pyrolysis) post-treatment: HCl wash activation 1:2 post-treatment: HCl wash	180 °C, 24 h, 5% in H ₂ SO ₄ dilluted	800	1M NaClO in EC:DC 1:1	80-10-10 HC-carbon black-PVDF	100	291	33	1930	3.7	1.57	[125]
			800									
			800									
Oatmeal		200 °C, 12 h	300	1M NaClO ₄ in EC:DMC 1:1	80-10-10 HC-PVDF- carbon black		75	33	5.8	4.18	0.41	[123]
			500									
			700									
			900									

Chapter 2

Materials & methods

This chapter describes the technics and devices used to characterise and synthetize the materials of this work. It includes the origin and preparation of the feedstock, the thermal treatments, and the chemical and physicochemical characterisations.

1. Raw biomass

Various feedstock, described in **Table 9**, were selected according to several criteria:

- The no- or under-valorisation of the material, all materials used in this work were considered as waste with no application
- the large availability of the resource, particularly in Europe, the area of the study
- a wide diversity of biomass from diverse categories with different properties

Table 9: *Origin of the feedstock*

	Moisture*	Specification	Origin
Woody products			
Driftwood, conifer	Wet	From Génissiat dam, usually removed for safety, stems	Ain, France
Driftwood, salix			
Driftwood, populus			
Driftwood, fraxinus	Wet	From Génissiat dam, usually removed for safety, bark	Ain, France
Driftwood, alnus			
Driftwood, alnus bark	Dry	From sawmills, ground bark	Aveyron, France
Oak bark	Dry	From sawmills, ground trunk	Aveyron, France
Soft wood			
Agricultural residues			
Reed	Wet	Wetland haying residue, straw	North Brabant, the Netherlands
Sedge	Wet	Wetland haying residue, weed	North Brabant, the Netherlands
Walnut shell	Dry	From food production plant, shell	Isère, France
Animal & human waste			
Sewage sludge	Wet	Sent from a waste water treatment plant	Italy
Horse manure	Wet	Collected from a farm	South Holland, the Netherlands
Industrial biomass waste			
Apple waste	Wet	Sent by Biokol Sverige AB, pomace	Sweden
Brewery waste	Wet	Sent by Biokol Sverige AB, residue from brewery	Sweden
Coffee waste	Wet	Sent by Biokol Sverige AB, spent coffee grounds	Sweden

**Wet biomass is used for moisture content superior to 60% while dry is for below 60%*

For shipping and storage convenience, the materials were dried and ground below 1 mm. It is important to note that in a real industrial plant, they are supposed to be used wet, directly after collecting, especially if the plant is nearby or the process integrated to the place of production of the raw materials. However, as the process is performed in water, the moisture of the raw material should not affect the properties of the product. Besides, all experiments are adapted in order to have the same solid/water ratio, first because it has a major impact on the product, and then to limit the influence of the storage condition.

After collecting, moisture content of the materials was immediately determined, as described in 3.1. The grinding was performed at different labs, following similar steps. Depending on the size of the feedstock, they were ground in several intermediate steps, to finish being ground by a hammer mill <1 mm. Between each step, the materials were dried at low temperature (about 40 °C) to facilitate the milling.

Animal and human waste were prepared differently due to biohazards. After collecting, they were stored in a cold room in a hermetic recipient. Horse manure was dried at 105 °C before grinding in a kitchen grinder (Braun). Sewage sludge was used directly in the reactor, with no filtration or grinding step due to its liquid state. At the opposite of most of the other material shipped, they were received undried.

2. Biochar & hard carbon synthesis

To obtain the final hard carbon that is suitable as battery electrode material, intermediate materials were first obtained, referred to as biochars. In this study, the biochars obtained by HTC are called hydrochars while the biochars obtained by low-temperature pyrolysis are called pyrochars.

All the experiments were carried out in duplicates, and all samples were characterized in triplicates. The values presented correspond to the mean and standard error of the mean.

2.1. Hydrothermal carbonisation

Hydrochars were produced in a 2 L high-pressure reactor (Parr series 4530 floor stand reactor), starting with 65 g of ground raw material (< 1 mm) and 1.3 L demineralised water (ratio solid/liquid 5 %). The reactor was purged with N₂ for 3 min before heating with a rate of 5 °C.min⁻¹ to the setpoint, and kept at the final temperature for a residence time of 4, 6, 10 or 12 h. It was let to cool down overnight at room temperature. Three 10 mL-gas sample were taken before opening with syringes, and characterized on the same day.

Four temperatures were used: 180, 200, 220 and 260 °C. Liquid and solid were separated by sieving (100, 45, 20 µm), and analysed separately.

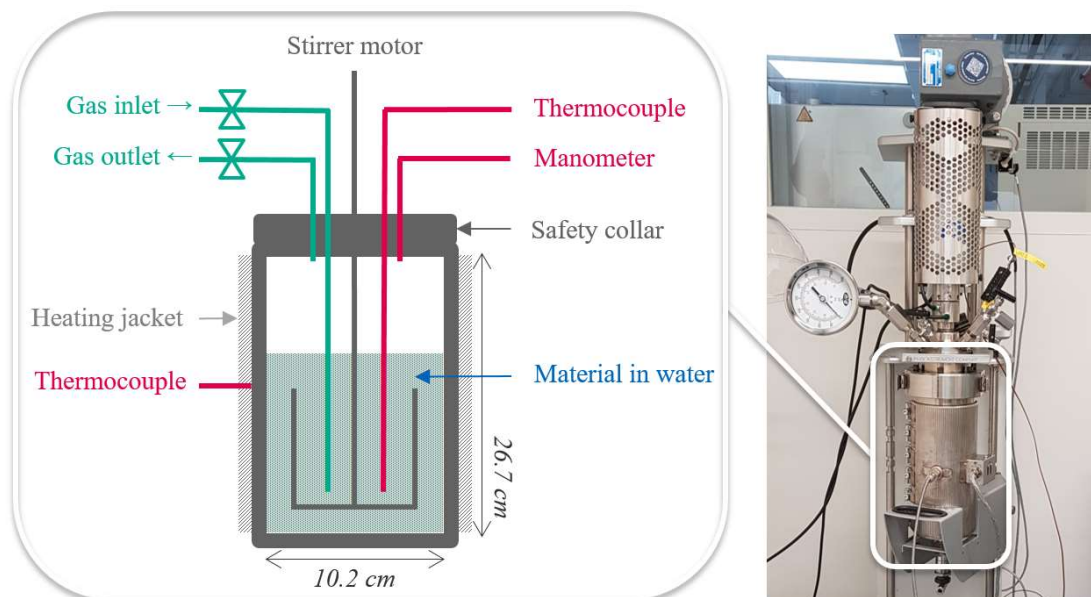


Figure 13: Hydrothermal carbonisation reactor schematic and picture

2.2. Low temperature pyrolysis

Pyrochars were produced in a homemade, stainless-steel reactor placed inside a muffle oven, starting with about 30 g of raw material under a N_2 flow of $130 L \cdot h^{-1}$. The temperature increased until $200\text{ }^\circ\text{C}$ at $10\text{ }^\circ\text{C} \cdot \text{min}^{-1}$, and hold for 115 min in order to remove the moisture and have homogenous heating transfer in the reactor. In a second step, it is then heated at $1\text{ }^\circ\text{C} \cdot \text{min}^{-1}$ until $450\text{ }^\circ\text{C}$, the final temperature. It was held for 20 min before cooling down to room temperature.

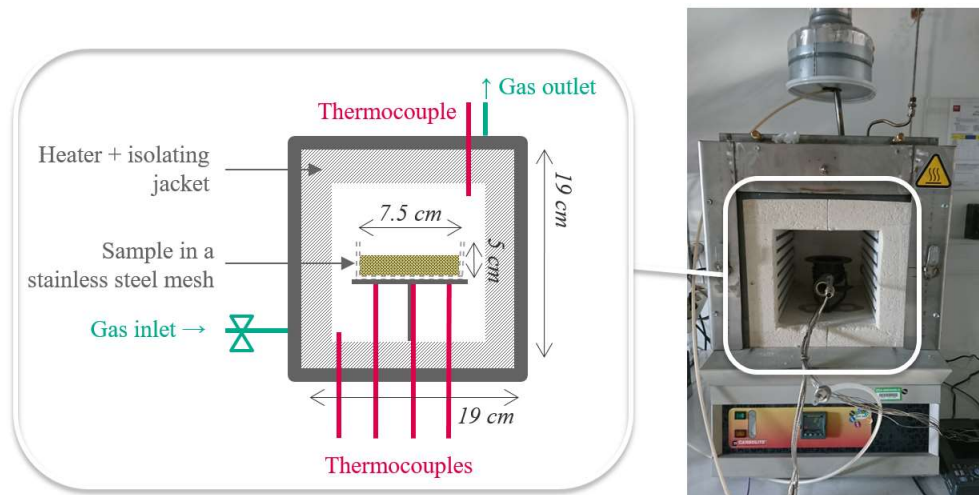


Figure 14: Low temperature pyrolysis oven schematic and picture

2.3. High temperature pyrolysis

Finally, hard carbons were synthesized through high-temperature pyrolysis of the biochars in a tubular furnace (Nabertherm GmbH model RHTH). Depending on the required material quantity, 2 to 15 g of biochar were placed on an alumina crucible. Its size was chosen depending on the quantity needed and temperature. They were heated to $1400\text{ }^\circ\text{C}$ with a heating rate of $5\text{ }^\circ\text{C} \cdot \text{min}^{-1}$ under an Ar flow of $15 L \cdot h^{-1}$. The temperature was held for 1 h, and let to cool down to room temperature overnight.

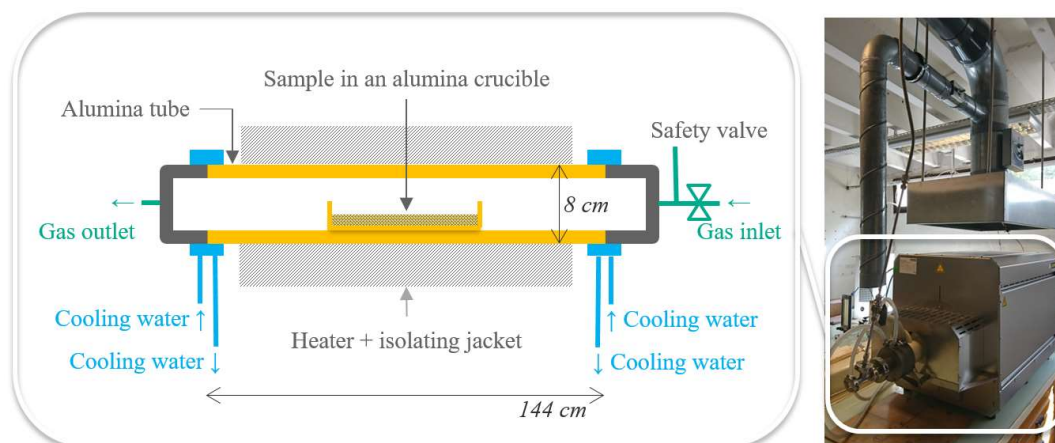


Figure 15: High temperature pyrolysis oven schematic and picture

3. Chemical composition of the materials

Chemical composition of the different materials; raw biomass, biochars and hard carbons; were measured as described in this part and summarized in **Table 10**.

Table 10: Summarize of the measures performed on the raw materials, biochars and hard carbons

Element / compound	Method	Standard	Unit
Moisture	Gravimetric	UNI 14774-2:2010	w%
C, H, N, S	CHNS	NF EN ISO 16948 (2015)	wdb%
Ash	Gravimetric	UNI 14775:2010	wdb%
	TGA	DIN 51719	
Al, Ca, Fe, Mg, K, Na	ICP-OES	ISO 16967	mg.kg db ⁻¹
Ba, Cr, Cu, Mn, Ni, Sr	ICP-OES	ISO 16968	mg.kg db ⁻¹
P	UV-vis	Adapted from [138]	mg.kg db ⁻¹
Si	UV-vis	Adapted from [105], [139]	mg.kg db ⁻¹
Extractives	Gravimetric	from [11]	wdb%
Cellulose, hemicellulose	HPLC	adapted from TAPPI standard T249 cm-85	wdb%
Lignin	Klason	TAPPI T222 om-83-1988	wdb%
gas	GC	-	%
C, N (liquid)	TOC/TIC/TN	-	mg.L ⁻¹

3.1. Moisture content

Moisture content determine the amount of water in a material, it is measured according to UNI 14774-2:2010 standard. About 2 g of material is weighted in an Al cap and placed for 24 hrs at 105 °C in a ventilated oven. The moisture content is the weight loss in % before and after drying as described by the following equation (1):

$$\text{moisture content} = \frac{m_{\text{final}} - m_{\text{cap}}}{m_{\text{initial}} - m_{\text{cap}}} \times 100 \quad (1)$$

Where: **moisture content** in (%)

m_{cap} is the mass of the empty cap (g)

m_{initial} is the initial mass of the sample + the cap (g)

m_{final} is the final mass after calcination of the sample + cap (g)

Sewage sludge being very liquid, a known mass is first dried slowly at 70 °C in order to avoid the sample to boil and spill in the oven. It is then dried at 105 °C as described before.

3.2. C, H, N, S, O contents

Elemental composition in C, H, N and S were measured according to standard NF EN ISO 16948 (2015) by the DTNM laboratory of CEA Grenoble. About 3 g of dried material is introduced in an oxydo/reduction reactor in tin. It is then heated to gasify the matter into CO₂, N₂, H₂O and SO₂, which are quantify by gas chromatography.

O content is calculated by difference of the remaining percent of C, H, N, S and ash content.

3.3. Ash content

Ash contents of raw biomass and biochars were measured according to UNI 14775:2010 standard. About 2 g of dried material were calcinated in an Al cap at 550 °C for 3 h. The ash content, in wdb%, is calculated by the ratio of the remaining mass and the initial mass. Due to the low quantity of materials, ash contents of hard carbons were determined by DIN 51719 standard. About 15 mg of material is weighted in a Ti crucible and suspended in a thermogravimetric analyser (TGA) (Setsys Evolution 1750). The sample is heated at 5 °C.min⁻¹ to 105 °C until the derivate of the mass is null, then it is heated again at 5 °C.min⁻¹ at 550 °C, under air. The temperature is held until the mass loss is null. It is then cooled down to room temperature at -20 °C.min⁻¹. The ash content is deduced similarly to the muffle furnace method, from the ratio between the final mass and the mass at 105 °C. The two methods were lead on several samples to compare the two and showed similar results.

The formulas to calculate the ash content with the muffle furnace and TGA methods are described respectively in equation (2) and (3):

$$\text{ash content}_{\text{furnace}} = \frac{m_{\text{final}} - m_{\text{cap}}}{m_{\text{initial}} - m_{\text{cap}}} \times 100 \quad (2) \quad \text{ash content}_{\text{TGA}} = \frac{m_{\text{final}}}{m_{105}} \times 100 \quad (3)$$

Where: **ash content**_{furnace} is the formula for the muffle furnace method (wdb%)

ash content_{TGA} is obtained by the TGA method (wdb%)

m_{cap} is the mass of the empty cap (g)

m_{initial} is the initial mass of the sample + the cap (g)

m₁₀₅ is the mass of the sample at 105 °C, which is dry (g)

m_{final} is the final mass after calcination (g)

3.4. Inorganic contents by ICP-OES

The majority of the inorganic elements (Al, Ba, Ca, Fe, Mg, K, Na, Cr, Cu, Mn, Ni and Sr) were measured by inductively coupled plasma optical emission spectroscopy (ICP-OES) (PerkinElmer, Avio 200). Inorganics were measured according to ISO 16967 for the determination of major elements (Al, Ca, Fe, Mg, K and Na) and ISO 16968 for minor elements (Ba, Cr, Cu, Mn, Ni and Sr).

Under inert atmosphere (Ar mainly), atoms receive energy through a plasma that make their electrons move to higher energy orbitals: they are ionised. Their desexcitation broadcast a spectre between 160 to 780 nm, which is collected and assimilated to an element. Indeed, each element emits at a specific wavelength which allow to identify the ray, its intensity is proportional to the concentration of the analyte [140].

Solids (raw biomass, biochars and hard carbons) were first digested (Mars 5 Duo Temp CEM microwave oven) by adding 10 mL of concentrated HNO₃ to 0.4 g of dried sample. They were heated at 165 °C in 10min at 1600 W, the temperature was maintained 1 min, and increased again at 175 °C and held for

5 min. The liquid samples were adjusted to match the 5 % nitric acid background of the calibration and rinsing solutions of the spectrometer.

The obtained results are concentrations in mg.L⁻¹ or µg.L⁻¹ respectively for major and minor elements, they are then converted into mg.kg db⁻¹ according to the following formula (4):

$$content = (c_{sample} - c_{blank}) \times DF \times \frac{V}{m_{sample}} \quad (4)$$

Where: **content** of one element (mg.kg db⁻¹)
c_{final} is the value measured by ICP-OES (mg.L⁻¹)
DF is the dilution factor
V the volume of the sample (L)
m_{sample} the mass of the digested sample (kg)

3.5. Inorganics by UV-visible spectrophotometry

Some elements could not be measured by ICP-OES for safety issues or convenience. Si is adsorbed at the surface of glass, which is the material of the inside of the ICP. To avoid this problem and desorb Si, HF is usually added in low quantity. However, besides being very dangerous, it consume SiO₂, and degrade the instrument. The device was not calibrated for P measurements. To quantify both, the molybdenum blue method is used for P content and adapted for Si content determination based on UV-visible spectroscopy [139].

Mo is a heavy metal which has the ability to form an intense blue complex in acidic conditions. The intensity of the colour is proportional to its concentration. It is used to determine different ions concentration, such as P, Si or As [141].

Spectroscopy uses the absorbance of molecules on the UV-visible range from about 190 to 800 nm. A beam at a selected wavelength go through the sample placed on a cuve and is collected on a detector. The intensity and absorbance are linked to the concentration by the Beer Lambert law [142] described in equation (5):

$$A_{\lambda} = \log\left(\frac{I_{\lambda}^0}{I_{\lambda}}\right) = \varepsilon_{\lambda} l c \quad (5)$$

Where: **λ** at a specific wavelength (nm) **ε** the specific absorbance coefficient (L.mol⁻¹ cm⁻¹)
A the absorbance **l** the length of the cell (cm)
I the intensity **c** the concentration (mol/L)

At a specific wavelength, ε and l are constant, which leads to an affine equation: $A = a \times c + b$, where a and b are constants, between the absorbance and the concentration. A calibration is made with

different solutions of known concentration, in order to obtain a linear equation. As a result, equation (6) is obtained, and conversion on the wanted unities is proceeded as described in equation (4).

$$c_{sample} = \frac{(A_{sample} - A_{blank}) - b}{a} \quad (6)$$

Where:

- at a specific wavelength λ (nm)
- c_{sample} the concentration of the sample ($\text{mg}\cdot\text{L}^{-1}$)
- A_{sample} the absorbance of the sample (no unit)
- A_{blank} the absorbance of the blank, the digested solution with no sample on it (no unit)
- a and b factors calculated by linear regression

3.5.1.P content

The molybdenum blue method uses a blue Mo(VI) complex where the intensity of the colour is proportional to the concentration. This method is well known and described in [138].

The sample has first to be digested to solubilize the P on an acid solution composed of concentrated H_2SO_4 where Se is dissolved (0.88 g for 250 mL) at 320 °C. After cool down, salicylic acid is dissolved at room temperature (7.2 g for 100 mL of solution). 0.3 to 0.4 g of dried sample is digested on 2.5 mL of the digestive mixture and let for 2 h at room temperature in order to form a nitro-salicylic acid compound to prevent the loss of nitrates. The complex is then reduced by heating at 100 °C for 2 h. To oxidize the organic material, 1 mL aliquots of H_2O_2 is gently added one by one, until the mixture stops bubbling due to O_2 formation. When it is stable, the reactive mixture is heated at 330 °C to finish to digest the material until the mixture turns from brown to colourless. To remove all the traces of peroxide, after cool down water is added with pumice and heat to gently boil, the volume is then adjusted to 50 mL for further measurements.

The digested samples were then measured according to the molybdenum blue method. 2 mL of digested sample is diluted in about 20 mL of demineralised water, and the pH is adjusted by addition of dropwise 2M NaOH until the colourless turns pink due to the addition of a few drops of phenolphthalein (pH indicator, $\text{pK}_a = 8.3$). A few drops of 2.5M H_2SO_4 are then added until it turns colourless again. 8 mL of a combined reagent composed of 10 mL 2.5M H_2SO_4 , 1 mL of potassium antimonyl tartrate solution (1.3715 g of $\text{K}(\text{SbO})\text{C}_4\text{H}_4\text{O}_6\cdot 4\text{H}_2\text{O}$ in 500 mL of water), 3 mL of heptamolybdate solution (20 g of $(\text{NH}_4)_6\text{Mo}_7\text{O}_{24}\cdot 4\text{H}_2\text{O}$ in 500 mL of water) and 6 mL of 0.1M ascorbic acid. It is filled up to 50 mL, and let 10 to 30 min to react. Phosphates from the sample and ammonium molybdate react to form phosphomolybdic acid, which is reduced by ascorbic acid into molybdenum blue, a polyoxomolybdate mixture with an intense blue colour. Its intensity is measured by UV-visible spectrophotometer (UV/VIS Lambda 365, Perkin Elmer) at 880 nm, where the absorbance for this complex is at its higher.

It is important to note that the intensity of this complex is highly dependent of the molybdenum concentration, a calibration curve has to be established each time with the combined reagent. This mixture

is stable only 4 h and has to be prepared each time. The calibration line is made from a standard solution of PO_4^{3-} at $5 \text{ mg}\cdot\text{L}^{-1}$. In order to avoid any contamination, all the glassware has to be acid-rinsed with 10 % HCl.

3.5.2. Si content

Similarly to P content, the sample has first to be digested in order to solubilize the Si. Molybdenum blue method is less known for Si, and the complex formed has a different nature. The protocol was adapted from [105], [139] and improved to fit the use in this study and increase safety. To avoid any Si contamination from glass, all the container and glassware are in plastic, acid-rinsed with 10 % HCl before use.

The material has to be calcinated at $550 \text{ }^\circ\text{C}$ for 3 h in order to have only the ash left, they are then dried overnight at $70 \text{ }^\circ\text{C}$. In a stainless steel 304 crucible, about 50 mg of dried ashes are added to 1.5 g of NaOH pellet, they are then melted in a muffle furnace oven at $350 \text{ }^\circ\text{C}$ for 1 h including the heating up. After cooling down about 15 min, 25 mL of demineralised water is added to the crucibles, and the melt is dissolved in a steam bath at $80 \text{ }^\circ\text{C}$ for 1 h. It is then transferred in a 1L-volumetric flask, diluted in about 400 mL of water before adding 20 mL of 50 % HCl, and completed to 1 L.

This siliceous acid solution is then used for the molybdenum blue method. 10 mL of the digested sample are diluted in about 50 mL of water, and 1.5 mL of ammonium molybdate (6.75 g of $(\text{NH}_4)_6\text{Mo}_7\text{O}_{24}\cdot 4\text{H}_2\text{O}$ + 10 mL of H_2SO_4 1:1 in 100 mL) and let to react 10 min in order to create a yellow complex, probably $\text{H}_4[\text{SiMo}_{12}\text{O}_{40}]$. Then, 4 mL of tartaric acid (10 g in 100 mL) and 1 mL of reducing solution (10 g of NaHSO_3 , 0.7 g of Na_2SO_4 , 0.15 g of 4-amino-3-hydroxynaphtalene-1-sulfonic acid (ANSA) in 100 mL) are added to adjust the pH and produce the Mo blue complex. Because its formation is slow, its intensity is measured by UV-visible spectrophotometer (UV/VIS Lambda 365, Perkin Elmer) at 650 nm after 1 h.

Similarly to P measurement, a calibration line is performed before the experiment. However, the reagents are more stable and doesn't need to be prepared each time. A calibration curve is made from a Si standard at 1000 ppm. However, the measurement is performed only on the ash, equation (4) has to be multiplied by the ash content to recover the Si content per material.

3.6. Macromolecules

Macromolecule composition were performed by the French Institute of Technology for Forest-based and Furniture Sectors (FCBA). They used an internal method to measure the extractives, using successively hot water and acetone under pressure. Lignin content was measured according to Klason method, following the standard TAPPI T222 om-83-1988 (from the Technical Association of the Pulp and Paper Industry). A known amount of extractive free biomass is hydrolysed in concentrated sulphuric acid, the remaining mass is the Klason lignin. Cellulose and hemicellulose are measured according to TAPPI standard T249 cm-85. An extractive-free sample is hydrolysed in sulphuric acid, the sugar monomers are then measured by high performance liquid chromatography (HPLC). A conversion coefficient for each biomass allows to calculate the hemicellulose and cellulose content from the saccharide concentrations.

The detail are their method can be found in [11].

3.7. Total organic and inorganic carbon, total nitrogen

The total organic carbon (TOC), total nitrogen (TN) and total inorganic carbon (TIC) content of the liquid product of HTC were analysed using a Shimadzu TOCv-cpn analyser.

TOC and TIC are determined by converting carbon into CO₂, by catalytic oxidation for organic carbon and acidifying to pH 1 – 2 for inorganic carbon, measured by a non-dispersive infra-red (NDIR) sensor.

TN was analysed using a Shimadzu TN module, through the combustion of the sample to convert the nitrogen into NO and NO₂. They react with ozone injected in the reactor chamber to produce excited NO₂ molecules, which, when falling back to the ground level, emit light that is measured using a chemiluminescence detector (Shimadzu Corporation, 2020).

Before the analyses, the samples were filtered using 0.45 µm cellulose-acetate membrane filters. For TOC and TN determination, the samples were preserved with sulfuric acid until a pH between 1 and 2 was achieved and stored at 4 °C until the analyses were carried out. Only the filtration step was carried out for TIC analysis, and the samples were frozen at -20 °C. Samples were diluted before analysis, with a dilution factor depending on the sample.

3.8. Gas composition

Gas produced during HTC were characterized by gas chromatography (GC) (SCION 456-GC) with helium as a carrier gas. The oven column temperature was between 25 and 28 °C in all the measurements. The thermal conductivity detector (TCD) temperature was 140 °C, while the electron capture detector (ECD) temperature was 250 °C.

As the reactor headspace was purged with nitrogen gas to remove air, the gas was assumed to be composed only of N₂ and CO₂. The ideal gas law was then used for the calculation of the mass of gas, considering the free volume of 0.7 L left in the headspace of the reactor and the temperature and pressure left in the reactor when the gas samples were taken and the mass percentage of CO₂ found with the GC. The volume of the biomass fed to the reactor was neglected for this calculation, as it represents about 4 % of the total volume. The gas yield was calculated

3.9. Yield definitions and calculations

By definition, the mass yield is the ratio between the obtained and the theoretical masses. However, the exact amount can't be precisely known due to the lack of knowledge both of the biomass composition and the reactions that occurs during HTC and pyrolysis.

In the ideal theoretical reaction, all the carbon from the biomass is converted into hard carbon, which implies the number of moles of C in the biomass is the same as hard carbon's, as described by the following chemical progress table:

	$C_{biomass}$	→	$C_{hard\ carbon}$
<i>Initial</i>	$n_{C,biomass} = \frac{m_{C,biomass}}{M_C}$		/
<i>Final</i>	0		$n_{C,biomass}$

For this calculation, the C content (%) is used to consider only the mass of C in the materials, hence the molar mass M_C can be simplified, the yield is then expressed as:

$$CY = \frac{m_{HC} \times C\%_{HC}}{m_{biomass} \times C\%_{biomass}} \times 100 \quad (7)$$

Where: **CY** the carbon yield (%)
 m_{HC} and **$m_{biomass}$** respectively the final mass of hard carbon obtained and the initial mass of biomass (g)
 $C\%_{HC}$ and **$C\%_{biomass}$** the C content of respectively the hard carbon and biomass (wdb%)

To express the quantity obtain from the thermal treatments, the term solid yield (SY) is used and defined as follow:

$$SY = \frac{final\ mass}{initial\ mass} \times 100 \quad (8)$$

Where: **SY** the solid yield (%)
final mass the mass obtained after reaction (g)
initial mass the mass introduced in the reactor (g)

3.10. Elemental balance calculations

In **Chapter 4** and **Chapter 6**, elemental balances are established as follows:

$$normalised\ remaining\ inorganic\ (\%) = \frac{biochar\ content \times (0.01 \times SY)}{raw\ content} \times 100 \quad (9)$$

Where: **normalised remaining inorganic** (%)
biochar content and **raw content** the elemental content in the biochar and feedstock respectively (mg.kg db⁻¹)
SY the reaction solid yield described in equation (8)

In **Chapter 5**, element balances between hydrochars and liquids are established as follows:

$$hydrochar\ content_{raw\ db} = hydrochar\ content\ (mg.kg\ char\ dry^{-1}) \times SY \quad (10)$$

$$\text{liquid content}_{\text{raw db}} (\text{mg.kg raw dry}^{-1}) = C_{\text{final}} (\text{mg.L}^{-1}) \times DF \times \frac{V_{\text{initial}} (\text{L})}{m_{\text{raw biomass}} (\text{kg})} \quad (11)$$

Where: **hydrochar content**_{raw db} and **liquid content**_{raw db} the contents normalised to the initial feedstock content to compare them (mg.kg raw dry⁻¹)

hydrochar content the content measured in the hydrochar (mg.kg char dry⁻¹)

SY the solid yield described in equation (8)

C_{final} the value measured by ICP-OES on liquids (mg.L⁻¹)

DF the dilution factor

V_{initial} the volume of water introduced in the reactor (L)

m_{raw biomass} the sample mass introduced in the reactor (kg)

4. Physicochemical properties

Physicochemical properties of the different materials; raw biomass, biochars and hard carbons; were characterized as described in this part and summarised in **Table 11**.

Table 11: Summarize of the physicochemical characterisations performed on the raw materials, biochars and hard carbons

Characterisation	Method	Unit
Structure	XRD	-
	TEM	-
	Raman	-
Surface	SEM-EDX	-
Porosity	N ₂ & CO ₂ adsorption	m ² .g ⁻¹

4.1. Structure by XRD

X-ray diffraction (XRD) is a non-destructive method that allow to study crystalline structure. An X-ray beam (λ about 0.1 nm) is headed through the material, it is diffracted at the surface of an atom or electron on a specific angle following the Bragg law (12):

$$n\lambda = 2d \sin (\theta) \quad (12)$$

Where: **n** the diffraction order (whole number)

λ the wavelength (nm)

d the specific interreticular distance between 2 similar layer (nm)

θ the diffracted angle (rad)

The intensity of the diffracted ray by one atom is low, but the diffraction of crystalline area gives a higher signal, leading to information on the structure [143].

XRD are usually used to characterise crystalline materials, which is not the case of hard carbons. However, they are composed of turbostratic stacked graphene layers areas which can be observed by

XRD. They appear as broad peaks: the first one, more intense, at $2\theta = 22 - 25^\circ$ that corresponds to the diffraction of the graphite basal planes (002), and the second at $2\theta = 42 - 45^\circ$ for diffraction of the plan perpendicular to the graphene layers (100). Hard carbons are defined by their distance between the graphene layers d_{002} , calculated by the Bragg's law, and the size of the turbostratic domains L_c and L_a calculated by the Scherrer equation (13):

$$L_{a,c} = \frac{k\lambda}{\beta \cos(\theta)} \quad (13)$$

Where: L_a the length and L_c the depth of the turbostratic domain (nm)
 k the dimensionless shape factor, of 1.84 for L_a and 0.9 for L_c
 λ the wavelength (nm)
 β the line broadening at half the maximum intensity (rad)
 θ the diffracted angle (rad)

The structure of the biomasses and hydrochars was analysed by a D8 Advance Bruker AXS diffractometer with a copper cathode ($\lambda_{K\alpha} = 15,418 \text{ \AA}$). The 2θ angle was varied from 5° to 80° using a step size of 0.05° and a counting time of 1 s. The different organic and inorganic crystalline phases were identified with the PDF4+ database, supplied by the ICDD. Phase identification was made using EVA software and interlayer distance were calculated with TOPAS software.

4.2. Structure defects by Raman spectroscopy

Raman spectroscopy were performed by the Institute of Material Science of Mulhouse (IS2M). Measurements were performed at room temperature using a LabRAM BX40 (Horiba Jobin-Yvon) spectrometer equipped with a He-Ne excitation source (532 nm wavelength).

A monochrome light is applied to the material. A small portion of the photons will be diffused with a slight variation of frequency due to the interaction light-matter, an inelastic diffusion. The diffused light is collected and its intensity measured, each band being characteristic to the material.

4.3. Surface characterisation

4.3.1. Electron microscopy by SEM-EDX and TEM

Hard carbons were characterized by SEM-EDS (Zeiss LEO 1530 and JEOL JMS-6610A). ESD cartographies were performed with a 20 kV operating voltage with a 10 mm working distance.

Hard carbons graphene nanodomains are observed by high resolution HR-TEM (JEOL ARM-200 F) operating at 200 kV. It was performed by the Institute of Material Science of Mulhouse (IS2M).

Electronic microscopy allows to have a precise image of the surface of the material at smaller scale than optic microscopy by using smaller wavelength and beam opening. It uses the interaction of an electron beam with matter: the delivered energy interacts on the orbital and electronic level leading to electronic

and electromagnetic emissions. The analysis of the different signals and quantification give different analysis

Scanning electron microscopy (SEM) uses the electronic emissions to obtain an image of the surface. Electrons go through the material and are randomly redirected in a small bulk area before going out of the material, they are then collected. The intensity depends on the distance, which allows to obtain an image corresponding to the topography of the surface.

It is possible also to characterise the nature of the atom under the beam by characterisation of X-photons and Augers electrons that are emitted. Atoms are ionised under the beam, where the desexcitation emits with an energy characteristic to the nature of the atom. This characterisation is performed by an energy dispersive spectrometer (EDS) coupled to the SEM.

Transmission electron microscopy (TEM) uses a higher energetic beam to obtain smaller scale pictures. It allows to visualize the atomic level, the graphitic layers in our case.

4.3.2. Porosity by N₂ & CO₂ adsorption

Porosity is characterised by N₂ & CO₂ adsorption (Micromeritics ASAP 2420), performed by the Institute of Material Science of Mulhouse (IS2M).

Gas adsorption is a method that allow to characterize the pore size and specific surface area. as explained in **Chapter 1**, the two gas access to different area due to their size difference, giving information of the size of the pores. The sample is first degassed under vacuum to remove any species at its surface, then a known volume of gas at a certain pressure and temperature is sent to get adsorbed on the accessible porosity. The addition of gas is made by aliquots after equilibrium until the relative pressure is stable. The gas desorption is lead similarly by removing gas until stable. The isotherm curve profile obtained is characteristic to the pore distribution.

The relative pressure is linked to the quantity of gas adsorbed, which allows to measure surface area. Before the measure, the sample is degassed under vacuum and He is added to measure the dead volume. Brunauer-Emmett-Teller (BET) specific surface area (SSA) was determined from the linear plot in the relative pressure (0.05–0.3) P/P_0 for N₂ and (0.01–0.03) for CO₂.

5. Electrochemical tests

5.1. Battery assembly

Hard carbon samples were first ground in a mortar and sieved at 100 µm. Electrodes were formulated in a slurry ink with 90 % of hard carbon as active material, 5 % of carbon black Super C65 from IMERYS as conductive additive, and 5 % of polyvinylidene fluoride (PVDF) (10 % in N-methylpyrrolidone (NMP)) as a binder. First, the two powders were mixed on a mortar with cyclohexane to insure the intimate mixing of them. After evaporation of the solvent, PVDF (SOLEF 5130 from Solvay) was added, and NMP (Aldrich) was dropwise poured in order to obtain a slurry. It was then coated on an Al foil using a Elcometer 4340

lab coater and a 100 μm thick doctorblade. After drying overnight at 55 $^{\circ}\text{C}$, it was then cut into 14 mm diameter electrodes. These electrodes were pressed in a hydraulic press at 5 t and dried under vacuum during 2 days at 80 $^{\circ}\text{C}$.

Then, coin cells (CR2032) were assembled in an Ar filled glove box using Na metal as counter electrode (half-cells) as described in **Figure 16**. Na electrodes are prepared from Na solid cube, sliced and coated manually, unlike Li where commercial rolls are available. To avoid its oxidation, O and H_2O contents in the glovebox are kept below 5 ppm. A CELGARD® 2400 membrane was used as separator and a VILEDON® membrane was used to ensure electrolyte's accessibility. 150 μL of the electrolyte used constituted of a solution of 1M NaPF_6 (from Stella) in ethylene carbonate (EC) with dimethyl carbonate (DMC) in a 1:1 volume ratio (from UBE) and addition of 2 wt% of fluoroethylene carbonate (FEC) (from Solvay).

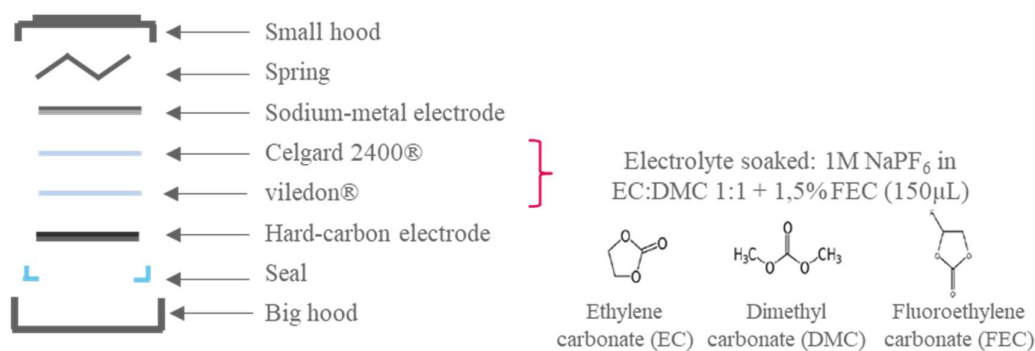


Figure 16: Half-cell assembly.

5.2. Galvanostatic tests

The cycling tests were performed using an Arbin Instruments BT2000 battery cycler. The cycling behaviour is tested by applying a current and measuring the potential by alternatively charging and discharging the battery, called galvanostatic test. A potentiostatic floating is added at the end of each reduction, where a potential is applied and the current measured, as described below. During the discharge, Na ions are inserted in the hard carbon working electrode. During the charge, the opposite phenomenon occurs.

The theoretical capacity of the material is calculated by the Faraday's law:

$$Q = \frac{n F}{3.6 M} \quad (14)$$

Where: **Q** the theoretical capacity of the material (Ah.g^{-1})
n the number of electrons exchanged during the charge or discharge
F the Faraday's constant (96500 C.mol^{-1})
M the molar mass of the material (g.mol^{-1})

For example, in the case lithium intercalation into graphite, it is well known that the maximum lithium intercalation compound is LiC_6 . From this point of view, the theoretical capacity Q of graphite for lithium intercalation can be easily calculated, given $M = 6 \times 12 = 72 \text{ g.mol}^{-1}$ and $n = 1$. $Q_{\text{graphite}} = 372 \text{ mAh.g}^{-1}$.

For hard carbon, the sodium insertion mechanism theory is very complex and not clearly established, as detailed in **Chapter 1**. From this point of view, the maximum reachable number of exchange electrons is not known. Moreover, Na poorly intercalates into graphite.

Most commonly, galvanostatic tests are performed at a constant gravimetric current density expressed in mA.g^{-1} and given as follows:

$$j = \frac{i}{m} \quad (15)$$

Where: **j** the current density (A.g^{-1})
i the applied current (A)
m the mass of active material (g)

This gravimetric current density can be associated to a C-rate, expressed as follows:

$$C - rate = \frac{C}{n} \quad (16)$$

Where: **C** the total charge or discharge capacity (Ah.g^{-1})
n the time of the total charge (or discharge) capacity (h)

It has to be noted that, as explain above, for the rest of this study, we arbitrarily decided to use the theoretical capacity of lithium intercalation into graphite as the C value. $Q_{\text{graphite}} = 372 \text{ mAh.g}^{-1}$. Hence, for example a C-rate of C/10 corresponds to a current density $j = 37.2 \text{ mA.g}^{-1}$.

The coulombic efficiency of the cell expresses the reversibility of the system at each cycle. It is given as follows:

$$CE = \frac{\text{charge capacity}}{\text{discharge capacity}} \times 100 \quad (17)$$

Where: **CE** the initial coulombic efficiency (%)
Charge and discharge capacity in (mAh.g^{-1})

In this study, we are particularly interested by the coulombic efficiency during the first cycle, so called Initial Coulombic Efficiency (ICE). Indeed, among other phenomena, it characterises the irreversible degradations of the electrolyte species which occur at the surface of the material.

The cells were cycled at a C/10 C-rate during 5 cycles, and then at 1C until the 100th cycle. Reduction (sodium uptake in hard carbon) — oxidation (sodium extraction from hard carbon) cycles ran between 3 V vs Na⁺/Na and 10 mV vs Na⁺/Na. At the end of each reduction in order to avoid sodium plating, the cell did not reach 0 V and was set to a constant voltage step of 10 mV until the current density reach the value corresponding to C/100. This floating lasts 30 s. At least two coin cells were tested for each hard carbon sample to ensure the reproducibility of the measurements.

Chapter 3

Hydrothermal carbonisation operational condition influence on the hard carbon properties

This chapter evaluates in one hand the influence of the temperature and residence time of hydrothermal carbonisation, and on the other hand the impact of the wood genera on the hydrochar. All hydrochars are then pyrolysed and the resulting hard carbons are characterised for sodium battery electrode application. It settle the bases for the further analysis in the next chapters.

This work was partly carried out in the frame of the MSc thesis of Abdullah Qatameh, and the results have been published in Journal of Environmental Chemical Engineering in 2021 [12].

1. Experimental campaign settlement

In order to understand better the influence of HTC pre-treatment, various conditions are tested both in temperature and residence time on an available feedstock: driftwood. Temperature is known to impact more the lignocellulose degradation while the residence time has a role on the morphology of the resulting hydrochar, as explained in **Chapter 1**. In order to cover a large range of macromolecule decomposition, three temperatures and residence time are selected in accordance with the usual ones used in the literature: 180, 200 and 220 °C, and 4, 6 and 12 h. The experimental campaign is described **Figure 17A)** and the nomenclature of the materials is reported **Table 12**.

For this study, driftwood is chosen as feedstock due to its large availability and under valorisation. Driftwood is accumulating in dam and rivers, and as the same time it affects positively geomorphology and ecology of the river [144], it increases flood destructive effect and structure damages [145], [146]. For safety reason, there are removed and stored, and often combusted or landfilled [147]. Hence, various woods are mixed, and can't be dissociate easily. In this study, several genera have been identified: 5 stems and 1 bark. In order to determine if the genera of the tree have an impact or not, they are going to be carbonised and pyrolysed in the same conditions, and the materials compared. The experimental campaign is described **Figure 17B)** and the nomenclature of the materials is reported **Table 13**. The investigation on the operating condition is led on the alnus genera, which is the one collected in higher amounts.

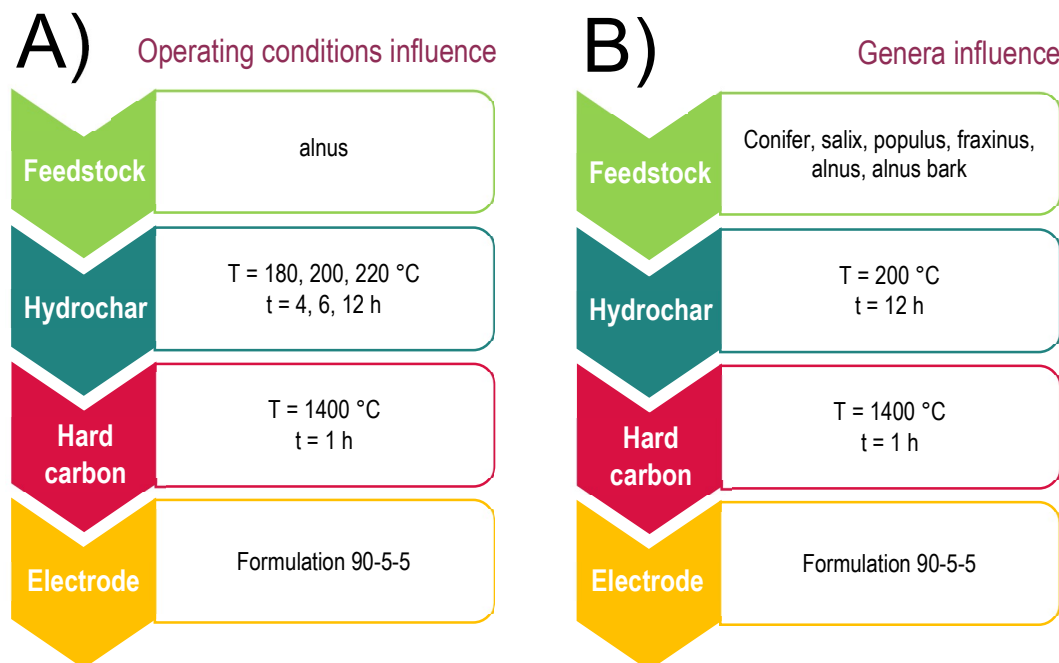


Figure 17: Experimental campaign of **A)** the operating condition and **B)** the genera influence.

Table 12: Nomenclature of the materials for the operating condition influence. The experiments are lead on alnus genera.

T (°C)	Conditions		Sample name	
		t (h)	Hydrochar	Hard carbon
180		4	180-4	HC-180-4
180		6	180-6	HC-180-6
180		12	180-12	HC-180-12
200		4	200-4	HC-200-4
200		6	200-6	HC-200-6
200		12	200-12	HC-200-12
220		4	220-4	HC-220-4
220		6	220-6	HC-220-6
220		12	220-12	HC-220-12

Table 13: Nomenclature of the materials for the genera influence study.

Feedstock		Raw material	Sample name	
Common name	Genera		Hydrochar	Hard carbon
Conifer stem	<i>Conifer</i>	conifer	h-conifer	HC-conifer
Willow stem	<i>Salix</i>	salix	h-salix	HC-salix
Poplar stem	<i>Populus</i>	populus	h-populus	HC-populus
Ash tree stem	<i>Fraxinus</i>	fraxinus	h-fraxinus	HC-fraxinus
Alder tree stem	<i>Alnus</i>	alnus	h-alnus	HC-alnus
Alder tree bark	<i>Alnus</i>	alnus_bark	h-alnus_bark	HC-alnus_bark

2. HTC pre-treatment

2.1. Raw biomass composition

2.1.1. Organic composition

The driftwoods are characterised, their CHNSO and ash, as well as their inorganics contents are reported in **Table 14**. Their macromolecular compositions are reported in **Table 15**.

Table 14: CHNSO and ash contents of the raw biomasses, for all the genera.

	C	H	N wdb%	S	O*	Ash
conifer	47.4 ± 0.4	6.7 ± 0.1	0.22 ± 0.02	0.10 ± 0.01	44.9	0.7 ± 0.1
salix	46.6 ± 0.2	6.35 ± 0.01	0.25 ± 0.1	0.13 ± 0	47.5	2.2 ± 0.1
populos	47.0 ± 0.3	6.46 ± 0.01	0.27 ± 0.01	0.11 ± 0.01	44.7	1.5 ± 0.1
fraxinus	46.56 ± 0.05	6.40 ± 0.03	0.27 ± 0.02	0.12 ± 0.03	45.6	1.1 ± 0.1
alnus	44.4 ± 0.2	6.44 ± 0.01	0.2 ± 0.1	0.26 ± 0.03	45.7	0.8 ± 0.1
alnus_bark	47.6 ± 0.5	6.15 ± 0.04	0.87 ± 0.03	0.16 ± 0.01	37.8	7.4 ± 0.1

* Calculated by difference

The major component of all the driftwood is C, which represents 46.6 to 48.8 wdb% of the biomass. The CHNS are very close for all the materials, which is coherent since they all are trees. These values are in accordance with literature [64], [148]. These elements constitute the macromolecules, and two tendencies are observed: in one hand the wood stems, which are composed from about 35 to 40 wdb% of cellulose, 25 to 29 wdb% of lignin and 19 to 24 wdb% of hemicelluloses, and in the other hand the bark which is composed of 48 wdb% of lignin while cellulose and hemicelluloses represent 15 and 19 wdb% respectively. It is coherent with literature which reports the trunks to be richer in cellulose than hemicelluloses and lignin, while barks are richer in hemicelluloses and lignin [79]. It is widely known that lignin forms a rigid structure, protecting the polysaccharides from microbial attacks [74], [75], it is indeed present in higher proportion in shells, husks and some bark [79].

Table 15: Macromolecular composition of the raw biomasses.

Macromolecule composition (wdb%) (± 5 %)	Conifer	Salix	Populus	Fraxinus	Alnus	Alnus bark
Lignin	27.65	29.22	25.14	26.76	24.91	44.81
Extractives	2.90	5.36	4.78	3.27	3.42	8.87
Polysaccharides						
Glucose	39.06	36.41	41.69	38.31	40.52	15.12
Xylose	6.21	11.75	10.32	12.94	15.28	9.29
Mannose	11.18	1.23	3.48	2.29	1.68	0.74
Galactose	2.18	0.72	0.69	0.65	0.76	1.26
Arabinose	1.00	0.29	0.00	0.80	0.00	3.32
Total cellulose	36.36	35.65	39.52	36.88	39.47	14.66
Total hemicelluloses	26.51	19.44	20.37	24.18	24.20	18.63
Acetyl	3.24	4.68	3.70	6.08	5.43	3.56
Glucomanan	16.06	2.71	6.34	4.37	3.50	2.46
Xylan	7.21	12.04	10.32	13.74	15.28	12.61

2.1.2. Inorganic composition

Inorganic contents are reported in **Table 16**. The ash contents are relatively low in the wood stems: salix is the richer material with 2.2 wdb% while the other genera are close to 1 wdb%. Unlike the stems, alnus bark contains 7.4 wdb% of ash. It is indeed known that the bark is richer in inorganics: it concentrates impurities like sand and soil [149], [150], and contain Ca oxalates that are end products of plant metabolism [151]. It is coherent with the important Ca content of 23900 mg.kg db⁻¹ the bark has compared to the stems, while the second higher content is 6500 mg.kg db⁻¹ for salix. It worth notice that the other genera contain between 1600 and 3700 mg.kg db⁻¹ of Ca, which is two to four times less concentrated than salix. The materials have low amounts of Si on the same range of K, while the other elements are below 100 mg.kg db⁻¹.

Table 16: Inorganic composition of the major elements in the raw biomasses.

	K	Na	Ca	Mg	Al	Mn	Fe	P	Si
	(mg.kg db ⁻¹)								
conifer	69 ± 6	26 ± 3	1600 ± 130	106 ± 9	70 ± 6	5 ± 1	70 ± 7	25 ± 2	350 ± 30
salix	520 ± 40	40 ± 4	6500 ± 500	330 ± 30	36 ± 3	7 ± 1	43 ± 4	80 ± 6	115 ± 10
populus	1440 ± 120	44 ± 4	3700 ± 300	350 ± 30	46 ± 4	10 ± 1	34 ± 3	75 ± 6	220 ± 20
fraxinus	760 ± 60	23 ± 2	2100 ± 200	370 ± 30	14 ± 1	2 ± 1	12 ± 1	93 ± 7	57 ± 5
alnus	460 ± 40	28 ± 3	2200 ± 200	220 ± 20	18 ± 2	3 ± 1	17 ± 2	71 ± 6	75 ± 7
alnus bark	860 ± 70	57 ± 6	23900 ± 2000	575 ± 50	190 ± 20	24 ± 2	87 ± 9	200 ± 20	450 ± 40

2.2. Operational condition influence

2.2.1. Composition

As said above, to define the influence of the temperature and residence time, experiments on the same driftwood genera are performed at three temperatures: 180, 200 and 220 °C, for three residence time: 4, 6 and 12 h. The compositions and solid yield of the reactions are reported **Table 17**. The inorganic contents have not been measured in the hydrochars and hard carbons.

Table 17: CHNSO and ash contents of the hydrochars and raw alnus, and solid yield of reactions for the materials obtained from the different temperature – 180, 200 and 220 °C – and residence time – 4, 6 and 12 h –. SY is calculated according to equation (8)

	SY w%	C	H	N wdb%	S	O*	Ash
alnus		48.8 ± 0.1	6.5 ± 0	0.1 ± 0		44.6	0.8 ± 0.1
180 - 4	69	51.31 ± 0.2	6.09 ± 0.01	0.36 ± 0.04	0.15 ± 0.08	42.1	0.2 ± 0.1
180 - 6	69	50.1 ± 0.4	6.22 ± 0.04	0.35 ± 0.01	< 0.3	43.4	0.2 ± 0.1
180 - 12	67	52.3 ± 0.3	6.00 ± 0.07	0.34 ± 0.05	< 0.3	41.3	0.2 ± 0.1
200 - 4	65	53.3 ± 0.3	6.08 ± 0.06	0.32 ± 0.02	< 0.3	40.3	0.2 ± 0.1
200 - 6	64	53.99 ± 0.06	5.98 ± 0.06	0.32 ± 0.04	< 0.3	39.7	0.2 ± 0.1
200 - 12	62	54.7 ± 0.6	5.81 ± 0.2	0.28 ± 0.07	< 0.3	39.2	0.2 ± 0.1
220 - 4	57	56.7 ± 0.5	5.9 ± 0	0.3 ± 0	< 0.3	37.1	0.2 ± 0.1
220 - 6	54	58.4 ± 0.2	5.8 ± 0.1	0.3 ± 0	< 0.3	35.5	0.2 ± 0.1
220 - 12	48	64.0 ± 0.4	5.5 ± 0	0.3 ± 0	< 0.3	30.2	0.2 ± 0.1

* Calculated by difference

In the tested conditions, the resulting hydrochar still have a high amount of O and H, as it is expected from HTC. The material is richer in C and N, while poorer in H and O and ash.

After HTC, the hydrochars are composed mainly of C, their amount range between 50.0 to 64.0 wdb% for 180 – 6 and 220 – 12 respectively, which is higher than the raw biomass content of 48.8 wdb%. The increase of temperature increases the carbon content but decrease the solid yield: considering the same residence time at the three different temperatures, C content increases from 6 to 12 wdb% for 4 and 12 h between 180 and 220 °C when the solid yield decrease from 12 to 18 % simultaneously. However, this trend is not as obvious for the residence time influence: at 180 and 200 °C, the C content and solid yield vary maximum of 2 %. However, at 220 °C the C content increases from 56.7 to 64.0 wdb% while the solid yield decreases from 10 %. At lower scale, H content also decreases with the increase both of the temperature and residence time, unlike N which remain stable no matter the operational conditions, its contents are higher in the hydrochar than in the raw materials, being 0.3 and 0.1 wdb% respectively, close to the limit of detection.

This range of values is consistent with works led on woody materials converted under similar conditions such as pine [152], wood sawdust [153] and spruce bark waste [154].

During the reaction, macromolecules are degraded by hydrolysis and decarboxylation. From the first mechanism, sugar monomers and phenylpropane derivate are released from polysaccharides and lignin respectively, degraded themselves into smaller molecules ending in the liquid phase. The second mechanism transforms carboxyl and carbonyl groups into respectively CO₂ and CO [97]. The production of organic acids and gas contributes to reduce the solid mass and hence the solid yield. The temperature contributes the hydrolysis process: hemicelluloses are fully degraded at 180 °C due to its disorganised and short branched chains between its various carbohydrate units, while cellulose requires 220 to 250 °C. The strong bonds between the lignin units make it difficult to degrade [95]. Smith and Ross [106] converted miscanthus at 200 and 250 °C from 0 to 24 h to evaluate the effect of residence time on a large range. They highlighted the very important impact of the temperature compared to the time on the biomass decomposition, and observed the increase of residence time allows polymerisation and aromatisation reactions to occur. These mechanism contribute to microsphere formation at the surface of the hydrochar. Gao et al [107] described this mesoporous structure with a sponge-like morphology on water hyacinth hydrochars as the hydrolysed polysaccharides transformation, and also reported that the size of the microsphere increase with the reaction time.

The ash content is 0.2 wdb% for all hydrochars, no matter the residence time or temperature. It is lower than in the raw alnus which is 0.8 wdb%. They are mainly composed of Ca, K and Mg, alkali and alkaline earth metal tend to leach in the liquid phase in major proportion in this range of temperature [104], [105]. However, the initial quantities and the low temperatures used are not enough to determine a tendency in the ash behaviour.

2.2.2. Structure

To observe any difference on the structure, XRD patterns are reported **Figure 18**. The hydrochar exhibits three characteristic peaks at about 15, 22 and 35°, highlighting the presence of cellulose. The broadness of the peaks translates its disorganised structure. As showed in **Figure 18A**), the intensity and sharpness of the cellulose peaks are lower at 220 °C than at 200 and 180 °C. It highlights the degradation of the macromolecule at that temperature, while it looks intact below which confirm the discussion of the previous section. The influence of the residence time at 200 °C is showed in **Figure 18B**), all the profile are similar highlighting the limited impact of the residence time on the cellulose hydrolysis on this conditions.

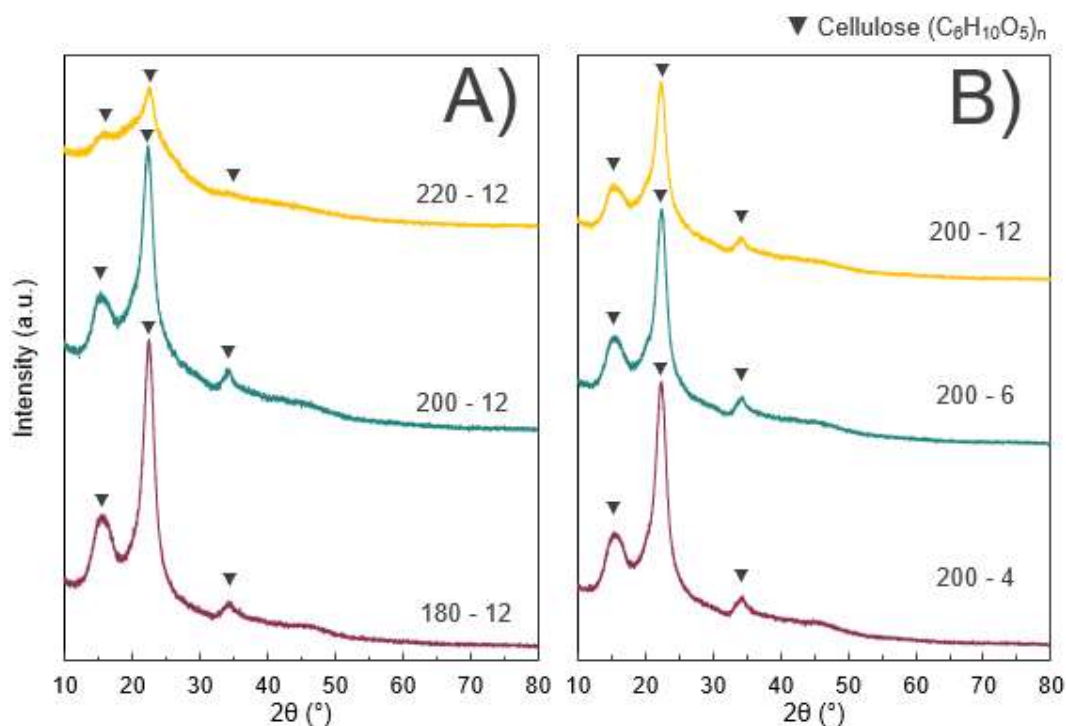


Figure 18: XRD patterns of the hydrochar from alnus **A)** at 220, 200 and 180 °C for 12 h and **B)** at 200 °C for 4, 6 and 12 h. Peaks are identified with symbols as: ▼ Cellulose- β ($C_6H_{10}O_5$)_n (PDF 00-060-1502).

To sum up, the temperature impacts strongly the macromolecule degradation and hence the composition of the hydrochar while the residence time have minor impact by comparison. However, higher temperature are required to fully hydrolyse the polysaccharides and allow better recondensation, polymerisation and aromatisation that are favoured by residence time. To determine if this observations can be made only for alnus driftwood, the other materials are all carbonised on the same condition of 200 °C for 12 h and are described below.

2.3. Genera influence

2.3.1. Composition

The six driftwoods are carbonised at 200 °C for 12 h, the composition and solid yields are reported in **Table 18**. The composition of the different raw materials are similar, leading to hydrochar with close composition as well. The C content in the hydrochars range between 54.7 to 58.9 wdb%, which is about

10 wdb% higher than in the raw material. At the opposite of O, H and S contents that decrease after reaction, while N remain the same.

As already described in the previous part, in these conditions the main mechanisms are hydrolysis and decarboxylation leading to a mass loss – decreasing the solid yield – and an increase of the C content. All the materials are wood product, and despite their similar CHNS composition, their macromolecular contents are not. Alnus bark contains twice more lignin than the other samples which is known to be not degraded in HTC conditions [155]. However, it also contains twice less cellulose than the stems, with a comparable amount of hemicelluloses. In the condition of the study, it was highlighted that only the hemicelluloses are hydrolysed and the cellulose almost untouched. In one hand the bark is richer in non-degradable lignin and extractible, but poorer in non-degradable cellulose with a similar amount of degradable hemicelluloses. It seems it compensate the mass loss to obtain similar solid yield between the bark and the stems despite their various composition.

Ash, on the other hand, behaves differently depending on the biomass. All the stems have their ash contents that decrease after reaction, lying between 0.2 and 1.4 wdb% which is 2 to 5 times lower than in the corresponding feedstock. However, the bark is the only sample that sees its content increase from 7.4 to 8.0 wdb%. As already mentioned in the previous part, some inorganics tend to leach during HTC, mainly the alkalis and alkaline earth metals however their form into the biomass as well as the HTC temperature has a major impact on their behaviour during the reaction. It seems that most of the inorganics remain in the hydrochar, and the mass loss participates to concentrate them in the material, increasing the ash content. In particular, high amount of Ca was measured in alnus_bark, which was reported to not leach entirely in the liquid phase [104].

Table 18: CHNSO and ash contents of the hydrochars and solid yield reactions for all the genera. SY is calculated according to equation (8).

	SY w%	C	H	N wdb%	S	O*	Ash
h-conifer	68	57.4 ± 0.2	5.9 ± 0.1	0.2 ± 0	< 0.3	36.3	0.2 ± 0.1
h-salix	64	56.2 ± 0.2	5.9 ± 0.1	0.2 ± 0	< 0.3	36.3	1.4 ± 0.1
h-populus	65	55.0 ± 0.7	5.8 ± 0.1	0.2 ± 0	< 0.3	38.5	0.5 ± 0.1
h-fraxinus	65	55.4 ± 0.2	5.9 ± 0	0.2 ± 0	< 0.3	38.3	0.2 ± 0.1
h-alnus	62	54.7 ± 0.6	5.8 ± 0.2	0.28 ± 0.07	< 0.3	39.0	0.2 ± 0.1
h-alnus_bark	69	58.9 ± 0.6	5.8 ± 0	0.7 ± 0	< 0.3	26.6	8.0 ± 0.1

* Calculated by difference

2.3.2. Structure

XRD are performed and patterns are reported **Figure 19**. Similarly to the previous part, the characteristic cellulosic pattern is observed in the stem samples with the three characteristic broad peaks at about 15, 22 and 35° that translate the insignificant cellulose hydrolysis. However, some additional peaks are observed in h-conifer, h-salix and h-alnus_bark sample. Whewellite is identified in h-salix and h-oak_bark, which is more concentrated in this last one as highlights the intensity of the peaks. It is a common bark constituent [79], [156], which is thought to impact the plant Ca regulation and photosynthesis [157]. Ca oxalates are reported to be soluble in acid waters only [158], despite of the acidity of the process water after HTC it seems whewellite remain in the hydrochar. Volpe et al [35] observed the same behaviour in

their hydrochars from *Opuntia ficus-indica* from 180 to 250 °C: the whewellite from their feedstock remains in the hydrochar. In addition, SiO₂ is identified in h-alnus_bark (cristobalite. high. syn, PDF 04-008-7643). It is indeed very common for plants to contain SiO₂ as opal, due to the absorption of silicic acids in the soils by the plant that precipitates in the plant cells. It gives rigidity to the plant, and are commonly found in the barks [79]. SiO₂ is known to be insoluble under this temperature and pressure [159].

All these species are in accordance with the higher amount of Ca in the raw salix and alnus_bark. Despite the alnus_bark Si content is not really important in accordance with the low intensity of the peak, it is still the highest among the samples. A sharp peak appears at 26.4° in h-conifer. It corresponds to berlinite structure (Aluminium phosphate, Berlinite, syn Al(PO₄), PDF 04-009-5761) despite the low Al content in the raw material. Heavy metals are reported to remain in the hydrochar unlike the alkali and alkaline earth metal than tend to leach in the liquid phase [105], leading to an increased concentration of the Al. It is worth to notice that conifer is the stem with the highest Al content of 70 mg.kg db⁻¹ when the other samples are comprised between 14 and 46 mg.kg db⁻¹.

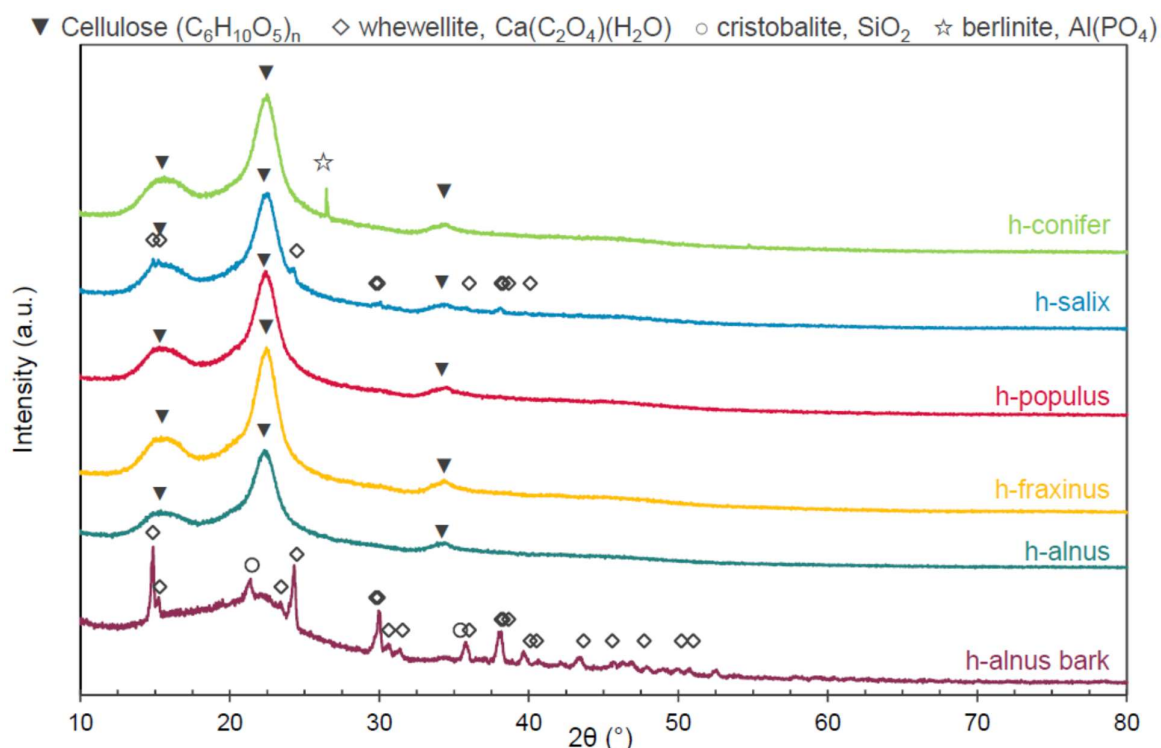


Figure 19: XRD patterns of the hydrochars obtained from the six driftwood. Peaks are identified as: ▼ Cellulose- β (C₆H₁₀O₅)_n (PDF 00-060-1502), ◇ Calcium oxalate hydrate, whewellite, Ca(C₂O₄)(H₂O) (PDF 04-025-6897), ○ Silicon oxide, cristobalite. high. syn SiO₂ (PDF 04-008-7643) and ☆ Aluminium phosphate, Berlinite, syn Al(PO₄) (PDF 04-009-5761).

3. Driftwood-based hard carbons and their properties

3.1. Operational conditions influence

3.1.1. Composition

The hydrochars are then pyrolysed at 1400 °C for 1 h under Ar to obtain hard carbon, as detailed in *part 1*. Their compositions are reported in **Table 19**. Their physico-chemical properties as well as the reaction yields are reported in **Table 20**.

They all have similar compositions, no matter the HTC conditions. The hydrochars obtained at higher temperature during longer reaction time were richer in C but the HTC solid yield were lower, after pyrolysis in the same conditions, the trend is opposite regarding the solid yield: the highest values are obtained at the highest HTC temperature. By calculating the chemical yield, the best carbon recovery from the raw biomass to the final hard carbon is obtained at the highest temperature. The hydrochars obtained on harder conditions contain less H and O, limiting decarboxylation mechanisms which could be one possibility to explain this difference.

Table 19: CHNS contents of the hard carbons from the hydrochars obtained at different temperature – 180, 200 and 220 °C – and residence time – 4, 6 and 12 h.

	C	H	N wdb%	S	O + ash*
HC-180-4	92.6 ± 0.3	0.39 ± 0	0.31 ± 0.01	0.08 ± 0.01	6.7
HC-180-6	92.6 ± 0.9	0.36 ± 0.03	0.31 ± 0.01	0.11 ± 0.02	6.7
HC-180-12	92.3 ± 0.6	0.38 ± 0.04	0.34 ± 0.2	0.15 ± 0.04	7.0
HC-200-4	91.2 ± 0.6	0.51 ± 0.01	0.36 ± 0.04	0.07 ± 0.03	7.9
HC-200-6	95.0 ± 0.8	0.22 ± 0.03	0.27 ± 0.09	0.11 ± 0.05	4.5
HC-200-12	92.68 ± 0.01	0.44 ± 0.03	0.3 ± 0.1	0.09 ± 0.02	6.5
HC-220-4	93.4 ± 0.2	0.32 ± 0	0.35 ± 0.04	0.12 ± 0.05	5.9
HC-220-6	92 ± 1	0.33 ± 0.05	0.34 ± 0.09	0.07 ± 0	7.1
HC-220-12	92.9 ± 0.3	0.40 ± 0.02	0.25 ± 0.02	0.10 ± 0.01	6.5

* Calculated by difference

As expected, they are mainly composed of carbon, containing between 91 to 95 wdb%. H and N represent about 0.3 wdb% and S represents 0.1 wdb% of all the materials. The other few percent are O and ash. The compositions are coherent with other biomass-based hard carbons [118]. They all have similar composition, no matter the HTC conditions.

Table 20: Physicochemical properties of the hard carbons. Solid yield SY and carbon yield CY are calculated according to equations (7) and (8), d_{002} the interlayer distance, ICE the initial coulombic efficiency, and C_{rev} the reversible capacity of the first cycle. Uncertainties are from the method used.

	SY (%) ± 1	CY (%) ± 3	d_{002} (Å) ± 0.05	N ₂ SSA (m ² .g ⁻¹) ± 5 %	CO ₂ SSA (m ² .g ⁻¹) ± 5 %	ICE (%) ± 1	C_{rev} (mAh.g ⁻¹) ± 10
HC-180-4	24	31	3.88	21.5	26.5	78	280
HC-180-6	24	31	3.87	11.3	17.7	81	300
HC-180-12	26	33	3.88	17.5	27.7	83	300
HC-200-4	26	32	3.84	10.7	16.5	81	300
HC-200-6	29	36	3.77	9.0	11.5	84	300
HC-200-12	31	37	3.86	11.1	16.1	83	300
HC-220-4	32	35	3.86	8.4	15.6	81	290
HC-220-6	38	39	3.89	13.0	19.2	82	300
HC-220-12	46	42	3.87	14.0	14.6	81	300

3.1.2. Structure

The XRD patterns of the hard carbons are reported **Figure 20** and the d_{002} in **Table 20**. The typical hard carbon pattern is composed of two broad peaks at about 22 and 43°, respectively corresponding to the diffraction of the X-rays perpendicular to the basal graphene planes (002) and parallel to them (100) respectively. Their patterns are very close, and the interlayer distance d_{002} is also similar: from 3.8 to 3.9 Å. As expected, these values are higher than the 3.35 Å of graphite [29], and are in accordance with other wood-based hard carbons [118]. It seems the HTC conditions of this study do not impact greatly the hard carbon structure.

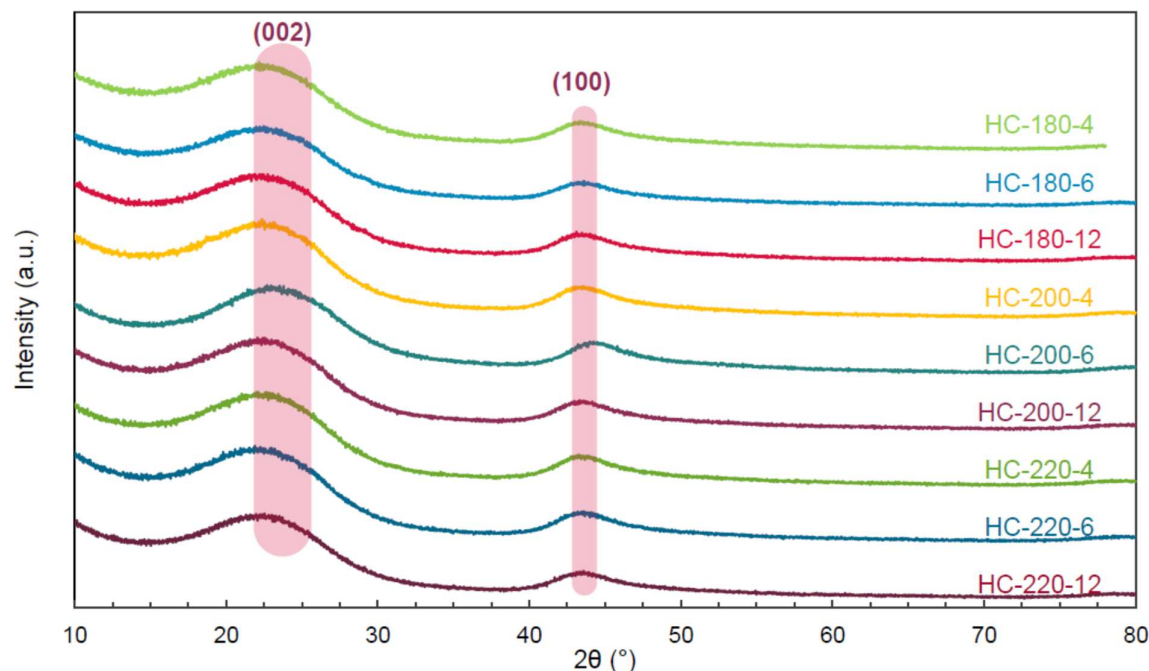


Figure 20: XRD patterns of the hard carbons obtained in the different HTC conditions.

3.1.3. Surface area

N_2 and CO_2 gas adsorptions had also been measured to determine the specific surface areas (SSA) of the materials. N_2 SSA range between 8.4 and 21.5 $m^2 \cdot g^{-1}$ while CO_2 SSA are slightly higher between 11.5 to 27.7 $m^2 \cdot g^{-1}$. Due to its size, CO_2 molecules can access to smaller pores and gives higher SSA than N_2 adsorption, which highlights the ultramicroporosity (pore size $<0.7nm$) [31]. But gas, no matter which one it is, can only be adsorbed where it has access: it gives information to the open porosity of the material only. All the hard carbons exhibit small N_2 SSA below 22 $m^2 \cdot g^{-1}$, and CO_2 below 30 $m^2 \cdot g^{-1}$. It highlights the small surface area of the materials, with no obvious correlation with the HTC conditions.

3.1.4. Electrochemical performances

Half cells were assembled and cycled, the results are presented in **Figure 21**. During the first cycle, irreversible reaction occurs at the surface of the negative electrode, the solid electrolyte interface (SEI), as explained in **Chapter 1**. To evaluate the reversibility of the system, the ratio between the charge and discharge capacity over the first cycle is calculated, which defines the initial coulombic efficiency (ICE). In all the cells, the ICE between 81 to 84 % with specific capacities of 300 $mAh \cdot g^{-1}$, except for HC-180-4

which has 78 % and 280 mAh.g⁻¹ respectively. This very high coulombic efficiencies and specific capacities are among the best of biomass-based hard carbon, and wood was already reported to provide this range of performances [118].

After the 5th cycle, a capacity drop can be observed due to the change from C/10 to C-rate. However, this difference is about 20 mAh.g⁻¹ which is small, highlighting the good capacity retention to the rate variation. Among 100 cycles, the cycling is very stable with a capacity loss at C-rate lower than 3 % for every hard carbon. All the hard carbons had similar composition, structure and surface area, it appears logical to obtain similar electrochemical performances as well.

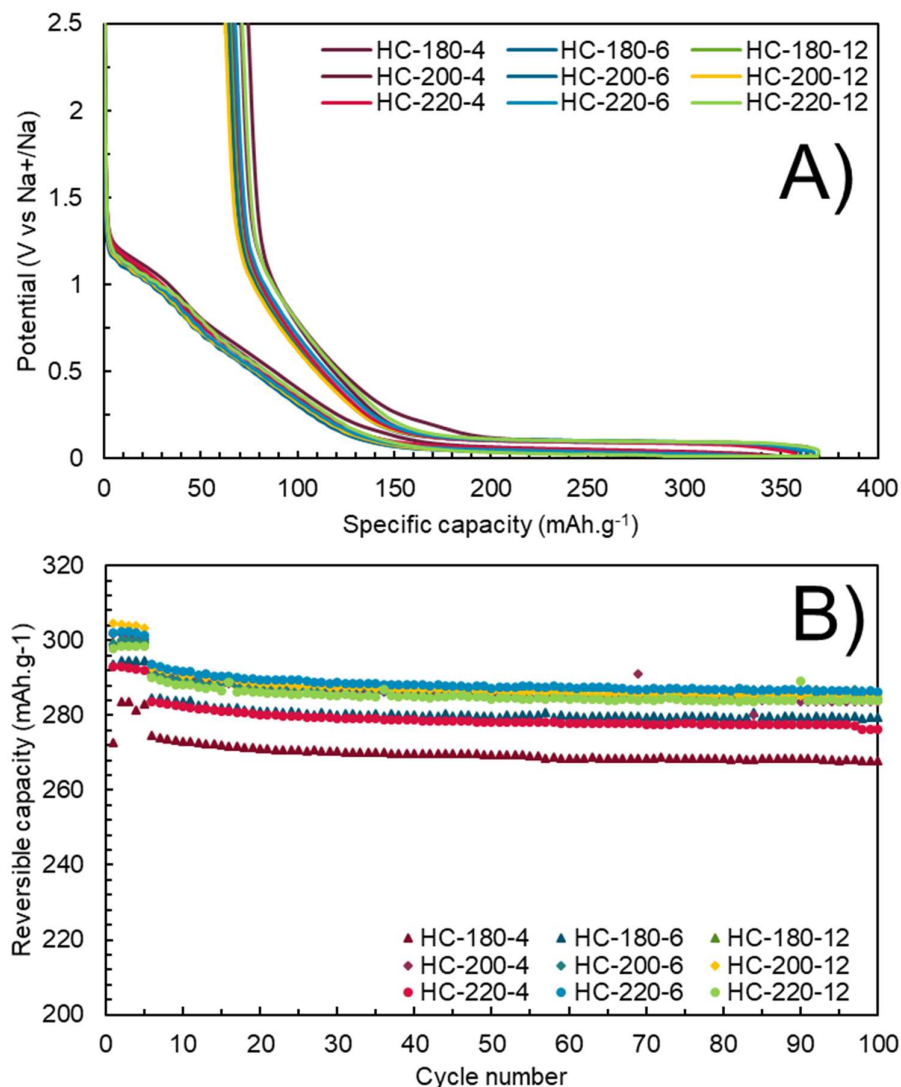


Figure 21: A) First cycle discharge-charge and **B)** cycling behaviour of the hard carbons from the hydrochars at the different conditions. The 5 first cycles are performed at C/10 then at 1C until the 100th cycle ($C = 372 \text{ mA.g}^{-1}$).

3.2. Genera influence

3.2.1. Composition

The composition of the hard carbons are reported in **Table 21**. Their physico-chemical properties are reported **Table 22**, and XRD patterns in **Figure 22**.

Hard carbons contain between 87.7 and 95.8 wdb%, and less than 0.5 wdb% of H, N and S. The few remaining percent are O and ash. The bark-based sample differs from the others, it has less C despite similar amounts of H, N and S than the others. It is most likely that it contains more ashes, like its hydrochar. At such temperature, most of the inorganic should be volatilised, however, they might remain as a stable compound as oxide or sulphide [11], or be trapped in the structure, preventing their release [160].

Table 21: CHNSO and ash contents of the hard carbons and solid yield of pyrolysis for all the genera

	C	H	N	S	O + ash*
			wdb%		
HC-conifer	93.5 ± 0.3	0.37 ± 0.03	0.24 ± 0.01	0.18 ± 0.03	5.7
HC-salix	95.8 ± 0.02	0.11 ± 0.02	0.19 ± 0	0.23 ± 0.09	4.2
HC-populus	95.7 ± 0.2	0.2 ± 0.1	0.19 ± 0.01	0.08 ± 0.1	3.9
HC-fraxinus	95.27 ± 0.01	0.26 ± 0.01	0.20 ± 0.02	0.09 ± 0.01	3.6
HC-alnus	92.68 ± 0.01	0.44 ± 0.03	0.3 ± 0.1	0.09 ± 0.02	6.4
HC-alnus_bark	87.7 ± 0.1	0.19 ± 0.06	0.16 ± 0	0.15 ± 0.02	11.8

* Calculated by difference

3.2.2. Structure

The XRD patterns show the typical (002) and (100) peak described in the previous part, however HC-salix and HC-alnus_bark exhibits other sharper peaks. Unlike their respective hydrochars, no whewhellite was found: under inert atmosphere at high temperature, calcium oxalate decomposes into calcium carbonate and carbon monoxide, which decomposes itself at higher temperature into calcium oxide and carbon dioxide [161]–[163]. The release of this last gas may also catalyse the carbon matrix volatilisation via Boudouard reaction: $C + CO_2 \rightarrow 2 CO$ [35]. Small intensity peaks corresponding to lime (CaO, lime syn, PDF 00-037-1497) are indeed found in HC-salix, as well as additional peak at 31°. This position as well as the composition of the raw material let think that it might be calcium carbide (CaC₂, PDF 04-015-4081), however the low intensity do not allow to clearly identify this compound. Bigger intensity and broader peaks corresponding to portlandite (Ca(OH)₂, PDF 00-044-1481) are identified in HC- alnus_bark. It is not common to find portlandite at such temperature, as it is reported to be unstable above 600 °C [163]. Pastor-Villegas also reported portlandite on their char from rockrose pyrolysed at 1000 °C, and suggested that it comes from the reaction with CaO and the moisture in the air during the storage time. However, other studies reported CaO in their hard carbons, without being hydrated by the ambient air or any Ca(OH)₂ species [118]. There is no longer traces of crystalline Al compound in HC-conifer diffractogram. Thermally stable heavy metals are not known to volatilise during pyrolysis [164], Al might remain in the hard carbon but not under a crystalline phase.

The d_{002} of the stem-based hard carbon are very close, from 3.8 to 3.9 Å. On the bark pattern, the (002) peak is confused with a sharper but still broad peak at 26°. Due to this overlap, to measure the d_{002} is

complicated. However the position of this second peak allows to calculate the interlayer distance of these organised areas, which is 3.5 Å. It is still bigger than the 3.35 Å of graphite [29], but smaller than the d_{002} of the stems. This organisation is a problem for the sodium insertion, as described in **Chapter 1**, at least 3.7 Å are required [53]. Inorganic elements such as K, Ca and Si catalyse the graphitisation during the pyrolysis [30], [118]. As discussed in section 2.1.2, alnus_bark contains the most of these elements and is particularly rich in Ca, which is in accordance with HC-alnus_bark XRD pattern. This phenomenon is common in biomass with raw biomass rich in these elements [118].

Table 22: Physicochemical properties of the hard carbons. Solid yield SY and carbon yield CY are calculated according to equations (7) and (8), d_{002} is the interlayer distance, ICE the initial coulombic efficiency, and C_{rev} the reversible capacity of the first cycle. Uncertainties are from the method used.

	SY* (%) ± 1	CY** (%)	d_{002} (Å) ± 0.05	N ₂ SSA (m ² .g ⁻¹)	CO ₂ SSA (m ² .g ⁻¹)	ICE (%) ± 1	C_{rev} (mAh.g ⁻¹) ± 10
HC-conifer	34	46	3.91 ± 0.05	16.0 ± 0.0	21.3 ± 1.1	83	310
HC-salix	33	43	3.83 ± 0.05	14.7 ± 0.0	23.1 ± 1.1	83	290
HC-populus	31	41	3.87 ± 0.05	16.4 ± 0.0	23.4 ± 1.7	85	310
HC-fraxinus	32	43	3.81 ± 0.05	5.0 ± 0.0	6.9 ± 0.2	83	300
HC-alnus	31	37	3.86 ± 0.05	14.0 ± 0.0	14.6 ± 0.7	83	300
HC-alnus bark	38	48	3.46*** ± 0.05	7.5 ± 0.0	17.8 ± 0.8	74	200

* value obtained from the graphitic peak symbolised by ▼ in Figure 22.

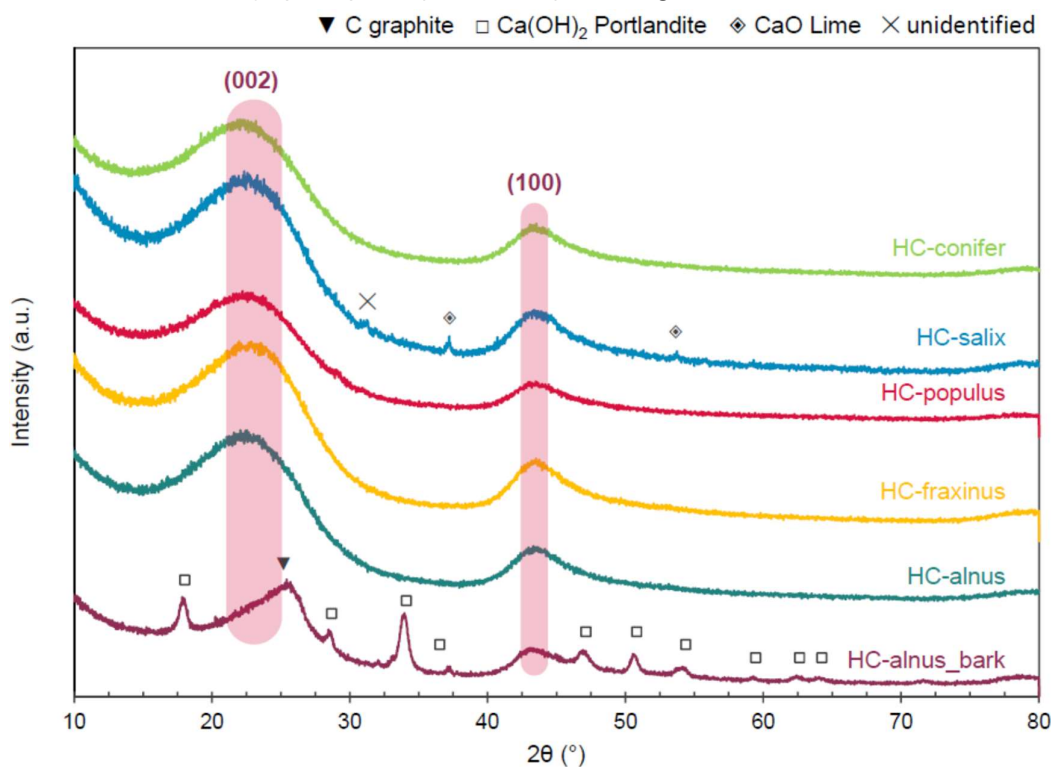


Figure 22: XRD patterns of the hard carbons from the different genera. Peaks are identified as: ▼ graphite-2H (PDF 01-075-1621), □ Ca(OH)₂ Portlandite, syn (PDF 00-044-1481), ◆ CaO, Lime, syn (PDF 00-037-1497), and × unidentified.

The organisation of the matter is also highlighted by the Raman spectras of selected hard carbons reported **Figure 23**. As mentioned in **Chapter 1**, the two typical D and G bands at 1350 and 1600 cm^{-1} noted in the figure, correspond to the defect-induced and crystalline graphite respectively. Their ratio gives an idea about the disorder degree: the highest the I_D/I_G , the highest the disorder. As expected, the HC_alnus_bark I_D/I_G ratio is smaller than the other materials, highlighting the better organisation of the material that is also showed by its stronger 2D band at 2500-3000 cm^{-1} , resulting from bulk graphite area.

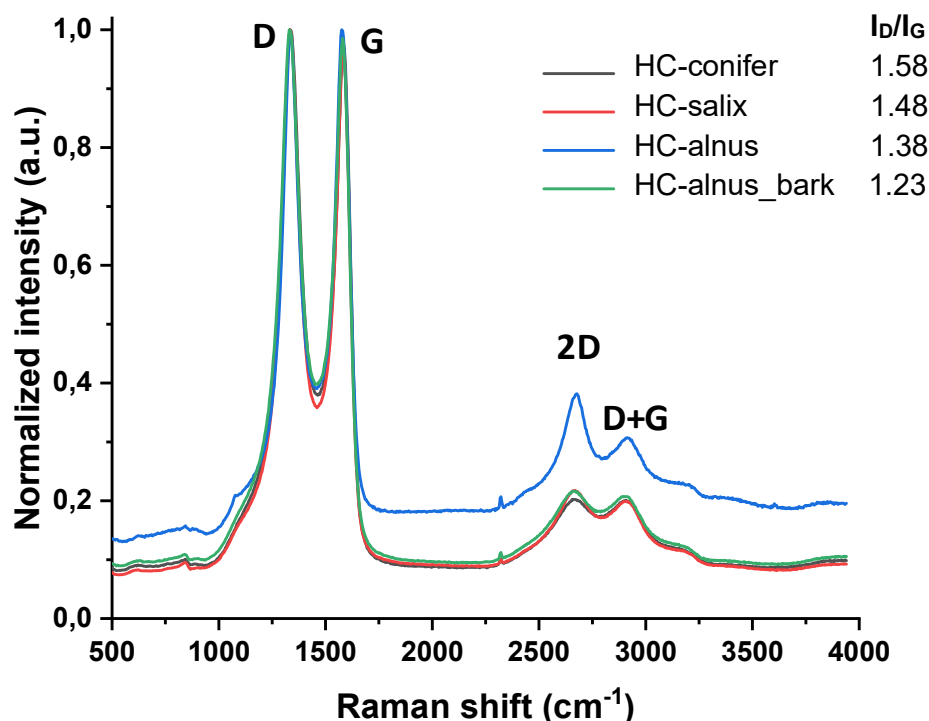


Figure 23: Normalised Raman spectra of selected hard carbons and their corresponding I_D/I_G ratios.

3.2.3. Surface area

Surface area are close between the materials: N_2 BET SSA range between 5.0 and 16.4 $\text{m}^2\cdot\text{g}^{-1}$ for HC-fraxinus and HC-populus respectively, while CO_2 BET SSA from 6.9 to 23.4 $\text{m}^2\cdot\text{g}^{-1}$ for HC-fraxinus and HC-populus respectively. As already discussed in the previous part, CO_2 is adsorbed in smaller pores and it is normal its BET SSA is higher than N_2 BET SSA. The two SSA being close, it exhibits the small ultramicroporosity of the materials. It worth notice than HC-alnus_bark has one of the lowest N_2 BET SSA of 7.5 $\text{m}^2\cdot\text{g}^{-1}$, but a CO_2 twice higher of 17.8 $\text{m}^2\cdot\text{g}^{-1}$ highlighting pores smaller than 0.7 nm. At the opposite, HC-fraxinus which exhibits both smaller N_2 and CO_2 BET SSA of 5.0 and 6.9 $\text{m}^2\cdot\text{g}^{-1}$ respectively are very close, it highlights the density of the material in which neither N_2 nor CO_2 can access. These materials exhibits relatively small SSA compared to other biomass, but are in the range of wood-based hard carbons [118].

3.2.4. Electrochemical performances

The hard carbons are then formulated into electrodes and assembled in half-cells, their cycling performances are showed in **Figure 24** and their performances reported in **Table 22**. Stem-based hard

carbons exhibits very good ICE of 83 to 85 %, while HC-alnus_bark have slightly lower ICE of 78 %. The irreversibility during the first cycle is mainly due to the surface area as explained in **Chapter 1**. As discussed above, the surface areas are similar among the materials and low compared to other biomass-based hard carbons in the literature [118]. However, its reversible capacity is only 200 mAh.g⁻¹ when the other materials' range between 290 and 310 mAh.g⁻¹. This material is more graphitized: it is well known that it is an obstacle for Na⁺ insertion, as already widely discussed in **Chapter 1** and in section 3.2.2. Such results were expected due to this organised structure. Until 95 cycles at C-rate, the cycling behaviour of all hard carbons are stable: their capacity loss is lower than 3 % not matter the raw material. Their stability is very good compared to other biomass-based hard carbon [11], in addition to the high specific capacity of stem-based hard carbons, it makes them very promising material for negative electrode in Na-ion batteries.

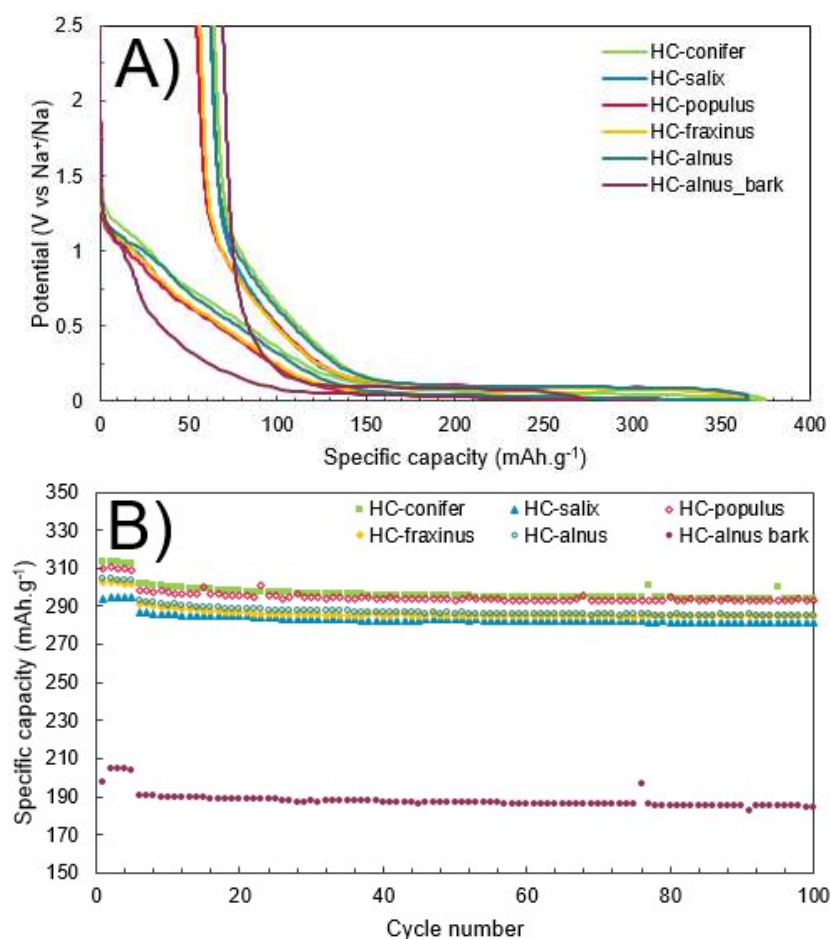


Figure 24: **A)** First cycle discharge-charge and **B)** cycling behaviour of the hard carbons from the six genera. The 5 first cycles are performed at C/10 then at 1C until the 100th cycle (C = 372 mA.g⁻¹).

To summarize, it appears that no matter the genera, all the drift stems provide hard carbons with similar properties: disorganised materials, with low SSA and very good both specific capacity and cycling stability. Nonetheless, the bark gives a more graphitized material that have poorer electrochemical performances due to its high initial inorganic content. Hence, there is no need to separate the driftwood genera for hard

carbon production, but the bark represents an obstacle for the performances of the cell. During the time spent in water and the transport in river, driftwood is naturally debarked [165] preventing from any other separation step.

Conclusions

During this study, driftwood was used as raw material for hard carbon synthesis for sodium battery application. The study was split in two in order to determine the influence of the operational conditions in one hand, and the driftwood genera in the second.

During HTC, the macromolecules are hydrolysed which provides smaller organic acids and releases inorganics in the liquid phase, however the mechanisms are highly dependent of the operating conditions: the temperature impacts the hydrolysis, at least 220 °C are required to decompose cellulose, while hemicelluloses are already depolymerised at 180 °C. It leads to a hydrochar with a higher C content, and less H and O. a similar trend in lower proportion is observed with longer residence time. After a high temperature pyrolysis, the hard carbons are similar both in structure and surface area, which gives close electrochemical performances. The main difference toward the whole reaction path, is the final chemical yield: a higher HTC temperature provides a better carbon recovery.

In parallel, it was proven that the genera of the wood is not as important as the part of the tree for HTC and pyrolysis. Indeed, there is a major difference in composition between the bark and the stem, in particular the macromolecules and the ash content, which lead to different reactions and hence products. During HTC, some inorganics are removed by leaching, however it depends on their chemical stability regarding the experiment conditions: whewellite or silicon oxide for instance are stable in such range of temperature and pressure and remain in the solid phase. This inorganics tend to catalyse local graphitization, leading to hard carbons with smaller interlayer space and thus poorer performances in sodium battery. It worth notice that the surface area doesn't seem too impacted. However, all materials provides very good cycling behaviour with capacity loss lower than 3 % among 95 cycles at C-rate, with specific capacities reaching 300 mAh.g⁻¹ for the best materials. It makes driftwood very promising materials for sodium battery electrode.

The HTC conditions were highlighted to have lower impact on the electrochemical properties than the composition of the feedstock. Hence a better understanding of the main parameter influencing the resulting hard carbon properties could be obtain with biomass with more various composition, as well as a characterisation of the composition of the hydrochar and hard carbon as well. This aspect is treated in the following chapter.

Chapter 4

Influence of the feedstock on the electrochemical performances

In this chapter, 11 biomasses from a broad diversity were investigated to highlight the influence of the starting material properties on the hard carbon properties and Na-ion battery performances. An HTC pre-treatment is performed, after the conclusion of the previous chapter. This study focuses on the chemical composition of the initial, intermediate and final product and try to highlight the influence of the feedstock and the pre-treatment on the resulting hard carbon performances.

1. Selection of the feedstock and conditions

The objective is to work on a wide scope of materials in order to draw a link between the benchmark composition and the electrochemical performances of the final hard carbons in Na-ion battery. The specificity of this study is that an HTC pre-treatment step has been added, compared to other studies dealing with a wide amount of feedstock only pyrolysed.

Feedstock were selected among 4 categories, according to Vassilev *et al.* [64] classification: wood and woody products, herbaceous and agricultural residue, animal and human wastes, and industrial biomass waste. They were chosen due to their large availability in the study area, as well as their wide diversity which offers an interesting panel to try to establish a link between the raw composition and the final product properties. They are reported in **Table 23**, as well as the nomenclature of all the material detailed in this chapter. More details about the origin of the biomasses are described in **Chapter 2**.

Table 23: Nomenclature of the materials.

Feedstock	Raw material	Hydrochar	Hard carbon
Wood & woody products			
Conifer driftwood	conifer	h-conifer	HC-conifer
Oak bark	oak_bark	h-oak_bark	HC-oak_bark
Soft wood	soft_wood	h-soft_wood	HC-soft_wood
Herbaceous & agricultural residue			
Reed straw	reed	h-reed	HC-reed
Sedge	sedge	h-sedge	HC-sedge
Walnut shell	walnut_shell	h-walnut_shell	HC-walnut_shell
Animal & human wastes			
Sewage sludge	sewage_sludge	h-sewage_sludge	HC-sewage_sludge
Horse manure	horse_manure	h-horse_manure	HC-horse_manure
Industrial wastes			
Apple pomace	apple	h-apple	HC-apple
Brewery waste	brewery	h-brewery	HC-brewery
Spent coffee grounds	coffee	h-coffee	HC-coffee

The ground biomasses are first pre-treated under HTC. As shown in **Chapter 3**, at least 220 °C are required to decompose cellulose, and long residence time favour microsphere formation at the surface of the material. HTC are then performed at 220 °C for 10 h. Industrial waste were carbonised during 12 h instead of 10, however tests on reproducibility and residence time impact between 10 and 12 h were lead and conclude on the similarity of the results. Hydrolysis and bond-breaking reaction are major at the beginning of the reaction, impacting the first 4 h are the most impacting on the hydrochar composition as widely explained in **Chapter 1**. Hydrochars are then pyrolysis at 1400 °C for 1 h under an argon flow of 15 L.h⁻¹. The choice of these conditions are explained in **Chapter 3** as well. Electrodes are then formulated and electrochemical tests are performed, similarly to the other studies of this manuscript. The experimental campaign is summarized in **Figure 25**.

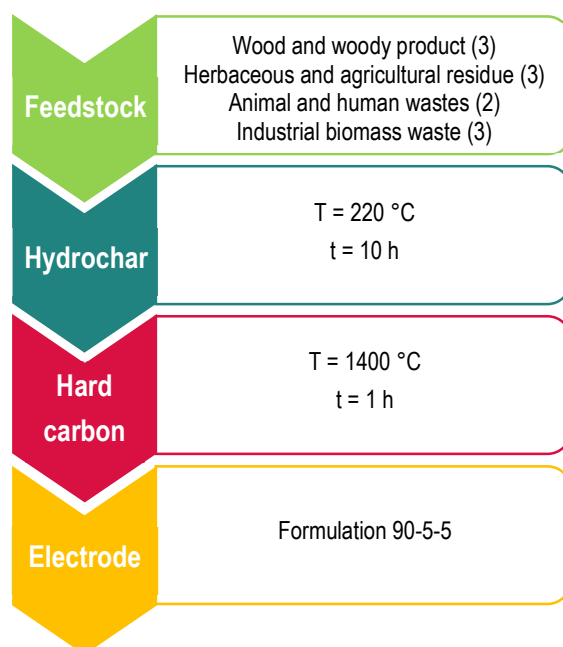


Figure 25: Experimental campaign

2. Raw biomass composition

2.1. Organic composition

The organic elemental compositions of the raw biomass are reported in **Table 24**.

The major component is C, which constitutes between 41.2 and 53.9 % of the material for respectively sewage sludge and conifer driftwood, followed by O. H contents are between 5.4 % for sewage sludge and 7.8 % for coffee waste, while N contents are between 0.2 % for soft wood and 4.1 % for sedge.

It appears that woody products and agricultural residues have similar contents of these elements, which is in agreement with literature [64], [148]. Their composition is also close to the one of industrial wastes used in this study. Indeed, this was expected as their origin (apple, hop and coffee) is agricultural residues too. However, they were transformed during their industrial processes and variation between the plant

they come from and the resulted product should be observed. Nonetheless, such range of values are in agreement with what was found for similar feedstock [166]–[169].

Human and animal wastes have the lowest contents of C and O which is balanced by their higher ash contents of 21.7 and 14.9 %. However, by considering only the organic matter in dry ash free (daf%), it appears that the C content is about 50 % for all biomass, only apple waste has a lower C daf content as already mentioned. It must be kept in mind that biomass composition is highly dependent from the place it came from and the year. Sewage sludge are particularly dependent on the water treatment process and place, however, the values obtained in this work are on the same range as other similar waste water treatment plant studies [170], [171]. Similarly, manure composition depends on the horse diet as well as the collecting conditions: contamination from sand and bedding should be avoided. Considering the bedding-free horse manure, the composition is in accordance with other studies on the same material [172].

Table 24: CHNSO and ash contents of all the materials. Contents are expressed in wdb%.

wdb%	C	H	N	S	O*	Ash
conifer	47.4 ± 0.4	6.7 ± 0.1	0.22 ± 0.02	0.1 ± 0.01	45.2	0.6 ± 0.1
oak_bark	47.7 ± 0.3	5.04 ± 0.1	0.49 ± 0.03	0.0321 ± 1	37.1	9.6 ± 0.1
soft_wood	50.6 ± 0.3	6.0 ± 0.1	0.2 ± 0.03	nd	42.6	0.6 ± 0.1
reed	49.5 ± 0.5	6.1 ± 0.1	0.42 ± 0.1	nd	42.8	1.22 ± 0.1
sedge	47.8 ± 0.5	5.8 ± 0.1	4 ± 1	nd	36.0	6.44 ± 0.1
walnut_shell	52.6 ± 0.5	6.3 ± 0.1	0.8 ± 0.1	nd	38.6	1.7 ± 0.1
sewage_sludge	41.2 ± 0.2	5.4 ± 0.2	3.5 ± 0.3	0.51 ± 0.05	27.7	21.7 ± 0.1
horse_manure	43 ± 2	5.8 ± 0.3	1.6 ± 0.2	0.5 ± 0.2	34.2	14.9 ± 0.1
apple	42.8 ± 0.1	6.9 ± 0	0.6 ± 0.1	0.3 ± 0.1	47.0	2.4 ± 0.1
brewery	46.1 ± 0.2	7.2 ± 0.1	3.34 ± 0.02	0.19 ± 0.01	39.6	3.6 ± 0.1
coffee	50.3 ± 0.3	7.8 ± 0.1	2.4 ± 0.6	0.1 ± 0.01	37.3	2.1 ± 0.1

* Calculated by difference

2.2. Inorganic composition

The ash contents are reported in **Table 24**, and inorganic elemental compositions are reported in **Table 25**. Ash contents are comprised between 0.6 and 21.7 wdb% for respectively both conifer driftwood and soft wood, and sewage sludge. As expected, human and animal waste seems to have the higher contents of 14.9 and 21.7 % for respectively horse manure and sewage sludge, while other materials are below 10 %. Wood stems, conifer and soft wood, have very low ash contents below 1 wdb%, also expected for such materials. There is no pattern among the 4 represented categories.

It is known that the bark is rich in inorganics, it tends to concentrate impurities like sand and soil [149], [150] and contains minerals from the plant metabolism [151], at the opposite of the stem. However, even if the values are very different, Ca is the most concentrated inorganic in each, from 790 to 31100 mg.kg db⁻¹ for respectively soft wood and oak bark. Conifer and soft wood have low content of inorganics, which makes it difficult to search for a tendency. In lower proportion, K and Si are the second more concentrated [11], [64].

Agricultural residues included very various feedstock, such as grass, straws and shells. Due to that, it is normal to have a wide range of composition. However, their ash content are between 1.2 and 6.4 wdb%

Table 25: Elemental composition and ash content of the raw materials..

<i>mg.kg db⁻¹</i>	K	Na	Ca	Mg	Al	Mn	Fe	P	Si
conifer	56 ± 1	17.9 ± 0.9	1680 ± 20	109.3 ± 0.2	33 ± 2	4.2 ± 0.1	60 ± 2	25 ± 2	350 ± 30
oak_bark	2250 ± 50	55 ± 3	31100 ± 400	620 ± 2	390 ± 10	373 ± 3	420 ± 20	220 ± 20	5500 ± 100
soft_wood	580 ± 40	13.8 ± 0.9	790 ± 40	140 ± 10	26 ± 4	62.1 ± 0.7	31 ± 8	63 ± 6	130 ± 20
reed	656 ± 8	95 ± 2	962 ± 7	281 ± 8	22 ± 2	5.4 ± 0.2	44 ± 5	190 ± 20	3400 ± 200
sedge	5720 ± 60	236 ± 4	5200 ± 200	1120 ± 30	200 ± 30	259 ± 4	370 ± 50	1200 ± 100	15300 ± 3700
walnut_shell	4200 ± 200	614 ± 30	1700 ± 60	436 ± 3	38 ± 2	16 ± 1	430 ± 30	810 ± 80	390 ± 40
sewage_sludge	128000 ± 12000	44600 ± 4500	62000 ± 6000	9900 ± 1000	5000 ± 500	375 ± 40	6400 ± 600	10800 ± 800	23000 ± 800
horse_manure	14700 ± 600	1460 ± 50	4600 ± 300	2180 ± 70	900 ± 100	133 ± 6	1050 ± 30	6100 ± 600	37900 ± 500
apple	7350 ± 30	76 ± 4	756 ± 1	501 ± 1	11.4 ± 0.4	6.10 ± 0.01	18.4 ± 0.8	960 ± 70	80 ± 20
brewery	776 ± 2	407 ± 1	1710 ± 30	1870 ± 20	12 ± 2	32.3 ± 0.2	73 ± 3	4590 ± 30	5300 ± 300
coffee	8350 ± 50	200 ± 20	880 ± 10	1170 ± 20	6 ± 2	14.0 ± 0.3	25 ± 3	710 ± 30	17 ± 8

Table 26: Sugar monomer and macromolecule composition of the raw biomass. na. are non-applicable.

	Sugar monomer (wdb%) (± 5 %)					Macromolecules (wdb%) (± 5 %)			
	Glucose	Xylose	Manose	Galactose	Arabinose	Cellulose	Hemicelluloses	Lignin	Extractives
conifer	43.39	7.05	12.42	2.42	1.14	40.40	29.27	27.65	2.90
oak_bark	20.06	10.22	0.00	1.22	1.83	20.06	17.45	30.29	16.16
soft_wood	43.46	5.59	11.17	1.67	0.98	40.77	26.06	26.48	4.11
reed	38.67	22.75	0.30	0.80	2.00	38.49	31.29	22.1	4.97
sedge	30.17	15.18	0.72	1.95	4.63	29.75	26.21	59.60	9.62
walnut_shell	21.90	15.72	1.00	1.25	0.62	20.90	25.28	31.98	13.82
sewage_sludge	na	na	na	na	na	na	na	na	na
horse_manure	25.28	15.44	0.20	1.18	2.49	25.15*	22.05*	55.2*	16.37
apple	17.57	3.11	1.23	2.30	3.91	16.34*	13.88*	12.11	47.66
brewery	16.48	12.12	0.63	0.91	7.04	**	**	16.51	29.99
coffee	8.68	0.27	22.63	11.19	2.32	**	**	23.27	21.98

* to be taken carefully

** no data due to the lack of information on the conversion factors of these materials between the monomers and polymer.

for reed and sedge respectively. These two are richer in Si with respectively 3400 and 15300 mg.kg db⁻¹, while the shell is richer in K with 4200 mg.kg db⁻¹.

Similarly to agricultural residues, human and animal waste materials regroups feedstock from very different origins, it is difficult to find any tendency with this choice of materials. The two chosen biomasses of this study are rich or very rich in Si, K and Ca. The only element present in lower quantity than 1000 mg.kg db⁻¹ is Mn.

Industrial waste are more homogeneous on their ash contents, they lie between 2.1 and 3.6 wdb% for respectively coffee and brewery waste. Apple and coffee waste are richer in K – respectively with 7352 and 8354 mg.kg db⁻¹ –, while brewery waste is rich in P and Si with 4590 and 5277 mg.kg db⁻¹ respectively.

These observations are in agreement with what is usually found in the literature [11], [64], as explained in **Chapter 1**.

2.3. Macromolecule content

As mentioned in **Chapter 1**, plants are lignocellulosic biomass and are composed of cellulose, hemicellulose, lignin, extractives and ash. Sugar monomer and macromolecule compositions are reported in **Table 26** when applicable. Indeed, sewage sludge is not plant-based, and hence are not considered as lignocellulose. Similarly, industrial wastes were processed by different steps which could have degraded their macromolecules. The polysaccharide measurements where led on the monomers, the macromolecule contents were calculated based on them. However, the process might have degraded and broken the macromolecule bonds. The cellulose and hemicellulose composition has to be taken carefully due to that.

The macromolecule composition is very dependent on the biomass type. Lignin contents are between 26 and 60 wdb% for woods and agricultural residues, while they are between 12 and 23 wdb% for industrial wastes. Lignin gives a rigid structure to the plant, protecting the polysaccharides from microbial attacks [74], [75]. It is then logical that their content is higher in rigid biomass such as trees and shells than in fruits and digestates. However, a very important amount was measured in sedge. Lignin is rarely reported higher than 30 wdb% in grass, and especially sedge which usually contains between 10 to 15 wdb% [173], [174]. Moreover, the addition of cellulose, hemicelluloses, lignin, extractives and ashes is higher than 100 % for sedge and horse manure. Silica and silicic acid naturally present in plants can precipitate into insoluble compound, which tend to overestimate the lignin measures [175]. These two materials are rich in Si as reported in section **2.2**, which could explain these high amounts.

Tree stems are usually richer in cellulose than hemicelluloses and lignin, which is the case in this study for both conifer and soft wood. Conversely, barks are richer in hemicelluloses and lignin [79]. Cellulose content is twice higher in the stem fraction (conifer, soft wood) than in the bark (oak bark), which is close to the shell's content (walnut shell). Woods have more cellulose than hemicelluloses, unlike agricultural

residues which are more feedstock dependant. Indeed, this category gathers more various materials such as shells, grass or straws, where the physicochemical properties are various.

Extractives include molecules from very different nature, such as polyphenols, proteins or fatty acids, every molecules that leach in water, ethanol or any other solvent used to extract interest molecules [79]. Soft wood is twice more concentrated in extractives than conifer, which could be explained by their leaching in water by immersion with the time and environmental conditions.

The composition of the woods and agricultural residues is consistent with what is usually found for these biomasses [79], [148].

Industrial waste is globally richer in extractives and poorer in macromolecules. As mentioned, it could come from the bond breaking during the industrial process. Furthermore, under high moisture content and temperatures, fruit waste starts fermenting in short periods; thus, sugars start degrading, producing weak-acidic compounds [169]. The macromolecules being degraded and the conditions being acidic, it could also explain the high extractive content on apple waste. However, lignin bonds are strong and difficult to break – they are usually measured by the remaining mass after a strong hydrolysis in very acidic conditions –, their content could be close from the apple, hop and coffee beans they come from. The values found between 12 and 23 wdb% are coherent with what is typically found for these kind of biomass [166]–[169].

2.4. Structure

The XRD patterns of all materials are reported in **Figure 26**, separated by category. The different crystalline phases are identified by symbols, as described in **Chapter 2**.

Characteristic cellulosic pattern is observed in woody products and agricultural residues, which is coherent with the lignocellulosic composition already discussed in **Chapter 3**. It appears as 3 wide peaks: the more intense at about 22 °, a wider at about 15 ° and a smaller at 35 °. The broadness of the peaks translates the disorganised structure of the cellulose. Indeed, this macromolecule is known to have crystalline areas linked by amorphous zones make the material semi-crystalline [71]. Its pattern is more intense on materials where the cellulose contents were the higher. The typical pattern is not as obvious in oak bark despite its lignocellulosic nature, which could come from the intense other peaks which flatten the cellulose ones. Hemicellulose and lignin can't be observed on XRD because of their amorphous structure.

A cellulose-like pattern could be observed on horse manure and apple. It is not enough to determine the presence of this macromolecule on the material, but can be explained by the origin of the feedstock before processing. Horse manure is digested straw, while apple waste is pomace. They both originally were lignocellulosic material, and the transformation they suffered might not have depolymerized the macromolecules.

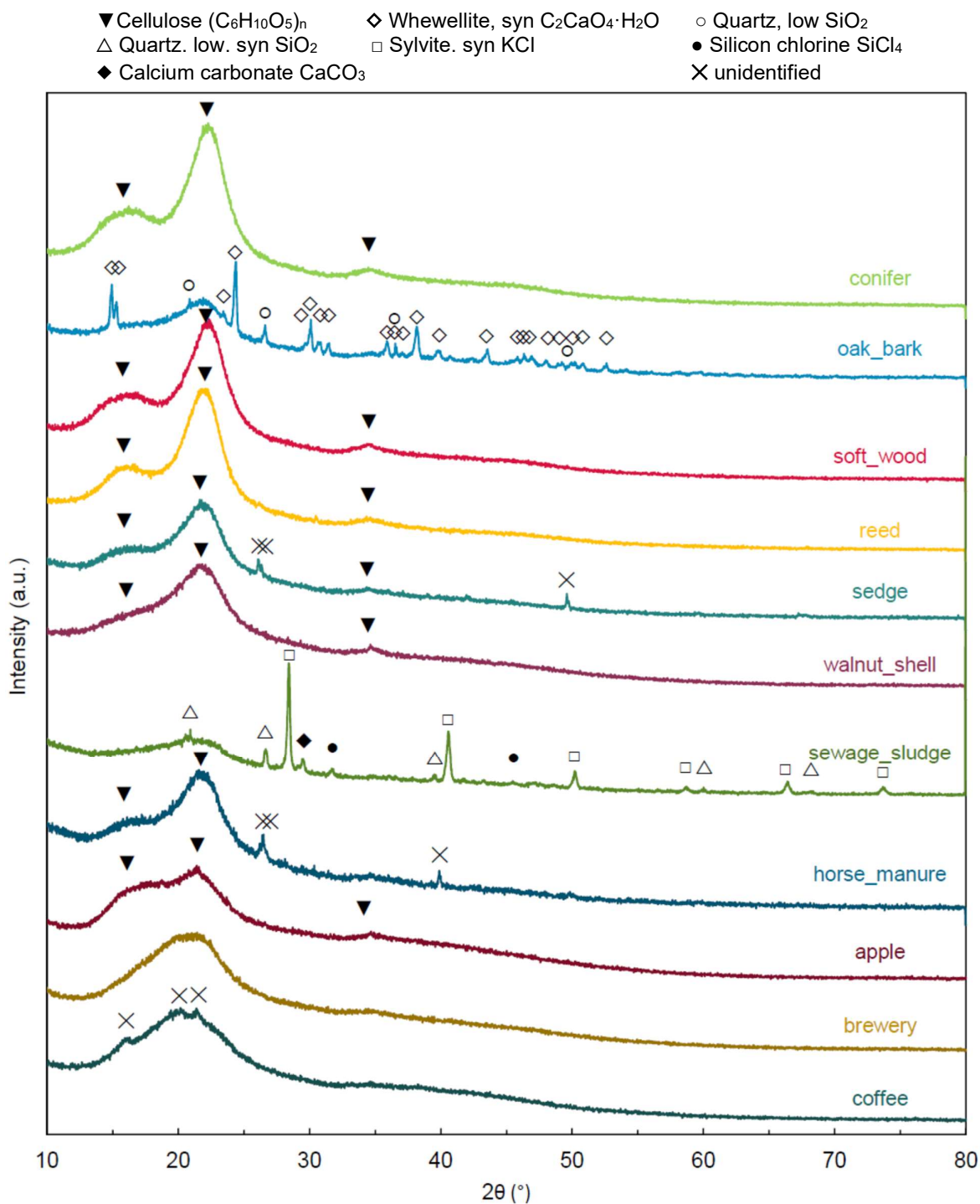


Figure 26: XRD patterns of the raw biomass.. Peaks are identified with symbols as: ▼ Cellulose- β ($C_6H_{10}O_5$)_n PDF 00-060-1502, ◇ Whewellite, syn $C_2CaO_4 \cdot H_2O$ PDF 00-020-0231, ○ Quartz, low SiO_2 PDF 00-005-0490, △ Silicon oxide quartz, low. syn PDF 03-065-0466, □ Potassium chloride sylvite, syn KCl PDF 04-005-9297, ● Silicon chlorine $SiCl_4$ PDF 00-010-0220 ◆ Calcium carbonate calcite-III $CaCO_3$ 00-017-0763, and ✕ unidentified

Sharp peaks highlight the presence of crystalline structures in oak bark, sedge, sewage sludge, horse manure and coffee waste. Whewellite, syn $C_2CaO_4 \cdot H_2O$ (PDF 00-020-0231) and quartz, low SiO_2 (PDF 00-005-0490) are present in the bark, which is in accordance with the very high Ca and Si content already discussed. Calcium oxalate is a common plant constituent [79], [156], which is thought to impact Ca regulation and photosynthesis [157]. Quartz is a common soil mineral which was reported many times on biomass. However, SiO_2 seems to be more present as disorganised opal on plants, which results broad area between 20 and 30° [79], [176].

Sewage sludge exhibits SiO_2 pattern too, as quartz. low. syn (PDF 03-065-0466) phase, consistent with its high Si content. It also contains potassium chloride sylvite. syn KCl (PDF 04-005-9297), Silicon chlorine $SiCl_4$ (PDF 00-010-0220) and calcium carbonate calcite-III $CaCO_3$ (PDF 00-017-0763), which is in accordance with its composition which is rich in K, Si and Ca. Silicon oxide and calcium carbonate has already been reported in XRD of dried sewage sludge [177], [178].

Sedge, horse manure and coffee patterns exhibit unidentified peaks, where the intensities were not enough to determine the component with accuracy. Both sedge and horse manure exhibit a sharp peak at about 26° which could correspond to SiO_2 , as their high Si contents suggest. However, the small intensity and the lack of secondary peaks that could be lost in the background do not allow to conclude on the nature of this phase. Coffee exhibits a different pattern than all the other materials, with small sharp peaks at about 16, 20, 21 and 25°. Due to their low intensity, it is difficult to identify these phases. However, similar patterns were also observed in literature for spent coffee grounds [179], [180].

The 11 selected feedstock exhibits a very large panel of composition and physical properties, which highlights the diversity of biomass. The obtained values are in accordance with similar feedstock in the literature. Hence, a wide scope can be studied, in order to link their properties to their behaviour during HTC and pyrolysis.

3. Hydrochar composition

3.1. Organic composition

Organics and ash contents, and HTC solid yields are reported in **Table 27**.

C is the major element in all hydrochars, ranging between 50 and 72 % for respectively h-sewage_sludge and h-coffee. The C content increases from the raw material to the hydrochar, from 9 to 27 wdb% respectively for h-sewage_sludge and h-apple, unlike O and H which tend to decrease. During HTC, dehydration mechanism occurs leading to a loss of H and O. Furthermore, the decomposition of the biomass macromolecules leads to smaller molecules such as furfurals or organic acids [94], [97] as mentioned in **chapter 1**. These smaller molecules end in the liquid phase, leading to a loss of C, H and O in the solid. This range of values is consistent with works led on olive mill [181], municipal waste [94], dairy manure [100] or water hyacinth [107]. At the opposite and according to literature [105], N behaviour

seems to be feedstock dependent: while it increases for most of the materials, h-sedge, h-sewage_sludge and h-horse_manure have a lower content than their raw materials.

However, when considering only the dry ash free material, it appears that the values less dispersed, as highlights the balance of the organic elements reported on **Figure 27**, especially for C. Tendencies are similar to what was discussed above.

Table 27: CHNSO and ash contents of the hydrochars, and solid yield SY of the reaction. SY is calculated according to equation (8). Contents are expressed in wdb%.

wdb%	SY %	C	H	N	S	O*	Ash wdb%	
		wdb%						
h-conifer	52 ± 2	67.5 ± 0.3	4.81 ± 0.03	0.43 ± 0.01	<0.3	27.1	0.2 ± 0.1	
h-oak_bark	58 ± 2	57.45 ± 0.3	4.655 ± 0.04	0.625 ± 0.03	<0.3	25.4	11.9 ± 0.1	
h-soft_wood	54 ± 2	68.08 ± 0.235	4.7 ± 0.1	0.35 ± 0.06	<0.3	26.8	0.1 ± 0.1	
h-reed	50 ± 2	66.65 ± 0.2	5.0 ± 0.1	0.925 ± 0.03	0.3 ± 0.1	26.3	0.8 ± 0.1	
h-sedge	50 ± 2	61 ± 2	5.51 ± 0.04	1.86 ± 0.03	<0.2	24.3	7.3 ± 0.1	
h-walnut_shell	52 ± 2	67.865 ± 0.2	5.975 ± 0.09	1.075 ± 0.01	<0.3	24.6	0.5 ± 0.1	
h-sewage_sludge	43 ± 2	50 ± 1	5.5 ± 0.4	2.8 ± 0.2	0.37 ± 0.02	18.8	22.5 ± 0.1	
h-horse_manure	52 ± 2	52 ± 5	5 ± 0.4	0 ± 0.1	0.23 ± 0.02	20.2	22.6 ± 0.1	
h-apple	42 ± 2	69.7 ± 0.9	5.6 ± 0.1	1.1 ± 0.1	0.10 ± 0.01	23.2	0.3 ± 0.1	
h-brewery	37 ± 2	71.5 ± 0.5	7.1 ± 0.1	3.9 ± 0.5	0.27 ± 0.01	16.7	0.5 ± 0.1	
h-coffee	46 ± 2	72.5 ± 0.5	8.00 ± 0.1	2.9 ± 0.5	0.16 ± 0.01	15.9	0.5 ± 0.1	

* Calculated by difference

3.1. Inorganic composition

Ash contents are reported in **Table 27**, and inorganics contents in **Table 28**.

Ash content is the least homogeneous among the feedstock and hydrochars. After carbonisation, the contents lie between 0.2 and 22.6 wdb%, for respectively h-soft_wood and h-sewage_sludge, with the same tendency than the raw materials, soft wood and sewage sludge being the two extremums as well. However, ash content behaviour depends on the feedstock: while it decreases for most of the materials, it increases on h-oak_bark, h-sedge, h-sewage_sludge and h-horse_manure. It looks like the ash are more concentrated on the hydrochar from biomass that have an ash content above 6 wdb%. As widely described in **Chapter 1**, HTC is known to leach inorganics during the process, but this depends on the composition of the material used [96], [104], [105].

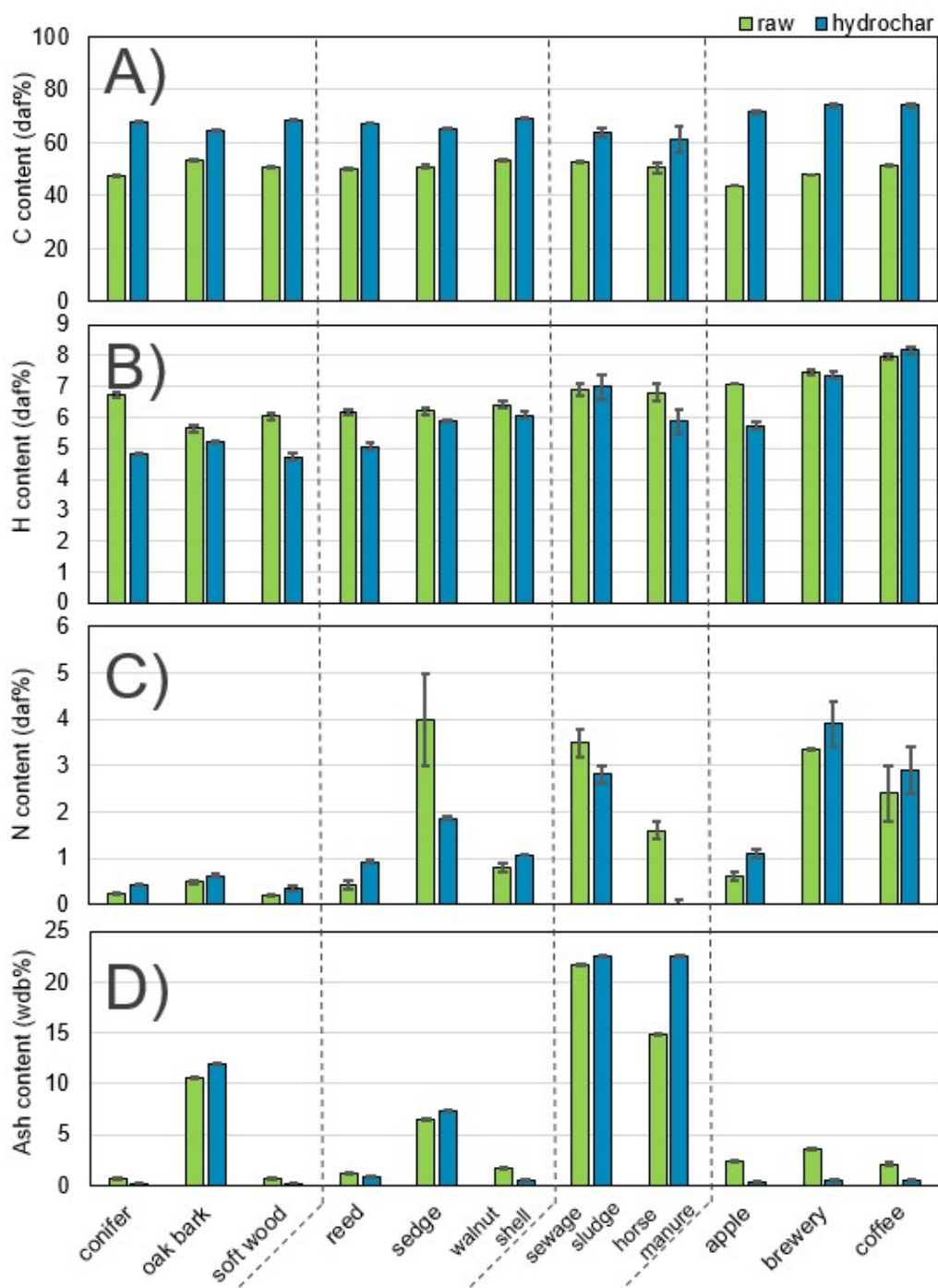


Figure 27: **A)** C, **B)** H and **C)** N content in daf% and **D)** ash content in wdb% on the raw materials (in green) and hydrochars (in blue). Uncertainties are the standard deviations between the replicates for C, H and N contents, and the method deviation for the ash.

K, Na, Mg and P contents globally decrease between the raw material and the hydrochar, while Al, Fe and Si tend to increase. At last, Ca and Mn do not seem to have tendency among the samples. In order to characterise the leaching, and more precisely which elements on what proportion remain in the hydrochar at the end of the reaction, the balance of inorganics is presented in **Figure 28**. To report on the quantities, each element is plot from **Figure 29** to **Figure 37** at the adapted scales.

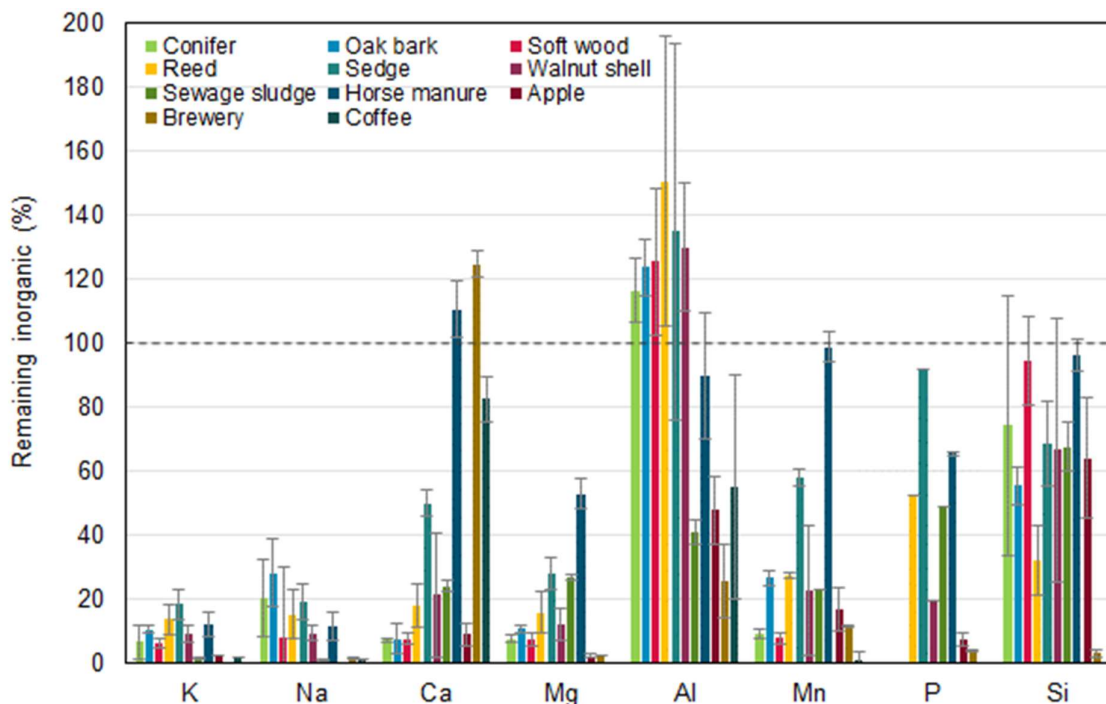


Figure 28: Balance of the inorganics that remain in the char after reaction in %. The lack of histogram bars comes from the hydrochar content that were below limit of detection. Uncertainties are experimental standard deviations.

K, Na and Mg contents are highly less concentrated on the hydrochars than the raw biomass, meaning these elements are solubilized on these experimental conditions. Less than 30 % of the original content of Na remains in the solid after reaction, and less than 20 % for K, no matter the feedstock. On most samples, less than 30 % of Mg also remain in the hydrochar, except for h-horse_manure where 53 % remains.

Ca seems to leach on different proportion depending on the feedstock. While more than 75 % is released from most of the materials, h-oak_bark, h-horse_manure and h-coffee_waste retain it. These three materials are also the three where the Ca content of the hydrochar is higher than the raw materials. Similarly, the quantity of P remaining in the hydrochar seems feedstock dependent. It is present in very low quantity in the raw woods, and is almost completely removed during the reaction. Although the concentration was higher on industrial wastes, the same trend is observed on these materials. No pattern can be deduced from agricultural and animal and human waste, while about 20 % remains in h-walnut_shell, more than 90 % remains in h-sedge.

Table 28: Inorganic compositions of the hydrochars from all categories.

<i>mg.kg db⁻¹</i>	K	Na	Ca	Mg	Al	Mn	Fe	P	Si
h-conifer	7 ± 3	7 ± 2	230 ± 10	16 ± 1	74 ± 1	0.74 ± 0.05	19 ± 1	<1600	500 ± 100
h-oak_bark	410.0 ± 20	27 ± 5	41000 ± 1400	115 ± 7	840 ± 20	172 ± 8	720 ± 30	<400	5300 ± 300
h-soft_wood	68 ± 6	2 ± 3	110 ± 10	19 ± 2	61 ± 1	9 ± 1	9 ± 1	<400	230 ± 20
h-reed	180 ± 30	29 ± 7	350 ± 60	90 ± 20	67 ± 7	3 ± 0	140 ± 20	200 ± 200	2200 ± 400
h-sedge	2100 ± 300	90 ± 10	5200 ± 100	630 ± 50	540 ± 70	300 ± 5	1000 ± 200	2210 ± 20	21000 ± 2000
h-walnut_shell	730 ± 90	110 ± 10	700 ± 300	100 ± 20	95 ± 5	7 ± 3	450 ± 40	300 ± 200	500 ± 200
h-sewage_sludge	3600 ± 400	1100 ± 200	35000 ± 1000	6280 ± 80	4800 ± 200	203 ± 0	3680 ± 70	12480 ± 70	36500 ± 1300
h-horse_manure	3400 ± 500	320 ± 60	9790 ± 70	2220 ± 60	1550 ± 90	253 ± 1	2300 ± 70	7670 ± 40	70200 ± 1400
h-apple	585 ± 2	<10	210 ± 30	35 ± 3	17 ± 1	3.2 ± 0.4	135 ± 1	220 ± 10	160 ± 20
h-brewery	<30	15 ± 2	5770 ± 40	117 ± 5	8.3 ± 0.9	10 ± 0	340 ± 30	470 ± 20	420 ± 60
h-coffee	430 ± 20	18 ± 2	1020 ± 50	205 ± 4	13 ± 1	16.5 ± 0.4	168 ± 2	690 ± 50	37 ± 7

Similar observations were reported on studies led on lignocellulosic biomass, led at different residence time and temperature [104]–[106], [182]. As Smith *et al.* [105] explains in detail, K, Na, Mg and P are present in different forms in the biomass: as water-soluble ionic salt, organically associated metals ionic or covalently bonded with tissue, or amorphous, crystalline or pure precipitated compounds. K and Na are mainly present in plants as nitrate and chloride salts that are water-soluble, while Ca and P are also present as precipitated compound or associated with macromolecules [183], their large or moderate leaching to the liquid phase was predictable. Furthermore, hot water extraction is performed to partially remove Ca, P, Mg and K in biomass, hence high temperature and pressure provided in HTC are not mandatory on these elements [184].

For most of the materials, about 50 to 70 % of Si remains in the solid independently of the category of biomass. However, h-soft_wood and h-horse_manure kept all the Si in their hydrochar while only 3 % remain in h-brewery. Its behaviour seems feedstock dependent, which is in accordance with literature: Smith *et al.* [105] reported only 20 % of the initial Si in its willow-based hydrochar, and Poerschmann *et al.* [185] 50 % on brewer's spent-based, while rice hulls [104], digestate [186] and sewage sludge [105] were found with an almost total retention. These three last materials were Si-rich, from 36000 to 332400 mg.kg⁻¹ that are much higher content than most of the materials in this study. In the previous part, SiO₂ was characterised in the raw oak bark and sewage sludge, which is known to be insoluble under this temperature and pressure [159]. Other Si species are easier to dissolve, as Si(OH)₄ that can be naturally present in plant tissue [187]. The relatively low leaching of Si in h-soft_wood could also come from the very small amount in the raw material, at the opposite of h-brewery where the raw content was significant. Brewery waste has been digested, which might free compounds trapped in the hop structure and hence increase their leaching.

Mn is present in traces in most of the raw biomasses and hydrochars, and the contents tend to decrease after reaction. Due to the low quantities, no balance can be precisely determined.

Conversely, Al is more concentrated in the hydrochar than the biomass, almost all the Al from lignocellulosic materials remains in the solid after reaction. The contents are low, which by comparison makes the uncertainty high compared to the value, which could explain the recovery above 100 %. Unlike woods and agricultural residue, the other materials don't retain Al as much, between 26 to 87 % for respectively h-brewery and h-horse_manure.

Fe, in the other hand, does not highlight a clear tendency between lignocellulose and other biomass. Half of the materials; h-reed, h-sedge, h-horse_manure, h-apple, h-brewery and h-coffee; exhibit a recovery superior to 100 %. It has to be kept in mind. The reactor being in stainless steel grade 316, these high value could come from a leach of Fe from the reactor. Due to this potential leaching, Fe balance should be taken carefully, and conclusion are difficult to make.

Other measured heavy metals, Cu, Cr, Co, Ni, are in too low quantity to make an accurate balance. However, they are only traces in the raw biomass, and don't seem to be removed during HTC, as reported by Reza *et al.* [104].

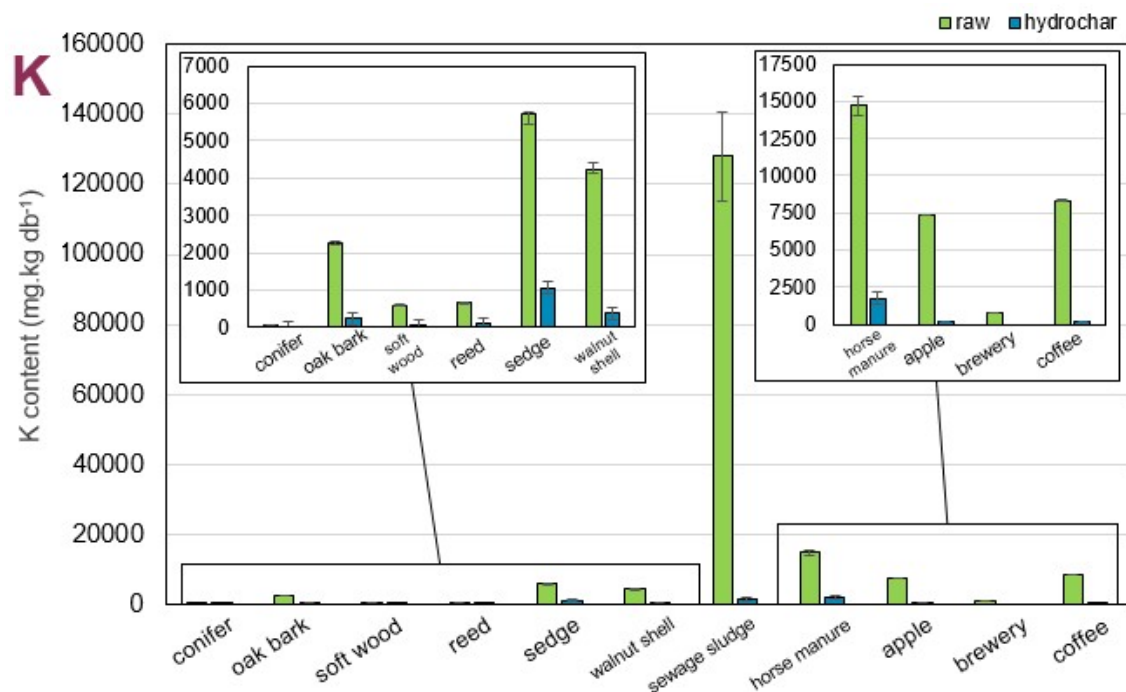


Figure 29: Balance of the K between the raw material (in green) and the hydrochar (in blue). To compare de value, hydrochar contents have been converted in mg.kg raw db⁻¹ according to equation (10).

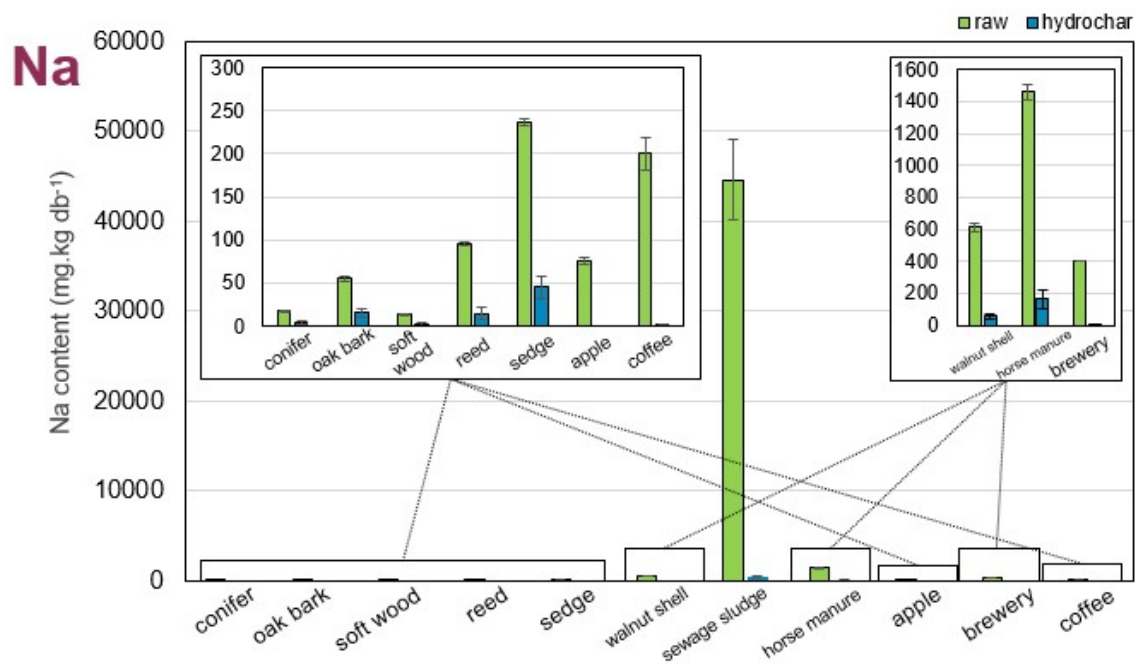


Figure 30: Balance of the Na between the raw material (in green) and the hydrochar (in blue). To compare de value, hydrochar contents have been converted in mg.kg raw db⁻¹ according to equation (10).

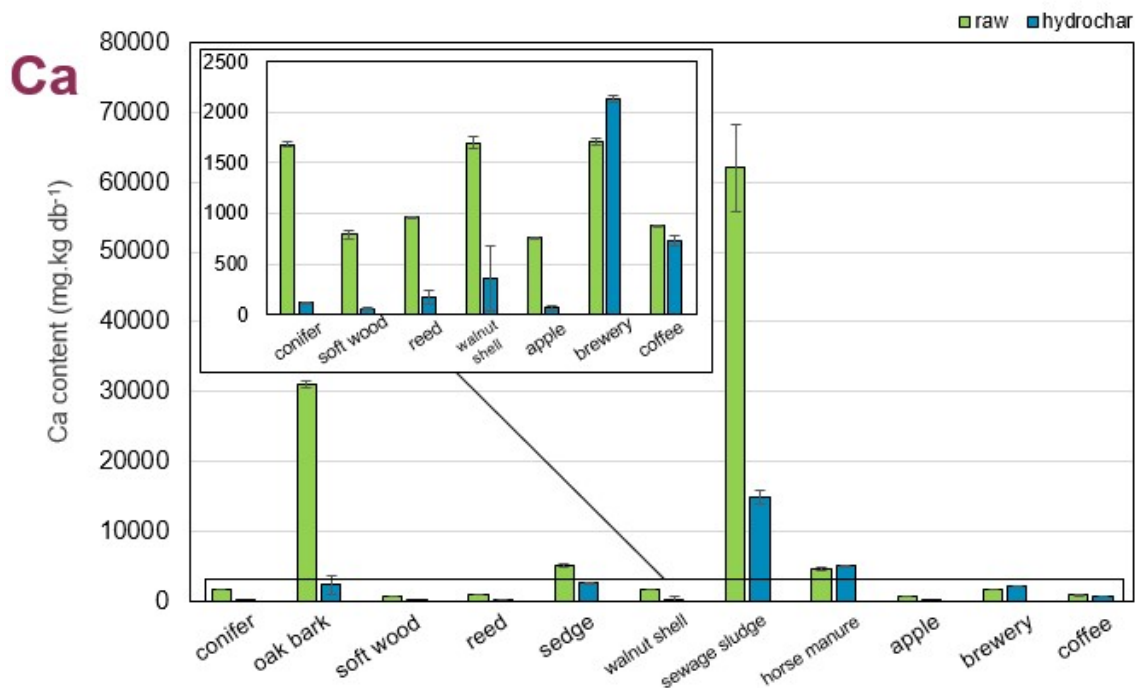


Figure 31: Balance of the Ca between the raw material (in green) and the hydrochar (in blue). To compare de value, hydrochar contents have been converted in mg.kg raw db⁻¹ according to equation (10).

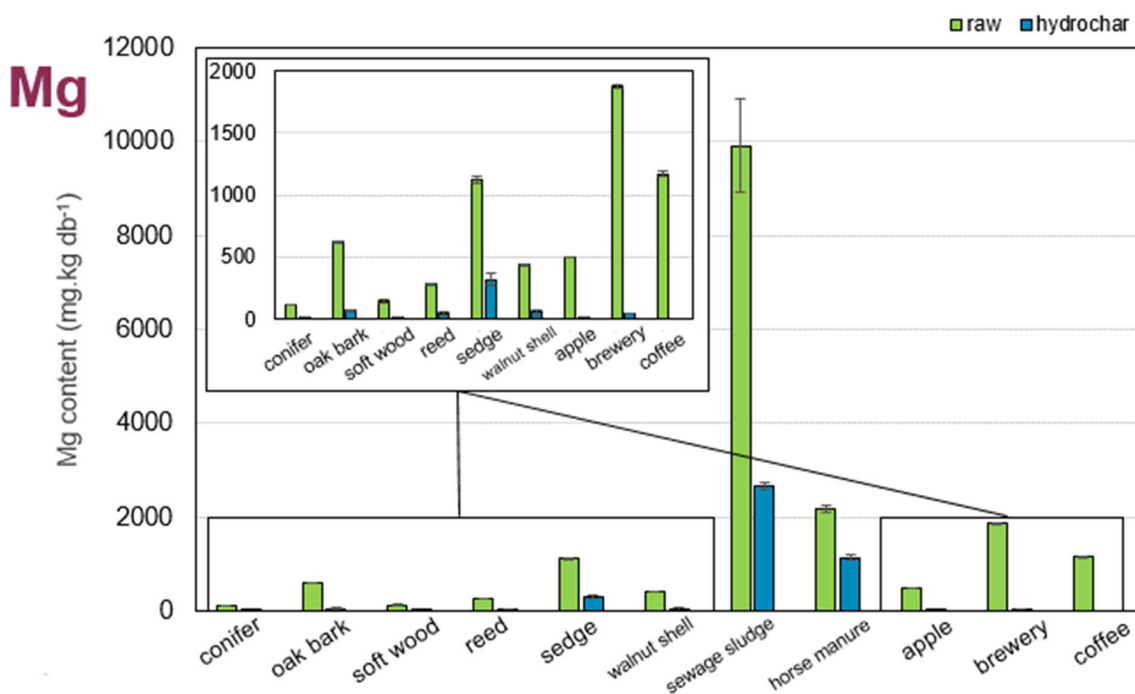


Figure 32: Balance of the Mg between the raw material (in green) and the hydrochar (in blue). To compare de value, hydrochar contents have been converted in mg.kg raw db⁻¹ according to equation (10).

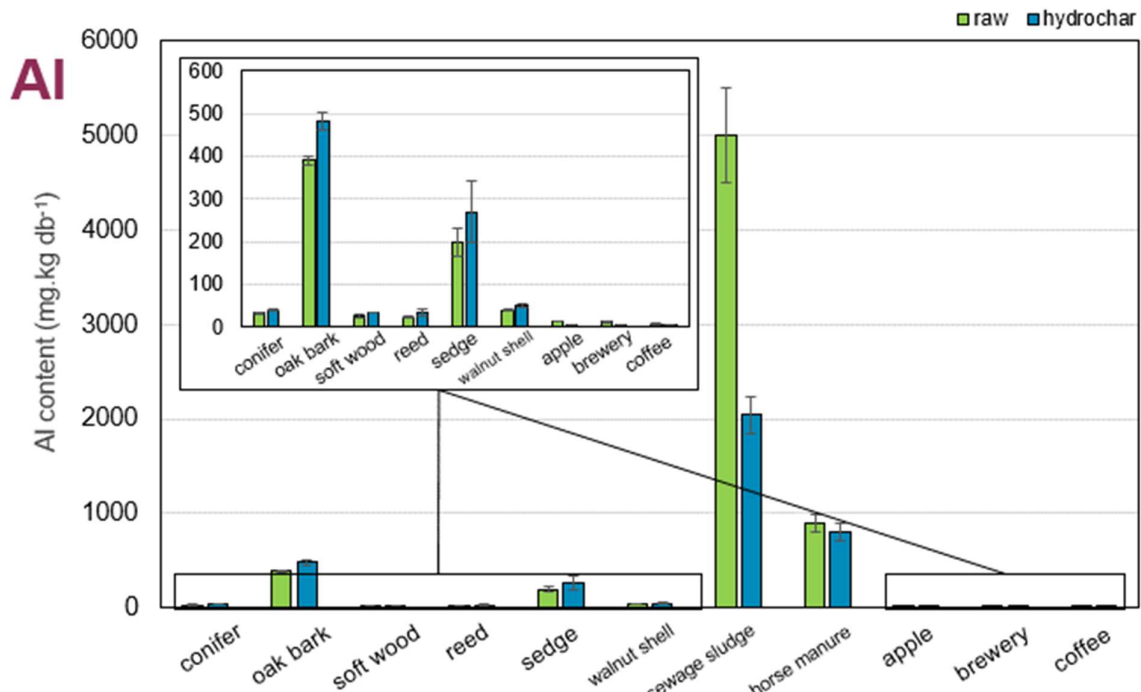


Figure 33: Balance of the Al between the raw material (in green) and the hydrochar (in blue). To compare de value, hydrochar contents have been converted in mg.kg raw db⁻¹ according to equation (10).

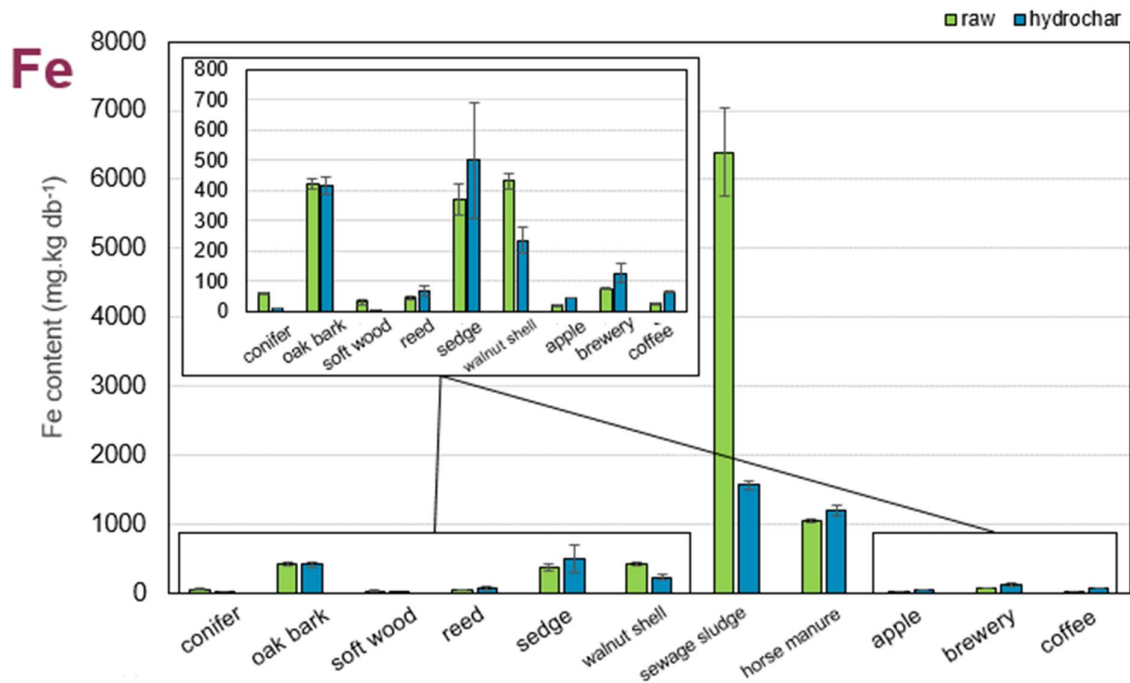


Figure 34: Balance of the Fe between the raw material (in green) and the hydrochar (in blue). To compare de value, hydrochar contents have been converted in mg.kg raw db⁻¹ according to equation (10).

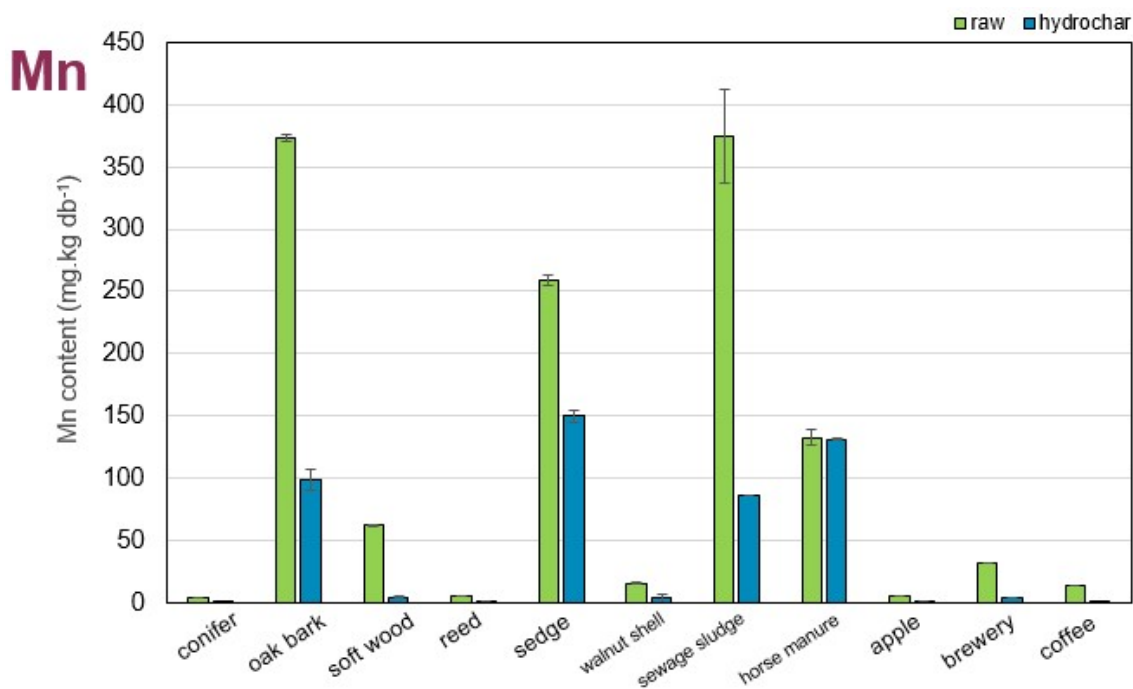


Figure 35: Balance of the Mn between the raw material (in green) and the hydrochar (in blue). To compare de value, hydrochar contents have been converted in mg.kg raw db⁻¹ according to equation (10).

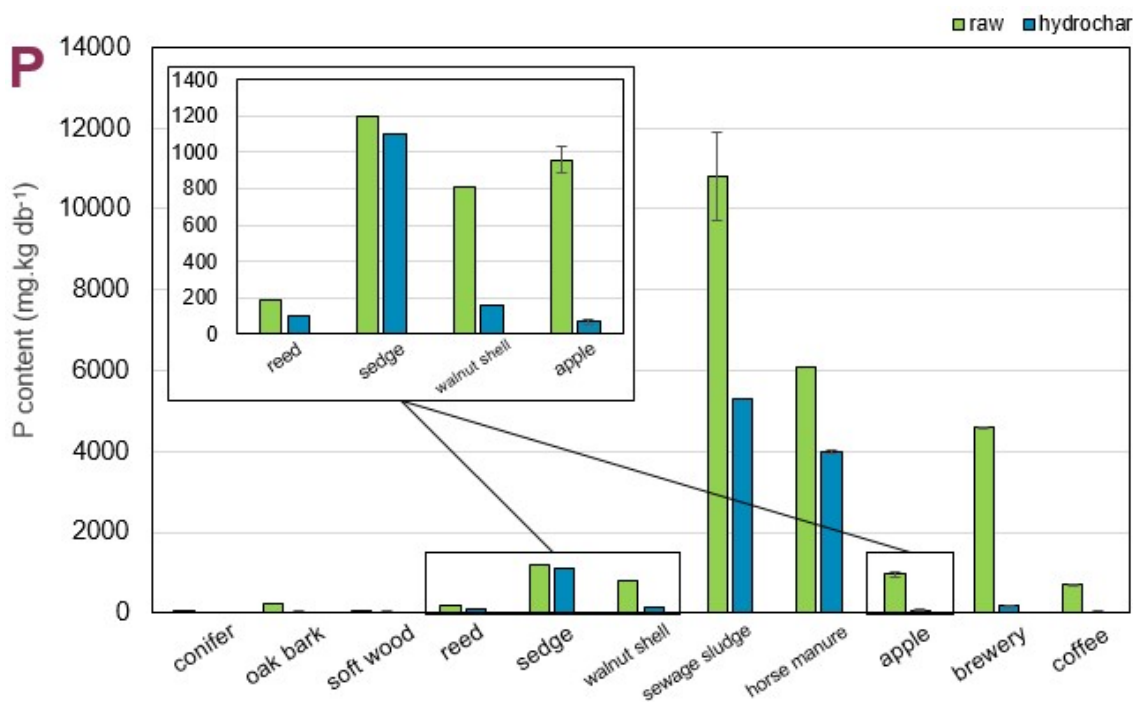


Figure 36: Balance of the P between the raw material (in green) and the hydrochar (in blue). To compare de value, hydrochar contents have been converted in mg.kg raw db⁻¹ according to equation (10).

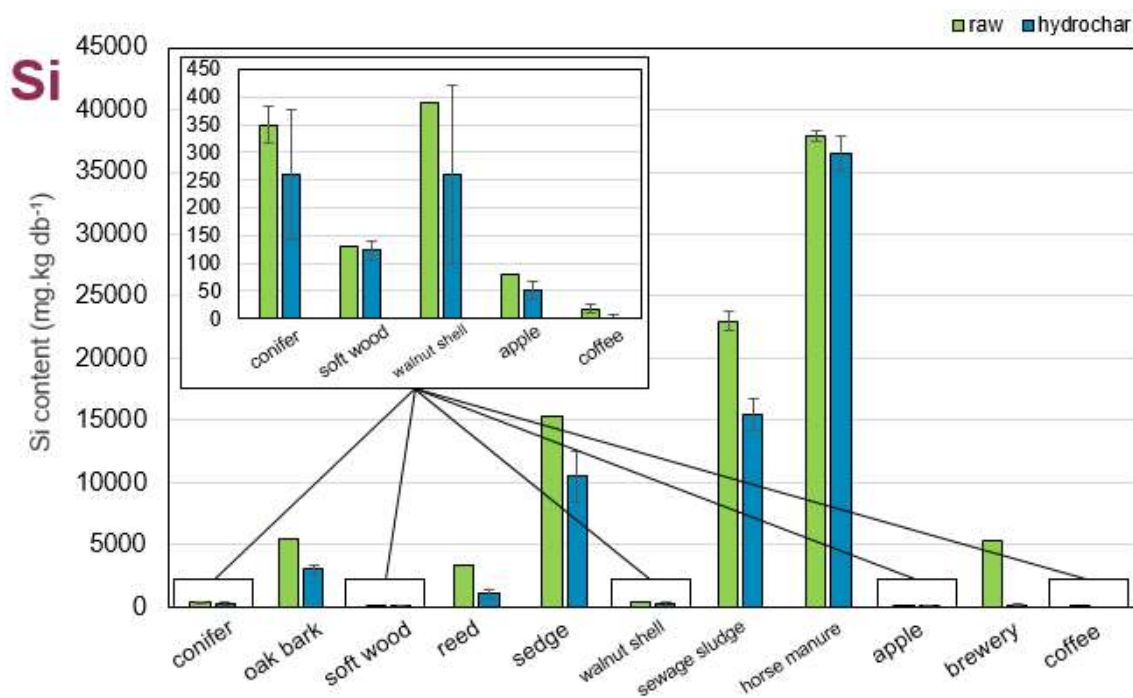


Figure 37: Balance of the Si between the raw material (in green) and the hydrochar (in blue). To compare de value, hydrochar contents have been converted in mg.kg raw db⁻¹ according to equation (10).

3.2. Structure

To identify the phase in the hydrochars, XRD are performed and patterns are reported in **Figure 38**.

The cellulose pattern that was present on the raw materials tends to disappear in the hydrochars, highlighting the degradation of the macromolecule. At such temperature, cellulose hydrolysis is predominant, which is enhanced by the long residence time [97]. Such observation was expected on lignocellulosic materials.

Sharp peaks appear after reaction in h-oak_bark, h-sedge, h-sewage_sludge, h-horse_manure and h-coffee materials, indicating the presence of crystalline structure compounds on the hydrochars. Characteristic peaks of whewellite and quartz that were already present in the raw oak bark are also on the hydrochar XRD patterns, these two compounds were not significantly degraded or solubilized during the reaction, moreover calcium oxalate is reported to be stable in water and in a large range of pH [156]. The limited loss of Ca and Si during the HTC could come from the poor solubility of these two species. This observation was also made on the alnus bark from **Chapter 3**.

Similarly, sewage sludge contains quartz both in the raw material and hydrochar, confirmed by their high Si content. However, the characteristic pattern of KCl found on the raw biomass is no longer present in the hydrochar, it is in accordance with the predominant K leaching discussed in the previous part. SiCl₄ and CaCO₃ from the raw material were also removed.

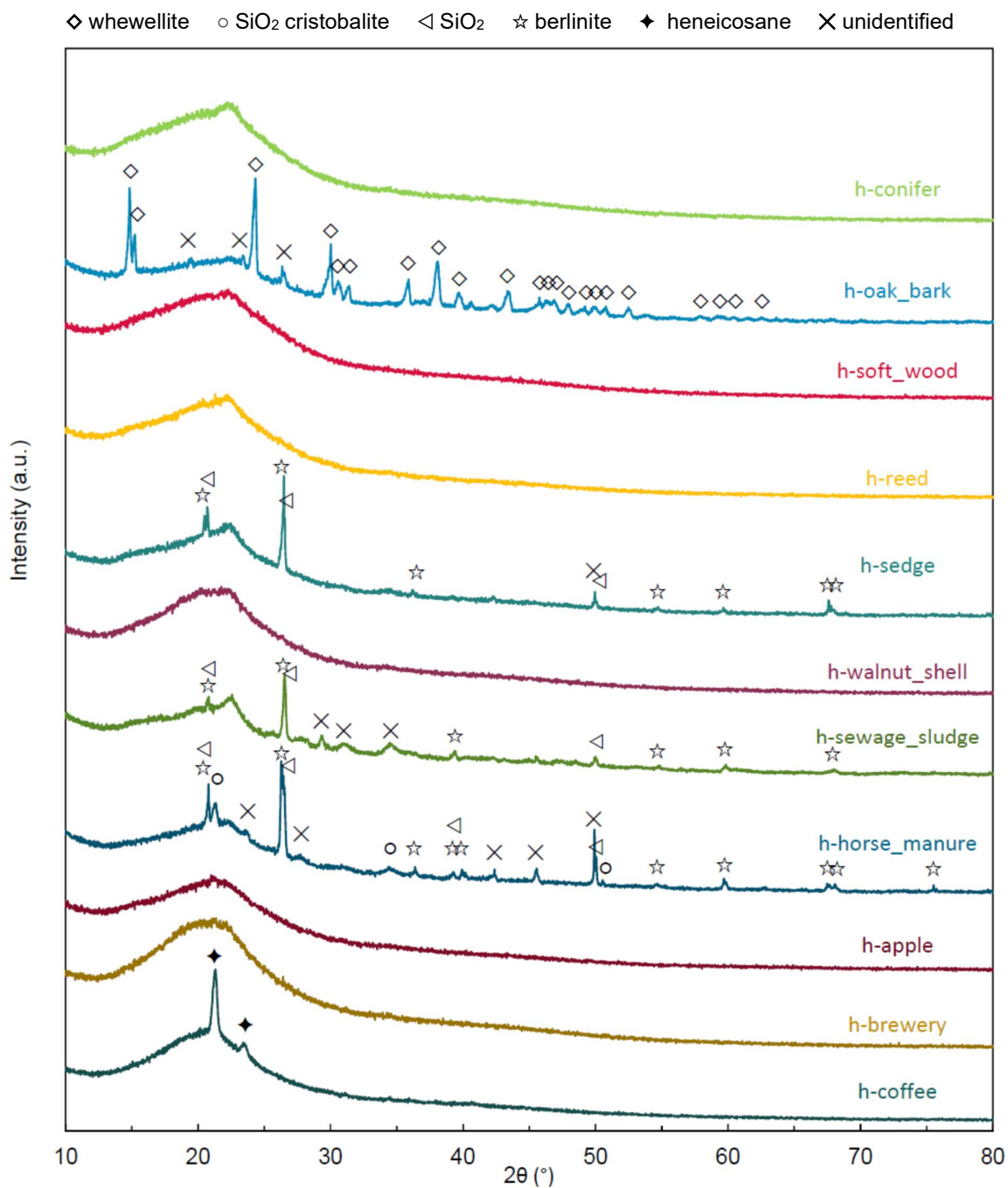


Figure 38: XRD patterns of the hydrochars. Peaks are identified with symbols as: ◇ whewellite, *syn* C₂CaO₄.H₂O (PDF 00-020-0231), ○ SiO₂ silicon oxide, cristobalite beta, *syn* (PDF 01-077-8630), ◁ Silicon oxide quartz, low SiO₂ (PFD 00-005-0490), ☆ berlinite, *syn* AlPO₄ (PDF 04-009-5761), ◆ *n*-heneicosane C₂₁H₄₄ (PDF 00-031-1705), and × unidentified.

Although peaks were present in too small intensity in raw sedge, coffee and horse manure, sharper and more intense peaks are present on hydrochar structures. Berlinite and cristobalite are found in h-sedge and h-horse_manure, which explain the Si, Al and P retention after HTC. In section **2.4**, SiO₂ was found in several raw materials, this compound is known to be insoluble under HTC conditions that could explain its retention in the hydrochars [159].

Coffee-based hydrochar was found to contain n-heneicosane. This alkane was already reported in fresh and fermented coffee beans [188] and is known to naturally occur in certain plants as a waxy solid [189]. Its presence cannot be highlighted by XRD in the raw biomass, however it can be screened by the presence of other amorphous compounds that are degraded after HTC.

This increase of crystalline species in hydrochars compared to raw biomass could come from the degradation of amorphous compounds. It is widely known that hemicelluloses are hydrolysed at 180 °C [97], which results an increase of concentration of the organised phases in the material and hence in crystallinity.

Even though the selected materials were from various origin and composition, some tendencies are observed: an increase of the C content to the detriment of H and O contents, characteristic of HTC products. In contrast to N and ashes, which behave differently depending on the feedstock: it was observed that the ash content tend to decrease after HTC in the hydrochar when the initial content is below 6 wdb%. By having a closer look at their composition, different behaviours were observed. First of all, the inorganics that mostly leach, the alkaline and alkali earth metal and particularly K, Na and Mg, due to their soluble ionic form in the biomass. Second, the remaining inorganics, like heavy metals, both due to their insoluble nature as well as the possibility they are trapped in the structure. At last, some inorganics are feedstock dependent and tend to mainly leach or not, it was attributed to the various form they can exist in the biomass and the possible inaccessibility to the liquid, particularly Ca, Si, P and Mn.

At it is widely explained along this thesis, the inorganics have a major influence on the graphitisation. The next step is to characterise and quantify the influence of the feedstock on the hard carbon properties, and which element contribute to the different hard carbon properties.

4. Hard carbons

4.1. Chemical composition

Composition of the hard carbons are reported in **Table 29** and **Table 30**, yields are reported in **Table 31**.

Table 29: CHNSO and ash contents of all the materials. Contents are expressed in wdb%.

wdb%	C	H	N	S	O*	Ash
HC-conifer	97.9 ±0.3	0.34 ± 0.01	0.29 ± 0.1	0.1 ± 0.03	0.3	1.1 ± 0.1
HC-oak_bark	82.3 ± 0.3	0.67 ± 0.09	0.19 ± 0.04	0.11 0.03	0.3	16.4 ± 0.4
HC-soft_wood	97.5 ± 0.02	0.37 ± 0.02	0.56 ± 0.01	0.059 ± 0.03	0.7	0.8 ± 0.3
HC-reed	97.8 ± 0.01	0.26 ± 0.01	0.55 ± 0.03	0.05 ± 0.01	0	1.5 ± 0.1
HC-sedge	86.88 ± 1	0.44 ± 0.03	0.5 ± 0.1	0.26 ± 0.07	0	19 ± 2
HC-walnut_shell	97.8 ± 0.6	0.24 ± 0.02	0.4 ± 0.02	0.06 ± 0.01	0	1.8 ± 0.1
HC-sewage_sludge	61.7 ± 2	0.5 ± 0.1	0.57 ± 0.06	0.47 0.02	0	47.6 ± 0.1
HC-horse_manure	69 ± 1	0.5 ± 0.1	0.79 ± 0.04	2 ± 1	0	54 ± 1
HC-apple	95.67 ± 0.1	0.844 ± 0.06	0.52 ± 0.02	0.08 ± 0.01	2.5	0.4 ± 0.1
HC-brewery	98.65 ± 0.2	0.281 ± 0.04	0.52 ± 0.03	0.10 ± 0.01	0	0.5 ± 0.1
HC-coffee	98.78 ± 0.1	0.22 ± 0.02	0.53 ± 0.02	0.12 ± 0.01	0.1	0.2 ± 0.1

* Calculated by difference

Obviously, carbon is found to be the major element for every hard carbon sample. Its content varies between 98.8 and 61.7 w% respectively for brewery and sewage sludge-based materials. On ash-free basis, they are only mainly composed of C, between 98 and 102 daf%. However, hard carbons with high ash content also present a non-negligible standard deviation due to the method used and the inhomogeneity of the ashes. These very high values of C is typically found for biomass-based hard carbons [30], [61], [118], [190]–[192].

The chemical yields are calculated based on the C content of the materials, they are comprised between 40 and 52 % for woods and agricultural residues, between 23 and 44 % for industrial wastes and between 21 and 34 % for animal & animal wastes. However, they don't seem to be linked to the raw composition, nor the other hard carbon properties.

To quantify the volatilisation, **Figure 39** represents the remaining inorganics in percent at the end of the pyrolysis. Inorganic contents in the hard carbons are globally higher than in hydrochars. K, Ca, Al and Si contents increase after the high temperature pyrolysis. At the opposite, Na, Mg and Mn seem to be in lower quantity in the final product. However, some elements are known to be partially or totally volatilised during pyrolysis, such as N, K, Na and Cl [160]. It is attributed to their chemical form: water-soluble or ion-exchangeable species are available for release, but not all of these actually leaves the material [91]. At temperature lower than 800 °C, non-volatile species such as Ca, Si, Mg, Al, Fe or Ti are reported to remain in the solid [36], but at higher temperature even heavy metal such as Pb or Zn were reported to be volatilised from algae pyrolysis [39]. At high temperature, metals are thought to be under gas phase, leading to their volatilisation. However, they don't always leave the material, and can also only migrate to the surface of the hard carbon [193].

Table 30: Inorganic contents of the hard carbons from all categories. P and Si were not measured on all the hard carbons due to the large amount of material required, it is reported as *nd* for no data.

<i>mg.kg db⁻¹</i>	K	Na	Ca	Mg	Al	Mn	Fe	P	Si
HC-conifer	41 ± 4	10 ± 1	2800 ± 300	27 ± 3	140 ± 10	< 1	< 1	<i>nd</i>	700 ± 100
HC-oak_bark	947 ± 9	3 ± 1	48200 ± 25000	< 0.2	5080 ± 70	3.4 ± 0.1	240 ± 10	<i>nd</i>	8800 ± 300
HC-soft_wood	180 ± 20	8 ± 1	1100 ± 100	22 ± 2	320 ± 30	0.6 ± 0.1	120 ± 10	<i>nd</i>	<i>nd</i>
HC-reed	348 ± 4	21 ± 2	1096 ± 3	72 ± 9	330 ± 10	1 ± 1	900 ± 1300	<i>nd</i>	3900 ± 100
HC-sedge	3220 ± 40	20 ± 1	6600 ± 300	70 ± 20	1100 ± 200	21 ± 2	230 ± 50	<i>nd</i>	61200 ± 8400
HC-walnut_shell	1076 ± 5	42 ± 4	2100 ± 20	< 0.2	349 ± 2	< 1	389 ± 7	<i>nd</i>	<i>nd</i>
HC-sewage_sludge	3790 ± 30	0.5 ± 0.3	73700 ± 1500	3500 ± 200	22000 ± 2000	86 ± 6	3100 ± 400	<i>nd</i>	98000 ± 15000
HC-horse_manure	4500 ± 300	39 ± 1	17500 ± 900	945 ± 3	4600 ± 200	59 ± 8	1300 ± 300	<i>nd</i>	223000 ± 5700
HC-apple	660 ± 90	7 ± 2	500 ± 50	< 0.3	28.6 ± 0.2	0.15 ± 0.07	100 ± 20	<i>nd</i>	<i>nd</i>
HC-brewery	90 ± 30	20 ± 10	1030 ± 20	< 0.3	11.2 ± 0.2	0.9 ± 0.4	354 ± 10	<i>nd</i>	<i>nd</i>
HC-coffee	460 ± 50	2 ± 2	2200 ± 50	< 0.3	10.01 ± 0.05	0.27 ± 0.07	190 ± 10	<i>nd</i>	<i>nd</i>

In our materials, the quantities measured of the main inorganics are lower than the raw material, but by taking the solid yield of the reaction into account, a small fraction is volatilised. As described in the previous part, an important fraction of the inorganics leached during the HTC, the remaining quantity could be trapped in the structure, or stable in the operating conditions.

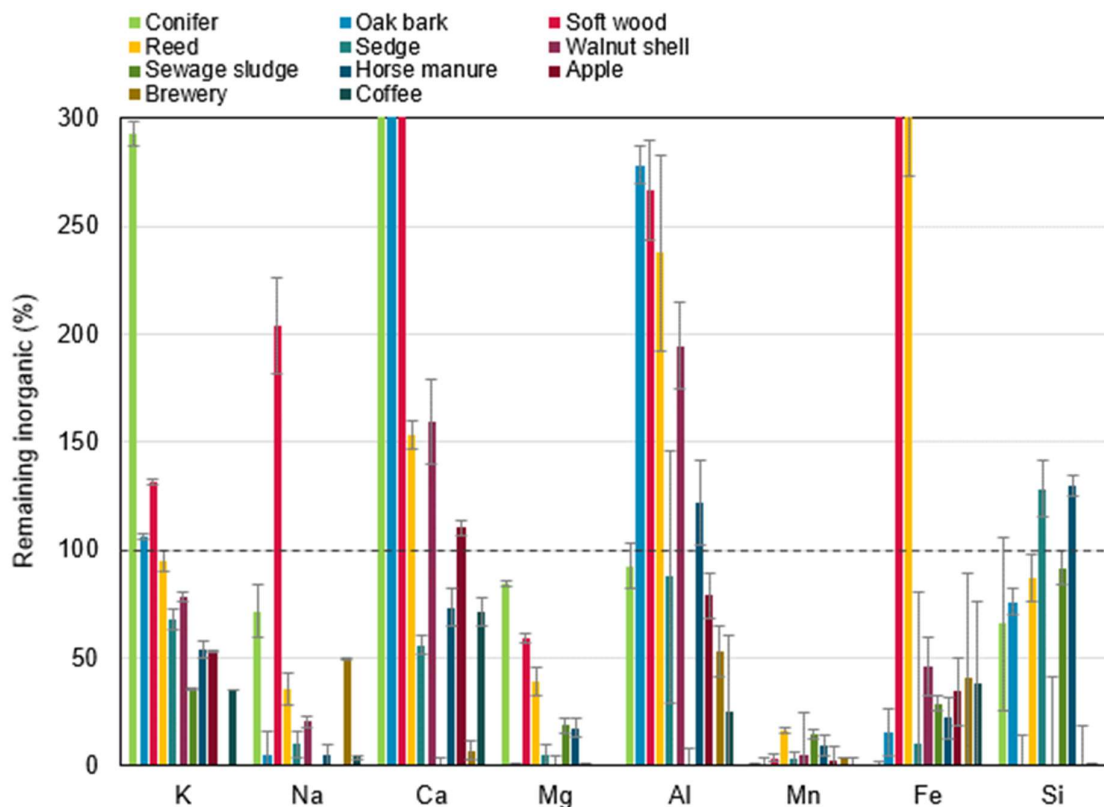


Figure 39: Balance of the inorganics that remain in the hard carbon after reaction in %. Values are calculated similarly to equation (9). The lack of histogram bars comes from the hydrochar content that were below limit of detection. Uncertainties are experimental standard deviations.

4.2. Structure

In order to characterise the inorganic species, XRD were performed and patterns are shown in **Figure 40**. The calculated d_{002} are reported in **Table 31**.

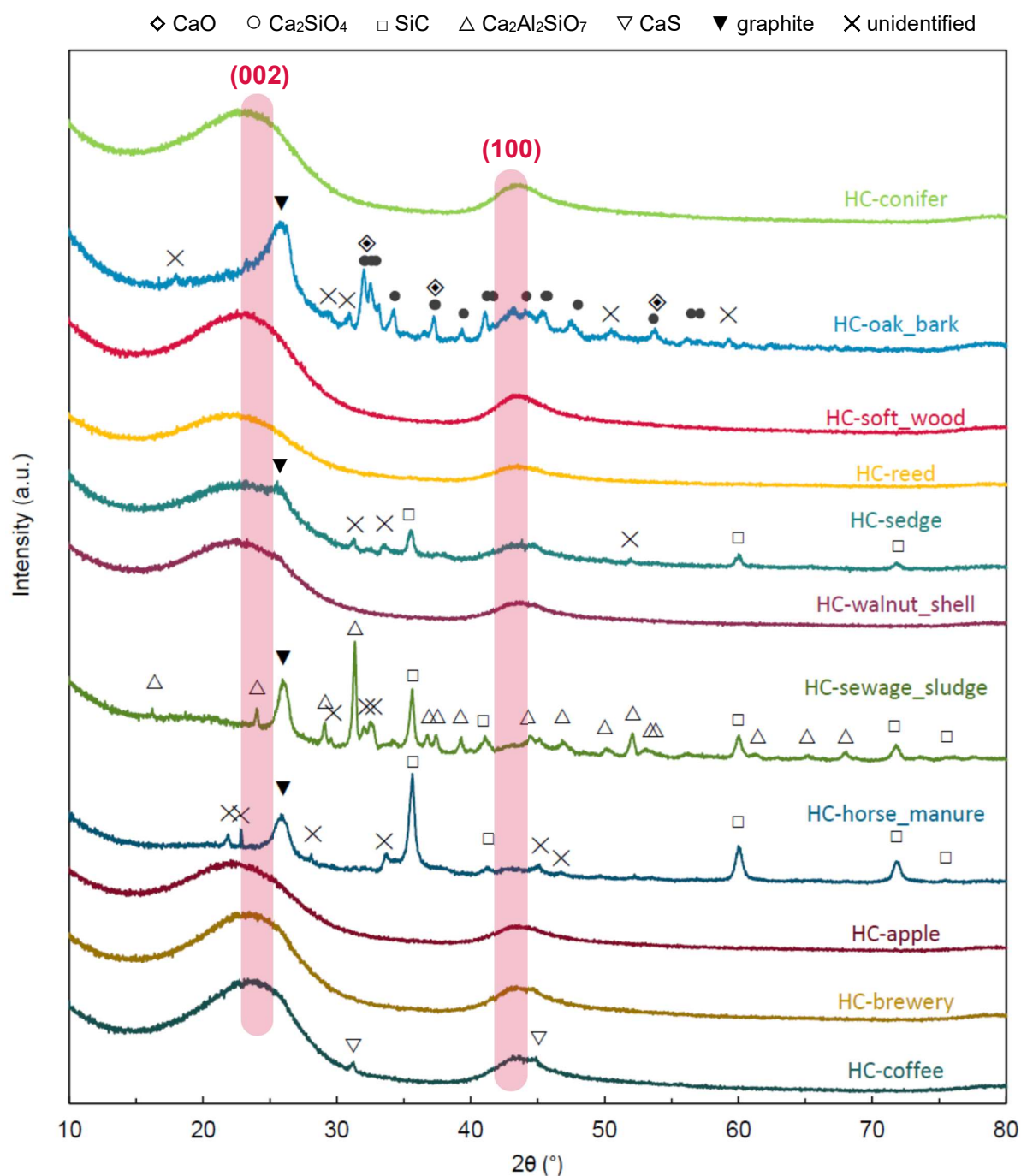


Figure 40: XRD patterns of the hard carbons. (002) and (100) peaks are identified in red. Peaks are identified with symbols as: ◇ Calcium oxide Lime. syn CaO (PDF 00-037-1497), ○ calcium silicate larnite. syn Ca₂SiO₄ (PDF 00-033-0302), □ Silicon carbide Moissanite-3C, syn SiC (PDF 00-029-1129), △ Calcium aluminium silicate Gehlenite Ca₂Al₂SiO₇ (PDF 4-001-6871), ▽ Calcium sulfide Oldhamite. syn CaS (PDF 04-004-3787), ▼ graphite-2H (PDF 01-075-1621), × unidentified

The typical hard carbon pattern is composed of two broad peaks at about 22 and 43°. However, this recognisable shape is screened on some material by the presence of intense sharp peaks that are due to the presence of crystalline phases. Nevertheless, by having a close look, hard carbon features can still be observed. Yet it is difficult to determine with precision the position of the (002) peak due to other sharper peaks in the same areas. Because of this, it was not possible to deduce d_{002} values from HC-oak_bark, HC-sewage_sludge and HC-horse_manure. The interlayer distance d_{002} lies between 3.70 and 3.89 Å, respectively for the industrial wastes and HC-reed. All the hard carbon have the similar d_{002} , of 3.70 Å for industrial wastes, 3.76 Å for woods and about 3.85 Å for agricultural wastes. These values are very close and no tendency is determined.

HC-oak_bark, HC-sewage_sludge and HC-horse_manure exhibit a sharp peak at 26°, screening the (002) peak. This indicates a clear graphitization of the samples with an average interlayer distance of 3.45 Å. The corresponding raw materials were the ones with the highest ash contents. Especially, important amounts of Ca and Si were found. These elements were already reported to catalyse graphitisation during biomass pyrolysis [30], [118]. Furthermore, Saavedra *et al.* [118] observed that a higher C content in the raw material leads to a larger d_{002} space while H content has the opposite impact. In this study, the 3 most graphitized materials are indeed from the feedstock with the lowest C content, despite they also present H content in the lower range of values among the materials. Feng *et al.* [117] observed a negative correlation between the hemicellulose content in the raw biomass and the d_{002} that they attributed to their degradation into misaligned graphene layers during the thermal process. However, such observation can only be done on lignocellulosic material, which is not the case for most of the hard carbon with high graphitisation.

In addition to graphite, other crystalline structures were identified. HC-sedge, HC-sewage_sludge and HC-horse_manure, the three materials presenting the highest concentration of Si, present silicon carbide pattern (Silicon carbide Moissanite-3C, syn SiC, PDF 00-029-1129), which was already reported on Si-rich biomass-based hard carbons [118]. HC-oak_bark contains lime (calcium oxide Lime, syn CaO, PDF 00-037-1497), and Iarnite (calcium silicate Iarnite, syn Ca_2SiO_4 , PDF 00-033-0302), in accordance with its high Ca and Si content. Coffee-based hard carbon presents CaS pattern (Calcium sulfide Oldhamite, syn CaS, PDF 04-004-3787), the intensity of the peaks is low that translates its small amount on a crystalline form in accordance with its composition that is not very high on both Ca and S. Sewage sludge presents the highest number of crystalline phases, with in addition to the already mentioned graphite and silicon carbide, Gehlenite (Calcium aluminium silicate Gehlenite $\text{Ca}_2\text{Al}_2\text{SiO}_7$, PDF 4-001-6871) and other unidentified compounds. No presence of the structures found on the hydrochars were also reported in the corresponding hard carbons, highlighting the transformation of the species.

Table 31: Physicochemical properties of the hard carbons. SY is the pyrolysis solid mass yield, CY the carbon yield from the biomass to the hard carbon calculated according to equations (7) and (8), d_{002} the interlayer distance, ICE the initial coulombic efficiency, and C_{rev} the reversible capacity of the first cycle. Uncertainties are from the method used.

	SY (%) ± 2	CY (%) ± 5	d_{002} (Å) ± 0.05	N ₂ SSA (m ² .g ⁻¹) $\pm 5\%$	CO ₂ SSA (m ² .g ⁻¹) $\pm 5\%$	ICE (%) ± 2	C _{rev} (mAh.g ⁻¹) ± 10
HC-conifer	50	47	3.76	11	18	74	290
HC-oak_bark	46	45	3.46*	21	18	57	170
HC-soft_wood	51	52	3.76	29	66	64	280
HC-reed	49	47	3.89	20	21	47	180
HC-sedge	44	40	3.86	27	29	61	210
HC-walnut_shell	53	41	3.82	4	3	79	240
HC-sewage_sludge	34	21	3.42*	80	70	31	80
HC-horse_manure	41	34	3.44*	68	81	39	100
HC-apple	47	45	3.70	28	53	68	270
HC-brewery	39	25	3.70	16	20	78	260
HC-coffee	33	24	3.70	14	7	78	250

* value obtained from the graphitic peak symbolised by ▼ in **Figure 40**.

4.3. Surface area and morphology

Gas adsorption BET specific surface areas (SSA) are reported in **Table 31**. Due to the size of the gas molecule, CO₂ highlights the microporosity while N₂ gives information on the mesoporosity, as explained in **Chapter 1**.

Animal & human-waste based HC are the most porous materials, with N₂ SSA superior to 68 m².g⁻¹ which is twice higher than any material from the other categories. The lowest N₂ SSA is observed on HC-walnut_shell with 4 m².g⁻¹, the other materials are comprised between 11 and 28 m².g⁻¹. Regarding CO₂ SSA, most of them show similar values of N₂ and CO₂ SSA. Only HC-apple and HC-soft_wood present a CO₂ SSA twice higher than N₂ SSA, highlighting the presence of an important microporosity.

SEM of the hard carbons are presented in **Figure 41** and **Figure 42**.

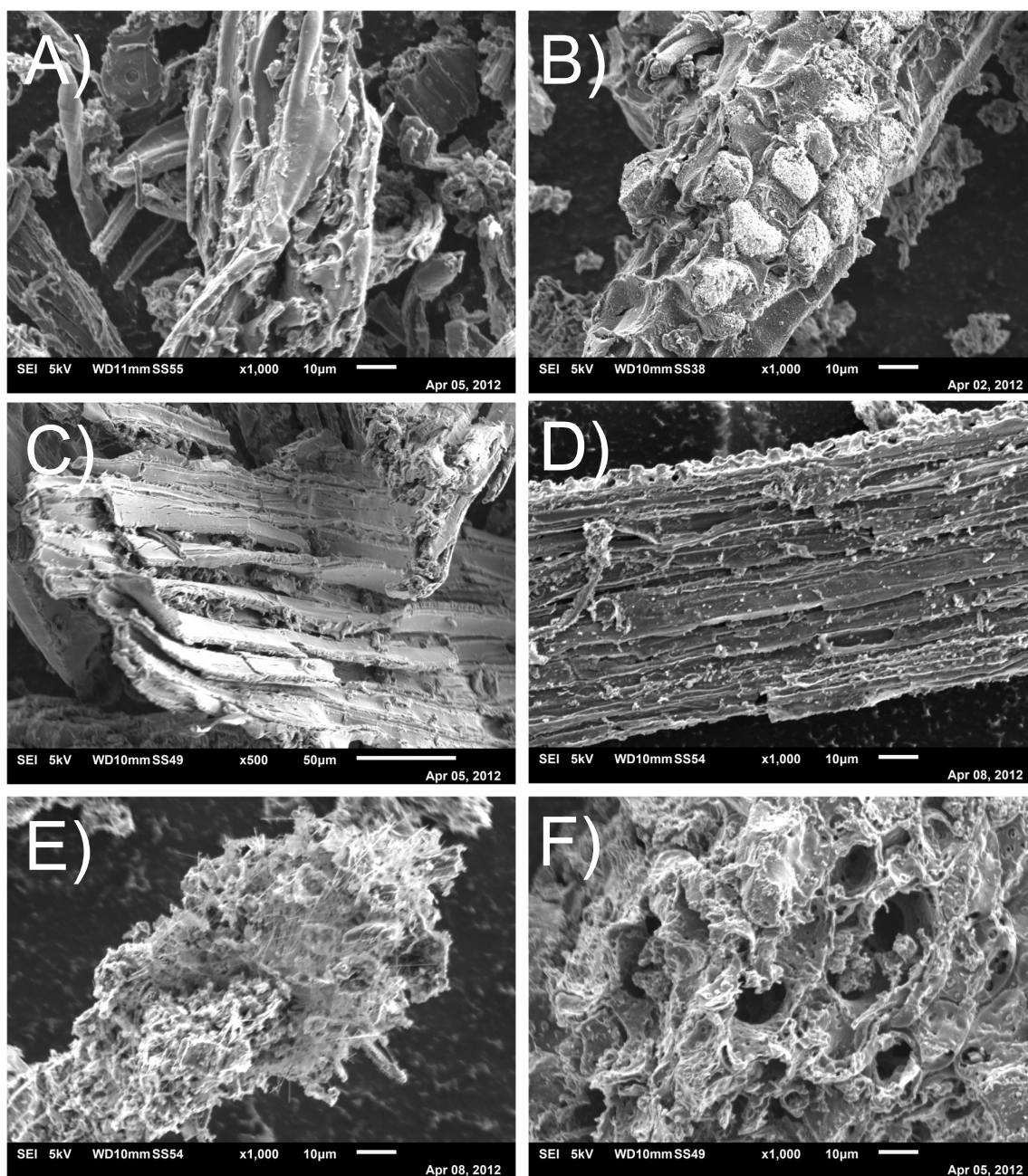


Figure 41: SEM pictures of **A)** HC-conifer, **B)** HC-oak_bark, **C)** HC-soft_wood, **D)** HC-reed, **E)** HC-sedge, and **F)** HC-walnut_shell.

Hard carbons usually keep the morphology of the raw materials [6], [194]. As already observed in literature for Si rich biomasses [118], SiC whiskers are observed on HC-sedge, HC-sewage_sludge and HC-horse_manure. This is consistent with XRD patterns and SEM-EDS presented in **Figure 43**.

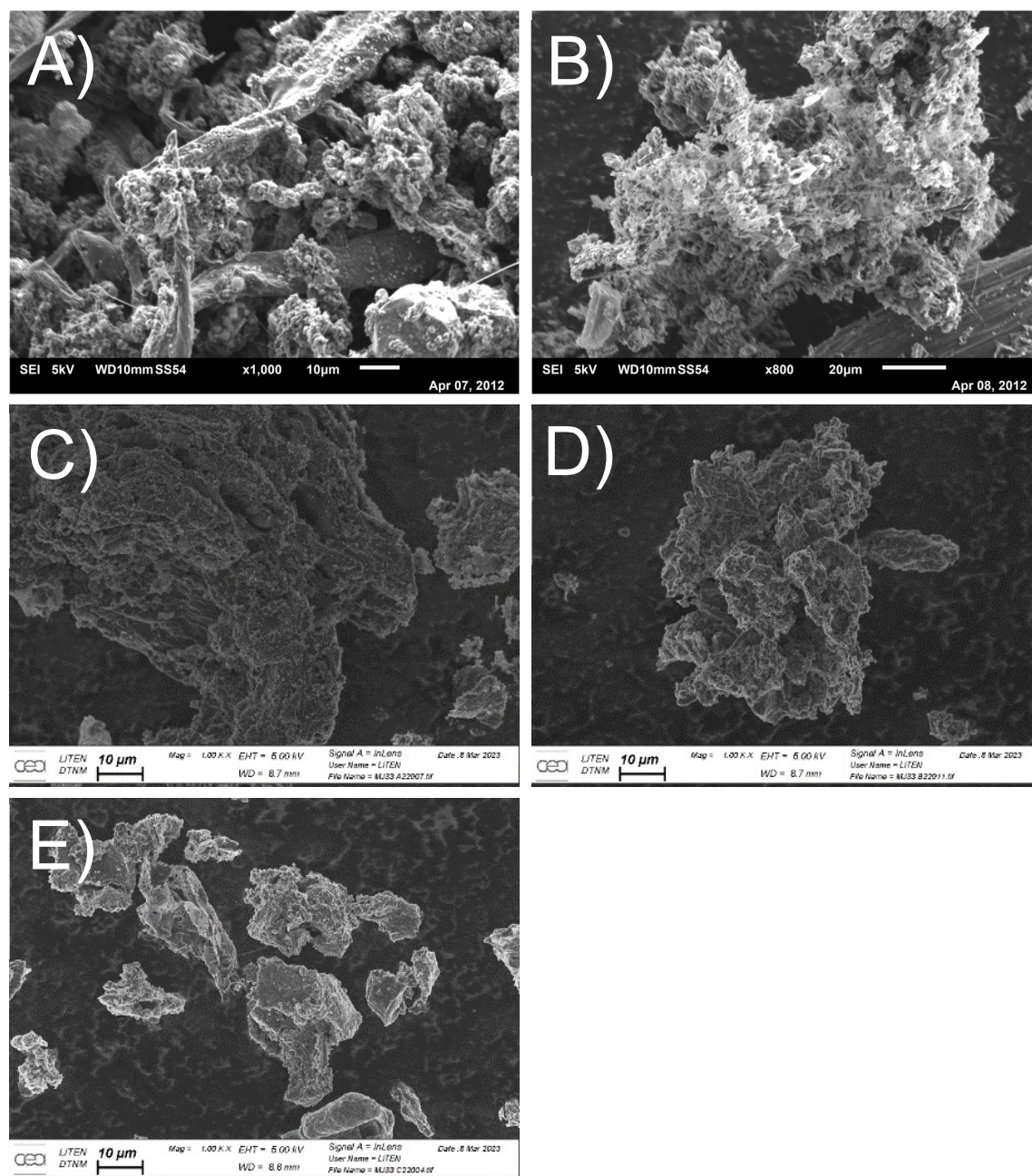


Figure 42: SEM pictures of **A) HC-sewage_sludge**, **B) HC-horse_manure**, **C) HC-apple**, **D) HC-brewery**, and **E) HC-coffee**.

In order to link the chemical composition of the raw biomass and the physico-chemical properties of the hard carbons, plots are displayed in **Figure 44**. It seems that biomasses rich in inorganics lead to hard carbons with higher surface area, and more graphitized, however there is no clear tendency: the materials have similar low surface area except from two materials, the animal & human wastes, which also have high ash content. Two isolated points result, insufficient to correlate both but enough to support the same trend reported by Beda *et al.* [30] and Saavedra *et al.* [118].

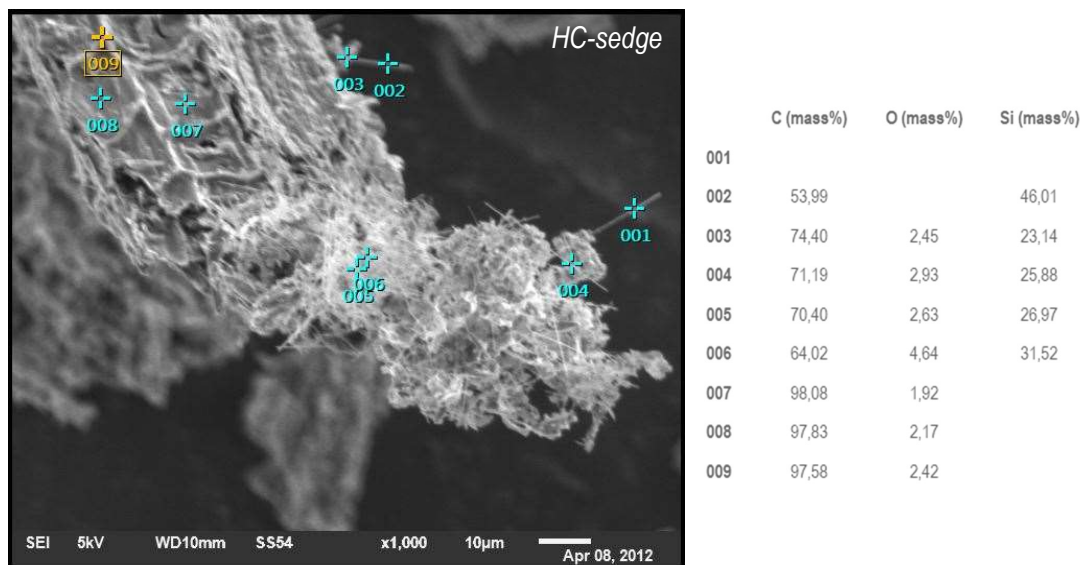


Figure 43: SEM-EDS of HC-sedge on the SiC whiskers.

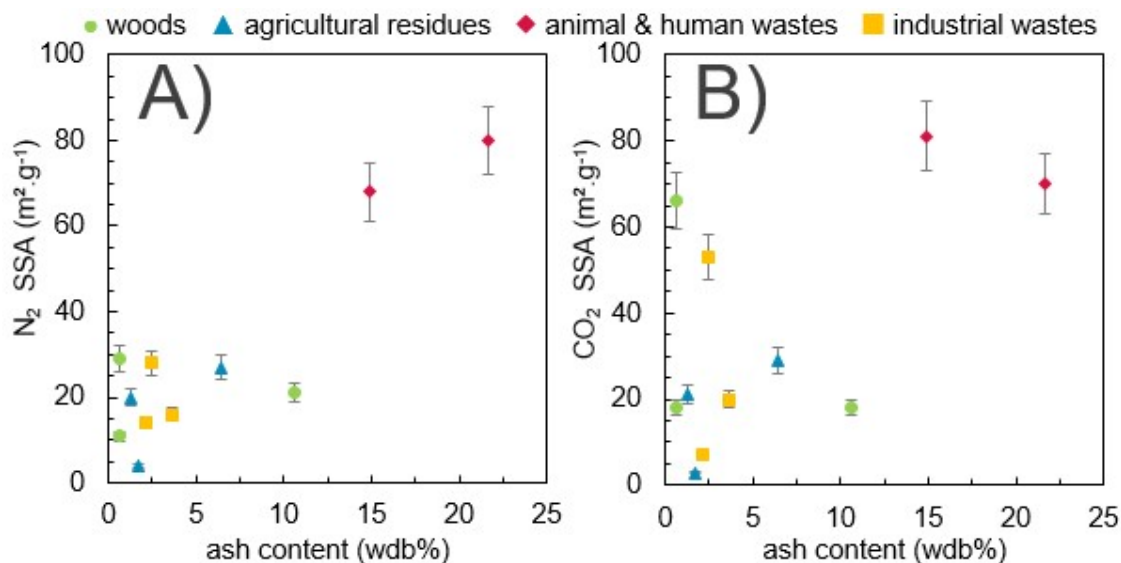


Figure 44: Influence of the raw biomass ash content on **A)** the N₂ SSA and **B)** the CO₂ SSA of the hard carbon. Uncertainties are from the method used.

Ash is generally composed of a wide variety of compounds, as widely detailed in **Chapter 1**, to go further on the investigation the influence of every inorganic is studied. The specific area depending on the content of each elements in the raw material, hydrochar and hard carbon are plotted in **Figure 45**, **Figure 46** and **Figure 47**.

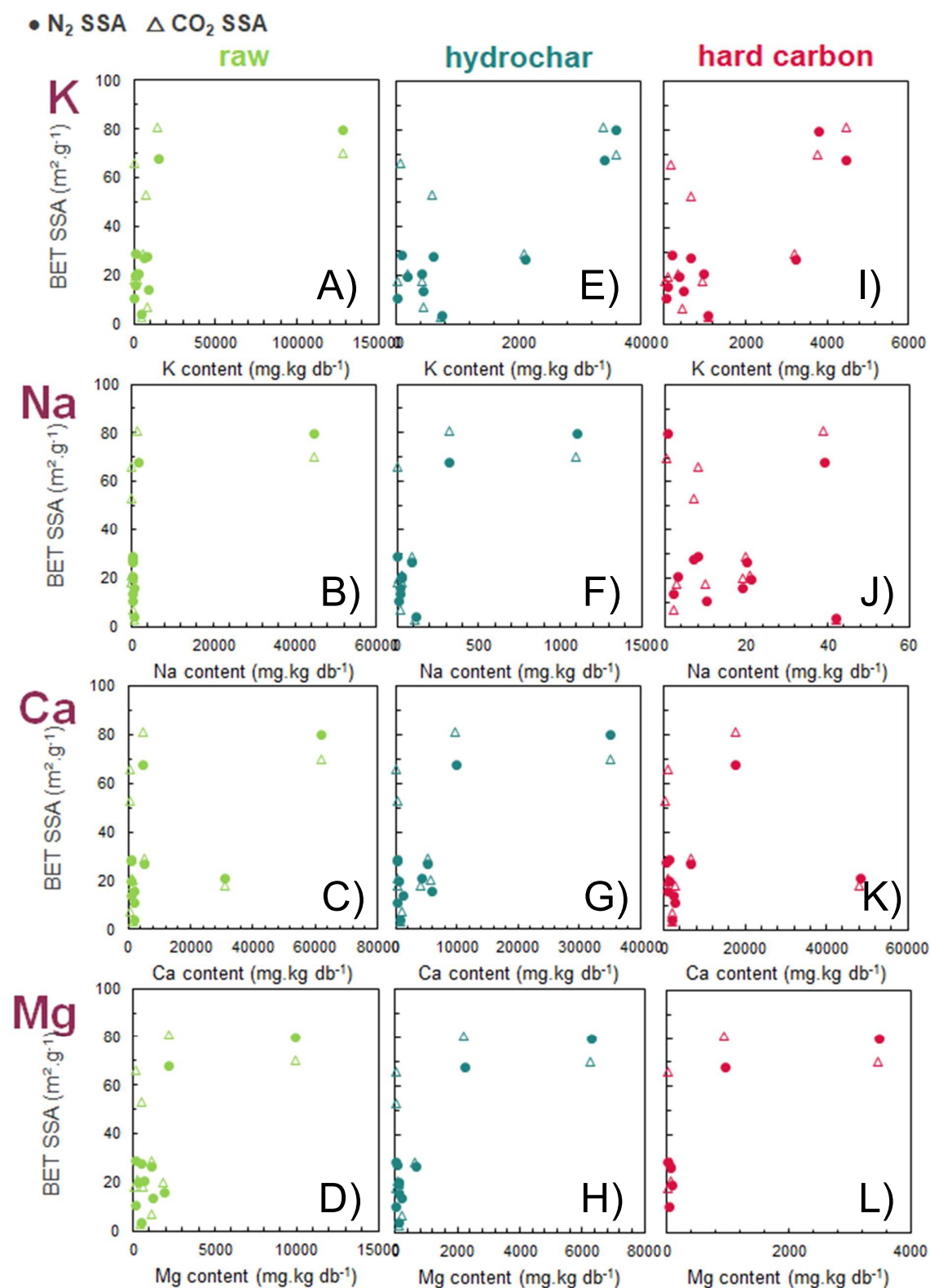


Figure 45: Influence of the K, Na, Ca and Mg contents of **A-D)** the raw material (green), **E-H)** hydrochar (blue) and **I-L)** hard carbon (red) on the hard carbon N₂ (●) and CO₂ (△) SSA.

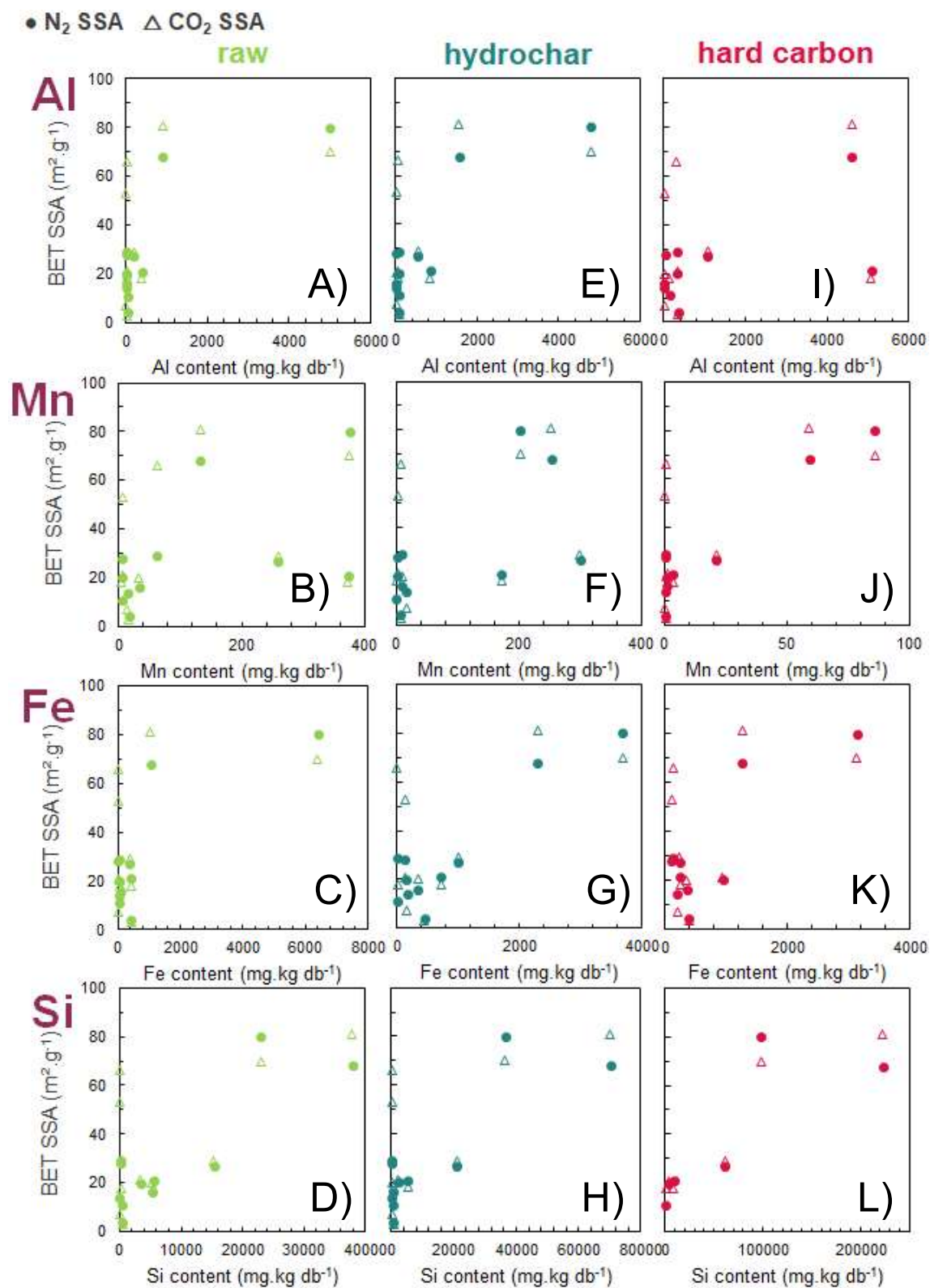


Figure 46: Influence of the Al, Mn, Fe and Si contents of **A-D)** the raw material (green), **E-H)** hydrochar (blue) and **I-L)** hard carbon (red) on the hard carbon N₂ (●) and CO₂ (Δ) BET SSA.

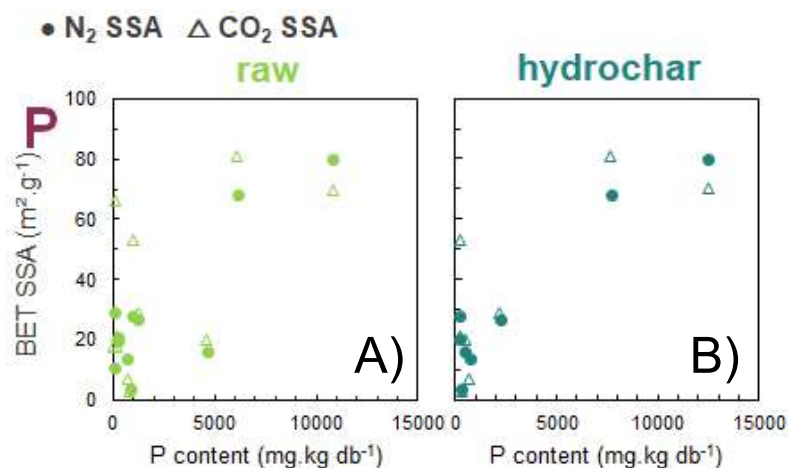


Figure 47: Influence of the P content of **A)** the raw material (green) and **B)** hydrochar (blue) on the hard carbon N₂ (●) and CO₂ (△) SSA.

First of all, according to **Figure 45A-D)**, **Figure 46A-D)** and **Figure 47A)**, it seems the raw material composition is not directly linked to the final BET SSA, unlike hydrochar and hard carbon. It is coherent with the observations in the previous parts: during HTC, some elements leach in major proportion, since they are no longer in the hydrochar their influence on the pyrolysis is limited. In section 3.1, it was highlighted that K, Na, Mg are mostly removed from the hydrochar, while Ca, P, Si and Mn remains in various proportion and Al, Fe stay completely. It is expected to find similar results from raw and hydrochar in the elements that remains in the hydrochar, the heavy metals.

Regarding to **Figure 45E) and I)**, **Figure 46E-L)** and **Figure 47B)** the composition of the hydrochars and hard carbons, it seems higher K, Si, P, Al and Fe contents were measured on materials with higher N₂ BET SSA. It goes on the same direction as observed by Saavedra *et al.* [118] they deduced based on the two-steps pyrolysis of 25 lignocellulosic biomass from various composition. However, their study considered the raw material composition and they did not measure the pyrochar nor the hard carbon. In their study, Beda *et al.* [30] investigated the influence of inorganics by washing raw materials and hard carbons and comparing the obtained materials with pristine. They measured both the feedstock and hard carbon, and highlighted that the compounds based on K, Ca, Si, and Mg lead to an increase of porosity and a decrease of the graphene interlayer space. However, it has to be kept in mind that most of the plots shows two points shifted to the right, which are enough to observe a link, but not enough to conclude on a clear correlation.

At high temperature, K from the feedstock have been reported to react with the carbon matrix to form K₂CO₃, which is itself decomposed and volatilised, leading to pore formation [11], [195]. They decompose into metal oxide, activating the carbon matrix to form metal and release CO [30]. K₂CO₃ is used as catalyst in gasification, it increases both pyrolysis and gasification process, and contribute to increase the carbon gas release [196]. Metal carbonates are usually reported to be volatilised at such temperature, however a fraction remains in our materials, as explained in 4.1. The remaining K after HTC is thought to be trapped in the structure, preventing its release as gas.

Furthermore, XRD patterns and EDS spectrums allowed to characterise SiC whiskers at the surface of HC-sedge, HC-sewage_sludge and HC-horse_manure that was already reported to contribute to increase the surface area [130] in accordance with the results presented.

Regarding the reactivity of K, Ca and Si mentioned, it is coherent with the observations made. Heavy metals were not reported to particularly impact the surface area, however, as mentioned in the previous part, they are thought to migrate at the surface during the high temperature pyrolysis.

4.4. Electrochemical performances

Hard carbons are then formulated in electrodes and assembled in sodium half cells. The first discharge-charge is represented in **Figure 48**. The values are reported in in **Table 31**.

Discharge and charge have two different profiles, as described below. As explained in **Chapter 1**, the distance between the two curves at 2.5 V vs Na⁺/Na highlights the irreversibility of the system: the closer the curves, the higher the ICE. The obtained ICE are comprised between 31 % for HC-sewage_sludge and 78 % for both HC-brewery and HC-coffee.

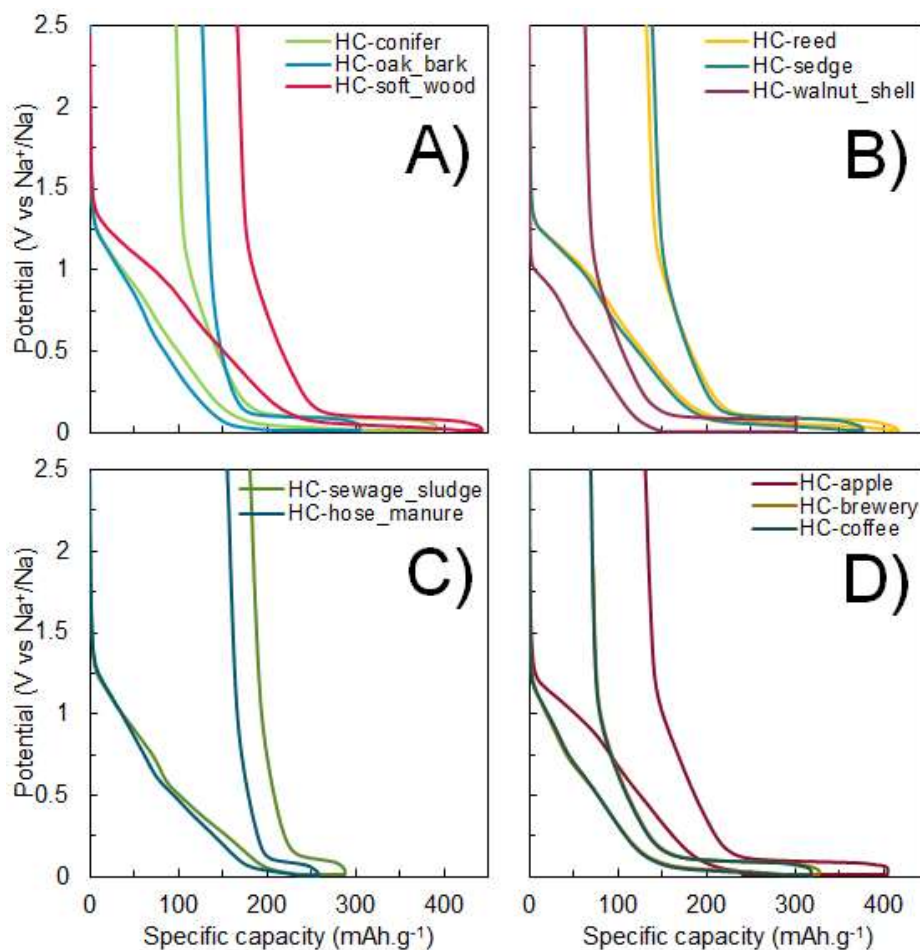


Figure 48: First cycle discharge-charge of **A)** woody product, **B)** herbaceous and agricultural residue, **C)** animal and human wastes and **D)** industrial biomass wastes.

During the first discharge, the curve highlights an irregular profile, characteristic of the formation of the solid electrolyte interface (SEI). Despite its composition and mechanism are not well known, some models allow a better understanding of its nature [11]. At about 1.25 V vs Na⁺/Na, the SEI formation begins, leading to the first slope break observed. A second slope break happens about 0.55 V vs Na⁺/Na, at this potential several phenomena were reported on similar cellulose-based hard carbons. Fondard *et al.* [197] observed a similar behaviour when adding FEC to the electrolyte and concluded it is due to its reduction. This additive allows better performances by stabilizing the system upon cycling. Simone *et al.* [13] observed a similar plateau-like at about 0.5 V vs Na⁺/Na when using carbon black as conducting additive. Both FEC and carbon black are also used in our system. This phenomenon is observed in every materials and doesn't seem linked to the hard carbon itself.

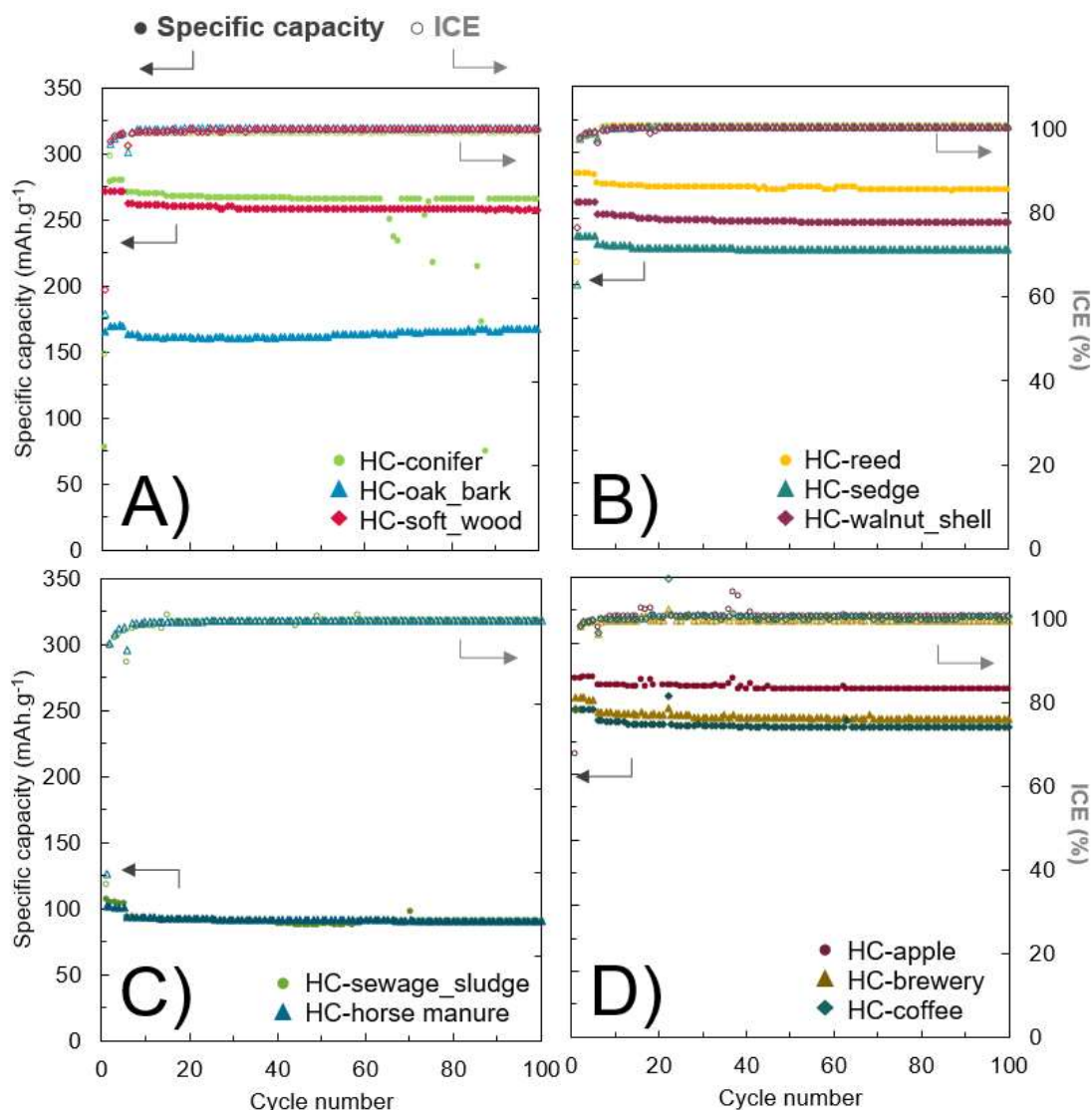


Figure 49: Cycling behaviour of **A)** woody product, **B)** herbaceous and agricultural residue, **C)** animal and human wastes and **D)** industrial biomass wastes. The 5 first cycles are performed at C/10 then at 1C until the 100th cycle ($C = 372 \text{ mA.g}^{-1}$).

The cycling behaviour are represented in **Figure 49**. As it is highlighted by the horizontal CE curve, the SEI is fully formed and stable during the first cycle. The coulombic efficiency is close to 100 % from the second cycle, and the capacity loss lower than 4 % among 95 cycles at C-rate. There is a small drop of capacity occurring between the cycles 5 and 6, due to the change of current density. However, the capacity loss is small. The best performances are obtained for wood stems, reed and apple pomace-based materials with an average of 260 mAh.g⁻¹ after 100 cycles. Agricultural residues HC-sedge and HC-walnut_shell, and the industrial wastes HC-brewery and HC-coffee have performances between 225 and 245 mAh.g⁻¹, while HC-oak_bark and animal and human wastes have the lowest performances of 170 mAh.g⁻¹ and 90 mAh.g⁻¹. These three materials also exhibit the lowest ICE.

4.4.1. Influence of the graphitisation on the performances

As explained in **Chapter 1**, sodium ions poorly insert in graphite, which is the reason hard carbon is used instead. Cao *et al.* [53] while working on the sodium insertion mechanism evaluated the critical minimum space between the layers, they calculated at least 0.37 nm is required where there is only 0.335 nm in graphite [29]. It is in accordance with the results of this study: the most graphitised materials hard carbons showing an extra intense graphitic pic with an interlayer space inferior of 3.4 Å, HC-oak_bark, HC-sewage_sludge and HC-horse_manure, exhibit significantly lower performances than the other materials.

4.4.2. Influence of the surface area on the performances

To understand better these results, **Figure 50** highlights the link between electrochemical performances and the hard carbon BET specific surface areas measured by N₂ and CO₂ adsorption. As it is well known and explained in **4.4**, during the first cycle irreversible SEI formation occurs at the surface of the material. From this point of view, a higher N₂ BET SSA leads to a smaller ICE, which is indeed observed in this study. The surface measured by N₂ adsorption is accessible by the electrolyte, unlike the CO₂ adsorption that also highlights the microporosity. The trend in **Figure 50A)** is indeed stronger than in **Figure 50B)**. The trend is not as obvious regarding C_{rev}, despite high N₂ BET SSA leads to low capacity, at low surface area the correlation is not as obvious. CO₂ BET SSA seems to have no link with C_{rev}. A large specific area leads to a poor capacity and a decrease of the cycling behaviour [54], but it also allows electrolyte percolation which is needed for a high power capability [27]. It has been explained in section **4.3** that the composition of the material impacts the surface of the hard carbon. The detail of the resulted impact are presented in the next section.

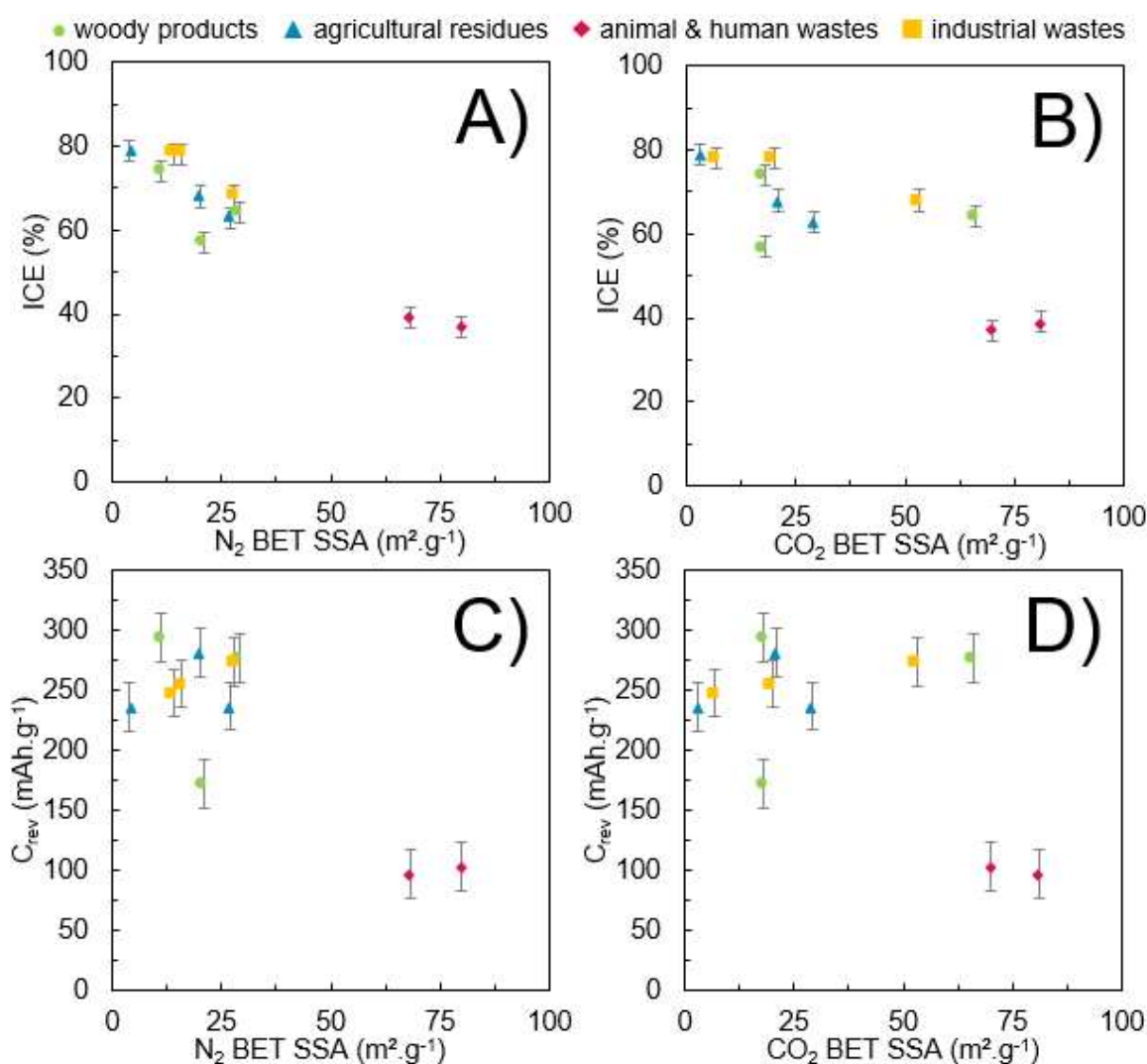


Figure 50: ICE depending on the **A)** N_2 BET SSA and the **B)** CO_2 BET SSA of the hard carbon, and C_{rev} depending on the **C)** N_2 BET SSA and the **D)** CO_2 BET SSA of the hard carbon. Uncertainties are from the method used.

4.4.3. Influence of the composition on the performances

To investigate the role of the ash on the performances, C_{rev} depending on the ash content is represented in **Figure 51A)**. A negative correlation is found between the feedstock ash content and C_{rev} , in accordance with other biomass study [118]. However, assuming that inorganics do not contribute directly to the capacity, they are considered as dead weight. To take into account this effect, the specific capacity per gram of carbon is taken in consideration, as explained in **Chapter 2**, instead of the total mass of material and presented in **Figure 51B)**. It is clear that the ash in the raw biomass has a negative impact on the reversible capacity. However, during HTC, the inorganics are partially removed from the material, to see the influence both plot with the ash content of the hydrochar and hard carbon are showed in **Figure 51C)** and in **Figure 51D)** respectively. It appears that, even with the reduction of the inorganics, materials with the most inorganics are also the ones with the lowest performances, however the trend is not as linear, especially for low ash contents.

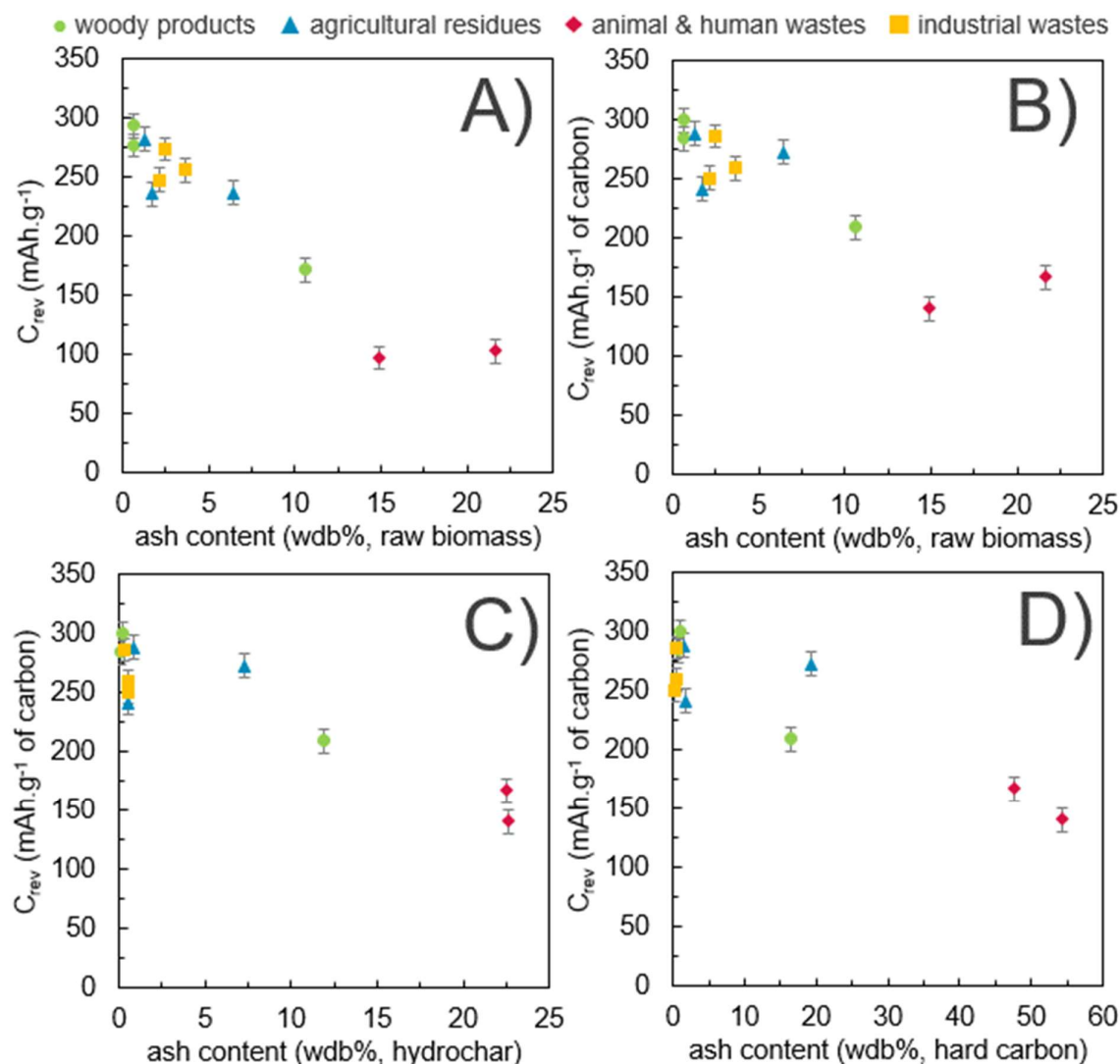


Figure 51: A) C_{rev} per gram of material depending on the raw biomass ash content, and C_{rev} per gram of carbon depending on the ash content in B) the raw biomass, C) the hydrochar and D) the hard carbon.

As explained in section 4.3, it was suggested that a trend exists between contents in K, Si, P, Al and Fe in the hydrochars and the hard carbon surface area, and that K, Ca and Si catalyse graphitisation. To understand the influence of these elements on the electrochemical properties, the C_{rev} and ICE depending on the composition of the raw material, the hydrochar and the hard carbon are represented in **Figure 52** and **Figure 53**. By having a closer look on the hydrochar and hard carbon composition, more interesting observation can be established. First of all, an interesting tendency regarding K and Si can be observed: the materials with the highest contents – both in the hydrochar and the hard carbon – also presents the lowest C_{rev} and ICE. As explained in section 4.4.2, the negative impact of the surface area on the electrochemical performances is due to the SEI formation. Concerning Ca, Al and Fe, only two points are shifted to the right when all the others are regrouped on the left. It seems they also have a negative impact on the performances, but the lack of information cannot allow to deduce a clear tendency. Moreover, they catalyse graphitisation, reducing the d_{002} which is an important factor during sodation mechanism as explained in 4.4.1.

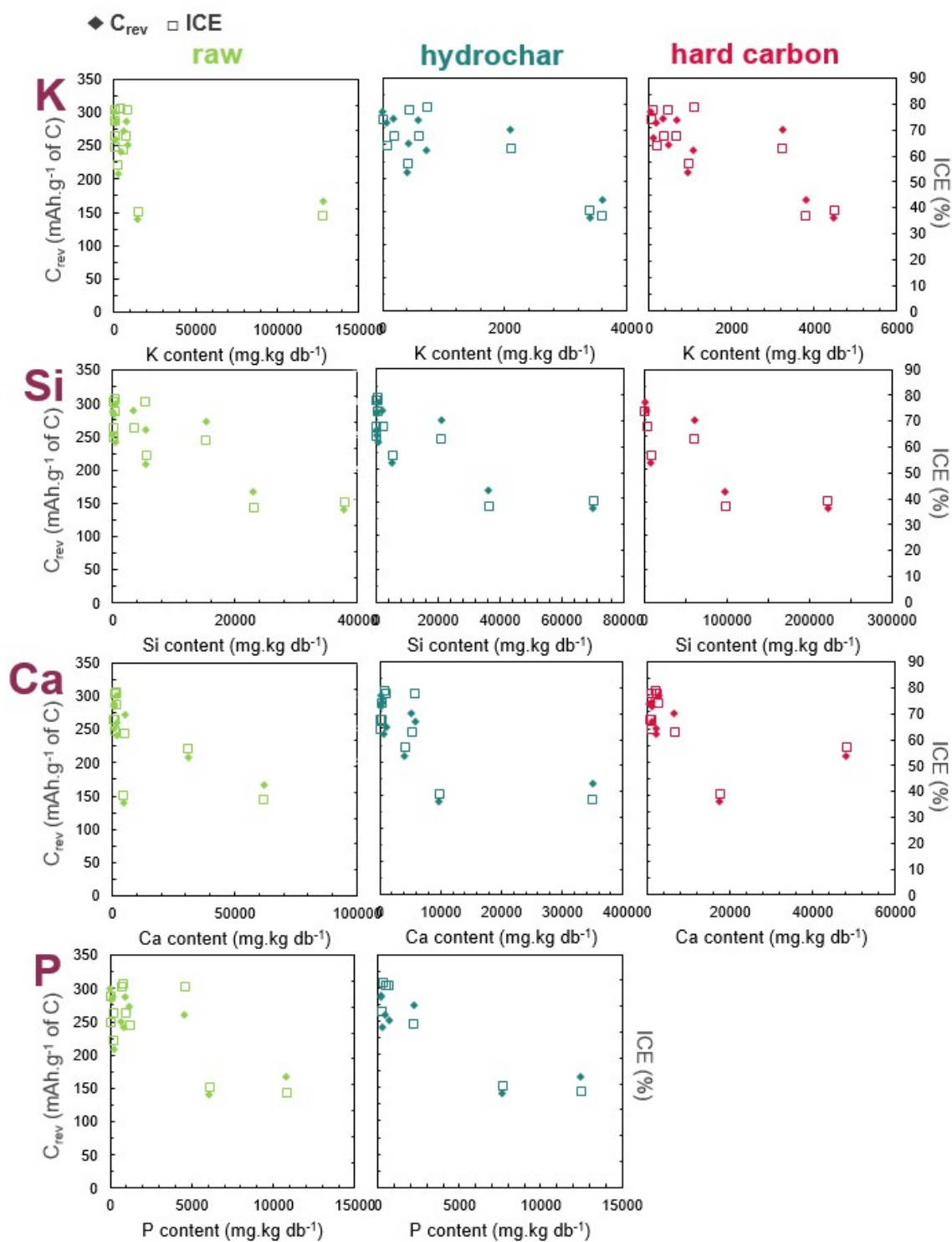


Figure 52: Influence of the K, Si, Ca and P contents of the raw material (green), hydrochar (blue) and hard carbon (red) on the reversible capacity C_{rev} (◆) and ICE (□). The axis for C_{rev} is on the left, while the secondary axis for ICE is on the right. P content in the hard carbon was not measured.

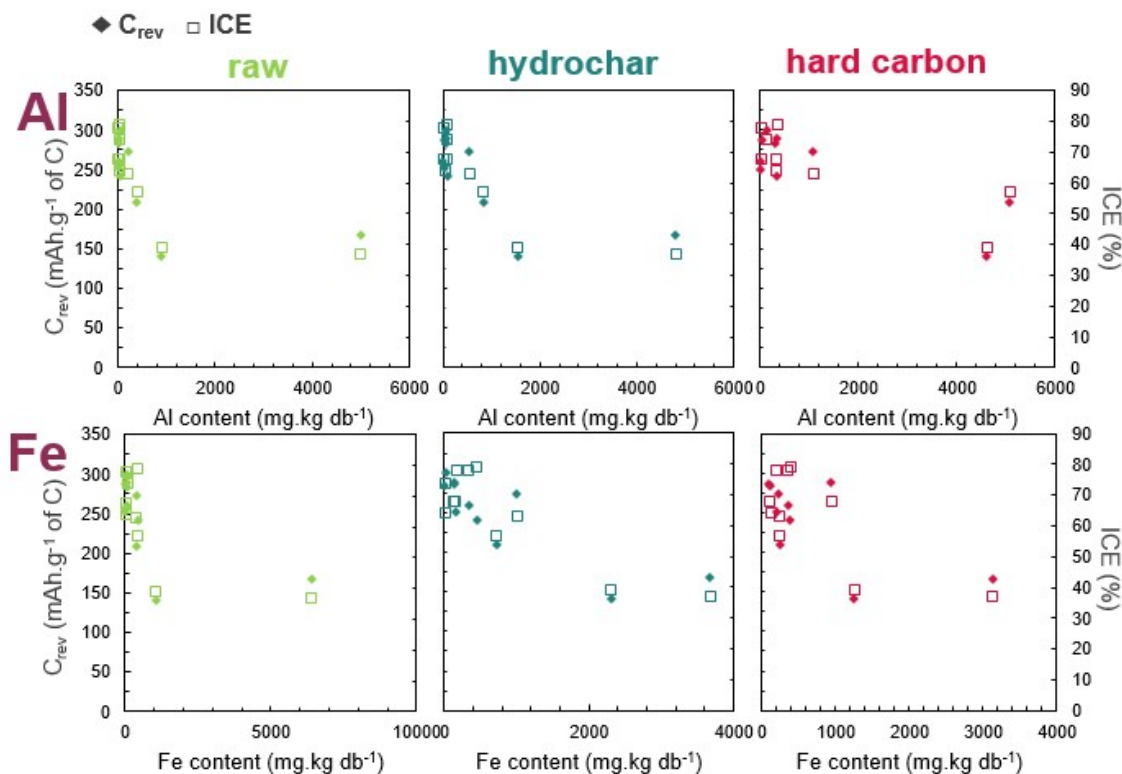


Figure 53: Influence of the K, Si, Ca and P contents of the raw material (green), hydrochar (blue) and hard carbon (red) on the reversible capacity C_{rev} (◆) and ICE (□). The axis for C_{rev} is on the left, while the secondary axis for ICE is on the right.

4.4.4. Influence of the hard carbon properties on the slope and plateau capacity

To go further on the investigation, the slope and plateau capacities are quantified as well. The charge profile is composed of two stages: a slop area at potentials higher than 0.15V vs Na^+/Na and a voltage plateau below 0.15 V vs Na^+/Na . The contribution of each area as well as the irreversible part is represented **Figure 54**.

It appears that the charge capacity is mostly due to the plateau: it represents from 53 to 75 % of the capacity for HC-sewage_sludge and HC-oak_bark respectively. Saavedra *et al.* [118] observed a similar tendency while working with 25 biomass-based hard carbon: they measured a major influence of the plateau over the C_{rev} . However, as already described in **Chapter 1**, the mechanism is not fully understood yet, and several models are proposed. According to the adsorption-insertion model, the plateau is attributed the Na^+ insertion between the graphene layers, while according to the three-stage model, the lowest potential part of the plateau is due to the pore adsorption at the surface. HC-sewage_sludge and HC-horse_manure exhibit a very small low voltage plateau compared to the other materials with a steeper slope, they also have the biggest irreversibility of the reactions. HC-oak_bark exhibits a similar charge pattern, with a longer plateau. These three materials have an interlayer space too small for Na insertion, in the same range of 3.4 Å, the mesoporosity at the opposite is three times lower for HC-oak_bark. These observations are not enough to clearly validate one of the mechanisms.

To try to see a tendency, both capacities depending on the surface area and the composition of the hard carbon are investigated below.

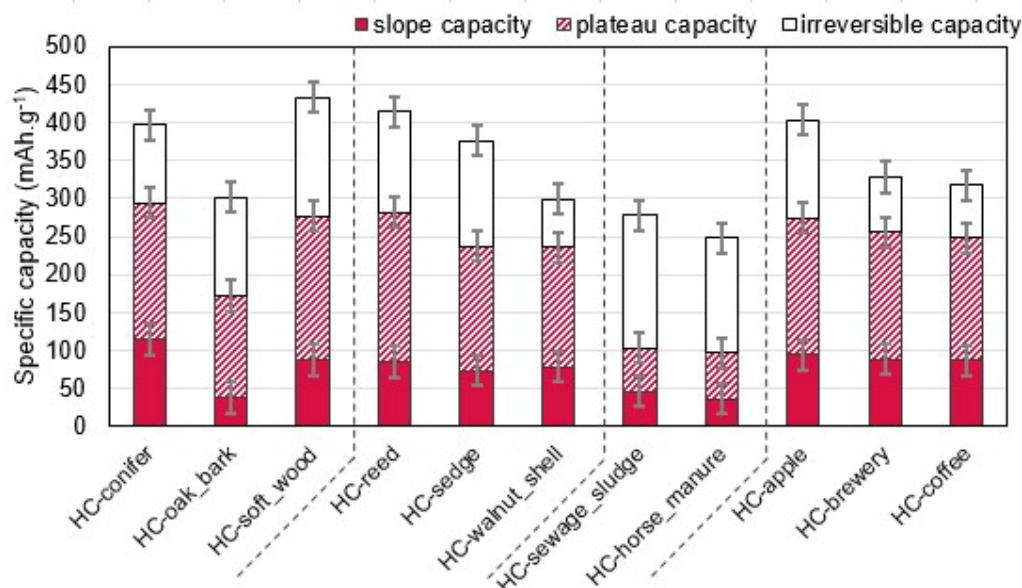


Figure 54: Slope and plateau capacities of the charge and irreversible capacity at the discharge of the first cycle. Uncertainties are from the method used.

4.4.4.1. Surface area influence

Figure 55 represents the slope and plateau capacities depending on the SSAs.

As already mentioned several times in this chapter, the animal & human wastes have an important surface area, especially their N_2 BET SSA are more than three times superior to the other hard carbons that was attributed to the SiC whiskers observed. It creates two isolated points in the graphs, difficult to link properly to a linear correlation. However, it looks like higher N_2 BET SSA leads to lower both slope and plateau capacities, in accordance with the discussion from section 4.4.2. At the opposite, no obvious trend appears regarding the CO_2 BET SSA. It highlights the impact the SiC whiskers have on the electrochemical performances. In their study, Saavedra *et al.* [118], observed a decrease of the plateau capacity with the increase of the SSAs, they also worked on materials with a wider range of surface areas, with similar SiC whiskers on their materials with the highest Si content increasing the mesoporosity. The results of this study do not allow to refute nor confirm (to refute nor confirm their conclusion) their conclusion nor to confirm.

However, the materials with the lowest slope capacity also highlight the lowest C_{rev} , it would be more precise to compare the contribution proportion to each area instead of the raw capacity. It is represented in **Figure 56**.

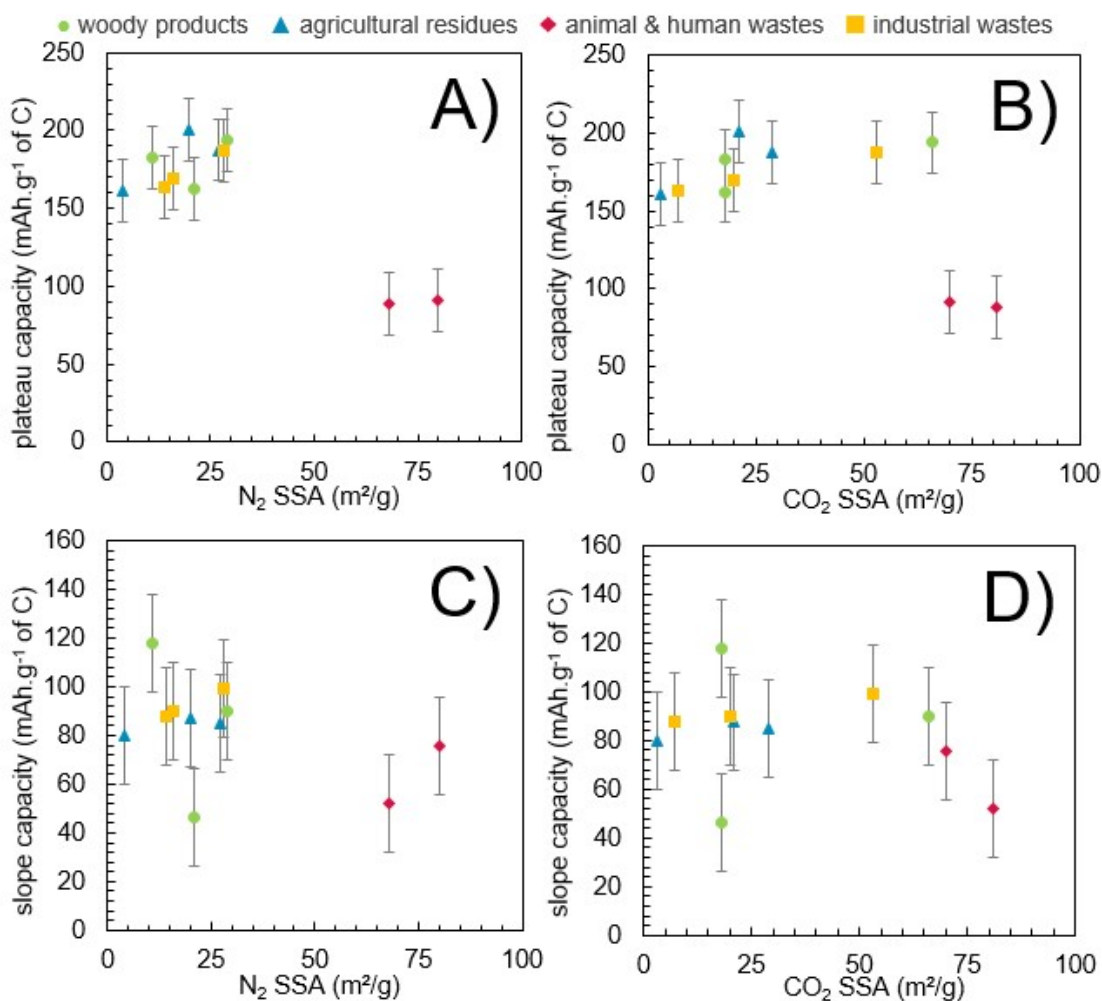


Figure 55: A) Plateau capacity depending on the A) N₂ SSA and the B) CO₂ SSA of the hard carbon, and slope capacity depending on the C) N₂ SSA and the D) CO₂ SSA of the hard carbon. Uncertainties are from the method used.

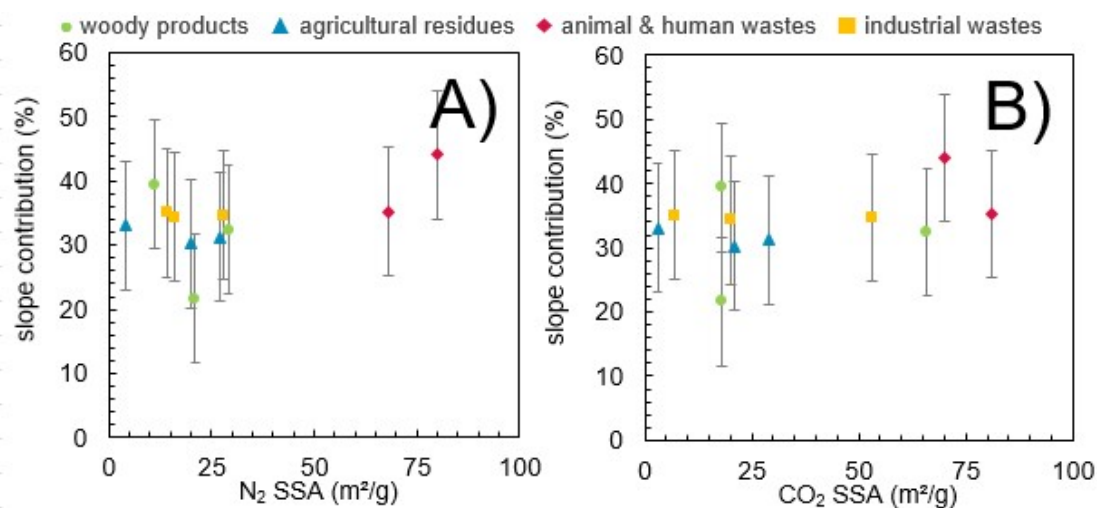


Figure 56: Percentage of the slope capacity contribution to the C_{rev} depending on the A) N₂ SSA and the B) CO₂ SSA of the hard carbon.

The characterisation of the slope contribution to the total C_{rev} allow to discredit that the CO_2 BET SSA favour the slope or the plateau. Indeed, as highlighted in **Figure 56**, the slope represents about the same amount of the reversible capacity no matter the SSA. It would highlight the surface area is not the main parameter that influence the slope and plateau capacity.

4.4.4.2. Composition influence

To understand better the influence of the composition on the slope contribution, the influence of each inorganic is represented in **Figure 57**. It was indeed observed in section **4.3** that the composition of the hydrochars and hard carbons seem to impact negatively the BET SSAs. However, they also impact the structure by graphitisation or the number of defects as detailed in the state of the art. It seems K, Mg and Fe might contribute to the increase of the slope proportion. However, this tendency is to be taken with caution: the increase is slight and only a few points have high contents. It was highlighted in section **4.3** that K and Si might increase the surface area, while in section **4.2**, inorganics and Ca, Si and K in particular tend to increase the graphitisation. Since the SSA influence have already been investigated above and no obvious link to the slope and plateau capacity have been observed, this beginning of trend between the inorganics contents might be due to the structure implied.

In this part, the role of the inorganics have been highlighted in the hard carbon properties: it seems that most of the inorganics from the hydrochar remain in the hard carbon after pyrolysis. They react with the carbon matrix at 1400 °C, either to remain in the solid as a stable compound or trapped in the material, or to be volatilised. During the reaction, they induce local graphitisation, especially Ca and Si, and seem to increase the surface area, both by leaving the structure, like K, or by forming whiskers at the surface, like Si, creating an important mesoporosity.

As a results, the hard carbon properties are impacted: graphitisation limits the insertion mechanism, while the enhanced surface area favour the SEI formation, and hence decrease the reversible capacity. In particular, the SiC whiskers where found to be a major obstacle for reversible reaction. Despite being present in the final material, by considering the carbon mass only, the active matter, the tendency with the materials rich in inorganics and the lower performances is observed. It highlights the impact they have on the material itself, and do not act only as a dead weight.

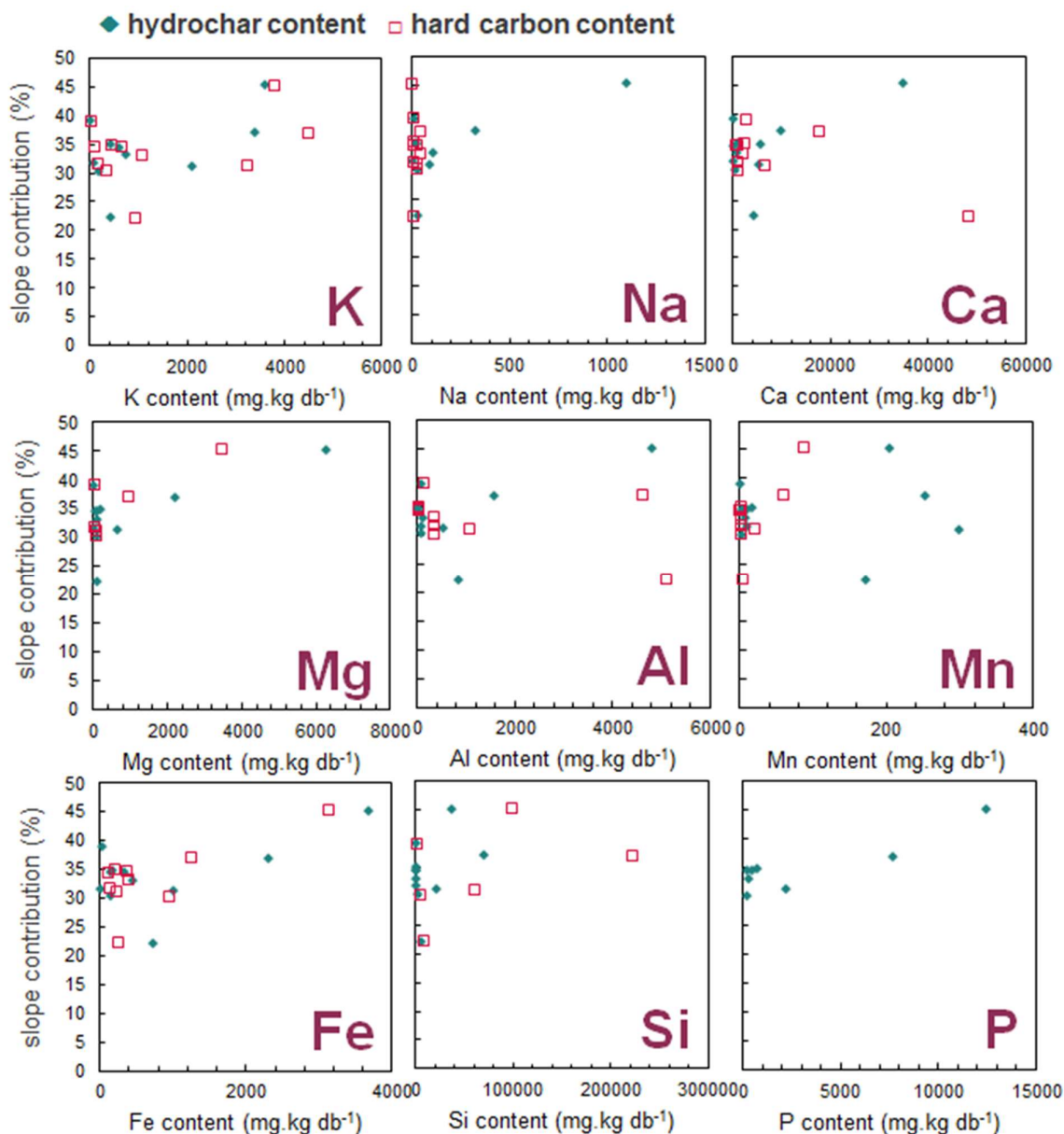


Figure 57: Contribution of the slope in C_{rev} depending of the inorganic contents in the hydrochars (◆) and hard carbons (□). P was not measured in the hard carbons.

Conclusions

This study gathered 11 biomasses from broad diversity in order to link their physico-chemical properties to the hard carbon in sodium battery performances. The ash content is already known to be important during the biomass-based hard carbon synthesis, and the impact of the HTC pre-treatment have been investigated: most of the K, Na and Mg is removed during the step, while the heavy metals remains. At last, some elements seem feedstock dependent: Ca, P and Si. This difference of behaviour was attributed to the chemical form the elements are present in, which can be water-soluble such as ionic salts, or insoluble such as silicon oxide or oxalates.

The remaining inorganics in the hydrochar impact greatly the hard carbon structure, in particular the graphitisation. The presence of elements as Si, K and Ca have been confirmed to catalyse graphitisation, moreover a slight increase of the surface area have been highlighted of the material containing higher amounts of K, Si, P, Al and Fe. As a results, the performances of the batteries were lower: the negative impact of the surface area and graphitisation toward the ICE and C_{rev} were established. Further investigations toward the elemental composition of the materials and the performances were tried, however no mechanism could be deduced.

This chapter showed the importance of the leaching on the hydrochar composition, and later on the hard carbon structure. Despite the leaching have been quantified, it is known to depend on the temperature and time of the reaction char [93], [96], [105]–[107]. It would then be interesting to understand better the mechanisms during the HTC pre-treatment towards the inorganics to predict better the hard carbon composition and properties, as well as optimise the process. To answer this question, the next chapter will focus on the fate of inorganics during HTC, depending on the temperature on three different raw materials.

Chapter 5

Fate of inorganics during hydrothermal carbonisation and its influence on the hard carbon properties

In this chapter, the behaviour of the inorganic elements during the HTC are investigated: a close balance before and after reaction at 3 different temperatures on 3 agro-food wastes are performed in order to determine which element tend to leach in the liquid phase, which tend to remain in the hydrochar, and which are feedstock or temperature dependant.

This chapter have been partly carried out in the frame of the MSc thesis of Maria J. Rivas-Arrieta and have been submitted for publication.

1. Experimental campaign settlement

The operational conditions have influence on the hydrochar structure and composition, as observed in **Chapter 3**. In particular, **Chapter 4** highlighted that the presence of inorganics have a major role on the resulting hard carbon: they impact the graphitisation and surface area, key factor for sodation mechanism and cell performances.

HTC have been widely investigated and used in various fields, making hydrochar a valuable product [198], as well as the liquid resulting from the reaction, rich in many interest molecules [199]. Among the uses, HTC is performed for N, P and K recovery mainly, for agricultural purposes mainly. Hence, they fate have been widely investigated at various conditions on many feedstocks [200]–[203]. Some papers also focus on Ca, Mg, or Na, but only a few deal with more elements. Moreover, they mainly focus on short residence time from few minutes to 1 h [104], [105], [204]. The few papers working on long residence time do not focus on the inorganics, even if they are measured, but on the macromolecule decomposition [106] or change the acidity of the reactive mixture [205]. Especially, no link regarding the hydrochar composition and the resulting hard carbon have been established.

Hence, to both optimise the HTC step and to possibly link it to the hard carbon properties, three agro-food wastes are carbonised at three temperatures. The feedstocks, apple pomace, brewery waste and spent coffee grounds, are selected due to their large availability on the study area. Furthermore, due to the process they are from, they can be used directly in HTC, which is interesting for industrial scale. In order to work at different state of decomposition of the materials, the carbonisations take place at 180, 220 and 260 °C. It was indeed highlighted in **Chapter 3** that at least 220 °C is required to observe cellulose

hydrolysis, and mentioned in **Chapter 1** that lignin and cellulose requires temperature about 250 °C. Similarly to the previous chapters, a long residence time is used to favour a spherical morphology. Each phase: both the solid and the liquid, resulting from the HTC is characterised. The hydrochars are then pyrolysed in the same conditions as the previous chapters, and half-cells assembled. The experimental campaign is summarised in **Figure 58**.

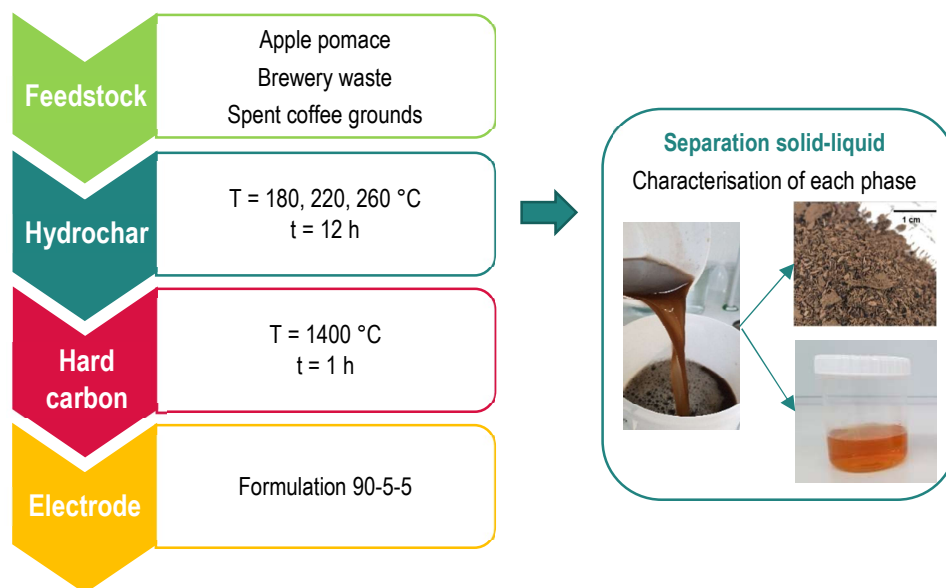


Figure 58: Experimental campaign.

For a better visualisation and clarity of the discussion in this chapter, the nomenclature of all the materials and liquids is detailed in Table 13. A diminutive of the three feedstock names is used, and a prefix is added for the derivate materials: h- and l- for respectively the solid – the hydrochar – and the liquid resulting from the HTC, and the suffix -180, -220 or -260 depending on the HTC temperature. After pyrolysis, the prefix HC- is used to distinguish the hard carbons. Raw materials are simply defined by the suffix -raw.

Table 32: Nomenclature of the samples of this study.

Feedstock	HTC temperature	Raw material	Sample name		
			HTC solid (hydrochar)	HTC liquid	Hard carbon
Apple pomace	180 °C	apple-raw	h-apple-180	l-apple-180	HC-apple-180
	220 °C		h-apple-220	l-apple-220	HC-apple-220
	260 °C		h-apple-260	l-apple-260	HC-apple-260
Brewery waste	180 °C	brewery-raw	h-brewery-180	l-brewery-180	HC-brewery-180
	220 °C		h-brewery-220	l-brewery-220	HC-brewery-220
	260 °C		h-brewery-260	l-brewery-260	HC-brewery-260
Spent coffee grounds	180 °C	coffee-raw	h-coffee-180	l-coffee-180	HC-coffee-180
	220 °C		h-coffee-220	l-coffee-220	HC-coffee-220
	260 °C		h-coffee-260	l-coffee-260	HC-coffee-260

2. Fate of inorganics during HTC

2.1. Raw biomass compositions

2.1.1. Organic composition

The macromolecules, organic and inorganic elemental composition of the three raw materials have been measured and are reported in **Table 33**, **Table 34** and **Table 35** respectively.

As expected, C is the main component and represents 42.8 wdb% to 50.3 wdb% of the materials, for apple-raw and coffee-raw respectively. In lower proportions, H contents lie between 6.9 wdb% and 7.8 wdb% for apple-raw and coffee-raw, while N contents range between 0.6 and 3.3 wdb% for apple-raw and brewery-raw respectively. S contents are below 0.3 wdb%, which is close to the detection limit from 0.1 to 0.2 wdb% depending of the mass of the sample. These C, H and O compose mainly lignin, cellulose and hemicelluloses; lignin contents lie between 12.1 and 23.3 wdb%, respectively for apple-raw and coffee-raw, while extractives are comprised between 22.0 to 47.66 wdb%, respectively for coffee-raw and apple-raw. Apple-raw and brewery-raw have very close cellulose contents of 16 wdb%, but brewery-raw has a higher hemicelluloses content of 23 wdb% compared to 14 wdb% for apple-raw. The polysaccharides content are calculated from the carbohydrate concentrations and conversion factor specific to every biomass, due to the lack of information in the literature towards spend coffee grounds, no value were deduced and only the monosaccharide contents were reported. Such range of values are in agreement with what was found for similar feedstock [166]–[169].

Table 33: Macromolecular composition of the raw biomass in wdb%. *na* stands for non-applicable.

Macromolecule composition wdb%	apple-raw	brewery-raw	coffee-raw
Lignin	12.11 ± 1.19	16.51 ± 0.98	23.27 ± 0.63
Extractives	47.66 ± 4.45	29.99 ± 0.58	21.98 ± 1.29
Polysaccharides			
Glucose	17.57 ± 1.60	16.48 ± 0.38	8.68 ± 0.00
Xylose	3.11 ± 0.08	12.12 ± 0.29	0.27 ± 0.02
Mannose	1.23 ± 0.04	0.63 ± 0.04	22.63 ± 0.32
Galactose	2.30 ± 0.18	0.91 ± 0.01	11.19 ± 2.32
Arabinose	3.91 ± 0.76	7.04 ± 0.07	2.32 ± 0.06
Total cellulose	16.34 ± 1.55	15.85 ± 0.34	<i>na</i>
Total hemicellulose	13.88 ± 1.37	22.58 ± 0.42	<i>na</i>
Acetyl	2.09 ± 0.27	1.25 ± 0.02	0.94 ± 0.02
Glucmannan	4.76 ± 0.27	2.18 ± 0.08	56.44 ± 0.78
Xylan	7.02 ± 0.84	19.15 ± 0.36	2.60 ± 0.03

2.1.2. Inorganic contents

Ash and inorganic elemental compositions are reported in **Table 34** and **Table 35** respectively. The ash contents of the three biomasses lie between 2.1 and 3.6 wdb% for coffee-raw and brewery-raw respectively, which is relatively low, and aligned with literature on similar feedstock [167], [168], [206].

Apple-raw is rich in K, with an amount of 7350 mg.kg db⁻¹. It is by far the most concentrated inorganic element in the material. Its amounts of P, Ca and Mg contents are 950, 750 and

500 mg.kg db⁻¹ respectively. At last, there is less than 100 mg.kg db⁻¹ of the other materials. it is in accordance with Skinner *et al.* [207], who reviewed apple pomace compositions in these ranges.

Brewery-raw on the contrary is rich in Si and P: their contents are about 5300 mg.kg db⁻¹ and 4600 mg.kg db⁻¹ respectively. It also contains important amounts of Ca and Mg of about 1800 mg.kg db⁻¹ each. At last, its K and Na contents are 780 mg.kg db⁻¹ and 400 mg.kg db⁻¹, while the other elements are below 100 mg.kg db⁻¹. Such contents are high compared to literature, Khidzir *et al.* [208] reported lower contents in Si, Mg and P. As explained in **Chapter 1** and **Chapter 4**, Si is present in agricultural residue, such as the barley and its husk the brewery waste comes from, due to its accumulation in the plant cell micropores [209].

At last, coffee-raw is more concentrated in K than any other element, reaching 8350 mg.kg db⁻¹. Second, Mg content is about 1200 mg.kg db⁻¹ which is seven times lower. P and Ca have a similar content of about 700 to 800 mg.kg db⁻¹. Except for Na with a content of 200 mg.kg db⁻¹, the other elements are below 25 mg.kg db⁻¹. These values are in accordance with literature [179], [210]. However Ballestreros *et al.* [179] also measured heavy metals amounts, reaching 18 mg.kg db⁻¹ for Cu, which is way higher than in our sample. These difference are probably due to the diversity of origin and process of the coffee beans and are not surprising.

At last, heavy metals were measured in very low quantity in all the feedstocks, ranging from 2 to 30 mg.kg db⁻¹, except from brewery-raw that is slightly richer in Fe with values close to 100 mg.kg db⁻¹. Such values agree with literature [105]. Values were found to be below detection limit of 1 mg.kg db⁻¹ for As, Cd, Cr, Ni and Pb and not reported.

Table 34: Organic composition of the raw materials and products: solid, liquid and gas, at the three HTC temperatures.

	Solid							Liquid				Gas	
	Solid yield %	Ash	C	H wdb%	N	S	O*	pH	Volume L	TOC mg.L ⁻¹	TN	CO ₂ wdb%	Max p** bar
Apple raw		2.4 ± 0.1	42.8 ± 0.1	6.9 ± 0.1	0.6 ± 0.0		47.1	4.0 ± 0.1					
180 °C	47	0.3 ± 0.1	61.2 ± 1.2	6.1 ± 0.0	1.0 ± 0.0	2.0 ± 0.1	31.4	3.4 ± 0.1	1.0 ± 0.2	2900 ± 100	40 ± 7	2.0 ± 0.1	11
220 °C	42	0.3 ± 0.1	69.7 ± 0.9	5.6 ± 0.1	1.1 ± 0.0	4.05 ± 0.01	23.3	3.8 ± 0.1	1.1 ± 0.2	2700 ± 500	40 ± 10	4.05 ± 0.01	25
260 °C	38	0.6 ± 0.1	75.1 ± 0.2	5.7 ± 0.2	1.1 ± 0.0	5 ± 2	17.4	4.0 ± 0.1	0.8 ± 0.2	5300 ± 1000	80 ± 20	5 ± 2	47
Brewery raw		3.6 ± 0.1	46.1 ± 0.2	7.2 ± 0.1	3.3 ± 0.0		39.5	4.1 ± 0.1					
180 °C	45	0.9 ± 0.1	63.2 ± 0.3	7.0 ± 0.1	3.2 ± 0.0	1.62 ± 0.02	25.5	4.0 ± 0.1	1.1 ± 0.2	6670 ± 70	930 ± 10	1.62 ± 0.02	11
220 °C	37	0.5 ± 0.1	71.5 ± 0.5	7.1 ± 0.1	3.9 ± 0.0	3.74 ± 0.02	16.7	4.4 ± 0.1	1.1 ± 0.2	6657 ± 10	875 ± 3	3.74 ± 0.02	18
260 °C	36	0.9 ± 0.1	76.0 ± 0.0	7.3 ± 0.0	4.1 ± 0.0	5.29 ± 0.03	11.5	5.0 ± 0.1	1.2 ± 0.2	5790 ± 30	884 ± 8	5.29 ± 0.03	47
Coffee raw		2.1 ± 0.1	50.3 ± 0.3	7.8 ± 0.0	2.4 ± 0.1		37.2	5.9 ± 0.1					
180 °C	52	0.3 ± 0.1	64.7 ± 0.9	8.0 ± 0.1	2.5 ± 0.0	1.1 ± 0.1	24.4	3.9 ± 0.1	1.1 ± 0.2	6390 ± 10	514 ± 7	1.1 ± 0.1	10
220 °C	46	0.5 ± 0.1	72.5 ± 0.5	8.0 ± 0.1	2.9 ± 0.1	3.3 ± 0.3	15.8	4.4 ± 0.1	1.1 ± 0.2	5700 ± 40	482 ± 1	3.3 ± 0.3	23
260 °C	42	0.6 ± 0.1	76.0 ± 0.2	8.3 ± 0.1	3.0 ± 0.0	4.6 ± 0.7	12	4.9 ± 0.1	1.2 ± 0.2	4980 ± 9	492 ± 0	4.6 ± 0.7	48

*Calculated by difference

**maximum pressure measured at the set temperature

Table 35: Inorganic composition of the solids: raw biomass and hydrochars in mg.kg db⁻¹. Standard deviation are experimental between the replicates.

	P	K	Na	Ca	Mg	Sr	Al	Cu	Cr	Mn	Fe	Ba	Ni	Si
	mg.kg db ⁻¹													
apple-raw	960 ± 70	7350 ± 30	76 ± 4	756 ± 1	501 ± 1	1.92 ± 0.04	11.4 ± 0.4	3.9 ± 0.5	< 1	6.10 ± 0.01	18.4 ± 0.8	< 1	< 60	80 ± 10
h-apple-180	149 ± 7	812 ± 8	< 10	80 ± 2	29 ± 2	< 1	8.8 ± 1	7.1 ± 0.6	< 1	< 1	87 ± 10	< 1	< 60	157 ± 9
h-apple-220	220 ± 10	585 ± 2	< 10	210 ± 30	35 ± 3	< 1	16 ± 1	8.5 ± 0.5	6 ± 1	3.2 ± 0.4	135 ± 1	< 1	< 60	160 ± 10
h-apple-260	830 ± 40	600 ± 100	< 10	980 ± 230	140 ± 30	2.0 ± 0.7	24 ± 3	10.4 ± 0.5	11 ± 3	9 ± 2	250 ± 20	< 1	< 60	100 ± 20
brewery-raw	4590 ± 30	776 ± 2	407 ± 1	1720 ± 30	1870 ± 20	12.6 ± 0.1	12 ± 2	10.6 ± 0.1	< 1	32.3 ± 0.2	73 ± 3	4.5 ± 0.3	< 60	5300 ± 300
h-brewery-180	420 ± 40	< 30	20 ± 1	290 ± 5	125 ± 9	< 1	7.6 ± 1	24.2 ± 0.3	5.2 ± 0.6	5.2 ± 0.2	198 ± 2	< 1	< 60	2500 ± 100
h-brewery-220	470 ± 20	< 30	15 ± 2	570 ± 40	117 ± 5	3.0 ± 0.2	8.3 ± 0.9	26.1 ± 0.3	50 ± 20	10.0 ± 0.3	340 ± 30	< 1	< 60	420 ± 60
h-brewery-260	1210 ± 30	< 30	13 ± 1	1170 ± 70	370 ± 30	7.9 ± 0.4	13.3 ± 0.7	23.1 ± 0.8	42 ± 1	15.9 ± 0.6	410 ± 10	6 ± 5	< 60	800 ± 100
coffee-raw	710 ± 30	8350 ± 50	200 ± 20	881 ± 10	1170 ± 20	2.6 ± 0.1	6 ± 2	20.0 ± 0.2	< 1	14.0 ± 0.3	25 ± 3	< 1	< 60	17 ± 8
h-coffee-180	110 ± 30	740 ± 60	26 ± 4	107 ± 10	123 ± 5	< 1	9 ± 1	42 ± 2	4 ± 1	5.19 ± 0.06	116 ± 8	< 1	< 60	8.3 ± 0.4
h-coffee-220	680 ± 40	430 ± 10	18 ± 2	1020 ± 50	205 ± 4	1.9 ± 0.1	12.9 ± 0.8	44.4 ± 0.3	16 ± 2	16.5 ± 0.4	168 ± 2	< 1	< 60	37 ± 7
h-coffee-260	810 ± 50	640 ± 50	40 ± 10	825 ± 50	201 ± 5	1.7 ± 0.2	17 ± 2	44 ± 1	60 ± 6	12 ± 1	424 ± 5	< 1	< 60	37.1 ± 0.9

2.2. Organic elemental distribution between the different phases

At the end of the reaction, gas aliquots are sampled for analysis, and solid and liquid are separated and characterised separately. Gas are produced in small portions, while liquid is the main product in close proportion to the solid. Organic compositions and phases properties are reported **Table 34** and their C and N distributions towards the different phases are illustrated in **Figure 59**. To make sure the balance is accurate, the element recovery – based on the ratio between the final and initial measured contents – are calculated and range between 80 and 90 % for C and 87 to 92 % for N. Such values are similar to those found in the same set-up, in our previous study in [12]. This balance can be considered as satisfactory for such experiment type and the missing elements may be explained by several sources of experimental errors.

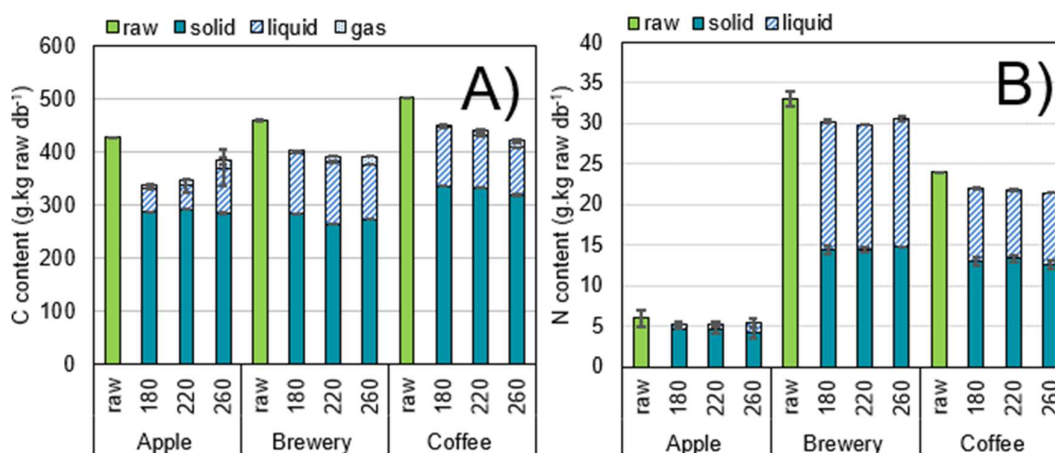


Figure 59: A) Carbon and B) Nitrogen balances at the different temperatures for the solid, liquid and gas fractions. The values were converted to g of element per kg of raw biomass dry basis. Carbon in the liquid is calculated from the total organic carbon of the total C. Carbon in the gas phase is deduced from the produced CO₂. Nitrogen in the liquid is deduced from the measured total nitrogen. Standard deviations are experimental between the replicates.

Solid yields are relatively close among the different feedstock at the same temperature, and lie between 36 and 52 w%, for h-brewery-260 and h-coffee-180 respectively, which is the range of value usually found in the literature. Coffee spent ground gives the highest solid yield; it is coherent with its lignin content that is the highest, which is known to decrease the solid yield due to its strong bonds difficult to break under HTC conditions. At the opposite, raw apple pomace and brewery waste have similar composition, which lead to close yields at each temperature. For every feedstock, the solid yield is 10 w% higher at 180 °C than at 260 °C. One should keep in mind that solid yield is used here to describe the mass ratio before and after reaction and not its efficiency.

Hydrochars are mainly composed of C, which represents between 61 wdb% for h-apple-180 and 76 wdb% for respectively h-brewery-260 and h-coffee-260. Their contents are higher than in the raw materials, which is expected in a carbonisation reaction. Furthermore, it increases with the temperature, while the solid yield decreases meaning the carbonisation is stronger at 260 °C.

Interestingly, all hydrochar C contents obtained at 260 °C reach the same value of 75 - 76 w%. At the same time that C content increases, H and O contents decrease with the temperature. It is widely known that during HTC, dehydration and decarboxylation occur, leading to H₂O loss and CO₂ production respectively that decreases the H/C and O/C ratios [97], [105]. These observations are in accordance with **Chapter 3**, where the increase of temperature lead to a more carbonaceous hydrochar, with a lower solid yield.

In the liquid phase, C is assimilated to the total organic content (TOC) measured. While it slightly decreases with temperature from 6670 to 5800 mg.L⁻¹ for brewery waste and 6390 to 4980 mg.L⁻¹ for spent coffee ground, it significantly increases from 2900 to 5300 mg.L⁻¹ for apple pomace. Other authors have reported a decrease with temperature for digestate and manure (Ekpo *et al.*, 2016). At low temperature, hydrolysis is the main reaction occurring, releasing organic acids among others, followed by recondensation and polymerisation at higher temperatures. The decrease of the TOC with the increase of the temperature might come from this different mechanisms occurring [211]. At the opposite, Reza *et al.* [212] observed a decrease of the TOC with the increase of the temperature from 180 to 260 °C during 5 and 30 min on cow manure. They measured at lower temperature a predominance of sugar and sugar derivate, while at higher temperature short-chain carboxylic acids are the main compounds, in accordance with the TOC increase they observed. It highlights the impact of the feedstock on the mechanism occurring, and thus the products.

During the reaction, a small fraction of gas is produced, mainly composed of CO₂. From 1.1 to 5.6 wdb% of CO₂ is produced, respectively for coffee at 180 °C and brewery at 260 °C, corresponding to 1 to 3 w% of the initial C. Its production increases with the temperature for every feedstock. It is reported that decarboxylation increases with temperature, which is coherent with this trend [97]. In their study, Reza *et al.* [212] also observed a gas quantity produced that doubled between 180 and 260 °C on cow manure.

As it is highlighted in **Figure 59A**), the majority of the initial C ends in the hydrochar, proportion that tend to increase with the temperature. However, it represents from 57 to 68 % of the initial feedstock, for h-brewery- 220 and h-apple-220 respectively, while soluble C represents from 10 to 22 %, for h-apple-220 and h-brewery-220 respectively. However, the proportion that ends in the gas phase increases with the temperature from 1 to 3 % from 180 °C to 260 °C, no matter the feedstock. It still remains a small portion of the initial raw biomass quantity.

Unlike C, H and O; N contents are higher in the hydrochars than in the raw materials, their values rangind from 1.0 to 4.1 wdb%, for h-apple-180 and h-brewery-260 respectively. It seems to be also slightly temperature dependent: brewery and coffee-based hydrochars have higher N contents with the heat increase, unlike apple materials which are constant. In their study lead on ten various feedstock, Smith *et al.* [105] also reported some N contents increasing with the temperature while other decreased and remain equals, highlighting the importance of the raw material. However,

some values are close to the limit of detection of 0.02 w% especially for the apple-based materials, enhancing the uncertainty.

In the liquid phase, N is assimilated to the total nitrogen (TN) measured. The values are very different from one biomass to another: while apple liquids range between 40 and 80 mg.L⁻¹, brewery and coffee liquids range from 875 to 930 mg.L⁻¹ and from 482 to 514 mg.L⁻¹ respectively. Apple pomace is also the material with the lowest initial content of 0.6 wdb%, which is coherent with its lower TN in its HTC liquids. Similarly, the highest values are measured in the brewery waste liquids, which is also the raw material with the highest N content of 3.3 wdb%.

In accordance with literature [212], no nitrogen was measured in the gas phase to complete the distribution. Furthermore, at the beginning of the reaction the reactor is flushed with N₂ to remove the air, the amount of N at the end of the reaction comes mainly from this initial load rather than a reaction product. It is indeed well known that the main gas produced is CO₂ but can also contain CO, H₂ and CH₄ [93], no N species were reported.

As it appears in **Figure 59B**, the distribution of N between the liquid and hydrochar are quite equal for brewery and coffee waste materials, unlike apple materials where at least two thirds ends in the hydrochar. This material has also the lowest initial amount of N, which could influence its distribution. Despite this, the temperature doesn't seem to have an influence on the distribution.

The S content, as discussed above, was around the detection limit in the biomass samples and was also logically found around this limit in the hydrochars.

2.3. Ash content in the solids

The ash content in the solids are reported in **Table 34**. This measurement is adapted for solids only and couldn't be performed on the other phases. We assumed that no inorganic and ash ends in the gas phase.

The ash content in the hydrochars are always lower than in the raw materials: their values lie between 0.3 and 0.9 wdb% while the lowest raw material ash content is 2.1 wdb%. This small amount is worth to notice since the precision is at 0.1 wdb% of the measurements. It means that less than a third of the ash content of the corresponding feedstock remains in the hydrochars.

Both h-apple-180 and h-coffee-180 have an ash content of 0.3 wdb% that increases to 0.6 wdb% at 260 °C. At the opposite, h-brewery-220 have a lower ash content 0.5 wdb% than at 180 and 260 °C of 0.9 wdb%. Both behaviours were reported on similar feedstock: similarly to brewery waste materials, Zhang *et al.* [213] observed on apple juice pomace a decrease of the ash content from 2 wdb% in the raw material to 0.02 wdb% at 225 °C with a residence time of 15 min, which was higher at 190 and 260 °C of 1.68 and 1.49 wdb% respectively. Similarly to apple and coffee hydrochars of this study, Afolabi *et al.* (2020) worked on spent coffee grains and reported an initial

ash content of 1.6 wdb% that decreased to 1.0 wdb% at 180 °C and increased to 1.3 wdb% at 220 °C for 5 h.

Hence, no obvious pattern between the ash content in the hydrochar and the temperature can be deduced, however ash regroups any inorganic compound, small molecule like oxide, phosphate or silicate, and any other compound that doesn't burn after calcination. A detailed analysis of the different phases are discussed below.

2.4. Inorganic elemental distribution between the different phases

Major and minor inorganics have been measured in both the hydrochars and liquid, they are reported in **Table 35** and **Table 36** respectively. To discuss the better distribution possible, the recovery of every element were measured and should ranks between 80 to 110 % for the majority of the elements. Only a few have less satisfactory balance: only 64 to 87 % of the initial P, and between 78 and 125 % for Cu and Al are recovered in the final products. For this reason, the conclusions towards these elements should be taken carefully. A complete balance between the different products phases are represented for every feedstock in **Figure 60** for apple pomace, **Figure 61** for brewery waste and **Figure 62** for spent coffee ground.

As it appears clearly that K and Na end mainly in the liquid phase. About 1 to 5 % of the initial K and about 1 to 8 % of Na remain in the solid, independent of the feedstock nor the temperature. A similar trend was reported on alga, digestate and animal manures [204] and sea lettuce [215]. According to Smith *et al.* (2016), K and Na are present in biomass in the form of ionic salts such as NaNO₃, KNO₃, NaCl and KCl. As these alkali metal salts are readily soluble in water, their large decrease in the hydrochars was expected. Moreover, the acidic conditions given both by the initial feedstock and the HTC process itself benefit hydrolysis reactions, thus promoting the removal of K and Na. As reported in **Table 34**, the liquids at the beginning and at the end of the reaction were acidic, and the pH lies between 3.4 and 5.0, for I-apple-180 and I-brewery-260 respectively, after reaction at each temperature. Apple waste-based liquids are more acidic than the two other materials', its higher pH being 4.0 at 260 °C when it's the lower value of the brewery and coffee liquids at 180 °C. Such acidic values are overall in agreement with literature, but, as discussed above, it is questionable to make more detailed comparisons with previous studies on similar feedstocks [211], [216], due to the different operating conditions. These acidic values can be partly explained by the hemicellulose degradation from HTC temperatures of about 180 °C, and the associated production of low molecular weight acids like acetic, formic, lactic, levulinic and propionic [211]. Subsequently, as temperature increases, pH increases as a result of re-polymerization of these intermediate products dissolved in the liquid phase into the solid phase.

While K and Na don't seem temperature dependant, Ca, Mg and P are more concentrated in the hydrochars obtained at 260 °C than at lower temperature, no matter the initial feedstock. While only 3 to 8 % of these elements remain in the solid at 180 °C (for Mg in h-apple-180 and P in

h-coffee-180 respectively), it reaches 7 to 53 % at higher temperature (for P in h-brewery-220 and Ca in h-coffee-220 respectively). For P, the retention was the highest at 260 °C for all feedstock. Such result extends the trend observed by Smith *et al.* (2016) from 200 to 250 °C, and seem to follow a linear behaviour under more critical conditions, as reported by Ekpo *et al.* [204] from 170 to 500 °C. One should keep in mind that at such temperature and hence autogenous pressure, the process is no longer HTC but hydrothermal liquefaction and subcritical water gasification. However, no such pattern was observed for Ca and Mg, which have a higher retention at 220 °C than 260 °C in coffee materials. Organic P is dissolved at low temperature with the hydrolysis of the feedstock, and precipitate back into inorganic phosphorous species with the dissolved organic products phase [217]. Moreover, P precipitates in presence of Ca under hydrothermal conditions into calcium phosphate, which decrease its solubility (Dai *et al.*, 2015). Shi *et al.* [218] also reported the precipitation of orthophosphates with metals, including Ca and Mg while Ghanim *et al.* (2018) suggested also the precipitation of apatite ($\text{Ca}_5(\text{PO}_4)_3(\text{F}, \text{Cl}, \text{OH})$). In addition to the precipitation with phosphate, Khazraie Shoulaifar *et al.* [220] suggested the presence of Ca into an acid-soluble oxalate form that would be released at low temperature, as well as some Ca and Mg ionic salts trapped into macromolecules. They also suggested that a fraction of Ca, Mg and Mn in the cell plant wall are bonded to carboxyl groups, which are degraded under HTC under decarboxylation, and are ion-exchangeable. Consequently, Ca could be liberated only to be re-adsorbed by the remaining or newly formed functional groups on the surface of hydrochars, which may enhance their cation exchange capacity [105].

Mn is present in trace amounts in most of the raw biomasses and hydrochars, and seems to be released at 180 °C and reincorporated in the solid at 260 °C similarly to Ca, Mg and P. However, due to the small quantities in both the raw material and the final products, no accurate balance is discussed. It could be released during the protein complexes break down of the biomass matrix where it is trapped during the HTC hydrolysis [221]. Shi *et al.* (2021) conjectured Mn precipitates with P as non-apatite inorganic specie, that explains its reincorporation in the solid.

Si was measured only on solid materials due to the unsuitable method for liquids. Hence, only Si on raw materials and hydrochars were measured. As mentioned, brewery-raw had a higher content than the other feedstock, which is also the case for its hydrochars. At 180 °C, 22 % of the initial Si remains in the hydrochar, while merely 3 and 5 % remained at 220 and 260 °C respectively that let suppose its leaching is also temperature dependant. Similar behaviour was observed in apple-based materials, with a decrease from 92 to 51 % at 180 and 260 °C respectively. The trend seemed opposite with coffee-based hydrochars, Si being more retained at higher temperatures. However, this trend must be taken with caution due to the low initial Si content of coffee-raw of 17 mg.kg db⁻¹, close to the limit of detection estimated for the method when considering blank samples of 8 mg.kg db⁻¹. Its behaviour seems to be feedstock dependant: while some authors reported important leaching of Si in willow-based hydrochar at 200 °C where about 20 % remains [105] and about 50 % on brewer's spent grain materials at 200 and 240 °C [185], other studies

reported almost no removal on rice hulls [104], digestate [186] and sewage sludge [105]. Their raw materials also contained very higher Si amount, from 36000 to 332400 mg.kg⁻¹ that are much higher content than the materials in this study. However, their behaviour differs depending on the temperature as well: Reza *et al.* [104] observed a decrease of the Si content with the increase of the temperature from 200 to 260 °C on their four lignocellulosic feedstock, at the opposite of Zhao *et al.* [186] who reported a higher leaching at 190 than at 250 °C, and concluded on a reincorporation of the silicon in the solid. To explain these differences, it can be found as stable silica hydrate in rice hulls to provide rigidity to the plant [104] or as extraneous minerals such as quartz and clay [79] that are stable in the range of studies temperatures. Si can also be dissolved as Si(OH)₄ in plant tissues [187], which may be easier to extract during HTC. Furthermore, during the brewery process hop is biochemically degraded that might lead to more accessible Si species.

The recovered measured amount of Fe are superior to 100 %, and reach remaining amount of 220 to 720 % in the hydrochars that obviously can't be discussed in detail. Such values are thought to be due to leaching of Fe from the reactor made up of stainless steel grade 316. To confirm this hypothesis, the "most critical scenario" was reproduced, adjusting the pH measured on the raw biomass slurries and conductivity by adding KCl and HCl respectively. The final solution presented a pH of 4.0 and a conductivity of 905 μS.cm⁻¹. It was then fed in the reactor under the same conditions as the experiments, namely 1.3 L heating up to 260 °C and kept at this temperature for 12 h. Similarly, a blank test with 1.3 L of demineralised water was performed. In the final liquid, the Fe content was ten times higher in the adjusted solution than in the blank (1.73 mg.L⁻¹ and 0.16 mg.L⁻¹ ± 0.02, respectively) even if no Fe was added. The only source of Fe being the vessel, this increase could come from the leaching of the reactor. Note that the balance was closed for the other elements.

Other measured heavy metals, Sr, Al, Cu, Cr, Ni and Ba, are in too low quantity to make an accurate balance. However, they are only traces in the raw biomass, and don't seem to be removed during HTC, as reported by Reza *et al.* [104].

Table 36: Inorganic composition of the liquids. They are presented in mg.L⁻¹ for P, K, Na, Ca and Mg, and in µg.L⁻¹ for Sr, Al, Cu, Cr, Mn, Fe, Ba and Ni. Standard deviation are experimental between the replicates.

	P	K	Na	Ca	Mg	Sr	Al	Cu	Cr	Mn	Fe	Ba	Ni
	mg.L ⁻¹					µg.L ⁻¹							
l-apple-180	33.3 ± 0.7	358 ± 0	3.33 ± 0.09	34.9 ± 0.7	22.1 ± 0.1	129 ± 3	41 ± 3	80 ± 20	3.1 ± 0.8	305 ± 9	1000 ± 200	108 ± 2	200 ± 50
l-apple-220	30.1 ± 0.4	352 ± 5	3.03 ± 0.08	26.7 ± 0.8	20.1 ± 0.2	105 ± 1	36.1 ± 0.3	48 ± 9	< 2	243 ± 8	900 ± 300	92.6 ± 0.5	590 ± 60
l-apple-260	19 ± 2	352 ± 1	3.01 ± 0.01	11 ± 3	14.4 ± 0.4	50 ± 10	50 ± 20	12 ± 4	< 2	240 ± 20	5610 ± 20	49 ± 6	300 ± 50
l-brewery-180	138 ± 1	37.6 ± 0.3	16.7 ± 0.1	74 ± 1	82.0 ± 0.3	567 ± 4	60 ± 1	130 ± 10	14.8 ± 0.7	1310 ± 20	2660 ± 40	402 ± 2	1080 ± 60
l-brewery-220	140 ± 6	37.6 ± 0.3	16.8 ± 0.1	65.0 ± 0.5	80.9 ± 0.2	499 ± 2	46 ± 1	11.9 ± 0.9	14 ± 2	1260 ± 20	3900 ± 200	354 ± 2	990 ± 20
l-brewery-260	134 ± 8	38.2 ± 0.3	16.9 ± 0.1	49.2 ± 0.1	74 ± 1	379 ± 1	43 ± 1	< 2	8.97 ± 0.05	1230 ± 10	3200 ± 300	291 ± 4	970 ± 20
l-coffee-180	20.3 ± 0.1	393 ± 3	8.8 ± 0.1	38.4 ± 0.2	50.9 ± 0.6	149 ± 1	39 ± 2	220 ± 40	6 ± 2	550 ± 10	90 ± 20	85.8 ± 0.9	180 ± 30
l-coffee-220	9.8 ± 0.7	401 ± 2	9.3 ± 0.1	14.7 ± 0.8	49.1 ± 0.2	84 ± 1	19.1 ± 0.5	19.8 ± 0.7	2.3 ± 0.2	310 ± 30	8 ± 2	65.9 ± 0.4	< 120
l-coffee-260	7 ± 2	403 ± 2	9.2 ± 0.1	14 ± 2	46.1 ± 0.4	62 ± 8	19 ± 4	< 2	< 2	490 ± 30	2000 ± 100	35 ± 3	< 120

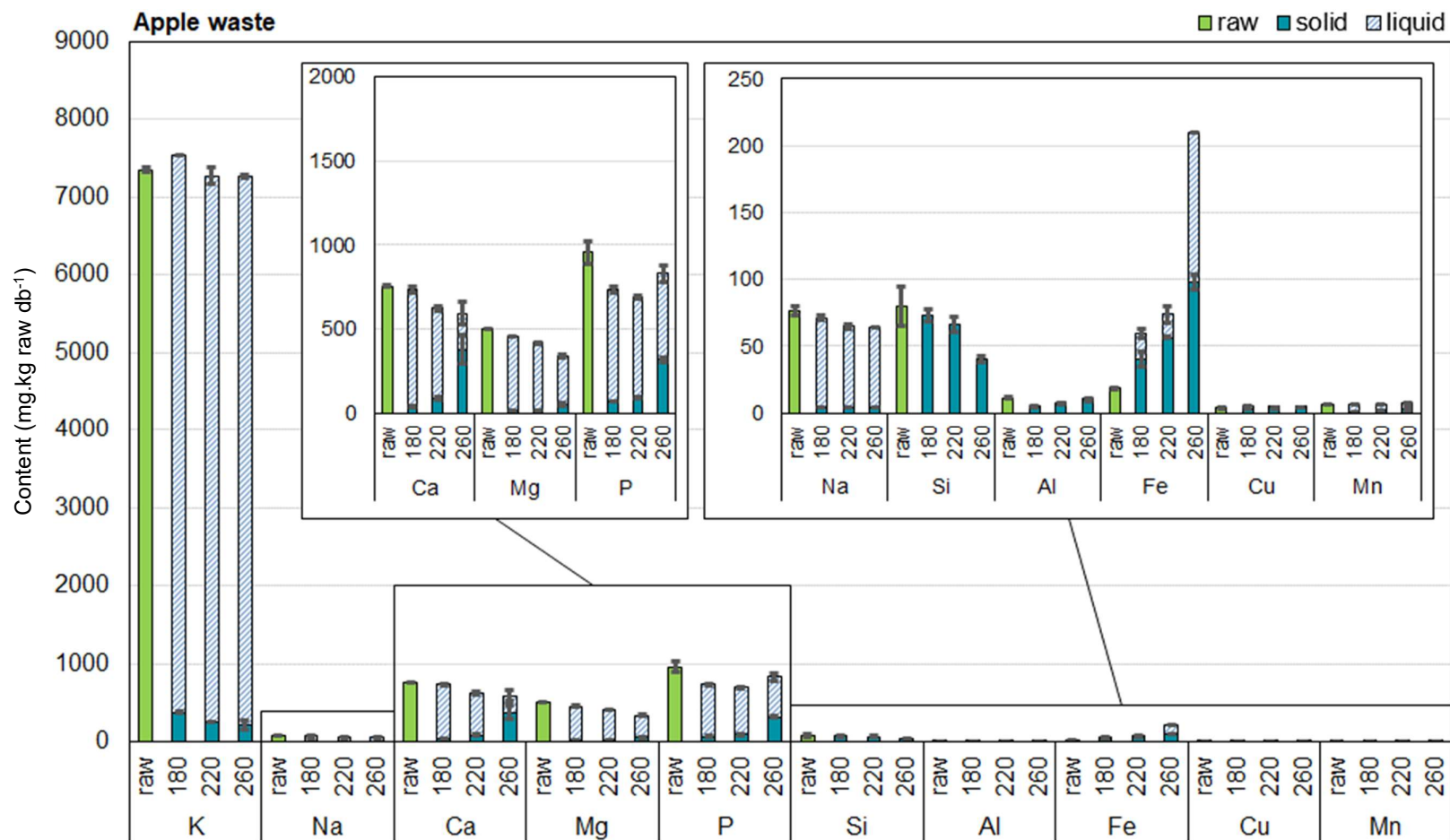


Figure 60: Balance of the inorganics between the raw material and the hydrochar (solid) and liquid at the different temperatures of 180, 220 and 260 °C from apple waste. The different elements were represented on different scale, depending on the content. The values were converted on mg of element per kg of raw biomass according to equations (10) and (11) for solids and liquids respectively in order to compare them together. Standard deviation are experimental between the replicates.

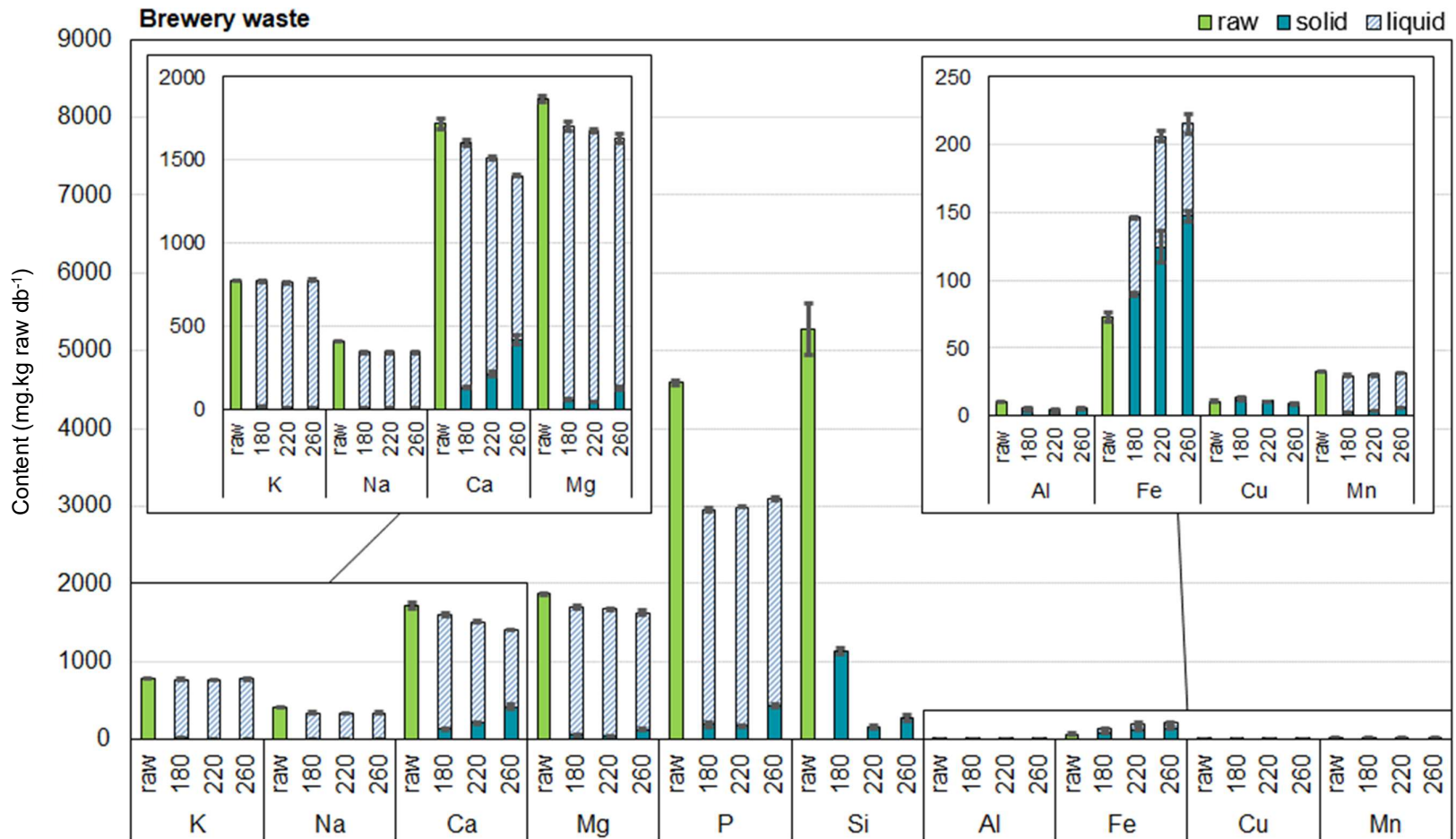


Figure 61: Balance of the inorganics between the raw material and the hydrochar (solid) and liquid at the different temperatures of 180, 220 and 260 °C from brewery waste. The different elements were represented on different scale, depending on the content. The values were converted on mg of element per kg of raw biomass according to equations (10) and (11) for solids and liquids respectively in order to compare them together. Standard deviation are experimental between the replicates.

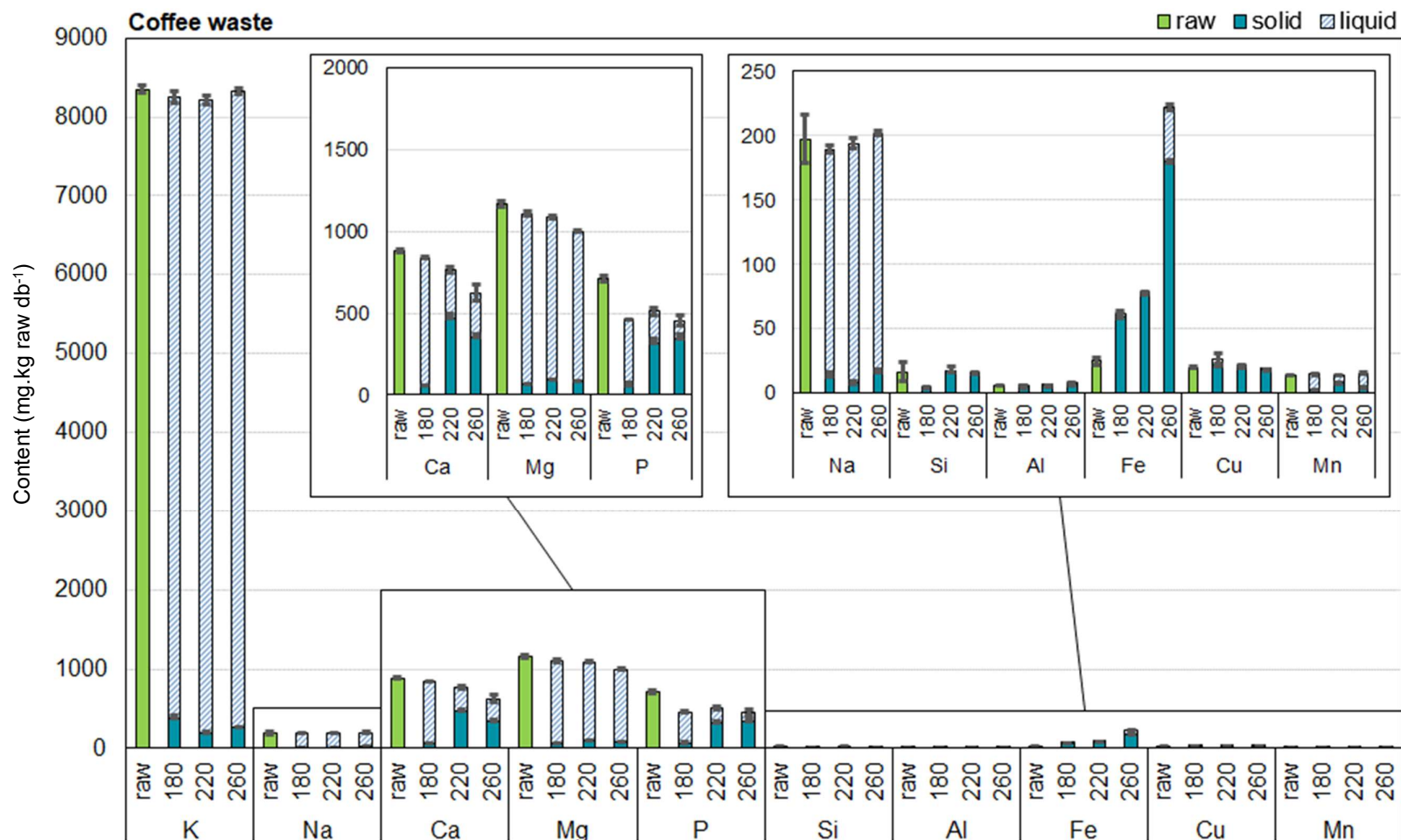


Figure 62: Balance of the inorganics between the raw material and the hydrochar (solid) and liquid at the different temperatures of 180, 220 and 260 °C from coffee waste. The different elements were represented on different scale, depending on the content. The values were converted on mg of element per kg of raw biomass according to equations (10) and (11) for solids and liquids respectively in order to compare them together. Standard deviation are experimental between the replicates.

2.5. Influence on the hydrochar structure

In order to identify the species in the solid materials, XRD are performed, phases are identified and pattern are reported in **Figure 63**.

Apple-raw presents 3 broad peaks at around 15, 23 and 35°. They are typically observed for lignocellulosic biomass and are generally attributed to semi-crystalline cellulose [130]. These peaks, which remain at 180 °C, tend to disappear at higher process temperatures, logically indicating the decomposition of this form of cellulose. The increase of peak intensity between the raw material and the hydrochar obtained at 180 °C could come from the degradation at this temperature of the amorphous compounds such as hemicelluloses, which concentrates the crystalline phases. It is indeed known that hemicelluloses begin to be hydrolysed at 180 °C while cellulose requires a higher temperature above 220 °C to be significantly degraded [97]. This observations are in accordance with **Chapter 3**.

Coffee-raw shows a rather different feature than apple-raw, between 15° and 25°. Indeed, besides the typical bump observed for apple-raw, sharper peaks, which are difficult to explain, appear at 16, 20, 21 and 25°. However, these sharp peaks could also be observed in literature for spent coffee grounds [179], [180]. XRD patterns of all coffee-based hydrochars showed sharp peaks identified as n-heneicosane (PDF 00-031-1705). They are much less obvious in the raw biomass; however it could be masked by the presence of other amorphous compounds that are decomposed after HTC. Heneicosane has been detected in fresh and fermented coffee beans [188] and is known to naturally occur in certain plants as a waxy solid [189].

Brewery-raw XRD pattern shows a less defined crystalline cellulose feature. It can be explained by the fact that brewery waste results from the fermentation of barley inducing degradation of the cellulose. This cellulose structure seems to reappear at 180 °C, which can also be attributed to the degradation of the other amorphous compounds. A sharp peak at 21° appears at 260 °C that can be attributed to silicate cristobalite beta, syn. PDF 01-077-8630). Indeed, this feedstock had the highest Si content, and while Si was largely removed from solid, the amount remaining in hydrochar may be sufficient for detection in XRD. Silicon oxide compounds have also been detected in hydrochars derived from sugarcane bagasse [205] and algal biomass [222].

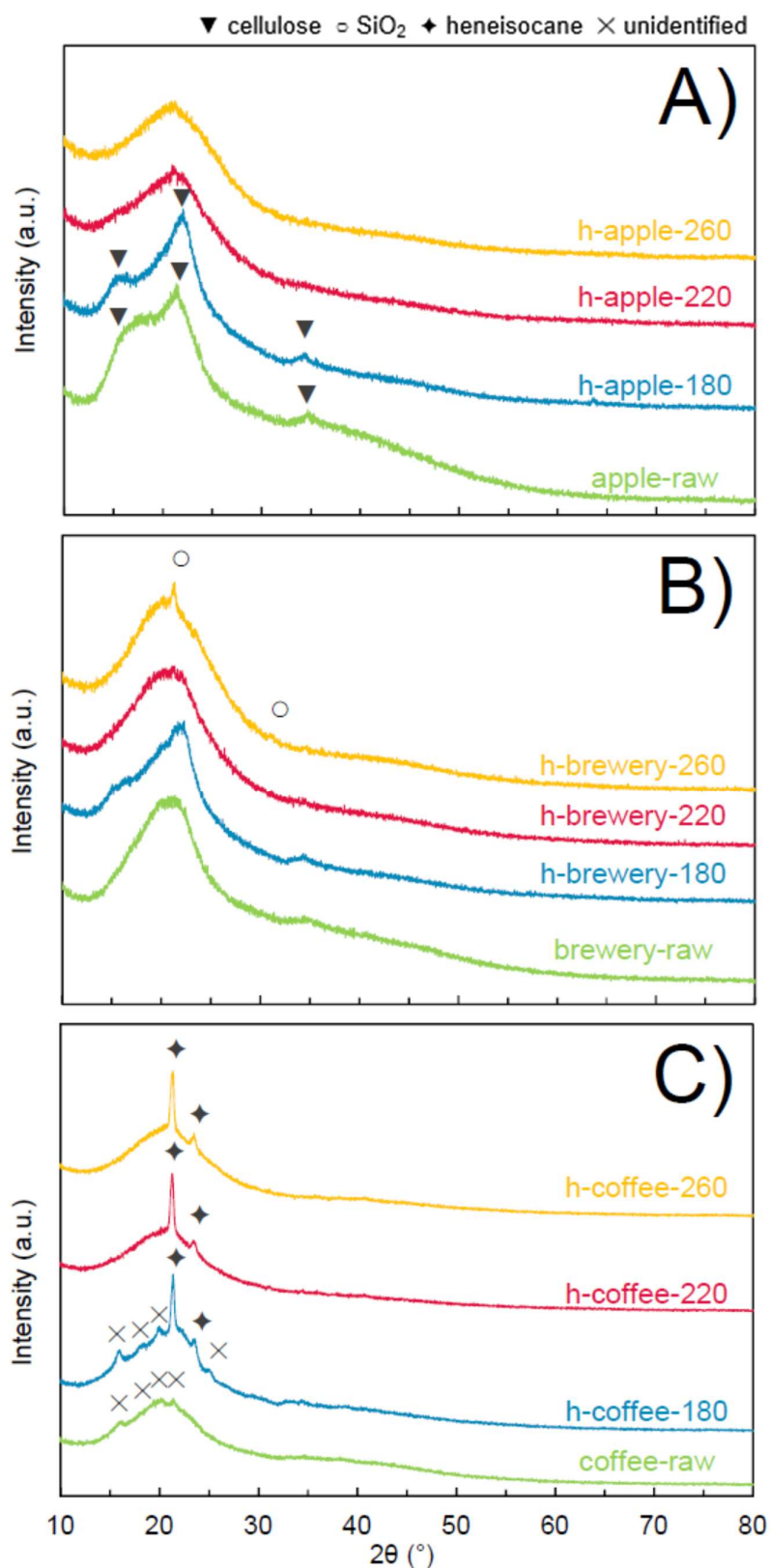


Figure 63: XRD patterns of materials from **A)** apple pomace, **B)** brewery waste and **C)** spent coffee grounds. Peaks are identified with symbols as: ▼ Cellulose- β ($C_6H_{10}O_5$)_n (PDF 00-060-1502), ○ cristobalite beta. Syn SiO_2 . (PDF 01-077-8630), ◆ *n*-heneicosane $C_{21}H_{44}$ (PDF 00-031-1705) and × unidentified.

As a result, the influence of the temperature on the hydrochars and liquid composition have been characterised and trend among the mechanisms observed. Starting at 180 °C, hemicelluloses hydrolysis begins leading to an increase of the C content while decreasing the H/C and O/C ratios. The degradation of inorganic phases contributes to concentrate the crystalline cellulose area leading to a more organised material. In the liquid, organic acids production decreases the pH that help to remove acid-soluble compounds naturally present in the biomass such as K and Na salts. Plant cell matrix degradation also allow to release inorganics trapped inside, which contribute to the leaching of Ca, Mg, P or Mn.

With the increase of the temperature, the dissolved organic molecules reacts themselves and with the solid to stronger its degradation: decarboxylation is stronger, as suggests the increase of CO₂ as well as the macromolecule degradation as highlights the XRD cellulose pattern loss. Some repolymerisation and recondensation mechanism can also occurs. The hydrochar becomes richer in C, while losing H an O. The composition of the liquid as well as the temperature and pressure in the reactor allows the formation of Ca, Mg, P and Mn complexes that are no longer soluble.

At last, some elements seems not impacted by the temperature, heavy metal for instance seem to remain in the hydrochar no matter the temperature nor feedstock.

Although some trends among the materials and temperature have been observed, most of the behaviour seem feedstock dependant: the leaching proportion and crystalline phases are peculiar to each biomass. The organisation, stability and chemical form were highlighted to be dependant of the initial material, leading to different observation among the three agro-food wastes, as well as the literature.

As already mentioned, most of the partially or almost complete removed inorganics, K, Ca and Si, are responsible for local graphitisation of the materials at high temperature pyrolysis. The impact on this leaching on the composition and structure of the hard carbons are described on the next part.

3. Impact on the hard carbon properties

3.1. Hard carbon compositions

All the hydrochars have been pyrolysed at 1400 °C for 1 h under Ar flow, their compositions and the yields of the reactions are reported in **Table 37**.

At the opposite of the HTC step, the reactions with the higher solid yield are the ones performed on hydrochars obtained at the highest temperature. As observed in section **2.2**, during the pre-treatment the hydrochars obtained at the highest temperature were the most degraded, leading to the higher C contents. Hence under the second pyrolysis step, since the raw structure is already altered, there are matter to volatilise. The resulting hard carbons have very high amounts of C, ranged between 95.7 to 98.9 wdb%, for HC-apple-220 and HC-coffee-180 respectively. These values are among the highest in the literature for biomass-based hard carbon that usually ranges from 70 to 98 % [30], [61], [118], [190]–[192]. The other few percent are O, H, N, S and ash. The C contents are very close and no obvious trend with the

HTC temperature can be observed. Unlike the solid yield which is only the mass ratio of the hard carbon obtained and the initial hydrochar introduced, the carbon yield considers the maximum theoretical mass based on the C content as described in equation (7). They lie between 27 w%, for HC-brewery-220 and HC-coffee-180, to 45 w% for HC-apple-260. Similarly to the C content from which it is calculated, no obvious pattern regarding the HTC temperature can be deduced.

After pyrolysis, the inorganics are in lower quantity than in the raw materials, as expected with the leaching during the HTC. In order to quantify their volatilisation during the pyrolysis, similarly to the previous part the remaining inorganics are compared by taking the solid yield into consideration with equation (8) adapted to hard carbons and graphical representation are plot **Figure 64**. Only the element in major quantity are represented: K, Na, Ca, Al, Mn and Fe. Some values are below the limit of detection and are not plot as well.

K and Ca are the main inorganics remaining in the hard carbons, about 50 % of K remains after pyrolysis in the apple-based hard carbons, while only 10 to 30 % in coffee-based materials. It is lower than Ca, where 50 to 70 % remains in the solid for most of the materials, whereas apple materials which retain it all. HC-brewery-180 retain only 7 % of the Ca from its hydrochar. Most of the Na from the hydrochar is volatilised, less than 12 % remains in the hard carbon, except for HC-brewery-220 that keep almost 35 % of the element. It was expected to observe a major volatilisation for most of these elements, especially at such temperature [36], [37], [223], [224]. Li *et al.* [37] characterised the volatilisation of alkali and alkaline earth metals of Victorian brown coal from 300 to 1200 °C and observed monovalent elements are easily removed in comparison of divalent. They measured at 1200 °C that 80 % of Na was able to be released, while only 40 % of Ca left. According to them, these elements are thought to interact with the char matrix through multiple bond-forming and bond-breaking reaction. However, a strong impact of the state of the element in the biomass as well of its accessibility impact its release during pyrolysis [160]. As it was observed in section 2.4, Mg, P and Ca tend to reprecipitate into secondary char, which could make them more available to volatilisation due to the poor interaction they have with the hydrochar. Strong operating conditions favour radical free production, which interact then with the alkali and alkaline earth metal linked to the char matrix and break the bond [225].

Most of the Mn from the hydrochar was released after pyrolysis, less than 4 % remains in all hard carbons. Lane *et al.* [39] observed no or low volatilisation of this elements from up to 1100 °C on algae. However, this lower temperature as well of the state Mn is present in the material might influence its volatilisation.

At last, Al and Fe seem to behave differently on the various materials, from about 10 to 40 % of the hydrochar's contents remain in the final material. It is usually considered as low-volatilisable elements, and are supposed to remain in the final product. They are usually not the elements of interest in literature and few informations are available regarding their fate above 1000 °C. Despite their quantities are usually not reported, some studies reports the phase change occurring during pyrolysis [226], [227]. It should be kept in mind that the Al quantities are very low and are to be taken with cautious.

Table 37: Yields and composition of the hard carbons obtained from the different hydrochars. Solid yield SY and carbon yield CY are calculated according to equations (7) and (8). Uncertainties are experimental.

	SY w%	CY w%	C wdb%	ash wdb%	K	Na	Ca	Mg mg.kg db ⁻¹	Al	Mn	Fe
HC-apple-180	36 ± 1	38	96.7 ± 0.1	0.4 ± 0.1	1070 ± 20	19 ± 4	230 ± 10	< 0.3	76 ± 1	0.317 ± 0.001	80 ± 3
HC-apple-220	47 ± 1	44	95.7 ± 0.1	0.4 ± 0.1	660 ± 90	7 ± 2	490 ± 50	< 0.3	28.6 ± 0.2	0.15 ± 0.07	100 ± 20
HC-apple-260	52 ± 1	45	98.5 ± 0.2	0.6 ± 0.3	< 10	< 3	< 3	< 0.3	< 0.3	< 0.3	< 0.3
HC-brewery-180	32 ± 1	30	95.3 ± 0.4	1.6 ± 0.2	133 ± 3	8 ± 2	673 ± 5	5 ± 4	7.1 ± 1	0.51 ± 0.07	67 ± 3
HC-brewery-220	37 ± 4	27	98.7 ± 0.2	0.5 ± 0.2	90 ± 30	20 ± 10	1030 ± 20	< 0.3	11.2 ± 0.2	0.9 ± 0.4	350 ± 10
HC-brewery-260	42 ± 1	32	98.4 ± 0.3	0.9 ± 0.1	95 ± 7	0.4 ± 0.1	2550 ± 60	55	9.42 ± 0.04	0.6 ± 0.2	285 ± 4
HC-coffee-180	27 ± 1	27	98.9 ± 0.1	0.5 ± 0.1	500 ± 30	1 ± 1	310 ± 20	< 0.4	8 ± 1	0.1 ± 0.05	130 ± 10
HC-coffee-220	33 ± 1	30	98.8 ± 0.1	0.2 ± 0.1	460 ± 50	2 ± 2	2200 ± 50	< 0.3	10.01 ± 0.05	0.27 ± 0.07	190 ± 10
HC-coffee-260	37 ± 1	29	97.5 ± 0.5	0.8 ± 0.1	290 ± 10	9.7 ± 0.6	1754 ± 3	< 0.3	13.67 ± 0.02	0.68 ± 0.05	482 ± 2

Table 38: Physicochemical properties of the hard carbons. d_{002} is the interlayer distance, ICE the initial coulombic efficiency, and C_{rev} the reversible capacity of the first cycle. Uncertainties are from the method used.

	d_{002} (Å)	N ₂ adsorption		CO ₂ adsorption		ICE (%)	C _{rev} (mAh.g ⁻¹)
		SSA (m ² .g ⁻¹) (±5%)	V _μ (cm ³ .g ⁻¹)	SSA (m ² .g ⁻¹) (±5%)	V _μ (cm ³ .g ⁻¹)		
HC-apple-180	3,80 ± 0.05	39	0.1	78	0.05	65 ± 2	273 ± 20
HC-apple-220	3,85 ± 0.05	28	0.05	53	0.05	68 ± 2	274 ± 20
HC-apple-260	3,86 ± 0.05	27	0.05	23	0.07	68 ± 2	272 ± 20
HC-brewery-180	3,72 ± 0.05	63	0.08	80	0.04	70 ± 2	262 ± 20
HC-brewery-220	3,70 ± 0.05	16	0.02	20	0.01	78 ± 2	256 ± 20
HC-brewery-260	3,68 ± 0.05	9	0.01	13	0.01	83 ± 2	242 ± 20
HC-coffee-180	3,71 ± 0.05	11	0.03	9	0.02	76 ± 2	257 ± 20
HC-coffee-220	3,70 ± 0.05	14	0.03	7	0.01	78 ± 2	248 ± 20
HC-coffee-260	3,69 ± 0.05	10	0.02	25	0.03	82 ± 2	231 ± 20

No data on the uncertainties of the pore volumes were given

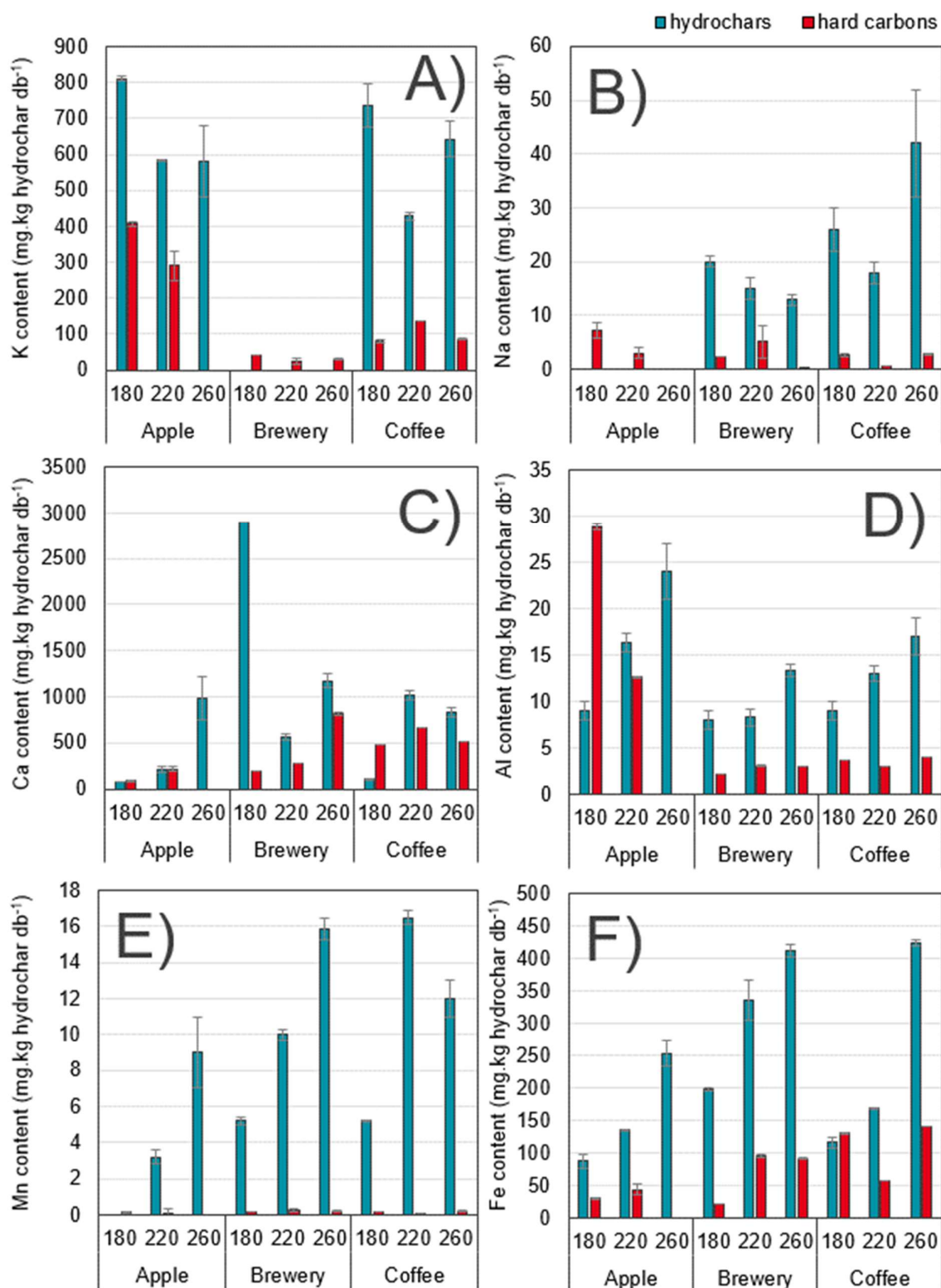


Figure 64: Remaining **A) K, B) Na, C) Ca, D) Al, E) Mn, F) Fe** contents in the hydrochar (blue) and the hard carbon (red) from all agro-food feedstock. The values were converted on mg of element per kg of hydrochar similarly to equation (10) in order to compare them together. Standard deviations are experimental between the replicates.

In order to try to understand better the retention or release of the different element, knowing the state they exist in the material would be interesting and might help to understand this difference of behaviour among the hard carbons. To that end, the structure is presented below

3.2. Hard carbons structures

XRD are performed on the hard carbons and reported in **Figure 65** and their d_{002} in **Table 38**.

The XRD patterns highlight the very typical hard carbon two broad peaks at about 22 and 43°, corresponding to the diffraction of the ray perpendicular to the graphene layers (002) and parallel (100) respectively. The interlayer distance d_{002} lies between 3.7 and 3.9 Å, which are in the same range. The material being disorganised, this variation is not significant enough to determine a trend regarding the HTC temperature among materials. This values are in accordance with typical biomass-based hard carbons [21], [30]. At least 3.7 Å is required for sodium insertion mechanism [53], making these materials promising for Na-ion batteries.

In some materials, HC-brewery-260 and HC-coffee-260, a small uncentered peak at 26° is cumulated to the broad (002) peak. This position is typical to graphite and could be due to graphitic area in the material. However, the low intensity doesn't allow to conclude on a significant organised area.

Small peaks can be observed at 33.3 and 45.0° on HC-brewery-260, HC-coffee-260 and HC-coffee-220. They are thought to be CaS, oldhamite. syn (PDF 04-004-3787). These three materials are indeed among the ones with the highest Ca content. CaS was also reported on sunflower seed shell- and papaya seed-based hard carbons, which contained 3480 and 9558 mg.kg⁻¹ of Ca [118]. The stability of this compound at such temperature is coherent with the low volatilisation of Ca mentioned in the previous section.

HC-brewery-180 also presents a small intensity peak at about 35°. This position corresponds to the most intense peak of SiC, already observed in **Chapter 4**. h-brewery-180 is indeed the hydrochar with the highest Si content, of 2500 mg.kg db⁻¹ when all the other hydrochars are below 200 mg.kg db⁻¹. Unfortunately, the measure couldn't be performed on the hard carbon to confirm the remaining of the element. However, the low intensity of the peak as well as the lack of the other characteristic peaks at 60 and 72°, which might be hidden by the background, is not enough to clearly identify this phase.

Despite it seems there is no link with the HTC temperature and the d_{002} , the composition impacts the structure as widely explained in **Chapter 1** and **Chapter 4**. The influence of the composition is analysed, and represented in **Figure 66**. In the range of value of the samples, it is very clear that the ash content itself does not impact the interlayer space. However, no link could be established with the elemental composition due to the close d_{002} , making any tendency clear to highlight. Ca was already reported to induce graphitisation, as well as Si and heavy metals [30], [118], [228]. Despite Si, Fe and Al are not obviously linked to the d_{002} , Ca seems to be retained in higher quantity in the hard carbons with the lowest d_{002} . However the values measured are close and low, this observation alone is not enough to confirm the correlation, but it is in accordance with literature [30], [118], [228].

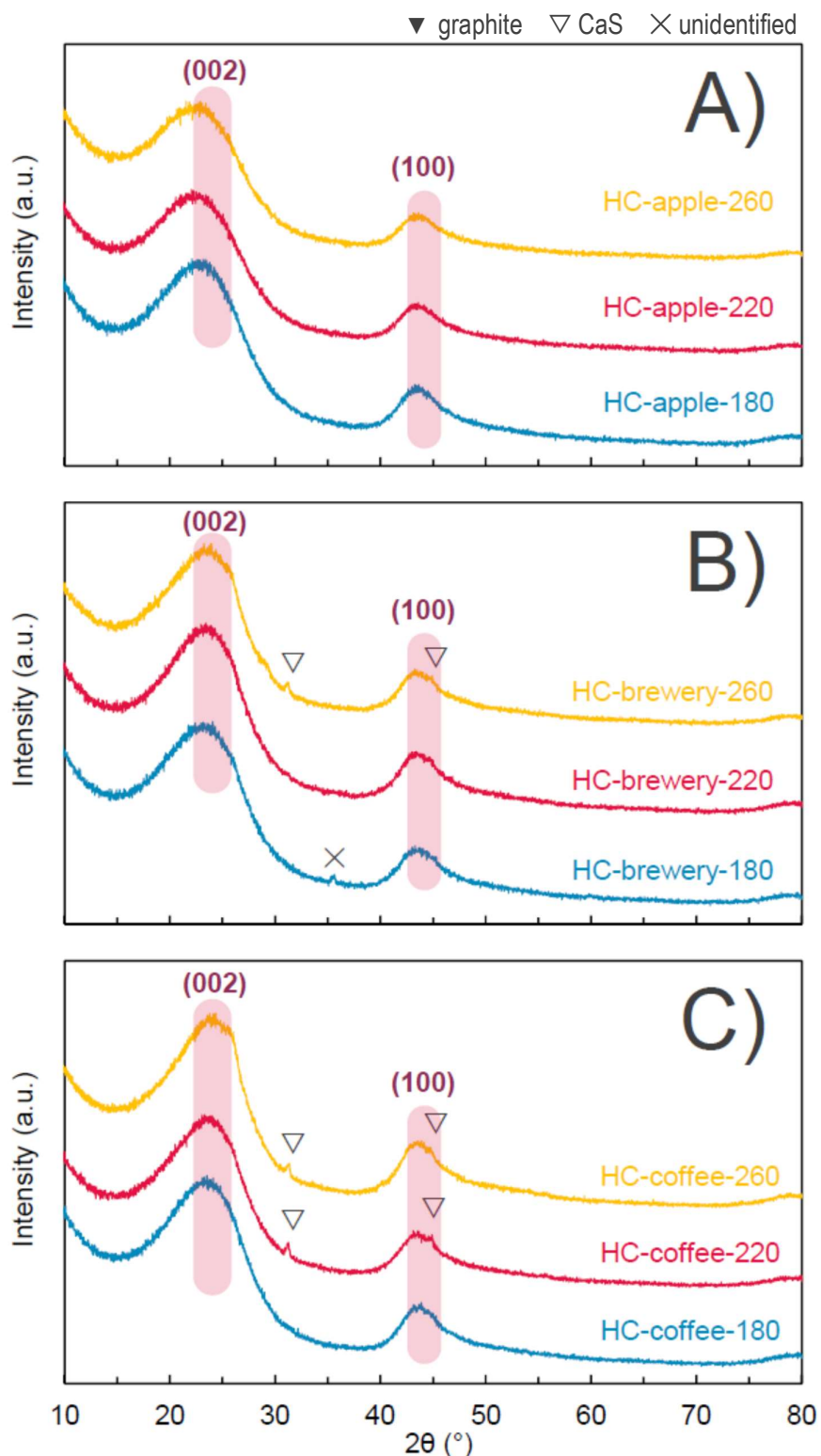


Figure 65: XRD patterns of the hard carbons at the different HTC temperatures from **A)** apple pomace, **B)** brewery waste and **C)** spent coffee ground. Peaks are identified with symbols as: ▽ Calcium sulfide Oldhamite, *syn* CaS (PDF 04-004-3787), and × unidentified.

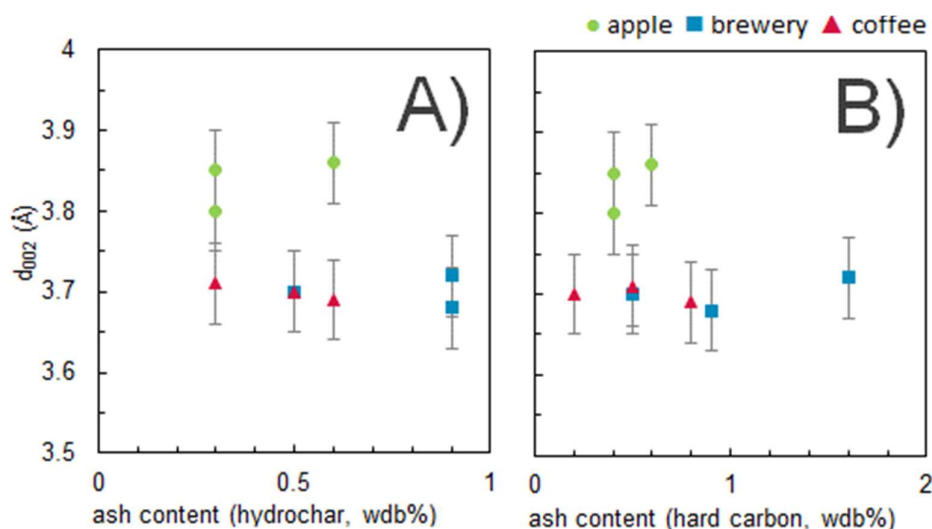


Figure 66: Influence of the ash content in the **A)** hydrochar and **B)** hard carbon on the d_{002} .

3.3. Hard carbon specific surface area

The N_2 and CO_2 adsorption have been performed on all the samples. The corresponding BET SSA as well as the pore volumes are reported in **Table 38**.

N_2 SSA values are between 9 and 63 $m^2 \cdot g^{-1}$, for HC-brewery-260 and HC-brewery-180 respectively, while CO_2 SSA are between 7 and 80 $m^2 \cdot g^{-1}$, for HC-coffee-220 and HC-brewery-180 respectively. As CO_2 molecules are smaller than N_2 , they allow to measure ultramicropores lower than 0.7 nm. This explains the higher SSA measured with this gas. These values are in accordance with other studies led on lignocellulosic materials. Hence, Saavedra *et al.* [118] obtained N_2 SSA below 900 $m^2 \cdot g^{-1}$ and CO_2 SSA between 0.5 and 338 $m^2 \cdot g^{-1}$ from 25 lignocellulosic biomasses through a two-steps pyrolysis. They observed that most of the high surface area materials were also the ones with the highest Si content due to the formation of SiC whiskers that created adsorption sites for gas molecules. The hard carbons with these SiC phases were all reported with an initial Si content higher than 1800 $mg \cdot kg \text{ db}^{-1}$ and reaching 64000 $mg \cdot kg \text{ db}^{-1}$. In this study, most of the Si was removed during the HTC, preventing from SiC formation. However, in the previous section, SiC was suspected in HC-brewery-180, which was indeed the material with the highest Si content. This material is also the one with the highest surface area of 63 $m^2 \cdot g^{-1}$.

Coffee-based hard carbons highlight the lower surface area below 10 $m^2 \cdot g^{-1}$ and 25 $m^2 \cdot g^{-1}$ for N_2 and CO_2 SSA respectively, while brewery-based range between 9 and 63 $m^2 \cdot g^{-1}$ and 13 to 80 $m^2 \cdot g^{-1}$, and apple-based materials between 27 and 39 $m^2 \cdot g^{-1}$ and 23 to 78 $m^2 \cdot g^{-1}$. Apple-based materials have bigger pores than the other materials. It appears that HC-brewery-180 and HC-apple-180 have higher surface area from their homologues at 260 °C: it seems to decrease with the temperature. Moreover, their CO_2 BET SSA are higher than their N_2 BET SSA, highlighting their important microporosity. Only coffee materials exhibit low porosity, no matter the HTC temperature. To understand this phenomena, the composition of the raw materials is considered: apple-raw have a significant higher extractive content than

the two other biomasses, while brewery waste seems to be rich in polysaccharides. Both are reported to be degraded and to leave the char matrix during the pyrolysis, leading to microporosity [229], which could explain this difference.

The surface area depending on the temperature is represented in **Figure 67**. As mentioned above, it seems the surface area drops with the increase of the pre-treatment temperature for materials with a significant surface area. During the HTC step, it was highlighted in part **0** that some species reprecipitate as small molecules. Ca in particular is reported to form microsphere at the surface of the hydrochar [110]. This proximity to the surface might help their volatilisation, and hence decrease the porosity.

K is one of the highest inorganics in the materials, despite it was significantly removed from the HTC step, it is still present in the hydrochars and most hard carbons. Depending on its form into the material, it is reported to contribute to the surface area: the volatilisation of K species forming active site and creating microporosity [130], [196], as described in **Chapter 4**.

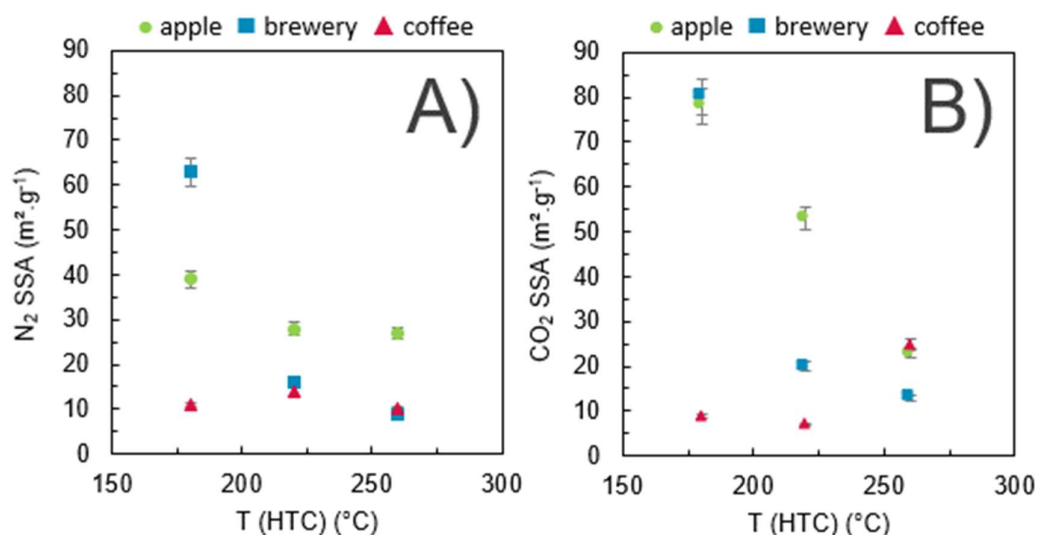


Figure 67: A) N₂ and B) CO₂ SSA of the hard carbon depending on the HTC temperature.

3.4. Electrochemical performances

Half cells were assembled and their performances are reported in **Table 38** and plotted in **Figure 68**. The values in the table is the average between at least two reproducible cells.

3.4.1. First cycle

The reversible capacity during the first cycle C_{rev} lies between 231 to 274 mAh.g⁻¹, for HC-coffee-260 and HC-apple-220 respectively, and the ICE between 65 to 83 %, for HC-apple-180 and HC-brewery-260 respectively. This values are in accordance with the results obtained in **Chapter 4**. and in the range of biomass-based hard carbon from agricultural residue [230]. To have a better overview of the influence of the HTC temperature on the first cycle performances, they are represented **Figure 69**.

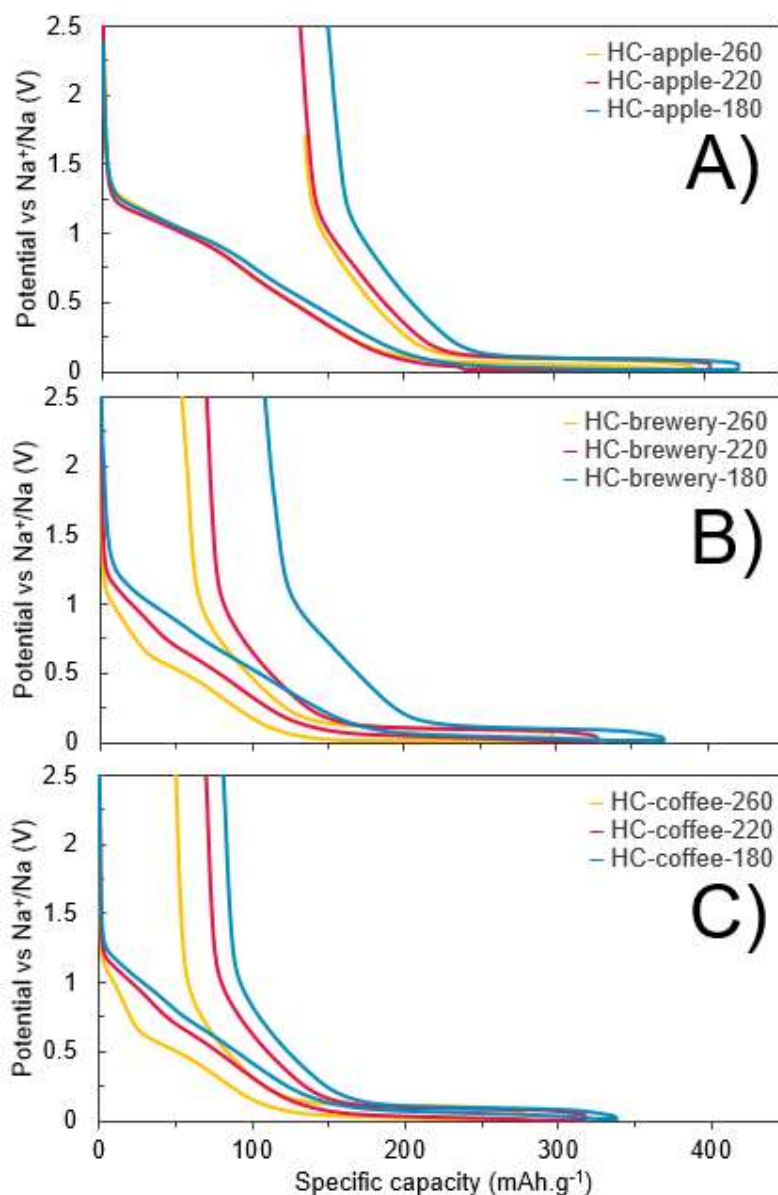


Figure 68: First reduction-oxidation profile of **A)** apple-, **B)** brewery- and **C)** coffee-based hard carbon from the hydrochar obtained at 180 °C (blue), 220 °C (red) and 260 °C (yellow) at 37.2 mA.g⁻¹. The plots are from 1 experimental cell, reproducible between replicates.

Apple-based hard carbon obtained similar ICE about 68 % no matter the HTC temperature. At the opposite, brewery- and coffee -based materials seem to have higher ICE from the 260 °C hydrochar than 180 °C. Indeed, 82 – 83 % are reached from the materials at the highest HTC temperature, while only 70 and 76 % were measured for the lowest temperature, for respectively brewery and coffee materials. As already discussed in 3.3, the surface area tends to decrease with the increase of the HTC temperature, which could explain the increase of ICE with the HTC temperature for brewery materials. Low N₂ BET SSA prevents from passivation layer formation at the surface of the electrode, and thus increase the ICE of the cell as it is widely known [22], [54], [55]. However, the ICE of the apple-based hard carbons do not seem to increase with the HTC temperature as well as the other materials. There might be a limit to its

influence, despite the important surface area decrease. At the opposite, coffee-based materials ICE increase with the HTC temperature, but not the surface area which stay similar. Only HC-coffee-260 has a higher CO₂ BET SSA with a similar N₂ BET SSA than the other coffee-based materials, which could explain its higher reversibility. However, the surface area is not the only influence parameter.

The materials with the highest reversible capacity during the first cycle are apple-based hard carbon with 270 mAh.g⁻¹ for all their materials. They also are the materials with the lowest ICEs, and the highest d₀₀₂. Gomez-Martin *et al.* [9] highlighted larger interlayer space leads to higher capacity by improving the Na intercalation.

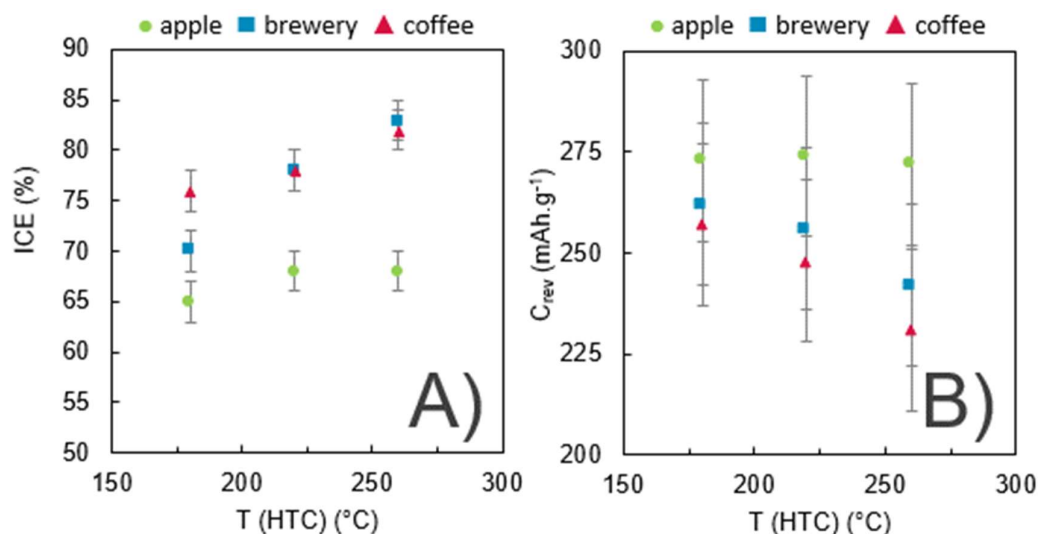


Figure 69: Impact of the HTC temperature on **A)** the ICE and **B)** C_{rev}.

The impact the inorganics have on the d₀₀₂ have been detailed in **3.2**, and on the electrochemical properties in **Chapter 4**.

To characterise the impact of the leaching on the resulting properties, C_{rev} depending on the ash and main inorganic contents of the hard carbons are represented in **Figure 70**. To prevent from the dead weight effect induced by the inorganics, C_{rev} is converted in mAh.g of C⁻¹. Despite the ashes themselves do not suggest to impact directly the reversible capacity, it seems that there is more Ca in the hard carbons with the lowest capacities. These three materials are the ones identified with CaS, which might be an obstacle for sodation by occupying the active sites [30], [118], [231]. However it should be kept in mind that this observation on these materials is not enough to conclude on a clear correlation.

Unfortunately, Si could not be measured as explained above. As explained in **3.2**, SiC is suspected in HC-brewery-180, it would be coherent to have important amount of Si in this material, which could explain its higher ash content compared to the others despite its K, Ca, Mn and Fe contents are in the same range as the other materials.

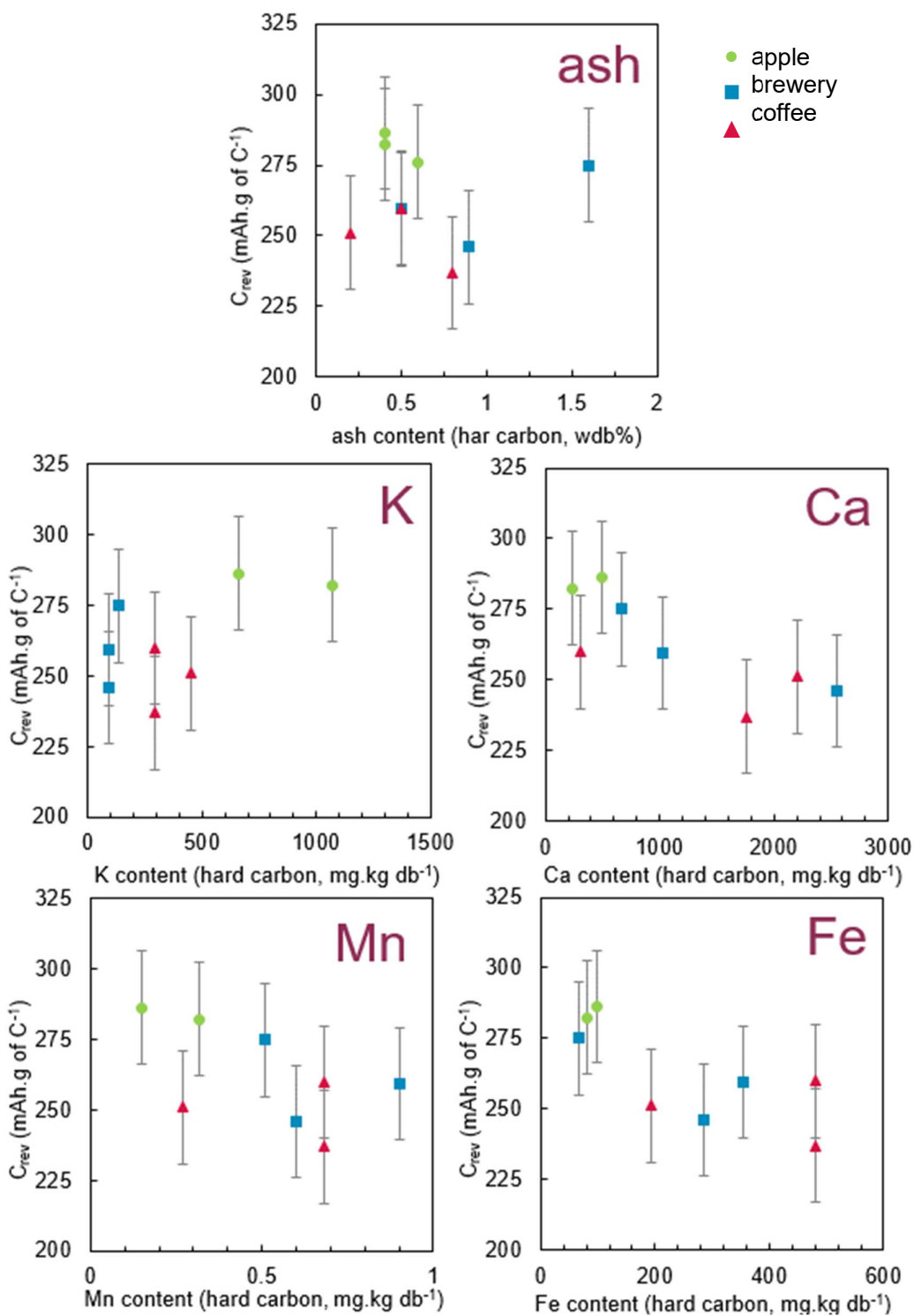


Figure 70: Impact of the ash composition on C_{rev} , considering the active mass only.

To go further on the investigation of the mechanism occurring during the cycling, the slope, plateau and irreversible capacities are measured and represented in **Figure 71**. The reduction of the irreversible reaction with the HTC temperature is highlighted, however it seems the slope contributes from 32 to 36 % of C_{rev} , no matter the temperature nor feedstock. The reduction of the irreversible capacity is in accordance with the decrease of N₂ BET SSA discussed above.

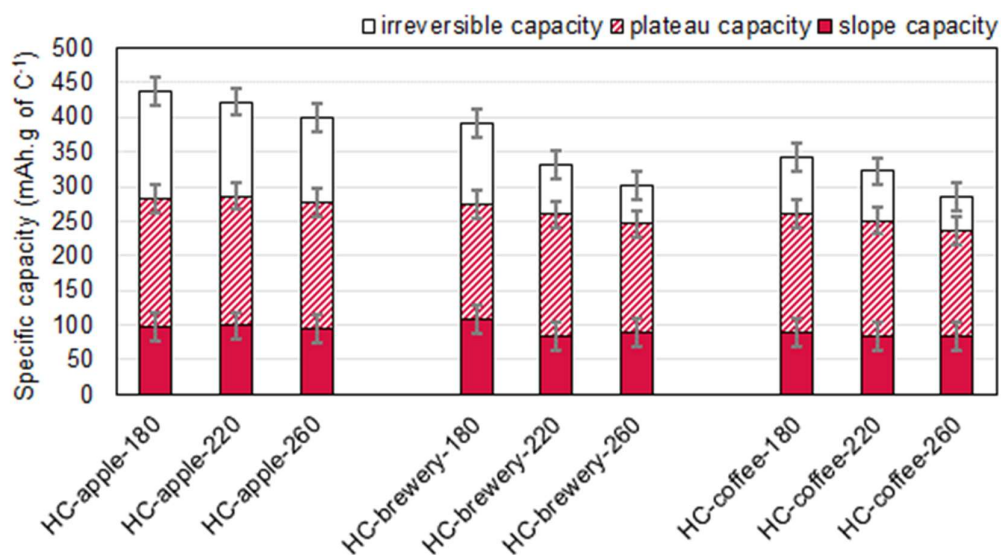


Figure 71: Slope and plateau capacities of the charge and irreversible capacity at the discharge of the first cycle. Uncertainties are from the method used.

3.4.2. Cycling behaviour

The cycling behaviour are reported in **Figure 72**. Among 100 cycles, most of the cells are very stable, with a capacity loss lower than 4 % at C-rate. After the 5th cycle, a small capacity drop occurs due to the change of current applied, from C/10 to C-rate. However the decrease is small, meaning the materials adapt well.

It worth to mention that some brewery materials highlight a capacity decrease around the 75 cycle. In a system where Na metal is used as electrode, the carbonate electrolyte might degrade and to form ethylene glycol bis-(methyl carbonate) (EGMC) that polymerise and lead to cell surcharge [232]. Furthermore, dendrites can be formed at the surface of the Na metal electrode, which results a decrease of capacity. These side reactions at low potential contributes to decrease the cell performances.

The high temperature pyrolysis leads to a disorganised carbonaceous material, reaching more than 95 wdb% of C. Most of the inorganics are removed both from the HTC leaching and the pyrolysis volatilisation, which lead to this carbon-rich material. However a portion remain in the solid, creating organised phase, identified as CaS for most of them, and increasing the surface area. The increase of the HTC pre-treatment temperature leads to a less porous material, which results a higher ICE in half-cell. It seems the pre-treatment mainly impact the surface, the d_{002} being not affected.

The final hard carbons have d_{002} between 3.7 and 3.9 Å that is favourable for Na intercalation, with surface area among the low range of the biomass-based hard carbon literature. The materials obtained show an interesting cyclability, with a coulombic efficacy reaching almost 100 % at each cycle.

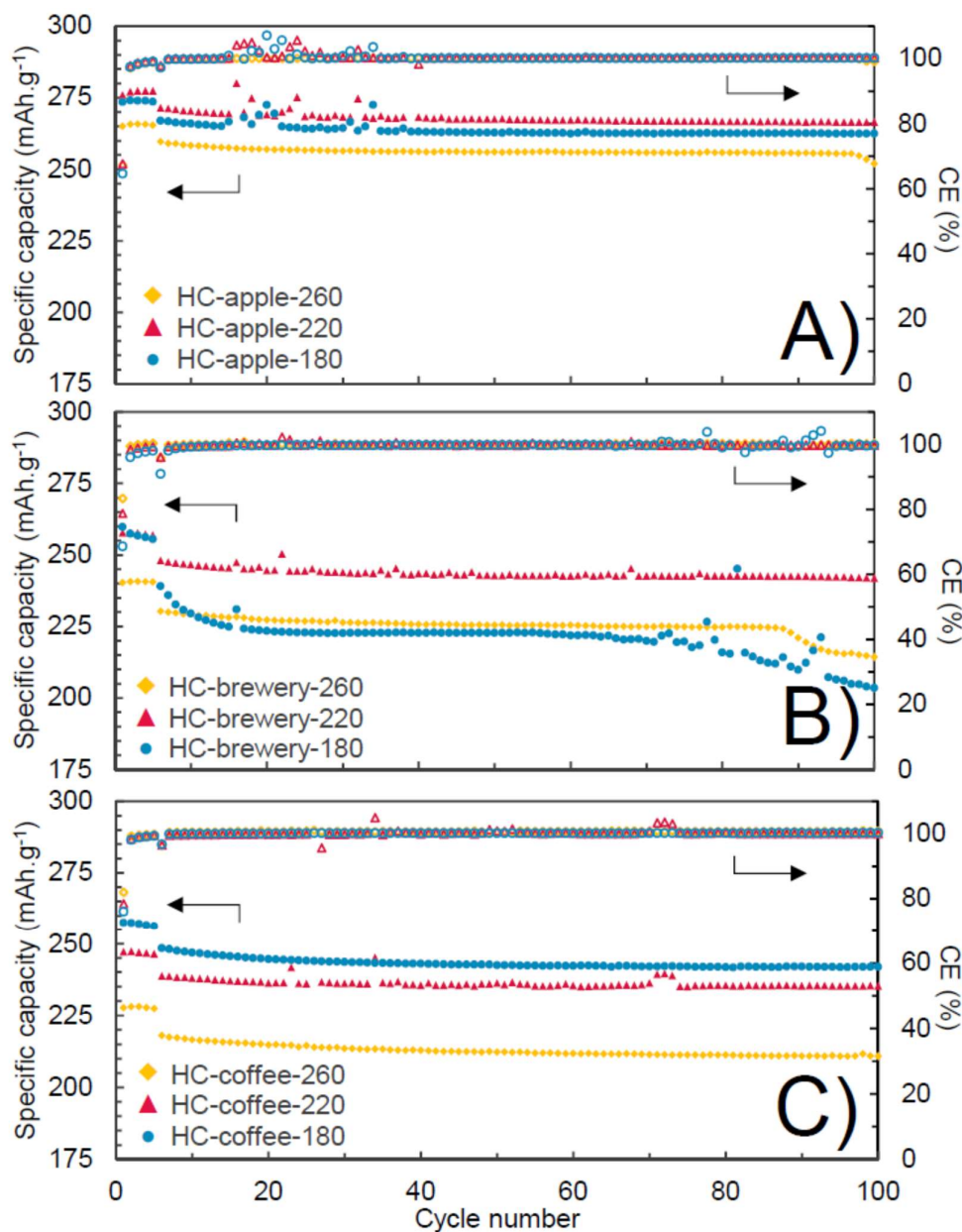


Figure 72: Cycling behaviour of **A)** apple-, **B)** brewery- and **C)** coffee-based material from the different hydrochar obtained at 180 °C (blue), 220 °C (red) and 260 °C (yellow). The 5 first cycles are performed at C/10 then at 1C until the 100th cycle (C = 372 mAh). The plots are from 1 experimental cell, reproducible between replicates.

Conclusions

During this study, the fate of inorganics during HTC have been investigated at three different temperatures on three agro-food wastes. It has been highlighted that the element behaviour is dependent both of the material used and the operating conditions. Alkali are mainly solubilised in the HTC acidic and high pressure conditions, no matter the temperature and feedstock. With the degradation of the plant cell matrix, most inorganics are released, including Ca, Mg, P or Mn, however with the increase of the

temperature they tend to react with the degradation products to precipitate and reincorporate the solid phase, leading to an increase of these inorganics in the hydrochar at higher temperature. At the same time, the temperature favours the hydrolysis and decarboxylation of the macromolecules, reducing the H/C and O/C ratio and degrading the cellulosic structure. The final product is richer in C and poorer in most of the inorganics.

After pyrolysis, part of the remaining inorganics are volatilised, leading to a hard carbon with more than 95 wdb% of C. Only the inorganic under a stable form remain, mainly CaS was identified, and a fraction might be trapped in the structure as well, preventing their release. The one volatilised might create mesoporosity, as it is the case for K as reported in literature. Their impact on the graphitisation of the material is limited: no graphite is detected, and the interlayer space is between 3.7 and 3.9 Å that lead to very interesting hard carbon performances in half cell. The materials with the best reversible capacity were found to be the ones with the highest interlayer space. The most impact the HTC temperature on the hard carbon is the specific surface area: the higher the temperature, the lower the porosity, leading to an increase of the ICE on the materials.

The impact the pre-treatment was highlighted: the increase of the HTC temperature favours the volatilisation of species that are thought to precipitate at the surface of the hydrochar, and reduces the amount of inorganics catalysing graphitisation. The resulting materials along this thesis are promising due to the high cyclability and high capacities of some of them. However, it is interesting to determine the impact the HTC pre-treatment has on the hard carbon compared to direct pyrolysis. This problematic is investigated on the following chapter.

Chapter 6

Hydrothermal carbonisation vs. pyrolysis as pre-treatment in biomass-based hard carbon synthesis for negative electrode in Na-ion battery: comparison of the two processes

In this chapter, the influence of the HTC is investigated: a complete characterisation of the raw material, hydrochar and hard carbon is performed in order to understand the advantages and drawbacks of the pre-treatment. To compare its impact, in parallel, a two-steps pyrolysis will be performed on the same raw materials and each intermediate and final materials will be compared, both on their compositions and structures. At the end, the hard carbons will be formulated into electrodes and the electrochemical performances will be compared, and linked to the material properties.

1. Experimental campaign settlement

In the previous chapters, the importance of the leaching during HTC have been investigated, as well at its impact on the resulting hard carbon. The importance of the inorganics on the graphitisation reduces the choice among the biomass for electrode production, which was already limited due to low moisture content required for the process. The very promising performances obtained in the previous chapters, especially on driftwoods and agro-food wastes, shows that it is possible to valorise wet biomass for energy storage application. But no evidence of the improvement of the HTC compared to the standard direct pyrolysis was performed. Some studies compare them, however they mainly use one material under various HTC conditions, and compare with a direct-pyrolysis material. Their studies are mainly focused on the HTC, and not on the advantages and drawback of each process [119], [120], [122], some studies go further on their investigations on biomolecules, such as glucose [233]. Furthermore, the inorganic aspects is often put aside, and the morphology and structure are displayed. It has to be kept in mind that many studies compare hydrochar and pyrochar from lignocellulosic wastes [96], [234], but they focus on the biochars only and do not synthesize hard carbon.

To fill this gap, two pre-treatments are compared: HTC and a low temperature pyrolysis, providing respectively a hydrochar and a pyrochar. Often, the product from pyrolysis is called biochar, however this term is also used for all biomass products after thermal treatment, which is the case of this study. No direct pyrolysis is performed due to the equipment constraints toward the gas released from raw biomass at such temperature.

Four materials are selected and are going to follow two processes: a HTC in one hand followed by a high temperature pyrolysis, and a two-step pyrolysis on the other hand. To avoid the drying step required for the two-step pyrolysis, three of the feedstock are dry, they were selected due to their various composition, mainly their ash contents: oak bark, softwood and walnut shell. The last one is wet feedstock, a driftwood. The selected genera was conifer (wet), to determine the potential influence of the time spent in water in the physico-chemical properties of the materials compared to the dry softwood of this study.

The HTC conditions are similar to the previous chapters: to favour a microporosity, a long residence time of 10 h is chosen, as well as a medium temperature of 220 °C. The low temperature pyrolysis was performed at 450 °C and the maximum temperature was held for 20 min. The high temperature pyrolysis providing the hard carbon is performed at 1400 °C for 1 h and then electrodes are formulated, in accordance with the previous chapters.

Both hydrochar and pyrochar were characterised, their structures and composition, as well of the resulting hard carbons and the raw materials. The experimental campaign is summarised in **Figure 73** and the nomenclature of the materials are detailed in **Table 13**.

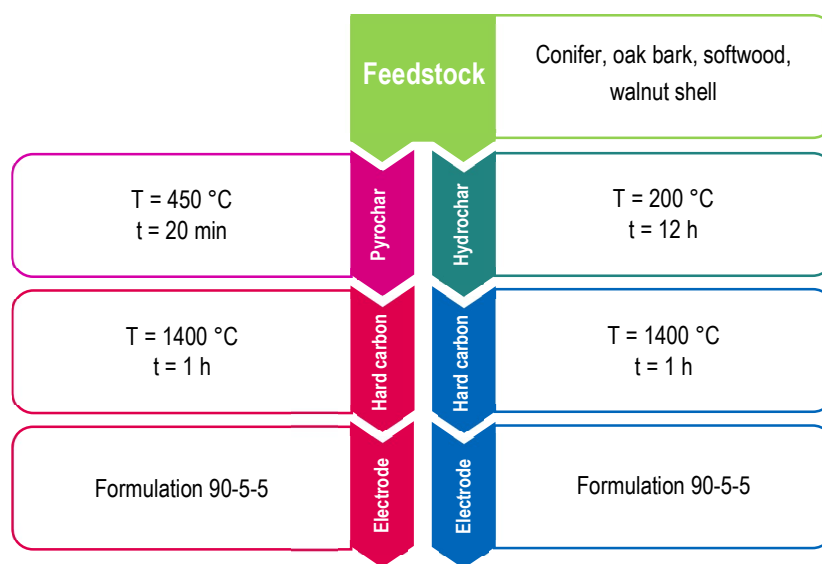


Figure 73: Experimental campaign.

Table 39: Nomenclature of the materials for the genera influence study.

Feedstock	Raw	From pyrolysis		From HTC	
		Pyrochar	Hard carbon	Hydrochar	Hard carbon
Conifer, driftwood (wet)	conifer	p-conifer	HC-p-conifer	h-conifer	HC-h-conifer
Oak bark	oak_bark	p-bark	HC-p-bark	h-bark	HC-h-bark
Softwood (dry)	softwood	p-softwood	HC-p-softwood	h-softwood	HC-h-softwood
Walnut shell	walnut_shell	p-shell	HC-p-shell	h-shell	HC-h-shell

2. Influence on the biochar

The elemental and ash composition of the raw materials and biochars are reported in **Table 40** and **Table 41**, the macromolecule composition of the raw biomasses are reported in **Table 42**.

2.1. Raw biomass composition

The raw biomasses compositions have already been discussed in **Chapter 4**, the main characteristics are summarised as follow. They are mainly composed of C, between 47.7 and 52.6 %, which is coherent with literature on similar feedstock [118]. The cellulose content is the highest in the stems, reaching 40 % of the macromolecular composition while the two other materials are twice less concentrated. By opposition, they are richer in lignin, known to give rigidity to the structure due to its strong bonds [74], [75]. These observations are coherent with can be found in literature on similar feedstock [79]. The two soft woods are very close in macromolecular composition, which is expected. The extractive contents is lower in the driftwood, conifer, which could come from the loss of some water-soluble compound during the time spend in the river before being collected, however the contents are low in both. While the wood stems have similar ash content of 0.6 and 0.7 wdb%, oak_bark have a higher content of 9.6 wdb%, which is characteristic from this part of the tree. Oak_bark has the highest Ca content of 31000 mg.kg db⁻¹ compared to the others where it is between 780 and 1700 mg.kg db⁻¹. Similarly, Si is the second highest element in the woods, reaching 5450 mg.kg db⁻¹ in the bark. Walnut_shell, unlike the woods, is richer in K with 4150 mg.kg⁻¹ which is twice higher than oak_bark, the second more concentrated.

Table 40: CHNS and ash contents of the raw biomass and biochars and solid yield of the reactions. The S content was below the limit of detection of 0.3 w% for all the samples and not reported in the table. The solid yield SY is calculated according to equation (8).

	SY (%)	Organic composition (wdb%)				Ash (wdb%)
		C	H	N	O*	
conifer		47.4 ± 0.4	6.7 ± 0.1	0.22 ± 0.02	49.9	0.7 ± 0.1
p-conifer	30 ± 1	77.3 ± 0.1	3.9 ± 0.1	0.28 ± 0.03	17.5	1.6 ± 0.1
h-conifer	52 ± 1	67.5 ± 0.3	4.8 ± 0.1	0.43 ± 0.03	27.3	0.2 ± 0.1
oak_bark		47.7 ± 0.3	5.0 ± 0.1	0.49 ± 0.03	37.1	9.6 ± 0.1
p-bark	46 ± 1	60.2 ± 0.2	2.9 ± 0.1	0.71 ± 0.03	15.3	20.9 ± 0.1
h-bark	58 ± 1	57.5 ± 0.3	4.7 ± 0.1	0.63 ± 0.03	25.4	12.0 ± 0.1
softwood		50.6 ± 0.3	6.0 ± 0.1	0.15 ± 0.03	42.7	0.6 ± 0.1
p-softwood	28 ± 1	75.7 ± 0.3	3.7 ± 0.1	0.30 ± 0.03	18.9	1.4 ± 0.1
h-softwood	54 ± 1	68.1 ± 0.2	4.7 ± 0.1	0.35 ± 0.03	26.8	0.1 ± 0.1
walnut_shell		52.6 ± 0.3	6.3 ± 0.2	0.79 ± 0.03	38.6	1.7 ± 0.1
p-shell	32 ± 1	74.2 ± 0.1	3.8 ± 0.1	1.24 ± 0.03	15.7	5.0 ± 0.1
h-shell	52 ± 1	68 ± 1	6.0 ± 0.1	1.08 ± 0.03	24.6	0.5 ± 0.1

* Calculated by difference

2.2. Biochars organic composition

After the thermal process, the biochars have a higher C and N content and a lower O and H content than the raw materials, as expected. However, hydrochar H, N and O contents are higher or equal to pyrochars' content, at the opposite of the C contents that are higher in the pyrochars than hydrochars. During both HTC and pyrolysis, dehydration occurs, which results a loss of H₂O. Furthermore, the decomposition of

the biomass macromolecules leads to smaller molecules such as furfurals, 5-(hydroxymethyl) furfural (HMF), organic acids for HTC; phenols or oligomers for pyrolysis [96]. These smaller molecules end in the liquid phase or are volatile, for HTC and pyrolysis respectively. The SY is higher for all HTC experiments compared to their pyrolysis analogues, however, the resulting C content is higher in the pyrochars, meaning there is a better carbonisation of the material. The carbonisation is not complete under these conditions, which explain why the C content are lower than 80% for pyrochars and 70% for hydrochars.

Similar trend was observed by Azzaz et al [234] from olive mill by-products. They compared both hydrochars and pyrochars obtained in the range of temperature than this study, and reported also pyrochars with higher C content, however they reported C contents higher than 90 wdb% on their pyrochars obtained from 400 to 600 °C, which is much higher than the range of our study that do not reach 80 %. At the opposite, Wang et al [235] observed higher C contents on their hydrochar obtained from napier grass at 200 to 240 °C for 2 h than in their pyrochars at 300 and 500 °C. While their materials were composed from 47 to 57 w% for their hydrochars, their pyrochars were composed from 45 to 49 w%. The reaction mechanism is widely dependent of the operating conditions and feedstock [91], [236], which could induce such differences.

2.1. Biochars inorganic composition

The ash contents is systematically higher in the pyrochars than in the hydrochars and raw materials. It is indeed known thanks to the previous chapters that inorganics leach during HTC, leading to a decrease of the ash content for raw materials having less than 6 wdb% of ash. To understand better what happen during both reaction, the balance of the inorganics that remains in the biochars are represented in **Figure 74**, obtained by equation (9).

It is obvious in **Figure 74A**) that almost all the inorganics stay in the pyrochar. Their volatilisation are highly temperature dependent: for exemple K and Si are partially released above respectively 700 and 500 °C [91], which is higher than the temperature of 450 °C used in this study. Also, interactions between the material and the elements can prevent from their volatilisation, as it is the case for K that can be stuck by phenolic or carboxyl group or intercalated in the char matrix [237]. At such temperature, it is expected to have no or very low volatilisation due both to the temperature [160] and to some elements that might be trapped in the structure.

At the opposite, most of the inorganics tend to leach during HTC as highlights **Figure 74B**), especially Mg, K and Na where only less than 25 % remains in the hydrochar, when Al and Si mostly remains completely. Ca and Fe seems feedstock dependent: less than 25 % of Ca remains in the hydrochars except for h-bark with 84 %, while about 15 % of Fe remains in h-conifer and h-softwood, 55 % in h-shell and 99 % in h-bark. It is attributed to the more or less available form and water-soluble properties the inorganics might be in the biomass. These leaching behaviour of these four materials was already widely explained in **Chapter 4**.

Table 41: Composition of the raw biomass and biochars in major elements and ash in w% and solid yield of the reactions. The S content was below the limit of detection of 0.3 % for all the samples and not reported in the table. SY refers to the solid yield in %, it is the massic ratio of the final biochar on the the initial raw biomass.

	Inorganic composition (mg.kg db ⁻¹)							
	K	Na	Ca	Mg	Si	Al	Mn	Fe
conifer	56 ± 1	18 ± 1	1680 ± 20	109 ± 1	350 ± 30	33 ± 2	4.2 ± 0.1	60 ± 2
p-conifer	173 ± 4	40 ± 1	5490 ± 30	352 ± 9	900 ± 100	75 ± 10	14 ± 1	210 ± 60
h-conifer	7 ± 3	7 ± 2	225 ± 10	16 ± 1	500 ± 100	74 ± 1	0.74 ± 0.05	19 ± 1
bark	2250 ± 50	55 ± 3	31100 ± 400	620 ± 2	5450 ± 130	390 ± 10	373 ± 3	420 ± 20
p-bark	5230 ± 80	122 ± 20	57992 ± 12000	1417 ± 20	20400 ± 2600	1090 ± 10	740 ± 6	910 ± 10
h-bark	410 ± 20	27 ± 5	41000 ± 1400	115 ± 7	5300 ± 300	840 ± 20	172 ± 8	719 ± 30
softwood	580 ± 40	14 ± 1	790 ± 40	140 ± 10	126 ± 10	26 ± 4	62.1 ± 0.7	31 ± 8
p-softwood	2200 ± 200	40 ± 4	3100 ± 300	550 ± 50	6630 ± 3200	81 ± 8	210 ± 20	100 ± 10
h-softwood	68 ± 6	2 ± 3	110 ± 10	19 ± 2	230 ± 20	61 ± 1	9 ± 1	9 ± 1
shell	4150 ± 200	600 ± 30	1700 ± 50	436 ± 3	380 ± 40	38 ± 2	16 ± 1	430 ± 30
p-shell	13300 ± 300	1900 ± 100	5440 ± 300	1360 ± 40	1215 ± 200	136 ± 2	50 ± 8	2100 ± 1100
h-shell	730 ± 90	110 ± 10	700 ± 320	100 ± 20	500 ± 200	95 ± 5	7 ± 3	450 ± 40

Table 42: Sugar monomer and macromolecule composition of the raw biomass.

	Sugar monomer (wdb%) (± 5 %)					Macromolecules (wdb%) (± 5 %)			
	Glucose	Xylose	Manose	Galactose	Arabinose	Cellulose	Hemicelluloses	Lignin	Extractives
Conifer (wet)	43.39	7.05	12.42	2.42	1.14	40.40	29.27	27.65	2.90
Oak bark	20.06	10.22	0.00	1.22	1.83	20.06	17.45	30.29	16.16
Soft wood	43.46	5.59	11.17	1.67	0.98	40.77	26.06	26.48	4.11
Walnut shell	21.90	15.72	1.00	1.25	0.62	20.90	25.28	31.98	13.82

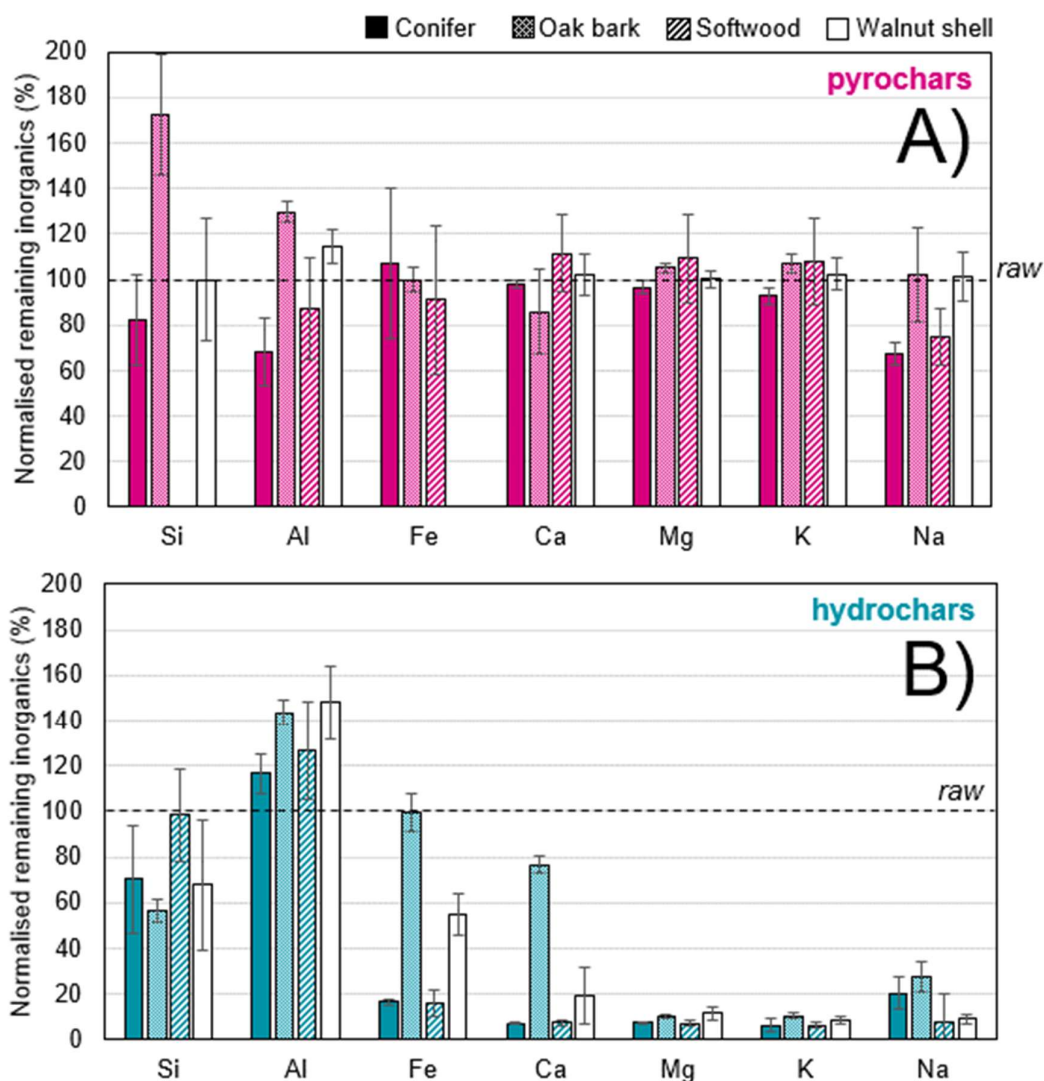


Figure 74: Normalised remaining inorganics in % of the major elements in **A)** the pyrochar and **B)** the hydrochar for the 4 biomasses. They were calculated according to equation (9). Standard deviations are experimental.

2.2. Structure

XRD patterns of the materials are reported in **Figure 75**. It is well known that the raw biomass are mainly composed of cellulose, hemicellulose and lignin where only cellulose has a semi crystalline structure visible by XRD [71]. As expected, all precursor show broad peaks at 14.99° , 16.49° and 22.78° which confirms the presence of crystalline cellulose. After reaction, the biochars do not exhibit this pattern, highlighting the degradation of this crystalline phase. The same phenomenon was already described in the previous chapters for hydrochars. During pyrolysis with the increase of the temperature, the macromolecules start to be depolymerised and condense, before being devolatilised and carbonised, leading to their complete degradation at about 400°C respectively [92]. Hence, the pyrolysis in this study being at 450°C , it is coherent to not find any of the cellulosic pattern in the pyrochars.

However, the broad peaks seem softer in pyrochars, it was highlighted thanks to the C contents that they were more carbonised. The angular shape in the hydrochars' pattern could come from an incomplete degradation of the cellulose. It is indeed known that 220 °C is not enough to fully degrade cellulose, as highlighted in **Chapter 3**.

Oak_bark also shows sharp peaks that highlights the presence of crystalline phases, identified as whewellite $C_2CaO_4.H_2O$ (PDF 00-020-0231) and quartz SiO_2 (PDF 00-003-0427). It is very coherent with the material composition already discussed in section **2.1**, which is rich in Ca and Si. These peaks are also present in the biochar's patterns, which means these species remain in the material even after the thermal process. Although, the peaks are more intense in the pyrochar than the hydrochar that highlights more of these phases coherent with the higher content of these inorganics due to the low volatilisation. As already mentioned in **Chapter 3** and **Chapter 4**, calcium oxalates and silicon oxide are common in bark and gives rigidity, as much as and silica minerals [79], [238]. They are not soluble in water, and don't seem degraded in these reaction conditions, thus they remain in the hydrochars. Regarding pyrolysis, Volpe et al [35] observed that Ca oxalate requires temperature about 700 °C to decompose under inert atmosphere, which is higher than the temperature of this study. SiO_2 is also reported to not degrade at 450 °C on lignocellulosic materials as teak bark saw dust or rice husk [239]. Higher temperature are required to decompose it, as observed Saavedra et al [130]. On their four lignocellulosic materials, each containing SiO_2 , they noted the presence in their final materials after pyrolysis at 450, 1000 and 1200 °C but not at 1400 °C. In addition to the compounds already present in the raw material, p-bark presents another crystalline structure identified as calcite $Ca(CO_3)$ (PDF 01-083-1762). It is naturally present in traces in marine algae, beechwood chips or switchgrass [79], several studies also reports this carbonate in pyrochars [130], [239]–[241]. Furthermore, calcite is identified as a decomposition product of whewellite under inert atmosphere, forming $CaCO_3$ and CO from 374 to 550 °C [162]. The calcite found in p-bark might be already present in the raw material but in too low quantity to be observed on the XRD pattern, or be induced by the calcium oxalate decomposition.

Both reactions have a different impact on the biochar: while HTC decreases the inorganic contents, pyrolysis tends to carbonize better the material. They lead to different materials, on the one hand, the hydrochar still shows partly its original lignocellulosic structure, and on the other hand, the pyrochar keeps the inorganic crystalline species.

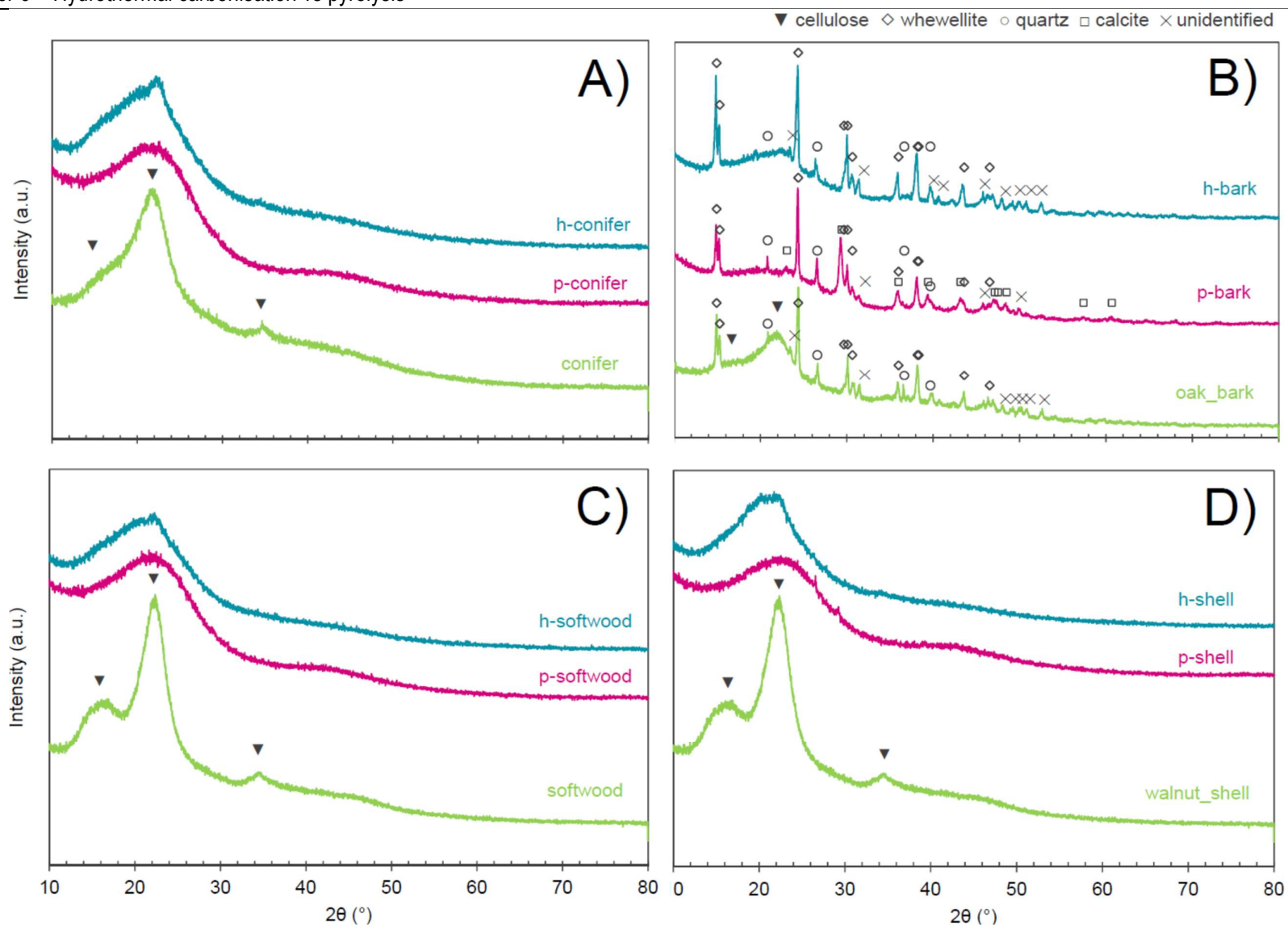


Figure 75: XRD patterns of the raw materials (green), pyrochar (pink) and hydrochar (blue) of **A)** conifer, **B)** oak bark, **C)** softwood, **D)** walnut shell. Peaks are identified as ▼ Cellulose- β ($C_6H_{10}O_5$)_n (PDF 00-060-1502), ◇ $C_2CaO_4 \cdot H_2O$ whewellite, syn (PDF 00-020-0231), □ $Ca(CO_3)$ calcite (PDF 01-083-1762) and ○ SiO_2 silicon oxide quartz (PDF 00-003-0427), and × unidentified.

3. Influence on the hard carbon properties

3.1. Composition of the hard carbons

Both hydrochars and pyrochars were then pyrolysed in the same conditions in order to obtain hard carbon to make electrodes. As described in *part 2*, their composition are different, mainly in terms of C and ash content. The compositions and yields of the hard carbons are reported in *Table 43*.

This high temperature step allows an almost complete carbonisation, with materials composed of more than 90 % of C, (up to 97 % for conifer and softwood materials). Both HC-p-bark and HC-h-bark have lower C contents of 80.1 and 82.3 % respectively, this observation is similar with the biochars compositions. HC-p-shell have a lower C content than HC-h-shell of about 5 %, which is balanced by a higher ash content. These very high C contents are coherent with biomass-based hard carbon composition [30], [118].

Ash contents increase after high temperature pyrolysis for all materials. It can be the result of a concentration of the metallic compounds, the organic matter being decomposed [30]. The ash contents in the hydrochar-based hard carbon are always lower than their pyrochar-based analogues, as it was expected due to the leaching of inorganics during the HTC step. However, no balance is represented at the opposite of the previous part, due to the very low quantities leading to uncertainties higher than the values after calculations. Some measures couldn't be performed due to the very small amounts of material: HC-p-softwood and HC-p-shell.

While almost all the inorganics remained during the low temperature pyrolysis, at 1400 °C the heat allow the volatilisation of part of them, as described in the previous chapters. Especially, the alkali and earth alkaline metals are reported to leave the material at temperature starting 700 °C [36], [39], as well as some heavy metals at higher temperatures [39]. The remaining inorganics at the end of the thermic treatment are either present as a stable compound, or thought to be trapped in the carbon matrix, creating defects on the structure and inducing local graphitisation, as explained in the previous chapters.

Pre-carbonisation is usually a step added for technical issue. During biomass pyrolysis an important amount of tar is released, splitting the thermal step in two allow to reduce the volatile species for the final pyrolysis [6], [11]. It also allow to reduce the volume of the sample and increase the C yield. At the industrial scale, it is more convenient to perform a direct pyrolysis, which is often the case in the literature. Hence, HTC pre-treatment is usually compared to direct pyrolysis instead of the two-steps. For this reason, to our knowledge no study compare these two pre-treatments.

3.2. Structure of the hard carbons

To complete this observations and determine both the inorganic compounds and the structural parameters, XRD and TEM are performed and reported in *Figure 76* and *Figure 77* respectively.

Table 43: Composition of the hard carbons and yields of the synthesis. The uncertainty comes from the standard deviation between the replicates. SY the solid yield of the last step in % is the massic ratio of the final hard carbon on the the initial raw biomass, while yield is the chemical yield, calculated by equations (7) and (8). nd stands for no data.

	SY (%)	Yield (%)	Organic content (w%)					Ash (wdb%)	Inorganic content (mg.kg db ⁻¹) (±10%)				
			C	H	N	S	O*		K	Na	Ca	Mg	Si
HC-p-conifer	70 ± 1	38	97.4 ± 0.3	0.3 ± 0.1	0.2 ± 0.03	0.07 ± 0.01	0.0 ± 0.8	2.16 ± 0.06	248	5	6943	4	2273
HC-h-conifer	50 ± 1	47	97.9 ± 0.3	0.3 ± 0.1	0.3 ± 0.03	0.10 ± 0.03	0.2 ± 0.9	1.2 ± 0.3	41	10	2761	27	656
HC-p-bark	60 ± 1	46	80.1 ± 0.2	0.16 ± 0.06	0.18 ± 0.01	<0.3	0 ± 1	21 ± 1	1049	4	76300	< 0.4	15250
HC-h-bark	46 ± 1	46	82.3 ± 0.3	0.7 ± 0.1	0.2 ± 0.03	0.11 ± 0.03	0.3 ± 0.8	16.4 ± 0.4	947	3	48200	0.4	8800
HC-p-softwood	71 ± 1	38	97.5 ± 0.1	0.10 ± 0.01	0.17 ± 0.04	<0.3	0.6 ± 0.3	1.7 ± 0.2	nd	nd	nd	nd	nd
HC-h-softwood	51 ± 1	53	97.5 ± 0.3	0.4 ± 0.1	0.6 ± 0.03	0.06 ± 0.01	0.7 ± 0.7	0.7 ± 0.3	175	6	1118	2.2	nd
HC-p-shell	nd	nd	94.2 ± 0.2	0.09 ± 0.01	0.23 ± 0.03	<0.3	0.9 ± 0.3	4.63 ± 0.08	11200	40	5000	8	nd
HC-h-shell	43 ± 1	42	97.8 ± 0.3	0.2 ± 0.1	0.4 ± 0.03	0.06 ± 0.01	0.0 ± 0.3	1.78 ± 0.02	1075	42	2104	< 0.2	nd

* Calculated by difference of the others

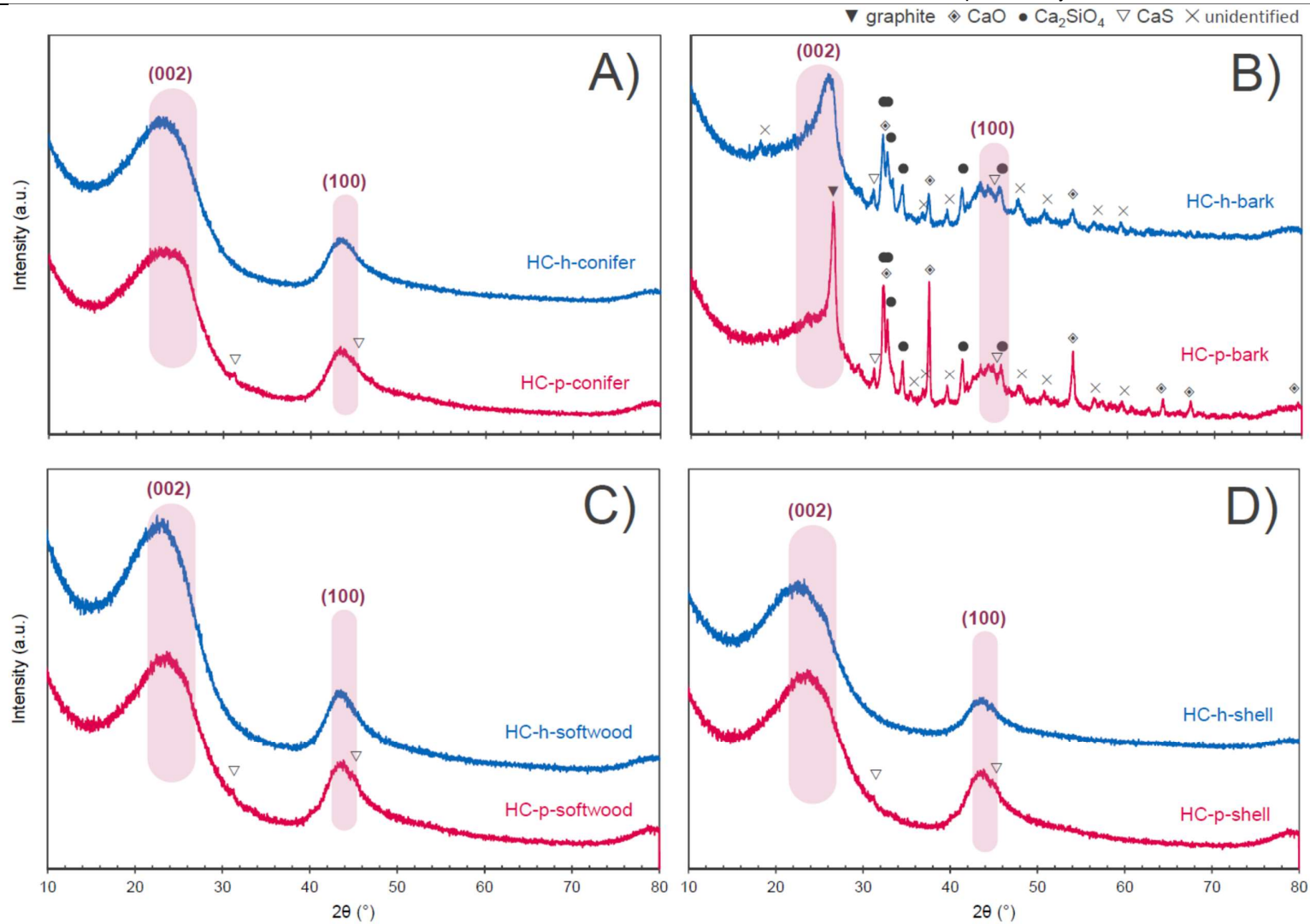


Figure 76: XRD patterns of the pyrochar-based (in blue) and hydrochar-based (in pink) hard carbons from **A)** conifer (wet), **B)** oak bark, **C)** conifer (dry) and **D)** walnut shell. Peaks are identified as ▼ C, Graphite (PDF 00-001-0640), ● Ca₂SiO₄, Larnite (PDF 00-033-0302) and ◆ CaO, Lime (PDF 00-037-1497), ▽ CaS Calcium sulfide Oldhamite, syn (PDF 04-004-3787), and × unidentified.

XRD patterns show that hard carbon have characteristic broad peaks about 23 and 41° which correspond respectively to the diffraction of the ray perpendicular to the graphene layers (002) and parallel (100). The position of the (002) peak allows to calculate the interlayer distance d_{002} which is reported in **Table 44**. The pyrochar-based hard carbon also exhibits small intensity peaks corresponding to CaS, Calcium sulfide Oldhamite, syn (PDF 04-004-3787). This product has already been reported on coal pyrolysis appearing from 700 °C, it was attributed to the degradation of the Ca compounds [226], [227].

Oak bark materials also present crystalline structures identified as Ca_2SiO_4 , Larnite (PDF 00-033-0302) and CaO, Lime (PDF 00-037-1497) which is coherent with their high amount of Ca already discussed. Lime is reported to be the final decomposition product of whewellite and calcite beyond 550 °C [161]–[163], which are indeed no longer in the hard carbon. As already described in section 2.2, SiO_2 crystalline structure is no longer in the material at 1400 °C [130], instead larnite is identified. Thy et al [242] observed the appearance of larnite at 718 °C by ashing wood ash, increasing with the temperature until 1425 °C. Compounds decomposition produces gas and activate the carbon matrix, which might allow secondary reactions to occur such as larnite production from quartz and whewellite decomposition. Interestingly, Thy et al reported the appearance of larnite in their ash product simultaneously as calcite disappeared. Peaks are more intense in HC-p-bark, highlighting the bigger amounts of these compounds in this material compared to HC-h-bark. It is coherent with the higher content observed by ICP, as already discussed.

Patterns are similar between pyrochar-based and hydrochar-based hard carbon for most of the materials, with similar d_{002} between 3.72 (HC-p-shell) and 3.88 Å (HC-p-conifer). Oak bark materials exhibit a sharp graphitic peak, which makes the d_{002} difficult to evaluate similarly to **Chapter 3** and **4**. These domains have lower interlayer distances, of 3.38 and 3.46 Å for respectively HC-p-bark and HC-h-bark. Moreover, HC-p-bark presents a sharp peak at 26.3° characteristic of graphite. As already explained in the previous chapters, recent works on lignocellulosic biomasses [30], [118] correlated inorganics such as K, Si and Ca tend to catalyse graphitisation, in accordance with HC-p-bark and HC-h-bark being rich in these three elements. Furthermore, graphene layers appear clearly on TEM pictures and highlight the disorganized structure and graphitization of the materials. The organised area are indeed bigger in oak bark materials, with longer domains made from more layers, as highlighted by the higher L_c and L_a calculated. It is coherent with the higher graphitization the XRD patterns show. Moreover, porosity is also highlighted in these two materials: the circular shape of the graphene plans highlights a closed porosity while HC-h-bark also exhibits white stains, characteristic of mesopores. Due to this, both the graphitization and porosity, oak bark materials are expected to give lower performances in Na-ion batteries than the others.

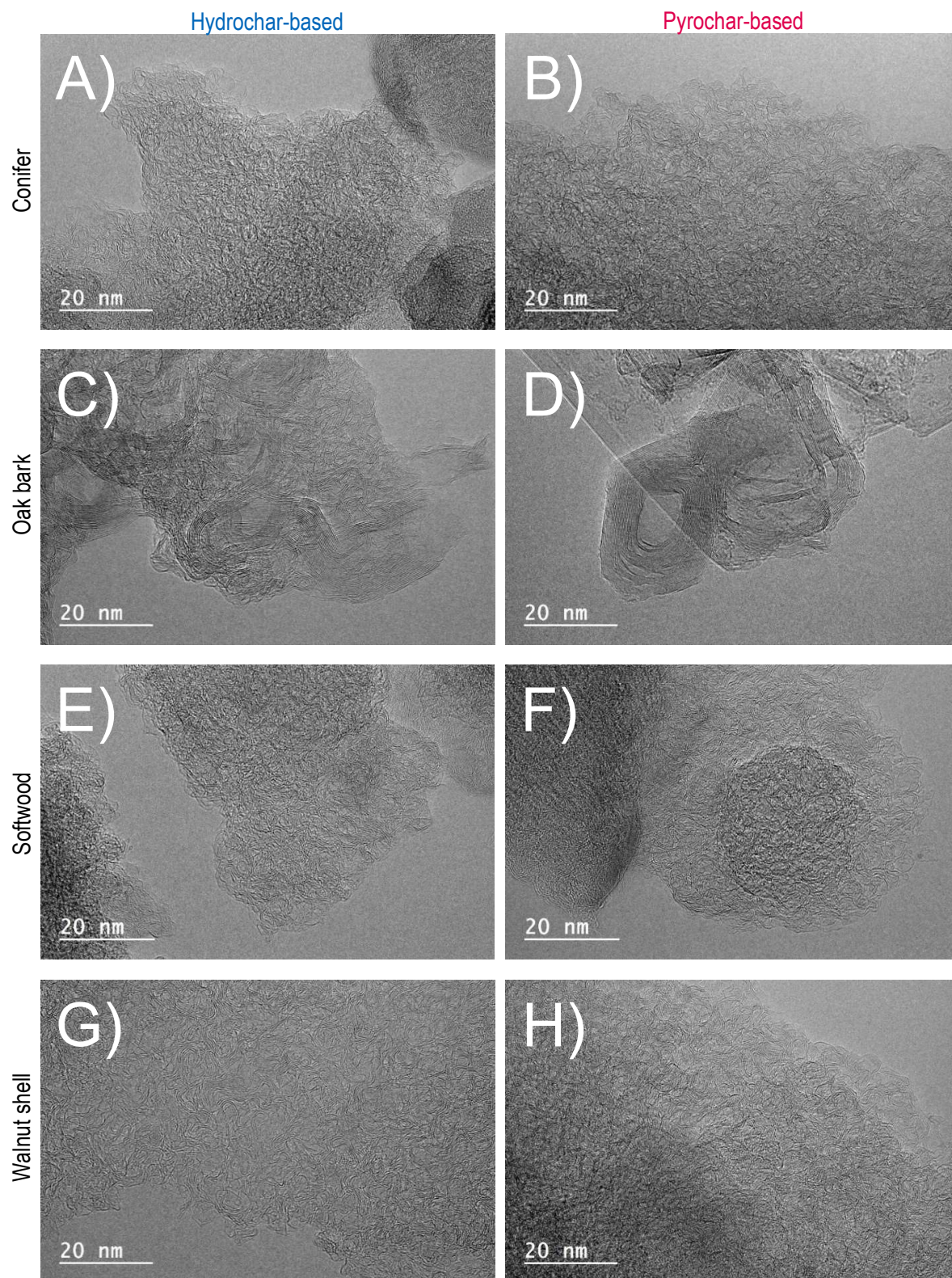


Figure 77: TEM of **A)** HC-h-conifer, **B)** HC-p-conifer, **C)** HC-h-bark, **D)** HC-p-bark, **E)** HC-h-softwood, **F)** HC-p-softwood, **G)** HC-h-shell and **H)** HC-p-shell.

Table 44: Structural characterisations of the hard carbons and electrochemical performances. d_{002} is the distance between the graphene layers. L_a and L_c are respectively the length and the depth of the turbostratic domain calculated with Scherrer equation (13). SSA is the specific surface area. C_{rev} is the first cycle specific reversible capacity. ICE is the initial coulombic efficiency and is the ratio between the first cycle reversible and irreversible specific capacity. Uncertainties are from the method and device used. na stands for non-applicable.

	d_{002} (Å) (±0.05)	L_c (nm)	L_a (nm)	N_2 SSA ($m^2.g^{-1}$) (±5 %)	CO_2 SSA ($m^2.g^{-1}$) (±5 %)	C_{rev} ($mAh.g^{-1}$) (±10)	ICE (%) (±1)
HC-p-conifer	3.88	0.17	0.34	2	10	286	84
HC-h-conifer	3.76	0.17	0.34	11	18	265	75
HC-p-bark	3.46*	2.49*	5.09*	8	6	170	68
HC-h-bark	3.38*	0.93*	1.90*	21	10	172	57
HC-p-softwood	3.77	0.15	0.31	8	13	304	79
HC-h-softwood	3.75	0.16	0.33	29	66	274	62
HC-p-shell	3.72	0.15	0.30	4	9	259	80
HC-h-shell	3.82	0.17	0.34	4	3	245	79

* value obtained from the graphitic pic symbolised by ▼ in Figure 76.

3.3. Surface area

N_2 and CO_2 BET SSA are reported in Table 44. As explained in the previous chapters, due to the smaller size of CO_2 compared to N_2 , it is adsorbed in smaller pores that highlight the ultramicroporosity (< 0.7 nm). For this reason, CO_2 BET SSA should be higher or similar to N_2 BET SSA. Yet, HC-h-bark presents a higher N_2 SSA of 21 $m^2.g^{-1}$ compared to CO_2 of 10 $m^2.g^{-1}$. While the pyrochar-based materials have N_2 and CO_2 BET SSA below 13 $m^2.g^{-1}$, the hydrochar-based have higher surface area and are feedstock dependent. The more porous material is HC-h-softwood with a N_2 BET SSA of 29 $m^2.g^{-1}$ and a CO_2 SSA of 66 $m^2.g^{-1}$. This values are in accordance with other studies lead on lignocellulosic materials, Saavedra et al [118] obtained N_2 BET SSA below 10 $m^2.g^{-1}$ and CO_2 BET SSA between 0.5 and 68 $m^2.g^{-1}$ on wood-based and walnut shell-based hard carbon from a two-step pyrolysis on the same conditions of our pyrochar-based hard carbons, values that are in the same range of the materials of this study.

Compared to direct pyrolysis, HTC pre-treatment is used to bring spherical morphology to the resulting hard carbon. During long residence time, hydrolysis products recondense in order to produce spherical secondary char at the surface of the material [95], [107], which is thought to allow fast ion and electron diffusion [233]. Moreover, Xu et al [233] observed that an HTC pre-treatment at 200 °C for 12 h on glucose-based hard carbon tend to increase the surface area while reducing the size of the pore compared to direct pyrolysis. This results are supported by Cong et al [119] from corn stalk wastes. The CO_2 SSA measured are in the range of N_2 SSA, resulting from a mesoporosity and microporosity, but few ultramicropores. Arie et al [137] deduced similar pore size between HTC pre-treated and direct pyrolysed spent tea leaves, the HTC-based materials having higher surface area.

In order to determine if the chemical composition have an impact on the surface area, the SSAs of the hard carbons depending on the hard carbons and biochar composition composition are represented in Figure 78 and Figure 79 respectively. It was suggested in Chapter 4 that inorganics have low impact on

the surface area, or that is was not the main influencing parameter. Obviously, it is coherent with what is observed here: the measured surface areas are close, making difficult any tendency to be brought out.

At 220 °C during HTC, macromolecule degradation products and inorganics tend to recondense and precipitate to form secondary char, as studied in **Chapter 5**. This smaller parts might be more available for volatilisation, which could explain this difference of surface area between pyrochar-based and hydrochar-based hard carbons. Furthermore, the gas released during their volatilisation might also activate the carbon matrix and decompose the accessible reprecipitate inorganics, leading to pore formation [11], [195].

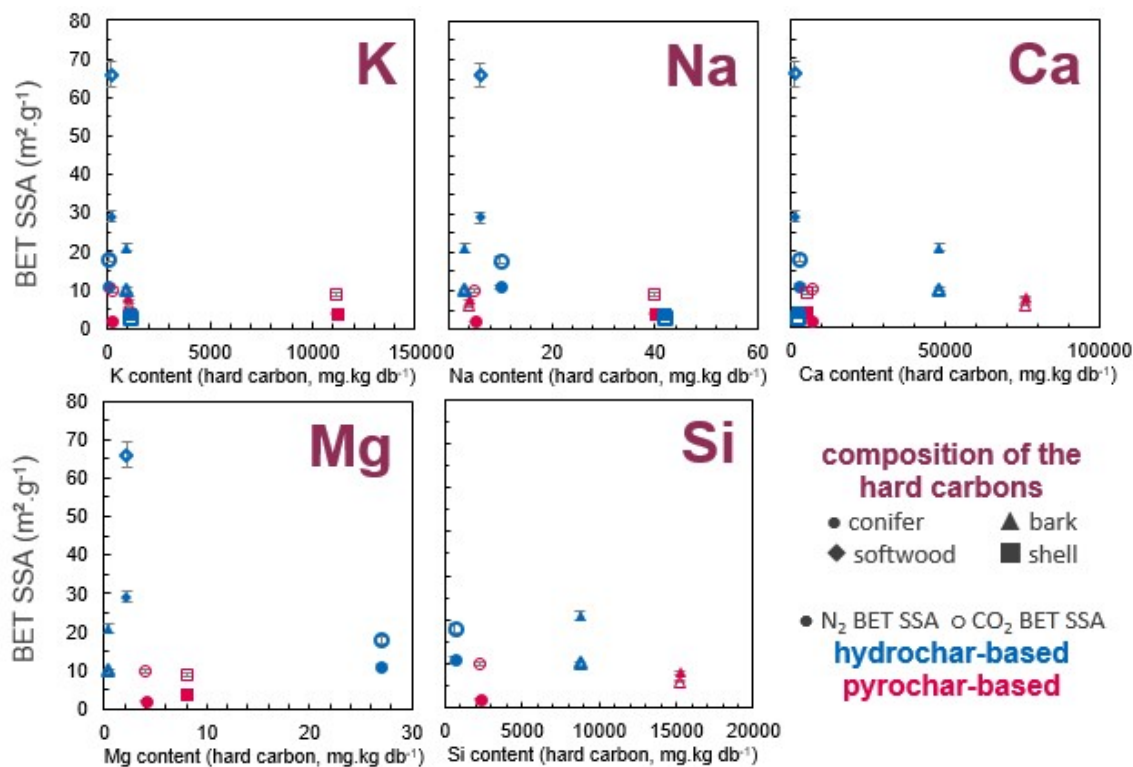


Figure 78: Influence of the inorganic contents in the hard carbon obtained from hydrochar (blue) and pyrochar (red) on N₂ (full shapes) and CO₂ (empty shapes) BET SSA.

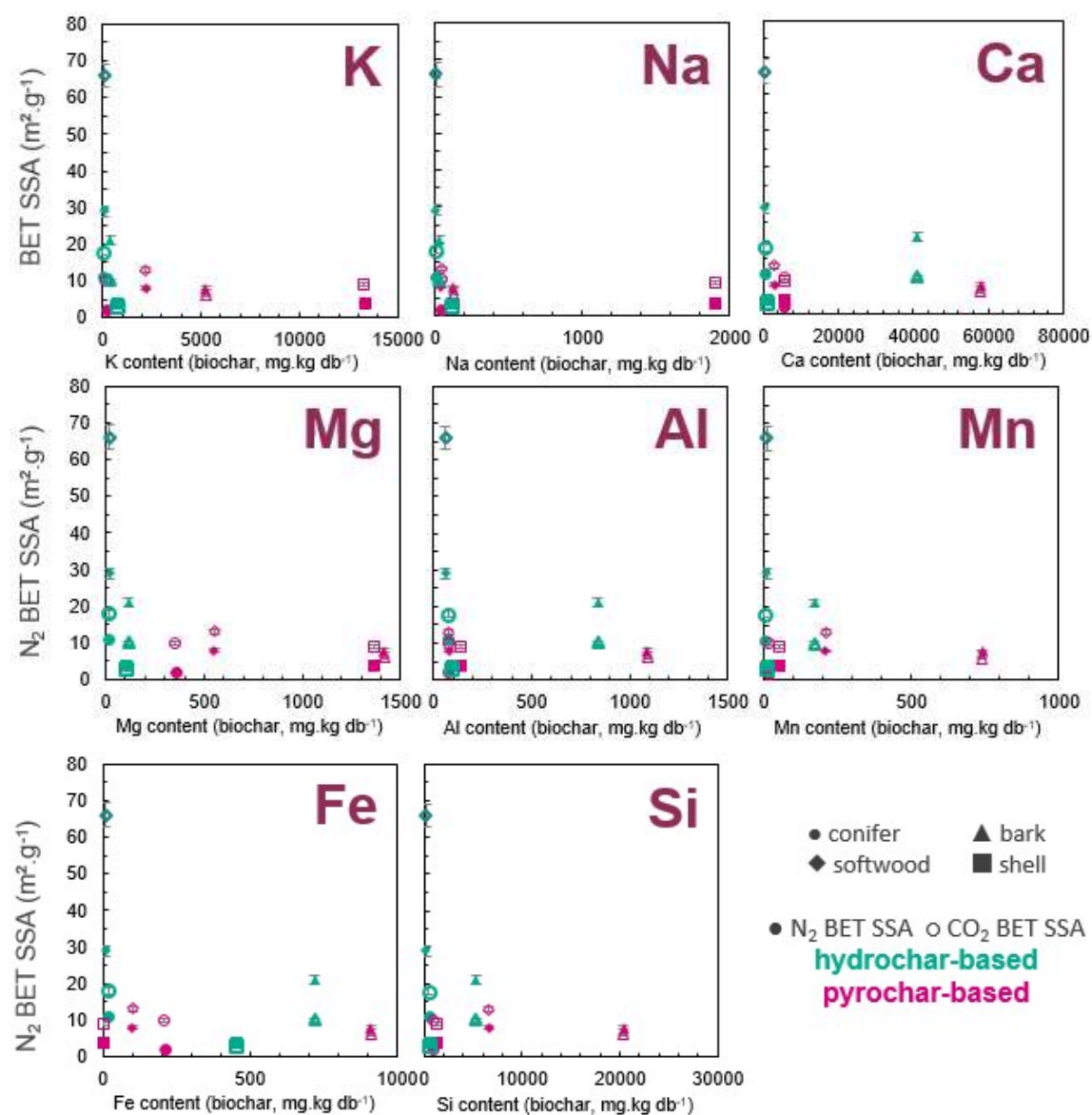


Figure 79: Influence of the inorganic contents in the biochars obtained from hydrochar (blue) and pyrochar (pink) on the ahrd carbon N₂ (full shapes) and CO₂ (empty shapes) BET SSA.

3.4. Electrochemistry

3.4.1. First cycle

Electrochemical results are shown in **Figure 80** and **Table 44**. By first having a look at the first cycle in **Figure 80**, a difference between the discharge and charge curves highlights the irreversible Solid Electrolyte Interface (SEI) formation at the surface of the electrode. This well-known phenomenon is responsible of the lower Initial Coulombic Efficiency (ICE), which is used to characterize this irreversibility. The ICE range from 57 to 84 %, for HC-h-bark and HC-p-conifer respectively. This range are consistent with literature [118]. To compare the pre-treatment influence, the reversibility of all pyrochar-based hard carbons are higher than hydrochar-based's of about 10 % for each feedstock, except walnut shell materials which have almost the same irreversibility. As explained in **3.3**, the wood-based materials

obtained after HTC have higher surface area than the ones from pyrolysis, it was then expected to obtain higher irreversibility due to the higher surface available for the SEI formation. This is confirmed by **Figure 81** that represents the first cycle performances depending on the surface area. It appears clearly that materials with the highest mesoporosity, related to the N_2 BET SSA, exhibit the lowest ICE. At the opposite, C_{rev} don't seem linear regarding to the surface area. These observations are in accordance with the previous chapters.

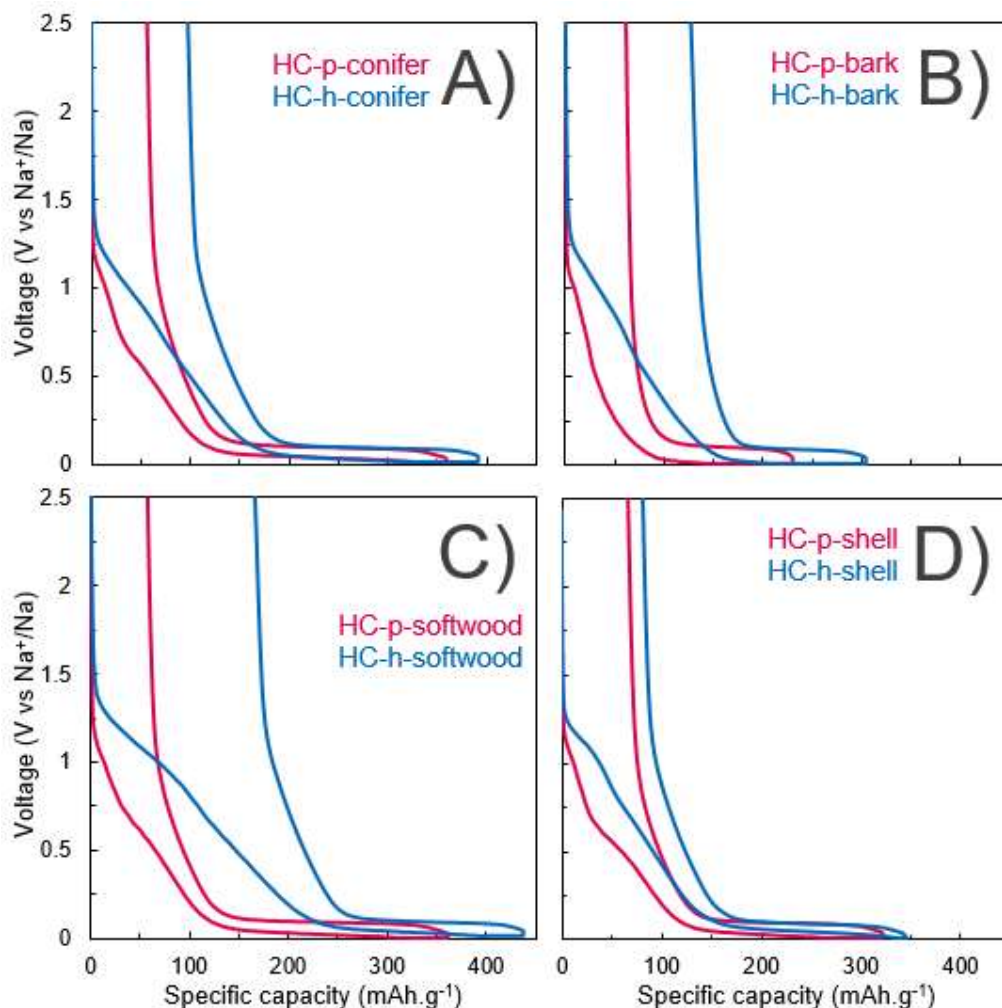


Figure 80: First reduction-oxidation profile of hard carbon from pyrochar (in red) and from hydrochar (in blue) from **A)** conifer (wet), **B)** oak bark, **C)** softwood, **D)** walnut shell at $C/10$ ($C = 372 \text{ mA.g}^{-1}$).

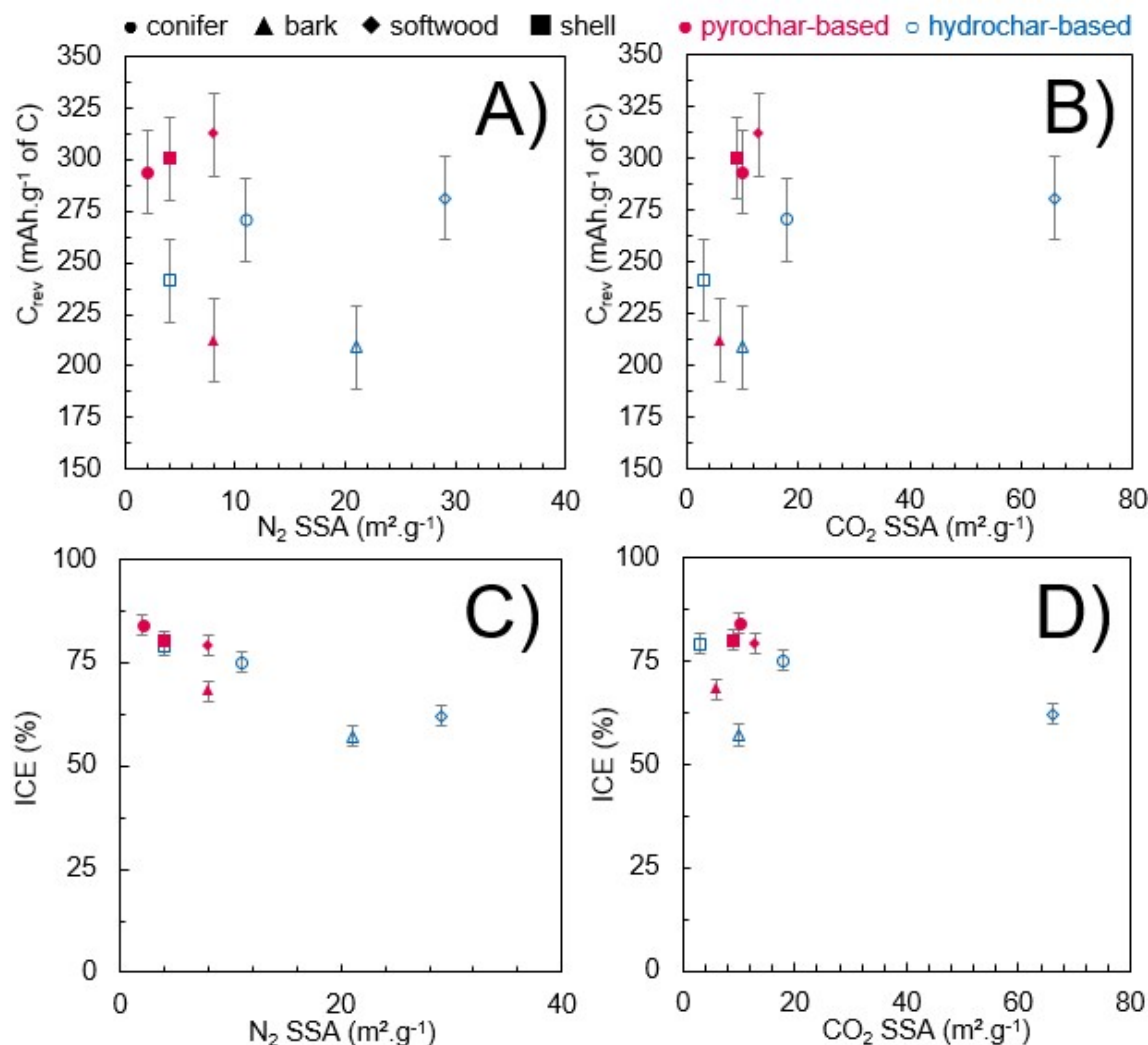


Figure 81: Influence of **A)** N₂ BET SSA, **B)** CO₂ BET SSA on the C_{rev} , and **C)** N₂ BET SSA, **D)** CO₂ BET SSA on the ICE. The pyrochar-based materials are represented in full red symbols, while hydrochars based are empty blue.

The typical pattern of the charge is composed of two areas, the slope area at high voltage and a plateau below 0.15 V vs Na⁺/Na, as explained in the previous chapters. The distribution of each area is represented in **Figure 82**. First of all, it appears clearly that oak bark exhibits a pattern different from the others: the slope between 1.25 and 0.15 V vs Na⁺/Na is steeper than the other hard carbons, highlighting a different sodation pathway than the others. All the materials exhibits a higher plateau capacity than the slope, which represents more than two thirds of the reversible capacity. However, the repartition between slope and plateau doesn't seem to have any trend regarding pyrochar-based and hydrochar-based.

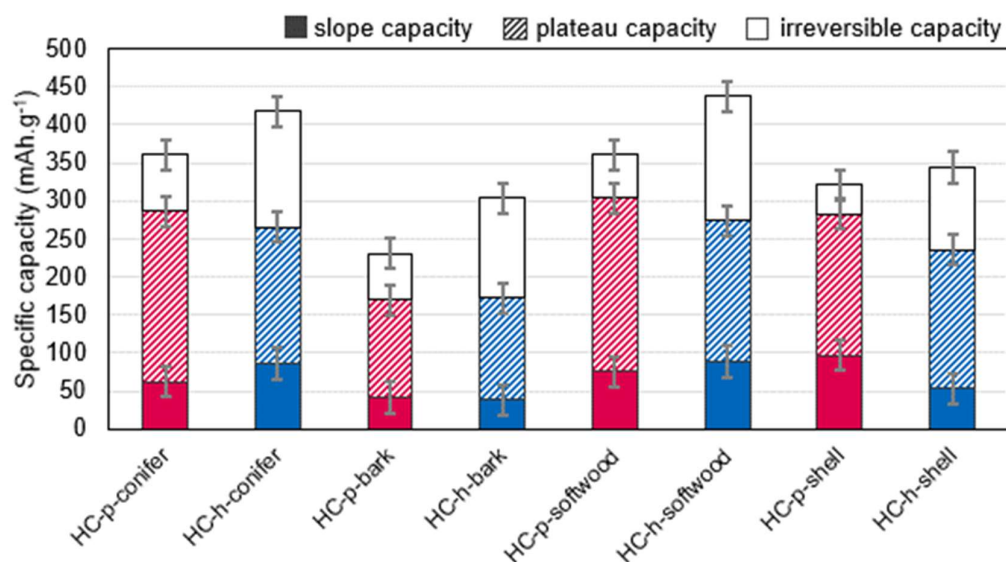


Figure 82: Slope, plateau and irreversible capacity distribution of the first cycle at $C/10$ ($C = 372 \text{ mA.g}^{-1}$).

3.4.2. Cycling behaviour

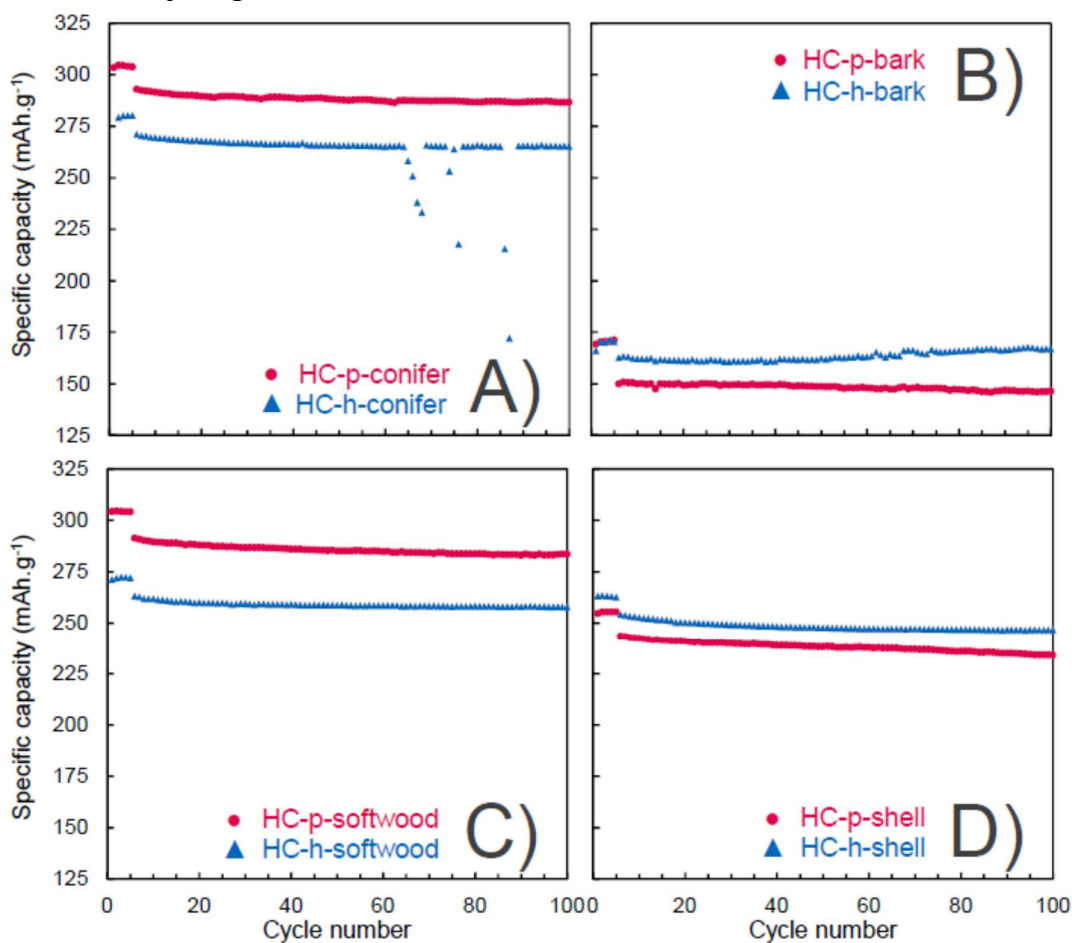


Figure 83: Cycling behaviour of hard carbon from pyrochar (in red) and from hydrochar (in blue) from **A)** conifer (wet), **B)** oak bark, **C)** softwood, **D)** walnut shell. The 5 first cycles are performed at $C/10$ then at $1C$ until the 100th cycle ($C = 372 \text{ mA.g}^{-1}$).

The cycling behaviour over 100 cycles are represented in **Figure 83**, all the materials show very good cyclability with a coulombic efficiency higher than 99% at each cycle after the 2nd, leading to a capacity loss lower than 4 % at C-rate after 95 cycles. By comparing together pyrochar- and hydrochar-based hard carbons from the same raw material, it appears there is about 20 mAh.g⁻¹ between both, with no obvious pattern. As the uncertainty of the measure from the device is ± 10 mAh.g⁻¹, this difference is not significant enough to conclude on a real impact.

Conclusions

In this study, 4 lignocellulosic residues were used to produce negative electrode for Na-ion batteries and allowed to achieve very promising performances. The HTC pre-treatment allows to reduce the ash content by leaching inorganics that would stay in the final material using only pyrolysis. In particular, it removes more than 85 % of K, Na and Mg which are present in lignocellulosic material as soluble salts. Heavy metals, by opposition, usually remain in the hydrochar. By contrast, some elements like Ca and Si seems to be more feedstock dependant: they are usually involved in structural compounds responsible of the rigidity of the material, in consequence they are difficult to remove due to their high stability. This thermal step provides a material less carbonised than by pyrolysis: less carbon, but less inorganics.

As a results, the hard carbon has indeed a lower ash content, but a difference on the graphitisation is visible only when the quantity of removed inorganic is significant: with low contents in the raw material, the d_{002} is similar. However, the main difference between the materials is the surface area: hydrochar-based materials exhibit higher N₂ and CO₂ BET SSA, leading to a decrease of 10 % of ICE compared to their analogues synthesized from pyrochar. However, the cycling behaviour doesn't seem impacted: all materials had a capacity loss lower than 4 % which mean they have a very good stability for this kind of materials.

Despite this higher surface area, HTC allows to valorise wet biomass as well, without a drying step that makes it an interesting valorisation process. It would be then interesting to optimise the surface structure by increasing ultramicroporosity instead of mesoporosity, as the same time as leaching the inorganics, to limit both the SEI formation and graphitisation. For further understanding, it could be interesting to compare the surface chemistry and functionalisation.

General conclusion

Conclusions & outlooks

During this work, several biomass from various composition have been investigated as potential raw material for Na-ion battery. This work was lead to open the possibility of feedstock for hard carbon production, as only a limited fraction of biomass suits the direct pyrolysis. This study highlighted several points, summarised and described below.

First of all, it was proven that undervalorized wet biomass such as river driftwoods could be used as precursors for Na-ion battery electrode materials with very promising performances. Moreover, they were used without any mandatory drying step compared to direct pyrolysis. However, it would be interesting to work on the influence of the particle size, and to determine any critical size or morphology.

It has been highlighted that the HTC temperature has more influence on the hydrochar composition and structure than the residence time, as reported in the literature. The heat contributes to the feedstock decomposition and secondary reactions with the intermediate degradation product, enhancing greatly the carbonisation. It was highlighted that at least 220 °C is required to significantly decompose the cellulose. As the same time, a major part of the initial K, Na and Mg leach to the liquid phase, at the opposite of heavy metals which remains in the hydrochar, no matter the temperature. At the opposite, elements as Ca, P and Si have a behaviour depending on the temperature and feedstock. During the pyrolysis, these elements remain in the hard carbon in various proportion, rending any trend difficult to deduce. However, most of them are reported in the literature to be volatilised at 1400 °C. Elements that remain in the final material react during the pyrolysis with the carbon matrix or the surrounding elements to form a stable compound, a part of them might be trapped in the matrix, preventing their volatilisation. In particular, Ca, K and Si seem to catalyse the graphitisation, while materials with high Si contents exhibit high mesoporosity. It was attributed to the formation of SiC whiskers during the pyrolysis. Hard carbons obtained after HTC at the highest temperature of 260 °C exhibit the lowest surface area, attributed to the volatilisation of the reprecipitate compounds at the surface. These parameters where highlighted to be an obstacle for good electrochemical performances. As a results, the materials pre-treated at 260 °C showed a better ICE than at 180 °C, but similar reversible capacity.

The study was focused on the pre-treatment, despite the final pyrolysis impacts greatly the resulting hard carbon. In particular, the temperature is reported to be the main factor influencing the final structure. Despite many studies reports the influence of this parameter [6], [7], [41], [43], they do not focus on the chemical composition of the hard carbon. There is a lack of investigation regarding the fate of inorganics during high temperature pyrolysis linked to electrode performances. Hence, further investigations regarding the chemical composition from hard carbons obtained in a wide range of temperature would complete this study.

Biomasses with high amount of inorganics provide graphitised hard carbon, with higher specific surface area and inorganic phases which occupy sodium storage sites and decrease the electrochemical performances of the material. Among 11 biomasses operated on the same conditions, they provide C-rich hydrochars, resulting from the degradation mechanisms and recondensation which concentrate the carbon. Inorganics leach accordingly to their solubility as described in the previous point. During the pyrolysis, an accessible fraction is volatilised while other elements reacts with the carbon matrix or their surrounding elements to form stable phases and remain in the hard carbon. These phases depend greatly of the initial composition, and contribute to porosity and structure of the final material. It has been clearly demonstrated that the negative impact the inorganic have on the hard carbon performances is indirect, regardless the leaching or not during HTC. They might reduce the sodium diffusion at the electrode, however the electrochemical properties are mainly influenced by the physicochemical properties they induce during the process, such as graphitisation and surface area.

Hard carbons both pre-treated by HTC and low temperature pyrolysis were compared, especially their composition. During the first step, pyrochars were more carbonised, however all the inorganics from the feedstock remain in the structure, unlike hydrochars, richer in H, N and O, but poorer in inorganics due to the leaching characterised above. After the final pyrolysis, hydrochar-based hard carbons exhibited higher surface area and mesoporosity, leading to ICE 10 % lower than the pyrochar-based. However, they both showed a very good cyclability, with less than 4 % of capacity loss among 95 cycles at C-rate.

To increase the performances of the materials obtained after HTC pre-treatment, the surface area must be controlled. However it still allow to use wet biomass, as well as reduce the dead weight in the electrode. It would be interesting to characterise more the surface chemistry and functionalisation to understand better the impact of the pre-treatment and resulting performances. Moreover, the main drawback seems to be the surface area, additional surface characterisation of the biochars would be interesting and might help to understand the properties observed in the hard carbons. This optimisation could be obtained by operating condition development, or by a post-treatment, for instance a washing or doping.

As mentioned in the first point of this chapter, HTC prevents from drying the material, but if an additional step is added, it might be an obstacle for industrial scale, the important amount of water resulting from HTC as well. HTC liquid is rich in organic molecules, in particular it contains 5-hydroxymethyl furfural (5HMF) from hexose degradation, which is a platform molecule. The HTC liquid is also used for biogas production via anaerobic digestion [243]–[245]. To incorporate hard carbon production in a biorefinery would diminish the environmental impact of the whole process.

Along this work, 16 biomass have been studied, and among them some provided very interesting performances in half cell. In particular wood stems, due to their low amounts in ash and lignin, allowed to obtain the best capacities. Despite this materials can be directly pyrolysed, driftwoods and their high moisture contents are excluded from this process. Hence, HTC pre-treatment an interesting option, which still need to be optimised regarding the surface area of the resulting material to provide hard carbons with better electrochemical performances.

References

- [1] U.S. Geological Survey, "MINERAL COMMODITY SUMMARIES 2021," 2021. doi: 10.3133/mcs2021.
- [2] L. Simonin, V. Simone, and S. Martinet, "Accumulateurs Na-ion : Doit-on/Peut-on remplacer le lithium ?," in *Batteries Li-ion: Du présent au futur*, D. Bloch, T. Priem, S. Martinet, and C. NGô, Eds. EDP SCIENCES (February 6, 2020), 2020.
- [3] H. Kim *et al.*, "Recent Progress in Electrode Materials for Sodium-Ion Batteries," *Adv. Energy Mater.*, vol. 6, no. 19, pp. 1–38, 2016, doi: 10.1002/aenm.201600943.
- [4] Z. Guan, X. Shen, R. Yu, Z. Wang, and L. Chen, "Chemical intercalation of solvated sodium ions in graphite," *Electrochim. Acta*, vol. 222, pp. 1365–1370, 2016, doi: 10.1016/j.electacta.2016.11.112.
- [5] P. Ge and M. Foulletier, "Electrochemical intercalation of sodium ion in graphite," *Solid State Ionics*, vol. 28–30, pp. 1172–1175, 1988.
- [6] H. Cheng, Z. R. Tang, X. Luo, and Z. Zheng, "Spartina alterniflora-derived porous carbon using as anode material for sodium-ion battery," *Sci. Total Environ.*, vol. 777, p. 146120, 2021, doi: 10.1016/j.scitotenv.2021.146120.
- [7] K. Wang *et al.*, "Low-Cost and High-Performance Hard Carbon Anode Materials for Sodium-Ion Batteries," *ACS Omega*, vol. 2, no. 4, pp. 1687–1695, 2017, doi: 10.1021/acsomega.7b00259.
- [8] T. Zhang *et al.*, "Pinecone biomass-derived hard carbon anodes for high-performance sodium-ion batteries," *RSC Adv.*, vol. 7, no. 66, pp. 41504–41511, 2017, doi: 10.1039/c7ra07231g.
- [9] A. Gomez-Martin, J. Martinez-Fernandez, M. Rutttert, M. Winter, T. Placke, and J. Ramirez-Rico, "Correlation of Structure and Performance of Hard Carbons as Anodes for Sodium Ion Batteries," *Chem. Mater.*, vol. 31, no. 18, pp. 7288–7299, 2019, doi: 10.1021/acs.chemmater.9b01768.
- [10] N. Sun *et al.*, "Extended 'Adsorption–Insertion' Model: A New Insight into the Sodium Storage Mechanism of Hard Carbons," *Adv. Energy Mater.*, vol. 9, no. 32, pp. 1–14, 2019, doi: 10.1002/aenm.201901351.
- [11] C. del M. Saavedra Rios, "Study of biomass-derived hard carbons for Sodium-ion battery application," Université Grenoble-Alpes, 2020.
- [12] A. F. Qatameh *et al.*, "River driftwood pretreated via hydrothermal carbonization as a sustainable source of hard carbon for Na-ion battery anodes," *J. Environ. Chem. Eng.*, vol. 9, no. 6, p. 106604, 2021, doi: 10.1016/j.jece.2021.106604.
- [13] V. Simone, "Développement d'accumulateurs sodium -ion," Université Grenoble-Alpes, 2016.
- [14] V. Pelé, "Nouveaux matériaux d' électrodes pour microbatteries au sodium," Université de Bordeaux, 2016.
- [15] J. Barrault *et al.*, "Les batteries de demain," *Actual. Chim.*, vol. 464, 2021.
- [16] H. Kim *et al.*, "New iron-based mixed-polyanion cathodes for lithium and sodium rechargeable batteries: Combined first principles calculations and experimental study," *J. Am. Chem. Soc.*, vol. 134, no. 25, pp. 10369–10372, 2012, doi: 10.1021/ja3038646.
- [17] P. Barpanda, G. Oyama, S. I. Nishimura, S. C. Chung, and A. Yamada, "A 3.8-V earth-abundant sodium battery electrode," *Nat. Commun.*, vol. 5, 2014, doi: 10.1038/ncomms5358.
- [18] Y. Li *et al.*, "Recent advances of electrode materials for low-cost sodium-ion batteries towards practical application for grid energy storage," *Energy Storage Mater.*, vol. 7, no. October 2016, pp. 130–151, 2017, doi: 10.1016/j.ensm.2017.01.002.
- [19] L. Yu *et al.*, "Understanding Fundamentals and Reaction Mechanisms of Electrode Materials for Na-Ion Batteries," *Small*, vol. 14, no. 16, pp. 1–22, 2018, doi: 10.1002/smll.201703338.
- [20] D. Alvira, D. Antorán, and J. J. Manyà, "Plant-derived hard carbon as anode for sodium-ion batteries: A comprehensive review to guide interdisciplinary research," *Chem. Eng. J.*, vol. 447, no. March, 2022, doi: 10.1016/j.cej.2022.137468.

- [21] C. de M. Saavedra Rios, A. Beda, L. Simonin, and C. Matei Ghimbeu, *Hard Carbon for Na-ion Batteries: From Synthesis to Performance and Storage Mechanism*. 2021.
- [22] X. Dou *et al.*, "Hard carbons for sodium-ion batteries: Structure, analysis, sustainability, and electrochemistry," *Mater. Today*, vol. 23, no. March, pp. 87–104, 2019, doi: 10.1016/j.mattod.2018.12.040.
- [23] B. E. Warren, "X-ray diffraction in random layer lattices," *Phys. Rev.*, vol. 59, no. 9, pp. 693–698, 1941, doi: 10.1103/PhysRev.59.693.
- [24] R. E. Franklin, "Crystallite growth in graphitizing and non-graphitizing carbons," *Proc. R. Soc. London. Ser. A. Math. Phys. Sci.*, vol. 209, no. 1097, pp. 196–218, 1951, doi: 10.1098/rspa.1951.0197.
- [25] L. L. Ban, D. Crawford, and H. Marsh, "Lattice-resolution electron microscopy in structural studies of non-graphitizing carbons from polyvinylidene chloride (PVDC)," *J. Appl. Crystallogr.*, vol. 8, no. 4, pp. 415–420, 1975, doi: 10.1107/s0021889875010904.
- [26] P. J. F. Harris and S. C. Tsang, "High-resolution electron microscopy studies of non-graphitizing carbons," *Philos. Mag. A Phys. Condens. Matter, Struct. Defects Mech. Prop.*, vol. 76, no. 3, pp. 667–677, 1997, doi: 10.1080/01418619708214028.
- [27] D. Saurel, B. Orayech, B. Xiao, D. Carriazo, X. Li, and T. Rojo, "From Charge Storage Mechanism to Performance: A Roadmap toward High Specific Energy Sodium-Ion Batteries through Carbon Anode Optimization," *Adv. Energy Mater.*, vol. 8, no. 17, pp. 1–33, 2018, doi: 10.1002/aenm.201703268.
- [28] D. A. Stevens and J. R. Dahn, "High Capacity Anode Materials for Rechargeable Sodium-Ion Batteries," *J. Electrochem. Soc.*, vol. 147, no. 4, p. 1271, 2000, doi: 10.1149/1.1393348.
- [29] L. F. Zhao *et al.*, "Hard Carbon Anodes: Fundamental Understanding and Commercial Perspectives for Na-Ion Batteries beyond Li-Ion and K-Ion Counterparts," *Adv. Energy Mater.*, vol. 11, no. 1, pp. 1–28, 2021, doi: 10.1002/aenm.202002704.
- [30] A. Beda, J. M. Le Meins, P. L. Taberna, P. Simon, and C. Matei Ghimbeu, "Impact of biomass inorganic impurities on hard carbon properties and performance in Na-ion batteries," *Sustain. Mater. Technol.*, vol. 26, 2020, doi: 10.1016/j.susmat.2020.e00227.
- [31] C. Matei Ghimbeu, J. Górká, V. Simone, L. Simonin, S. Martinet, and C. Vix-Guterl, "Insights on the Na⁺ ion storage mechanism in hard carbon: Discrimination between the porosity, surface functional groups and defects," *Nano Energy*, vol. 44, no. December 2017, pp. 327–335, 2018, doi: 10.1016/j.nanoen.2017.12.013.
- [32] J. Barbillat, D. Bougeard, G. Buntinx, M. Delhayé, P. Dhamelincourt, and F. Fillaux, "Spectrométrie Raman," *Tech. l'ingénieur*, vol. P2865 V2, 1999.
- [33] E. Irisarri, A. Ponrouch, and M. R. Palacin, "Review—Hard Carbon Negative Electrode Materials for Sodium-Ion Batteries," *J. Electrochem. Soc.*, vol. 162, no. 14, pp. A2476–A2482, 2015, doi: 10.1149/2.0091514jes.
- [34] X. Deglise and A. Donnot, "Bois énergie - Propriétés et voies de valorisation," *Tech. l'ingénieur*, 2020.
- [35] M. Volpe, J. L. Goldfarb, and L. Fiori, "Hydrothermal carbonization of *Opuntia ficus-indica* cladodes: Role of process parameters on hydrochar properties," *Bioresour. Technol.*, vol. 247, no. September 2017, pp. 310–318, 2018, doi: 10.1016/j.biortech.2017.09.072.
- [36] D. M. Keown, J. ichiro Hayashi, and C. Z. Li, "Effects of volatile-char interactions on the volatilisation of alkali and alkaline earth metallic species during the pyrolysis of biomass," *Fuel*, vol. 87, no. 7, pp. 1187–1194, 2008, doi: 10.1016/j.fuel.2007.05.056.
- [37] C. Z. Li, C. Sathe, J. R. Kershaw, and Y. Pang, "Fates and roles of alkali and alkaline earth metals during the pyrolysis of a Victorian brown coal," *Fuel*, vol. 79, no. 3–4, pp. 427–438, 2000, doi: 10.1016/S0016-2361(99)00178-7.
- [38] I. Obernberger, "Strategy for the application of novel characterization methods for biomass fuels: Case study of straw," *Energy and Fuels*, vol. 28, no. 2, pp. 1041–1052, 2014, doi: 10.1021/ef402249x.
- [39] D. J. Lane, P. J. van Eyk, R. de Nys, D. A. Roberts, A. J. Cole, and P. J. Ashman, "Mobilisation of trace elements during thermal conversion of algae cultivated in ash dam water," *Biomass and Bioenergy*, vol. 83, pp. 183–195, 2015, doi: 10.1016/j.biombioe.2015.09.013.
- [40] A. A. Arie, H. Kristianto, H. Muljana, and L. Stievano, "Rambutan peel based hard carbons as anode materials for

- sodium ion battery," *Fullerenes Nanotub. Carbon Nanostructures*, vol. 27, no. 12, pp. 953–960, 2019, doi: 10.1080/1536383X.2019.1671372.
- [41] V. Simone, A. Boulineau, A. de Geyer, D. Rouchon, L. Simonin, and S. Martinet, "Hard carbon derived from cellulose as anode for sodium ion batteries: Dependence of electrochemical properties on structure," *J. Energy Chem.*, vol. 25, no. 5, pp. 761–768, 2016, doi: 10.1016/j.jchem.2016.04.016.
- [42] X. S. Wu, X. L. Dong, B. Y. Wang, J. L. Xia, and W. C. Li, "Revealing the sodium storage behavior of biomass-derived hard carbon by using pure lignin and cellulose as model precursors," *Renew. Energy*, vol. 189, pp. 630–638, 2022, doi: 10.1016/j.renene.2022.03.023.
- [43] I. Izzanar, M. Dahbi, M. Kiso, S. Doubajji, S. Komaba, and I. Saadoune, "Hard carbons issued from date palm as efficient anode materials for sodium-ion batteries," *Carbon N. Y.*, vol. 137, pp. 165–173, 2018, doi: 10.1016/j.carbon.2018.05.032.
- [44] G. Hasegawa, K. Kanamori, N. Kannari, J. I. Ozaki, K. Nakanishi, and T. Abe, "Studies on electrochemical sodium storage into hard carbons with binder-free monolithic electrodes," *J. Power Sources*, vol. 318, pp. 41–48, 2016, doi: 10.1016/j.jpowsour.2016.04.013.
- [45] A. Beda, C. Vaultot, and C. Matei Ghimbeu, "Hard carbon porosity revealed by the adsorption of multiple gas probe molecules (N₂, Ar, CO₂, O₂ and H₂)," *J. Mater. Chem. A*, vol. 9, no. 2, pp. 937–943, 2021, doi: 10.1039/d0ta10088a.
- [46] M. Seredych, J. Jagiello, and T. J. Bandoz, "Complexity of CO₂ adsorption on nanoporous sulfur-doped carbons - Is surface chemistry an important factor?," *Carbon N. Y.*, vol. 74, pp. 207–217, 2014, doi: 10.1016/j.carbon.2014.03.024.
- [47] E. R. Buiel, A. E. George, and J. R. Dahn, "Model of micropore closure in hard carbon prepared from sucrose," *Carbon N. Y.*, vol. 37, no. 9, pp. 1399–1407, 1999, doi: 10.1016/S0008-6223(98)00335-2.
- [48] L. Xiao *et al.*, "Low-Defect and Low-Porosity Hard Carbon with High Coulombic Efficiency and High Capacity for Practical Sodium Ion Battery Anode," *Adv. Energy Mater.*, vol. 8, no. 20, pp. 1–7, 2018, doi: 10.1002/aenm.201703238.
- [49] Y. Zhen, Y. Chen, F. Li, Z. Guo, Z. Hong, and M. M. Titirici, "Ultrafast synthesis of hard carbon anodes for sodium-ion batteries," *Proc. Natl. Acad. Sci. U. S. A.*, vol. 118, no. 42, pp. 1–7, 2021, doi: 10.1073/pnas.2111119118.
- [50] C. Marino, J. Cabanero, M. Povia, and C. Villevieille, "Biowaste Lignin-Based Carbonaceous Materials as Anodes for Na-Ion Batteries," *J. Electrochem. Soc.*, vol. 165, no. 7, pp. A1400–A1408, 2018, doi: 10.1149/2.0681807jes.
- [51] E. Peled, "Film forming reaction at the lithium/electrolyte interface," *J. Power Sources*, vol. 9, no. 3, pp. 253–266, Jan. 1983, doi: 10.1016/0378-7753(83)87026-8.
- [52] X. Li *et al.*, "Review on comprehending and enhancing the initial Coulombic efficiency of anode materials in lithium-ion/sodium-ion batteries," *Nano Energy*, vol. 77, no. May, p. 105143, 2020, doi: 10.1016/j.nanoen.2020.105143.
- [53] Y. Cao *et al.*, "Sodium ion insertion in hollow carbon nanowires for battery applications," *Nano Lett.*, vol. 12, no. 7, pp. 3783–3787, 2012, doi: 10.1021/nl3016957.
- [54] L. Yang, M. Hu, Q. Lv, H. Zhang, W. Yang, and R. Lv, "Salt and sugar derived high power carbon microspheres anode with excellent low-potential capacity," *Carbon N. Y.*, vol. 163, pp. 288–296, 2020, doi: 10.1016/j.carbon.2020.03.021.
- [55] A. Adamson *et al.*, "Peat-derived hard carbon electrodes with superior capacity for sodium-ion batteries," *RSC Adv.*, vol. 10, no. 34, pp. 20145–20154, 2020, doi: 10.1039/d0ra03212c.
- [56] D. A. Stevens and J. R. Dahn, "The Mechanisms of Lithium and Sodium Insertion in Carbon Materials," *J. Electrochem. Soc.*, vol. 148, no. 8, p. A803, 2001, doi: 10.1149/1.1379565.
- [57] C. Bommier, T. W. Surta, M. Dolgos, and X. Ji, "New Mechanistic Insights on Na-Ion Storage in Nongraphitizable Carbon," *Nano Lett.*, vol. 15, no. 9, pp. 5888–5892, 2015, doi: 10.1021/acs.nanolett.5b01969.
- [58] S. Alvin *et al.*, "Revealing sodium ion storage mechanism in hard carbon," *Carbon N. Y.*, vol. 145, pp. 67–81, 2019, doi: 10.1016/j.carbon.2018.12.112.
- [59] B. Zhang, C. M. Ghimbeu, C. Laberty, C. Vix-Guterl, and J. M. Tarascon, "Correlation between Microstructure and Na Storage Behavior in Hard Carbon," *Adv. Energy Mater.*, vol. 6, no. 1, pp. 1–9, 2016, doi: 10.1002/aenm.201501588.
- [60] S. Komaba *et al.*, "Electrochemical Na insertion and solid electrolyte interphase for hard-carbon electrodes and application to Na-ion batteries," *Adv. Funct. Mater.*, vol. 21, no. 20, pp. 3859–3867, 2011, doi:

- 10.1002/adfm.201100854.
- [61] J. Ding *et al.*, "Carbon nanosheet frameworks derived from peat moss as high performance sodium ion battery anodes," *ACS Nano*, vol. 7, no. 12, pp. 11004–11015, 2013, doi: 10.1021/nn404640c.
- [62] P. Bai, Y. He, X. Zou, X. Zhao, P. Xiong, and Y. Xu, "Elucidation of the Sodium-Storage Mechanism in Hard Carbons," *Adv. Energy Mater.*, vol. 8, no. 15, pp. 1–9, 2018, doi: 10.1002/aenm.201703217.
- [63] S. Qiu *et al.*, "Manipulating Adsorption–Insertion Mechanisms in Nanostructured Carbon Materials for High-Efficiency Sodium Ion Storage," *Adv. Energy Mater.*, vol. 7, no. 17, pp. 1–11, 2017, doi: 10.1002/aenm.201700403.
- [64] S. V. Vassilev, D. Baxter, L. K. Andersen, and C. G. Vassileva, "An overview of the chemical composition of biomass," *Fuel*, vol. 89, no. 5, pp. 913–933, 2010, doi: 10.1016/j.fuel.2009.10.022.
- [65] Y. M. Bar-On, R. Phillips, and R. Milo, "The biomass distribution on Earth," *Proceedings Natl. Acad. Sci. United States Am.*, vol. 115, no. 25, pp. 6506–6511, 2018, doi: 10.1073/pnas.1711842115.
- [66] L. A. Becerra-Pérez, L. E. Rincón, and J. A. Posada-Duque, "Logistics and Costs of Agricultural Residues for Cellulosic Ethanol Production," *Energies*, vol. 15, no. 12, pp. 1–18, 2022, doi: 10.3390/en15124480.
- [67] N. S. Bentsen, C. Felby, and B. J. Thorsen, "Agricultural residue production and potentials for energy and materials services," *Prog. Energy Combust. Sci.*, vol. 40, no. 1, pp. 59–73, 2014, doi: 10.1016/j.pecs.2013.09.003.
- [68] European Union, "Brief on agricultural biomass production," 2018. doi: 10.2760/142177.
- [69] S. V. Vassilev and C. G. Vassileva, "Composition, properties and challenges of algae biomass for biofuel application: An overview," *Fuel*, vol. 181, pp. 1–33, 2016, doi: 10.1016/j.fuel.2016.04.106.
- [70] V. S. Sikarwar *et al.*, "An overview of advances in biomass gasification," *Energy Environ. Sci.*, vol. 9, no. 10, pp. 2939–2977, 2016, doi: 10.1039/c6ee00935b.
- [71] T. Zimmermann, E. Pöhler, and T. Geiger, "Cellulose fibrils for polymer reinforcement," *Adv. Eng. Mater.*, vol. 6, no. 9, pp. 754–761, 2004, doi: 10.1002/adem.200400097.
- [72] A. Ebringerová, Z. Hromádková, and T. Heinze, "Hemicellulose," *Adv. Polym. Sci.*, vol. 186, pp. 1–67, 2005, doi: 10.1007/b136816.
- [73] T. Foyle, L. Jennings, and P. Mulcahy, "Compositional analysis of lignocellulosic materials: Evaluation of methods used for sugar analysis of waste paper and straw," *Bioresour. Technol.*, vol. 98, no. 16, pp. 3026–3036, 2007, doi: 10.1016/j.biortech.2006.10.013.
- [74] B. U. Stambuk, E. C. A. Eleutherio, L. M. Florez-Pardo, A. M. Souto-Maior, and E. P. S. Bon, "Brazilian potential for biomass ethanol: Challenge of using hexose and pentose cofermenting yeast strains," *J. Sci. Ind. Res. (India)*, vol. 67, no. 11, pp. 918–926, 2008.
- [75] J. L. Wertz, D. Valbiom, G. Agro, and B. Tech, "La lignine," *Doc. ValBiom – Gembloux Agro-Bio Tech*, 2010.
- [76] J. L. Faulon, G. A. Carlson, and P. G. Hatcher, "A three-dimensional model for lignocellulose from gymnospermous wood," *Org. Geochem.*, vol. 21, no. 12, pp. 1169–1179, 1994, doi: 10.1016/0146-6380(94)90161-9.
- [77] C. Xu and F. Ferdosian, "Structure and properties of lignin," in *Conversion of Lignin into Bio-Based Chemicals and Materials*, Green Chem., L.-N. He, R. D. Rogers, D. Su, P. Tundo, and Z. C. Zhang, Eds. Germany: Springer-Verlag GmbH Germany, 2017, pp. 1–9.
- [78] C. U. Jensen, J. K. Rodriguez Guerrero, S. Karatzos, G. Olofsson, and S. B. Iversen, "Fundamentals of Hydrofaction™: Renewable crude oil from woody biomass," *Biomass Convers. Biorefinery*, vol. 7, no. 4, pp. 495–509, 2017, doi: 10.1007/s13399-017-0248-8.
- [79] S. V. Vassilev, D. Baxter, L. K. Andersen, C. G. Vassileva, and T. J. Morgan, "An overview of the organic and inorganic phase composition of biomass," *Fuel*, vol. 94, pp. 1–33, 2012, doi: 10.1016/j.fuel.2011.09.030.
- [80] T. A. Shah, L. Zhihe, L. Zhiyu, and Z. Andong, "Composition and role of lignin in biochemicals," in *Lignin - Chemistry, structure and application*, IntechOpen., A. Sand and J. Tuteja, Eds. 2023, pp. 1–20.
- [81] H. A. Markewich *et al.*, "Effects of storage methods on chemical composition of manure and manure decomposition in soil in small-scale Kenyan systems," *Agric. Ecosyst. Environ.*, vol. 139, no. 1–2, pp. 134–141, 2010, doi: 10.1016/j.agee.2010.07.010.

- [82] C. Yang and X. Lü, "Composition of plant biomass and its impact on pretreatment," in *Advances in 2nd Generation of Bioethanol Production*, Woodhead P., X. Lü, Ed. Woodhead Publishing, 2021, pp. 71–85.
- [83] T. Komiyama and T. Ito, "The characteristics of phosphorus in animal manure composts," *Soil Sci. Plant Nutr.*, vol. 65, no. 3, pp. 281–288, May 2019, doi: 10.1080/00380768.2019.1615384.
- [84] J. B. Reeves and J. A. S. Van Kessel, "Influence of ash on the fiber composition of dried dairy manures," *Environ. Pollut.*, vol. 120, no. 2, pp. 239–244, 2002, doi: 10.1016/S0269-7491(02)00154-9.
- [85] A. Magdziarz *et al.*, "Properties of ash generated during sewage sludge combustion: A multifaceted analysis," *Energy*, vol. 113, no. x, pp. 85–94, 2016, doi: 10.1016/j.energy.2016.07.029.
- [86] M. A. Shafii, E. C. M. Ling, and E. Shaffie, "The use of sewage sludge and its ash in construction and agriculture industry: a review," *J. Teknol.*, vol. 85, no. 5, pp. 81–90, 2019, doi: 10.11113/jt.v81.13486.
- [87] N. Gao, K. Kamran, C. Quan, and P. T. Williams, "Thermochemical conversion of sewage sludge: A critical review," *Prog. Energy Combust. Sci.*, vol. 79, 2020, doi: 10.1016/j.pecs.2020.100843.
- [88] A. Pettersson, L.-E. Åmand, and B.-M. Steenari, "Leaching of ashes from co-combustion of sewage sludge and wood—Part I: Recovery of phosphorus," *Biomass and Bioenergy*, vol. 32, no. 3, pp. 224–235, 2008, doi: 10.1016/j.biombioe.2007.09.016.
- [89] A.-L. Elled, L.-E. Åmand, B. Leckner, and B.-A. Andersson, "Influence of phosphorus on sulphur capture during co-firing of sewage sludge with wood or bark in a fluidised bed," *Fuel*, vol. 85, no. 12–13, pp. 1671–1678, 2006, doi: 10.1016/j.fuel.2006.02.008.
- [90] T. Dahou, "Contribution to the understanding of the role of inorganic elements in biomass steam gasification," Université Grenoble Alpes, 2020.
- [91] A. Anca-Couce, "Reaction mechanisms and multi-scale modelling of lignocellulosic biomass pyrolysis," *Prog. Energy Combust. Sci.*, vol. 53, no. 2016, pp. 41–79, 2016, doi: 10.1016/j.pecs.2015.10.002.
- [92] E. G. Koukios, "Progress in Thermochemical, Solid-State Refining of Biofuels — From Research to Commercialization," in *Bridgwater, A.V. (eds) Advances in Thermochemical Biomass Conversion*. Springer, no. 5, Dordrecht, 1993, pp. 1678–1692.
- [93] T. Wang, Y. Zhai, Y. Zhu, C. Li, and G. Zeng, "A review of the hydrothermal carbonization of biomass waste for hydrochar formation: Process conditions, fundamentals, and physicochemical properties," *Renew. Sustain. Energy Rev.*, vol. 90, no. December 2016, pp. 223–247, 2018, doi: 10.1016/j.rser.2018.03.071.
- [94] M. Lucian, M. Volpe, L. Gao, G. Piro, J. L. Goldfarb, and L. Fiori, "Impact of hydrothermal carbonization conditions on the formation of hydrochars and secondary chars from the organic fraction of municipal solid waste," *Fuel*, vol. 233, no. April, pp. 257–268, 2018, doi: 10.1016/j.fuel.2018.06.060.
- [95] S. A. Nicolae *et al.*, "Recent advances in hydrothermal carbonisation: From tailored carbon materials and biochemicals to applications and bioenergy," *Green Chem.*, vol. 22, no. 15, pp. 4747–4800, 2020, doi: 10.1039/d0gc00998a.
- [96] C. Rodriguez Correa, T. Hehr, A. Voglhuber-Slavinsky, Y. Rauscher, and A. Kruse, "Pyrolysis vs. hydrothermal carbonization: Understanding the effect of biomass structural components and inorganic compounds on the char properties," *J. Anal. Appl. Pyrolysis*, vol. 140, no. August 2018, pp. 137–147, 2019, doi: 10.1016/j.jaap.2019.03.007.
- [97] A. Funke and F. Ziegler, "Hydrothermal carbonization of biomass: A summary and discussion of chemical mechanisms for process engineering," *Biofuels, Bioprod. Biorefining*, no. 4, pp. 160–177, 2010, doi: 10.1002/bbb.198.
- [98] G. Ischia and L. Fiori, "Hydrothermal Carbonization of Organic Waste and Biomass: A Review on Process, Reactor, and Plant Modeling," *Waste and Biomass Valorization*, vol. 12, no. 6, pp. 2797–2824, 2021, doi: 10.1007/s12649-020-01255-3.
- [99] E. Sabio, A. Álvarez-Murillo, S. Román, and B. Ledesma, "Conversion of tomato-peel waste into solid fuel by hydrothermal carbonization: Influence of the processing variables," *Waste Manag.*, vol. 47, pp. 122–132, 2016, doi: 10.1016/j.wasman.2015.04.016.
- [100] K. Wu *et al.*, "Characterization of dairy manure hydrochar and aqueous phase products generated by hydrothermal carbonization at different temperatures," *J. Anal. Appl. Pyrolysis*, vol. 127, no. May, pp. 335–342, 2017, doi: 10.1016/j.jaap.2017.07.017.

- [101] S. Román *et al.*, "Hydrothermal carbonization: Modeling, final properties design and applications: A review," *Energies*, vol. 11, no. 1, pp. 1–28, 2018, doi: 10.3390/en11010216.
- [102] B. De Mena Pardo, L. Doyle, M. Renz, and A. Salimbeni, *Industrial Scale Hydrothermal Carbonization: new applications for wet biomass waste*, no. July. 2016.
- [103] M. T. Reza, R. Emerson, M. H. Uddin, G. Gresham, and C. J. Coronella, "Ash reduction of corn stover by mild hydrothermal preprocessing," *Biomass Convers. Biorefinery*, vol. 5, no. 1, pp. 21–31, 2015, doi: 10.1007/s13399-014-0122-x.
- [104] M. T. Reza, J. G. Lynam, M. H. Uddin, and C. J. Coronella, "Hydrothermal carbonization: Fate of inorganics," *Biomass and Bioenergy*, vol. 49, pp. 86–94, 2013, doi: 10.1016/j.biombioe.2012.12.004.
- [105] A. M. Smith, S. Singh, and A. B. Ross, "Fate of inorganic material during hydrothermal carbonisation of biomass: Influence of feedstock on combustion behaviour of hydrochar," *Fuel*, vol. 169, pp. 135–145, 2016, doi: 10.1016/j.fuel.2015.12.006.
- [106] A. M. Smith and A. B. Ross, "The influence of residence time during hydrothermal carbonisation of miscanthus on bio-coal combustion chemistry," *Energies*, vol. 12, no. 3, pp. 13–22, 2019, doi: 10.3390/en12030523.
- [107] Y. Gao *et al.*, "Effect of residence time on chemical and structural properties of hydrochar obtained by hydrothermal carbonization of water hyacinth," *Energy*, vol. 58, pp. 376–383, 2013, doi: 10.1016/j.energy.2013.06.023.
- [108] C. Nzediegwu, M. A. Naeth, and S. X. Chang, "Carbonization temperature and feedstock type interactively affect chemical, fuel, and surface properties of hydrochars," *Bioresour. Technol.*, vol. 330, no. March, p. 124976, 2021, doi: 10.1016/j.biortech.2021.124976.
- [109] C. He, A. Giannis, and J. Y. Wang, "Conversion of sewage sludge to clean solid fuel using hydrothermal carbonization: Hydrochar fuel characteristics and combustion behavior," *Appl. Energy*, vol. 111, pp. 257–266, 2013, doi: 10.1016/j.apenergy.2013.04.084.
- [110] J. Chen, Z. Chen, C. Wang, and X. Li, "Calcium-assisted hydrothermal carbonization of an alginate for the production of carbon microspheres with unique surface nanopores," *Mater. Lett.*, vol. 67, no. 1, pp. 365–368, 2012, doi: 10.1016/j.matlet.2011.10.017.
- [111] C. del M. Saavedra Rios, V. Simone, L. Simonin, S. Martinet, and C. Dupont, "Biochars from various biomass types as precursors for hard carbon anodes in sodium-ion batteries," *Biomass and Bioenergy*, vol. 117, no. July, pp. 32–37, 2018, doi: 10.1016/j.biombioe.2018.07.001.
- [112] E. Demir, M. Aydin, A. A. Arie, and R. Demir-Cakan, "Apricot shell derived hard carbons and their tin oxide composites as anode materials for sodium-ion batteries," *J. Alloys Compd.*, vol. 788, pp. 1093–1102, 2019, doi: 10.1016/j.jallcom.2019.02.264.
- [113] W. Lv *et al.*, "Peanut shell derived hard carbon as ultralong cycling anodes for lithium and sodium batteries," *Electrochim. Acta*, vol. 176, pp. 533–541, 2015, doi: 10.1016/j.electacta.2015.07.059.
- [114] F. Liberale, C. Dossi, R. Bettinetti, R. Ruffo, M. Fiore, and L. Magagnin, "Algae Derived Electrodes for Rechargeable Na-Ion Batteries: Materials Characterization and Electrochemical Performances," *ECS Trans.*, vol. 80, p. 349, 2017, doi: 10.1149/08010.0349ecst.
- [115] E. Gibertini *et al.*, "Algae-derived hard carbon anodes for Na-ion batteries," *J. Appl. Electrochem.*, vol. 51, pp. 1665–1673, 2021, doi: 10.1007/s10800-021-01609-2.
- [116] S. Bonnamy and A. Oberlin, "Chapter 4 - Transmission Electron Microscopy," in *Materials Science and Engineering of Carbon*, M. Inagaki, Ed. Butterworth-Heinemann, 2016, pp. 45–70.
- [117] Y. Feng *et al.*, "Chemical-enzymatic fractionation to unlock the potential of biomass-derived carbon materials for sodium ion batteries," *J. Mater. Chem. A*, vol. 7, no. 47, pp. 26954–26965, 2019, doi: 10.1039/c9ta09124f.
- [118] C. M. Saavedra Rios, L. Simonin, C. M. Ghimbeu, C. Vaulot, D. da Silva Perez, and C. Dupont, "Impact of the biomass precursor composition in the hard carbon properties and performance for application in a Na-ion battery," *Fuel Process. Technol.*, vol. 231, no. March, p. 107223, 2022, doi: 10.1016/j.fuproc.2022.107223.
- [119] L. Cong, G. Tian, D. Luo, X. Ren, and X. Xiang, "Hydrothermally assisted transformation of corn stalk wastes into high-performance hard carbon anode for sodium-ion batteries," *J. Electroanal. Chem.*, vol. 871, p. 114249, 2020, doi: 10.1016/j.jelechem.2020.114249.

- [120] P. Zheng *et al.*, "Enhanced Performance by Enlarged Nano-pores of Holly Leaf-derived Lamellar Carbon for Sodium-ion Battery Anode," *Sci. Rep.*, vol. 6, no. May, pp. 1–9, 2016, doi: 10.1038/srep26246.
- [121] J. Wang, L. Yan, Q. Ren, L. Fan, F. Zhang, and Z. Shi, "Facile hydrothermal treatment route of reed straw-derived hard carbon for high performance sodium ion battery," *Electrochim. Acta*, vol. 291, pp. 188–196, 2018, doi: 10.1016/j.electacta.2018.08.136.
- [122] Y. Gao, S. Piao, C. Jiang, and Z. Zou, "Navel orange peel-derived hard carbons as high performance anode materials of Na and Li-ion batteries," *Diam. Relat. Mater.*, vol. 129, no. July, p. 109329, 2022, doi: 10.1016/j.diamond.2022.109329.
- [123] D. Yan *et al.*, "Nitrogen-doped carbon microspheres derived from oatmeal as high capacity and superior long life anode material for sodium ion battery," *Electrochim. Acta*, vol. 191, pp. 385–391, 2016, doi: 10.1016/j.electacta.2016.01.105.
- [124] E. Canbaz, M. Aydin, and R. Demir-Çakan, "Investigation of hazelnut shells driven hard carbons as anode for sodium-ion batteries produced by hydrothermal carbonization method," *Turkish J. Chem.*, vol. 46, no. 2, pp. 356–366, 2022, doi: 10.55730/1300-0527.3312.
- [125] H. Wang, W. Yu, J. Shi, N. Mao, S. Chen, and W. Liu, "Biomass derived hierarchical porous carbons as high-performance anodes for sodium-ion batteries," *Electrochim. Acta*, vol. 188, pp. 103–110, 2016, doi: 10.1016/j.electacta.2015.12.002.
- [126] C. C. Wang and W. L. Su, "Ultrathin Artificial Solid Electrolyte Interface Layer-Coated Biomass-Derived Hard Carbon as an Anode for Sodium-Ion Batteries," *ACS Appl. Energy Mater.*, vol. 5, no. 1, pp. 1052–1064, 2022, doi: 10.1021/acsaem.1c03425.
- [127] L. Cao *et al.*, "Rape seed shuck derived-lamellar hard carbon as anodes for sodium-ion batteries," *J. Alloys Compd.*, vol. 695, pp. 632–637, 2017, doi: 10.1016/j.jallcom.2016.11.135.
- [128] H. Liu *et al.*, "A life cycle assessment of hard carbon anodes for sodium-ion batteries," *Philos. Trans. R. Soc. A Math. Phys. Eng. Sci.*, vol. 379, no. 2209, 2021, doi: 10.1098/rsta.2020.0340.
- [129] P. C. Rath, J. Patra, H. T. Huang, D. Bresser, T. Y. Wu, and J. K. Chang, "Carbonaceous Anodes Derived from Sugarcane Bagasse for Sodium-Ion Batteries," *ChemSusChem*, vol. 12, no. 10, pp. 2302–2309, 2019, doi: 10.1002/cssc.201900319.
- [130] C. D. M. Saavedra Rios, L. Simonin, A. De Geyer, C. M. Ghimbeu, and C. Dupont, "Unraveling the properties of biomass-derived hard carbons upon thermal treatment for a practical application in na-ion batteries," *Energies*, vol. 13, no. 14, p. 3513, 2020, doi: 10.3390/en13143513.
- [131] L. A. Romero-Cano *et al.*, "Surface functionalization to abate the irreversible capacity of hard carbons derived from grapefruit peels for sodium-ion batteries," *Electrochim. Acta*, vol. 326, pp. 1–12, 2019, doi: 10.1016/j.electacta.2019.134973.
- [132] N. Sun, H. Liu, and B. Xu, "Facile synthesis of high performance hard carbon anode materials for sodium ion batteries," *J. Mater. Chem. A*, vol. 3, no. 41, pp. 20560–20566, 2015, doi: 10.1039/c5ta05118e.
- [133] J. Barker, S. S. Meysami, and F. Mazzali, "WO 2020-GB50872 Preparation and use of hard-carbon containing materials as electrode for rechargeable batteries.pdf," 2020.
- [134] F. Xie *et al.*, "Unveiling the role of hydrothermal carbon dots as anodes in sodium-ion batteries with ultrahigh initial coulombic efficiency," *J. Mater. Chem. A*, vol. 7, no. 48, pp. 27567–27575, 2019, doi: 10.1039/c9ta11369j.
- [135] M. Dar, K. Majid, and M. Wahid, "In-plane ordering and nature of N-doping in hard carbon synthesized at low temperature govern the sodium-ion intercalation," *J. Electroanal. Chem.*, vol. 899, no. 2, p. 115669, 2021, doi: 10.1016/j.jelechem.2021.115669.
- [136] A. A. Arie, B. Tekin, E. Demir, and R. Demir-Cakan, "Hard carbons derived from waste tea bag powder as anodes for sodium ion battery," *Mater. Technol.*, vol. 34, no. 9, pp. 515–524, 2019, doi: 10.1080/10667857.2019.1586087.
- [137] A. A. Arie, B. Tekin, E. Demir, and R. Demir-Cakan, "Utilization of The Indonesian's Spent Tea Leaves as Promising Porous Hard Carbon Precursors for Anode Materials in Sodium Ion Batteries," *Waste and Biomass Valorization*, vol. 11, no. 6, pp. 3121–3131, 2020, doi: 10.1007/s12649-019-00624-x.
- [138] "Analysis of Phosphate by Visible Spectrophotometry," *Journal of the American Dental Association* (1939), 1971. .

- [139] G. H. Jeffery, J. Bassett, J. Mendham, and R. C. Denney, *Textbook of Quantitative chemical analysis*, Fifth edit. VOGEL's, 1989.
- [140] J. FRAYRET, J.-M. MERMET, and H. PAUCOT, "ICP-OES : couplage plasma induit par haute fréquence – spectrométrie optique," *Tech. d'analyse*, vol. 33, no. 0, 2012, doi: 10.51257/a-v2-p2719.
- [141] J. T. WOODS and M. G. MELLON, "Molybdenum blue solution A Spectrophotometric Study," *Ind. Eng. Chem.*, vol. 13, no. 11, pp. 760–764, 1941, doi: 10.1021/i560099a003.
- [142] P. Breuil and G. Bouchoux, "Spectrophotométrie d'absorption dans l'ultraviolet et le visible," *Tech. l'ingénieur*, vol. 33, no. 0, p. 20, 2014.
- [143] N. Broll, "Caractérisation de solides cristallisés par diffraction X," *Tech. l'ingénieur*, vol. PE 1 080, pp. 0–18, 1996.
- [144] A. M. Gurnell, H. Piégay, F. J. Swanson, and S. V. Gregory, "Large wood and fluvial processes," *Freshw. Biol.*, vol. 47, no. 4, pp. 601–619, 2002, doi: 10.1046/J.1365-2427.2002.00916.X.
- [145] A. C. Parola, C. J. Apelt, and M. A. Jempson, "Debris Forces on Highway Bridges," *NCHRP Rep.*, no. 445, 2000, Accessed: Aug. 19, 2021. [Online]. Available: <http://trid.trb.org/view.aspx?id=674405>.
- [146] P. F. Lagasse, L. W. Zevenbergen, and P. E. Clopper, "Impacts of Debris on Bridge Pier Scour," pp. 854–863, Oct. 2010, doi: 10.1061/41147(392)85.
- [147] P. Bartocci *et al.*, "Thermal degradation of driftwood: Determination of the concentration of sodium, calcium, magnesium, chlorine and sulfur containing compounds," *Waste Manag.*, vol. 60, pp. 151–157, Feb. 2017, doi: 10.1016/J.WASMAN.2016.08.035.
- [148] D. Da Silva Perez *et al.*, "Characterisation of the most representative agricultural and forestry biomasses in France for gasification," *Waste and Biomass Valorization*, vol. 6, no. 4, pp. 515–526, 2015, doi: 10.1007/s12649-015-9374-3.
- [149] M. Narodoslasky and I. Oberberger, "From waste to raw material—the route from biomass to wood ash for cadmium and other heavy metals," *J. Hazard. Mater.*, vol. 50, no. 2–3, pp. 157–168, 1996, doi: 10.1016/0304-3894(96)01785-2.
- [150] A. V. Someshwar, "Wood and combination wood-fired boiler ash characterization," *J. Environment Qual.*, vol. 25, no. 5, pp. 962–972, 1996, doi: 10.2134/jeq1996.00472425002500050006x.
- [151] F. Suarez-Garcia, A. Martinez-Alonzo, M. Llorente, and J. Tascon, "Inorganic matter characterization in vegetable biomass feedstocks," *Fuel*, vol. 81, no. 9, pp. 1161–1169, 2022, doi: 10.1016/S0016-2361(02)00026-1.
- [152] A. Magdziarz, M. Wilk, and M. Wądrzyk, "Pyrolysis of hydrochar derived from biomass – Experimental investigation," *Fuel*, vol. 267, no. January, 2020, doi: 10.1016/j.fuel.2020.117246.
- [153] S. Başakçılardan Kabakçı and S. S. Baran, "Hydrothermal carbonization of various lignocellulosics: Fuel characteristics of hydrochars and surface characteristics of activated hydrochars," *Waste Manag.*, vol. 100, pp. 259–268, 2019, doi: 10.1016/j.wasman.2019.09.021.
- [154] I. Bejenari, G. Hristea, C. Cărăușu, A. Mija, and I. Volf, "A Sustainable Approach on Spruce Bark Waste Valorization through Hydrothermal Conversion," *Processes*, vol. 10, no. 1, 2022, doi: 10.3390/pr10010111.
- [155] S. Kang, X. Li, J. Fan, and J. Chang, "Characterization of hydrochars produced by hydrothermal carbonization of lignin, cellulose, d-xylose, and wood meal," in *Industrial and Engineering Chemistry Research*, Jul. 2012, vol. 51, no. 26, pp. 9023–9031, doi: 10.1021/ie300565d.
- [156] B. Smieja-król and J. Janeczek, "Pseudomorphs of barite and biogenic ZnS after phyto-crystals of calcium oxalate (whewellite) in the peat layer of a poor fen," pp. 7227–7233, 2014, doi: 10.1007/s11356-014-2700-7.
- [157] C. Krieger, C. Calvaruso, C. Morlot, S. Uroz, L. Salsi, and M. P. Turpault, "Identification, distribution, and quantification of biominerals in a deciduous forest," *Geobiology*, vol. 15, no. 2, pp. 296–310, Mar. 2017, doi: 10.1111/GBI.12223.
- [158] B.-J. Skrifvars, P. Yrjas, J. Kinni, P. Siefen, and M. Hupa, "The fouling behavior of rice husk ash in fluidized-bed combustion. 1. Fuel characteristics," *Energy Fuels*, vol. 19, pp. 1503–1511, 2005.
- [159] P. Karásek, L. Šťavíková, J. Planeta, B. Hohnová, and M. Roth, "Solubility of fused silica in sub- and supercritical water: Estimation from a thermodynamic model," *J. Supercrit. Fluids*, vol. 83, pp. 72–77, 2013, doi: 10.1016/j.supflu.2013.08.012.

- [160] D. M. Keown, G. Favas, J. I. Hayashi, and C. Z. Li, "Volatilisation of alkali and alkaline earth metallic species during the pyrolysis of biomass: Differences between sugar cane bagasse and cane trash," *Bioresour. Technol.*, vol. 96, no. 14, pp. 1570–1577, 2005, doi: 10.1016/j.biortech.2004.12.014.
- [161] R. L. Frost and M. L. Weier, "Thermal treatment of whewellite - A thermal analysis and Raman spectroscopic study," *Thermochim. Acta*, vol. 409, no. 1, pp. 79–85, 2004, doi: 10.1016/S0040-6031(03)00332-0.
- [162] D. Hourlier, "Thermal decomposition of calcium oxalate: beyond appearances," *J. Therm. Anal. Calorim.*, vol. 136, no. 6, pp. 2221–2229, 2019, doi: 10.1007/s10973-018-7888-1.
- [163] J. Pastor-Villegas, V. Gómez-Serrano, C. J. Durán-Valle, and F. J. Higes-Rolando, "Chemical study of extracted rockrose and of chars and activated carbons prepared at different temperatures," *J. Anal. Appl. Pyrolysis*, vol. 50, no. 1, pp. 1–16, 1999, doi: 10.1016/S0165-2370(99)00022-4.
- [164] W. D. Chanaka Udayanga, A. Veksha, A. Giannis, G. Lisak, V. W. C. Chang, and T. T. Lim, "Fate and distribution of heavy metals during thermal processing of sewage sludge," *Fuel*, vol. 226, no. February, pp. 721–744, 2018, doi: 10.1016/j.fuel.2018.04.045.
- [165] H. Piégay, B. Moulin, and C. R. Hupp, "Assessment of transfer patterns and origins of in-channel wood in large rivers using repeated field surveys and wood characterisation (the Isère River upstream of Pontcharra, France)," *Geomorphology*, vol. 279, pp. 27–43, Feb. 2017, doi: 10.1016/J.GEOMORPH.2016.07.020.
- [166] S. B. Kang, H. Y. Oh, J. J. Kim, and K. S. Choi, "Characteristics of spent coffee ground as a fuel and combustion test in a small boiler (6.5 kW)," *Renew. Energy*, vol. 113, pp. 1208–1214, 2017, doi: 10.1016/j.renene.2017.06.092.
- [167] M. A. Coronado *et al.*, "Physicochemical characterization and SEM-EDX analysis of brewer's spent grain from the craft brewery industry," *Sustainability*, vol. 12, no. 18, p. 7744, 2020, doi: 10.3390/su12187744.
- [168] F. J. Cerino-Córdova, N. E. Dávila-Guzmán, A. M. García León, J. J. Salazar-Rabago, and E. Soto-Regalado, "Revalorization of Coffee Waste," in *Coffee - Production and Research*, Intechopen., D. T. Castanheira, Ed. London, 2020, pp. 1–26.
- [169] A. C. Gowman *et al.*, "Physicochemical analysis of Apple and Grape Pomaces," *BioResources*, vol. 14, no. 2, pp. 3210–3230, 2019, doi: 10.15376/biores.14.2.3210-3230.
- [170] L. F. Calvo, A. I. García, and M. Otero, "An Experimental Investigation of Sewage Sludge Gasification in a Fluidized Bed Reactor," *Sci. World J.*, vol. 2013, 2013, doi: 10.1155/2013/479403.
- [171] M. Li, B. Xiao, X. Wang, and J. Liu, "Consequences of sludge composition on combustion performance derived from thermogravimetry analysis," *Waste Manag.*, vol. 35, pp. 141–147, 2015, doi: 10.1016/j.wasman.2014.10.004.
- [172] J. P. Chastain, "Composition of Equine Manure as Influenced by Stall Management," *Agric.*, vol. 12, no. 6, 2022, doi: 10.3390/agriculture12060823.
- [173] G. Zhang *et al.*, "Effects of water table on cellulose and lignin degradation of carex cinerascens in a large seasonal floodplain," *J. Freshw. Ecol.*, vol. 33, no. 1, pp. 311–325, 2018, doi: 10.1080/02705060.2018.1459324.
- [174] M. Chen, X. Zhu, C. Zhao, P. Yu, M. Abulaizi, and H. Jia, "Rapid microbial community evolution in initial Carex litter decomposition stages in Bayinbuluk alpine wetland during the freeze–thaw period," *Ecol. Indic.*, vol. 121, 2021, doi: 10.1016/j.ecolind.2020.107180.
- [175] N. H. Do *et al.*, "The novel method to reduce the silica content in lignin recovered from black liquor originating from rice straw," *Sci. Rep.*, vol. 10, no. 1, pp. 1–10, 2020, doi: 10.1038/s41598-020-77867-5.
- [176] D. K. Smith, "Opal, cristobalite, and tridymite: Noncrystallinity versus crystallinity, nomenclature of the silica minerals and bibliography," *Powder Diffr.*, vol. 13, no. 1, 1998.
- [177] S. Ledakowicz, P. Stolarek, A. Malinowski, and O. Lepez, "Thermochemical treatment of sewage sludge by integration of drying and pyrolysis/autogasification," *Renew. Sustain. Energy Rev.*, vol. 104, no. December 2018, pp. 319–327, 2019, doi: 10.1016/j.rser.2019.01.018.
- [178] P. C. Hsiau and S. L. Lo, "Characteristics of four alkaline biosolids produced from sewage sludge," *Resour. Conserv. Recycl.*, vol. 21, no. 3, pp. 185–197, 1997, doi: 10.1016/S0921-3449(97)00035-9.
- [179] L. F. Ballesteros, J. A. Teixeira, and S. I. Mussatto, "Chemical, Functional, and Structural Properties of Spent Coffee Grounds and Coffee Silverskin," *Food Bioprocess Technol.*, vol. 7, no. 12, pp. 3493–3503, Jun. 2014, doi:

- 10.1007/s11947-014-1349-z.
- [180] I. Block, C. Günter, A. D. Rodrigues, S. Paasch, P. Hesemann, and A. Taubert, "Carbon adsorbents from spent coffee for removal of methylene blue and methyl orange from water," *Materials (Basel)*, vol. 14, no. 14, 2021, doi: 10.3390/ma14143996.
- [181] A. A. Azzaz *et al.*, "Physico-chemical properties of hydrochars produced from raw olive pomace using olive mill wastewater as moisture source," *Comptes Rendus Chim.*, vol. 23, no. 11–12, pp. 635–652, 2020, doi: 10.5802/CRCHIM.61.
- [182] J. Zhang *et al.*, "Co-hydrothermal carbonization of polyvinyl chloride and lignocellulose biomasses for chlorine and inorganics removal," *Waste Manag.*, vol. 156, no. December 2022, pp. 198–207, 2023, doi: 10.1016/j.wasman.2022.11.039.
- [183] P. Marschner, *Marschner's Mineral Nutrition of Higher Plants*, 3rd editio. Academic Press, 2012.
- [184] A. Saddawi, J. M. Jones, A. Williams, and C. Le Coeur, "Commodity fuels from biomass through pretreatment and torrefaction: Effects of mineral content on torrefied fuel characteristics and quality," *Energy and Fuels*, vol. 26, no. 11, pp. 6466–6474, 2012, doi: 10.1021/ef2016649.
- [185] J. Poerschmann, B. Weiner, H. Wedwitschka, I. Baskyr, R. Koehler, and F. D. Kopinke, "Characterization of biocoals and dissolved organic matter phases obtained upon hydrothermal carbonization of brewer's spent grain," *Bioresour. Technol.*, vol. 164, pp. 162–169, 2014, doi: 10.1016/j.biortech.2014.04.052.
- [186] X. Zhao *et al.*, "Fertilizer and activated carbon production by hydrothermal carbonization of digestate," *Biomass Convers. Biorefinery*, vol. 8, no. 2, pp. 423–436, 2018, doi: 10.1007/s13399-017-0291-5.
- [187] D. Boström *et al.*, "Ash transformation chemistry during combustion of biomass," *Energy and Fuels*, vol. 26, no. 1, pp. 85–93, 2012, doi: 10.1021/ef201205b.
- [188] A. C. de Oliveira Junqueira *et al.*, "First description of bacterial and fungal communities in Colombian coffee beans fermentation analysed using Illumina-based amplicon sequencing," *Sci. Rep.*, vol. 9, no. 1, pp. 1–10, 2019, doi: 10.1038/s41598-019-45002-8.
- [189] V. Vanitha, S. Vijayakumar, M. Nilavukkarasi, V. N. Punitha, E. Vidhya, and P. K. Praseetha, "Heneicosane—A novel microbicial bioactive alkane identified from *Plumbago zeylanica* L.," *Ind. Crops Prod.*, vol. 154, no. May, p. 112748, 2020, doi: 10.1016/j.indcrop.2020.112748.
- [190] W. Nie *et al.*, "Surface organic nitrogen-doping disordered biomass carbon materials with superior cycle stability in the sodium-ion batteries," *J. Power Sources*, vol. 522, no. December 2021, p. 230994, 2022, doi: 10.1016/j.jpowsour.2022.230994.
- [191] C. Nita, B. Zhang, J. Dentzer, and C. Matei Ghimbeu, "Hard carbon derived from coconut shells, walnut shells, and corn silk biomass waste exhibiting high capacity for Na-ion batteries," *J. Energy Chem.*, vol. 58, pp. 207–218, 2021, doi: 10.1016/j.jechem.2020.08.065.
- [192] E. M. Lotfabad *et al.*, "High-density sodium and lithium ion battery anodes from banana peels," *ACS Nano*, vol. 8, no. 7, pp. 7115–7129, 2014, doi: 10.1021/nn502045y.
- [193] C. Matei Ghimbeu, B. Zhang, A. Martinez de Yuso, B. Réty, and J. M. Tarascon, "Valorizing low cost and renewable lignin as hard carbon for Na-ion batteries: Impact of lignin grade," *Carbon N. Y.*, vol. 153, no. 0, pp. 634–647, 2019, doi: 10.1016/j.carbon.2019.07.026.
- [194] Y. Li, Y. S. Hu, M. M. Titirici, L. Chen, and X. Huang, "Hard Carbon Microtubes Made from Renewable Cotton as High-Performance Anode Material for Sodium-Ion Batteries," *Adv. Energy Mater.*, vol. 6, no. 18, pp. 1–9, 2016, doi: 10.1002/aenm.201600659.
- [195] G. Wang *et al.*, "Chemically activated hollow carbon nanospheres as a high-performance anode material for potassium ion batteries," *J. Mater. Chem. A*, vol. 6, no. 47, pp. 24317–24323, 2018, doi: 10.1039/c8ta09751h.
- [196] T. Dahou, F. Defoort, M. Jeguirim, and C. Dupont, "Towards understanding the role of K during biomass steam gasification," *Fuel*, vol. 282, no. July, p. 118806, 2020, doi: 10.1016/j.fuel.2020.118806.
- [197] J. Fondard, E. Irisarri, C. Courrèges, M. R. Palacin, A. Ponrouch, and R. Dedryvère, "SEI Composition on Hard Carbon in Na-Ion Batteries After Long Cycling: Influence of Salts (NaPF₆, NaTFSI) and Additives (FEC, DMCF)," *J. Electrochem. Soc.*, vol. 167, no. 7, p. 070526, 2020, doi: 10.1149/1945-7111/ab75fd.

- [198] H.-P. Schmidt, "55 Uses of Biochar," *Ithaka J.*, vol. 25, no. 1/2012, pp. 13–25, 2012.
- [199] A. T. Jamal-Uddin, M. T. Reza, O. Norouzi, S. A. Salaudeen, A. Dutta, and R. G. Zytner, "Recovery and Reuse of Valuable Chemicals Derived from Hydrothermal Carbonization Process Liquid," *Energies*, vol. 16, no. 2, 2023, doi: 10.3390/en16020732.
- [200] J. Xiong, S. Chen, J. Wang, Y. Wang, X. Fang, and H. Huang, "Speciation of main nutrients (N/P/K) in hydrochars produced from the hydrothermal carbonization of swine manure under different reaction temperatures," *Materials (Basel)*, vol. 14, no. 15, 2021, doi: 10.3390/ma14154114.
- [201] G. Mannarino, S. Caffaz, R. Gori, and L. Lombardi, "Environmental Life Cycle Assessment of Hydrothermal Carbonization of Sewage Sludge and Its Products Valorization Pathways," *Waste and Biomass Valorization*, vol. 13, no. 9, pp. 3845–3864, 2022, doi: 10.1007/s12649-022-01821-x.
- [202] M. J. Alhndi, D. Wüst, A. Funke, L. Hang, and A. Kruse, "Fate of Nitrogen, Phosphate, and Potassium during Hydrothermal Carbonization and the Potential for Nutrient Recovery," *ACS Sustain. Chem. Eng.*, vol. 8, no. 41, pp. 15507–15516, 2020, doi: 10.1021/acssuschemeng.0c04229.
- [203] K. Wu, X. Zhang, and Q. Yuan, "Effects of process parameters on the distribution characteristics of inorganic nutrients from hydrothermal carbonization of cattle manure," *J. Environ. Manage.*, vol. 209, pp. 328–335, 2018, doi: 10.1016/j.jenvman.2017.12.071.
- [204] U. Ekpo, A. B. Ross, M. A. Camargo-Valero, and P. T. Williams, "A comparison of product yields and inorganic content in process streams following thermal hydrolysis and hydrothermal processing of microalgae, manure and digestate," *Bioresour. Technol.*, vol. 200, pp. 951–960, 2016, doi: 10.1016/j.biortech.2015.11.018.
- [205] C. C. Silva, C. A. Melo, F. H. Soares Junior, A. B. Moreira, O. P. Ferreira, and M. C. Bisinoti, "Effect of the reaction medium on the immobilization of nutrients in hydrochars obtained using sugarcane industry residues," *Bioresour. Technol.*, vol. 237, pp. 213–221, 2017, doi: 10.1016/j.biortech.2017.04.004.
- [206] F. Lyu, S. F. Luiz, D. R. P. Azeredo, A. G. Cruz, S. Ajlouni, and C. S. Ranadheera, "Apple pomace as a functional and healthy ingredient in food products: A review," *Processes*, vol. 8, no. 3, pp. 1–15, 2020, doi: 10.3390/pr8030319.
- [207] R. C. Skinner, J. C. Gigliotti, K. M. Ku, and J. C. Tou, "A comprehensive analysis of the composition, health benefits, and safety of apple pomace," *Nutr. Rev.*, vol. 76, no. 12, pp. 893–909, 2018, doi: 10.1093/nutrit/nuy033.
- [208] K. M. Khidzir, N. Abdullah, and P. Agamuthu, "Brewery spent grain: Chemical characteristics and utilization as an enzyme substrate," *Malaysian J. Sci.*, vol. 29, no. 1, pp. 41–51, 2010, doi: 10.22452/mjs.vol29no1.7.
- [209] N. Liu, K. Huo, M. T. McDowell, J. Zhao, and Y. Cui, "Rice husks as a sustainable source of nanostructured silicon for high performance Li-ion battery anodes," *Sci. Rep.*, vol. 3, pp. 1–7, 2013, doi: 10.1038/srep01919.
- [210] S. I. Mussatto, L. M. Carneiro, J. P. A. Silva, I. C. Roberto, and J. A. Teixeira, "A study on chemical constituents and sugars extraction from spent coffee grounds," *Carbohydr. Polym.*, vol. 83, no. 2, pp. 368–374, 2011, doi: 10.1016/j.carbpol.2010.07.063.
- [211] P. J. Arauzo, M. P. Olszewski, and A. Kruse, "Hydrothermal carbonization brewer's spent grains with the focus on improving the degradation of the feedstock," *Energies*, vol. 11, no. 11, p. 3236, 2018, doi: 10.3390/en11113226.
- [212] M. T. Reza, A. Freitas, X. Yang, S. Hiibel, H. Lin, and C. J. Coronella, "Hydrothermal Carbonization (HTC) of Cow Manure: Carbon and Nitrogen Distributions in HTC Products," *Environ. Prog. Sustain. Energy*, vol. 35, no. 4, pp. 1002–1011, 2014, doi: 10.1002/ep.12312.
- [213] B. Zhang *et al.*, "Hydrothermal carbonization of fruit wastes: A promising technique for generating hydrochar," *Energies*, vol. 11, no. 8, pp. 1–14, 2018, doi: 10.3390/en11082022.
- [214] O. O. D. Afolabi, M. Sohail, and Y. L. Cheng, "Optimisation and characterisation of hydrochar production from spent coffee grounds by hydrothermal carbonisation," *Renewable Energy*, vol. 147, pp. 1380–1391, 2020, doi: 10.1016/j.renene.2019.09.098.
- [215] A. Shrestha, B. Acharya, and A. A. Farooque, "Study of hydrochar and process water from hydrothermal carbonization of sea lettuce," *Renew. Energy*, vol. 163, pp. 589–598, 2021, doi: 10.1016/j.renene.2020.08.133.
- [216] L. Suárez, I. Benavente-Ferraces, C. Plaza, S. de Pascual-Teresa, I. Suárez-Ruiz, and T. A. Centeno, "Hydrothermal carbonization as a sustainable strategy for integral valorisation of apple waste," *Bioresour. Technol.*, vol. 309, no. March, p. 123395, 2020, doi: 10.1016/j.biortech.2020.123395.

- [217] Y. Deng *et al.*, "Mechanisms and modelling of phosphorus solid-liquid transformation during the hydrothermal processing of swine manure," *Green Chem.*, vol. 22, no. 17, pp. 5628–5638, 2020, doi: 10.1039/d0gc01281e.
- [218] Y. Shi *et al.*, "Migration and transformation mechanism of phosphorus in waste activated sludge during anaerobic fermentation and hydrothermal conversion," *J. Hazard. Mater.*, vol. 403, no. May 2020, p. 123649, 2021, doi: 10.1016/j.jhazmat.2020.123649.
- [219] B. M. Ghanim, W. Kwapinski, and J. J. Leahy, "Speciation of Nutrients in Hydrochar Produced from Hydrothermal Carbonization of Poultry Litter under Different Treatment Conditions," *ACS Sustain. Chem. Eng.*, vol. 6, no. 9, pp. 11265–11272, Sep. 2018, doi: 10.1021/acssuschemeng.7b04768.
- [220] T. Khazraie Shoulaifar, N. Demartini, M. Zevenhoven, F. Verhoeff, J. Kiel, and M. Hupa, "Ash-forming matter in torrefied birch wood: Changes in chemical association," *Energy and Fuels*, vol. 27, no. 10, pp. 5684–5690, 2013, doi: 10.1021/ef4005175.
- [221] M. H. Marzbali *et al.*, "Investigations into distribution and characterisation of products formed during hydrothermal carbonisation of paunch waste," *J. Environ. Chem. Eng.*, vol. 9, no. 1, p. 104672, 2021, doi: 10.1016/j.jece.2020.104672.
- [222] J. de S. Castro *et al.*, "Hydrothermal carbonization of microalgae biomass produced in agro-industrial effluent: Products, characterization and applications," *Sci. Total Environ.*, vol. 768, p. 144480, 2021, doi: 10.1016/j.scitotenv.2020.144480.
- [223] Y. Zhao, D. Feng, Y. Zhang, Y. Huang, and S. Sun, "Effect of pyrolysis temperature on char structure and chemical speciation of alkali and alkaline earth metallic species in biochar," *Fuel Process. Technol.*, vol. 141, pp. 54–60, 2016, doi: 10.1016/j.fuproc.2015.06.029.
- [224] T. Okuno, N. Sonoyama, J. I. Hayashi, C. Z. Li, C. Sathe, and T. Chiba, "Primary release of alkali and alkaline earth metallic species during the pyrolysis of pulverized biomass," *Energy and Fuels*, vol. 19, no. 5, pp. 2164–2171, 2005, doi: 10.1021/ef050002a.
- [225] H. Wu, D. M. Quyn, and C. Z. Li, "Volatilisation and catalytic effects of alkali and alkaline earth metallic species during the pyrolysis and gasification of Victorian brown coal. Part III. The importance of the interactions between volatiles and char at high temperature," *Fuel*, vol. 81, no. 8, pp. 1033–1039, 2002, doi: 10.1016/S0016-2361(02)00011-X.
- [226] Z. Ma *et al.*, "Mineral transformation in char and its effect on coal char gasification reactivity at high temperatures, part 2: Char gasification," *Energy and Fuels*, vol. 28, no. 3, pp. 1846–1853, 2014, doi: 10.1021/ef402382m.
- [227] J. Dang, Q. Xie, D. Liang, X. Wang, H. Dong, and J. Cao, "The fate of trace elements in yanshan coal during fast pyrolysis," *Minerals*, vol. 6, no. 2, 2016, doi: 10.3390/min6020035.
- [228] A. Ōya and H. Marsh, "Phenomena of catalytic graphitization," *J. Mater. Sci.*, vol. 17, no. 2, pp. 309–322, 1982, doi: 10.1007/BF00591464.
- [229] M. Tripathi, J. N. Sahu, and P. Ganesan, "Effect of process parameters on production of biochar from biomass waste through pyrolysis: A review," *Renew. Sustain. Energy Rev.*, vol. 55, pp. 467–481, 2016, doi: 10.1016/j.rser.2015.10.122.
- [230] Y. Jin *et al.*, "From Waste Biomass to Hard Carbon Anodes: Predicting the Relationship between Biomass Processing Parameters and Performance of Hard Carbons in Sodium-Ion Batteries," *Processes*, vol. 11, no. 3, 2023, doi: 10.3390/pr11030764.
- [231] J. Conder, C. Vaultot, C. Marino, C. Villeveille, and C. M. Ghimbeu, "Chitin and Chitosan - Structurally Related Precursors of Dissimilar Hard Carbons for Na-Ion Battery," *ACS Appl. Energy Mater.*, vol. 2, no. 7, pp. 4841–4852, 2019, doi: 10.1021/acsaem.9b00545.
- [232] V. Simone, L. Lecarme, L. Simonin, and S. Martinet, "Identification and Quantification of the Main Electrolyte Decomposition By-product in Na-Ion Batteries through FEC: Towards an Improvement of Safety and Lifetime," *J. Electrochem. Soc.*, vol. 164, no. 2, pp. A145–A150, 2017, doi: 10.1149/2.0671702jes.
- [233] Z. Xu *et al.*, "The Role of Hydrothermal Carbonization in Sustainable Sodium-Ion Battery Anodes," *Adv. Energy Mater.*, vol. 12, no. 18, 2022, doi: 10.1002/aenm.202200208.
- [234] A. A. Azzaz, C. M. Ghimbeu, S. Jellai, L. El-Bassi, and M. Jeguirim, "Olive Mill by-Products Thermochemical Conversion via Hydrothermal Carbonization and Slow Pyrolysis: Detailed Comparison between the Generated Hydrochars and Biochars Characteristics," *Processes*, vol. 10, no. 2, 2022, doi: 10.3390/pr10020231.

- [235] J. Wang *et al.*, "Comparison of cadmium adsorption by hydrochar and pyrochar derived from Napier grass," *Chemosphere*, vol. 308, no. P3, p. 136389, 2022, doi: 10.1016/j.chemosphere.2022.136389.
- [236] F. X. Collard and J. Blin, "A review on pyrolysis of biomass constituents: Mechanisms and composition of the products obtained from the conversion of cellulose, hemicelluloses and lignin," *Renew. Sustain. Energy Rev.*, vol. 38, pp. 594–608, 2014, doi: 10.1016/j.rser.2014.06.013.
- [237] S. C. van Lith, P. A. Jensen, F. J. Frandsen, and P. Glarborg, "Release to the gas phase of inorganic elements during wood combustion. Part 2: Influence of fuel composition," *Energy and Fuels*, vol. 22, no. 3, pp. 1598–1609, 2008, doi: 10.1021/ef060613i.
- [238] A. Pettersson, M. Zevenhoven, B. Steenari, and L.-E. Åmand, "Application of chemical fractionation methods for characterisation of biofuels, waste derived fuels and CFB co-combustion fly ashes," *Fuel*, vol. 87, no. 15–16, pp. 3183–3193, 2008, doi: 10.1016/j.fuel.2008.05.030.
- [239] M. Bardalai, D. K. Mahanta, and B. Das, "Production and Characterisation of Teak Tree Saw Dust and Rice Husk Biochar," in *Pollutants from Energy Sources, Characterisation and control*, Pollutants., R. Agarwal, A. A., T. Gupta, and N. Sharma, Eds. Singapore: Springer, 2018.
- [240] S. S. Sahoo, V. K. Vijay, R. Chandra, and H. Kumar, "Production and characterization of biochar produced from slow pyrolysis of pigeon pea stalk and bamboo," *Clean. Eng. Technol.*, vol. 3, p. 100101, 2021, doi: 10.1016/j.clet.2021.100101.
- [241] G. Mujtaba, R. Hayat, Q. Hussain, and M. Ahmed, "Physio-chemical characterization of biochar, compost and co-composted biochar derived from green waste," *Sustain.*, vol. 13, no. 9, pp. 1–22, 2021, doi: 10.3390/su13094628.
- [242] P. Thy, B. M. Jenkins, S. Grundvig, R. Shiraki, and C. E. Lesher, "High temperature elemental losses and mineralogical changes in common biomass ashes," *Fuel*, vol. 85, no. 5–6, pp. 783–795, 2006, doi: 10.1016/j.fuel.2005.08.020.
- [243] E. Nyktari, E. Danso-Boateng, A. Wheatley, and R. Holdich, "Anaerobic digestion of liquid products following hydrothermal carbonisation of faecal sludge at different reaction conditions," *Desalin. Water Treat.*, vol. 91, pp. 245–251, 2017, doi: 10.5004/dwt.2017.20782.
- [244] R. Ferrentino, G. Sacchi, D. Scrinzi, G. Andreottola, and L. Fiori, "Valorization of swine manure for a circular approach through hydrothermal carbonization," *Biomass and Bioenergy*, vol. 168, no. November 2022, p. 106689, 2023, doi: 10.1016/j.biombioe.2022.106689.
- [245] U. Choe, A. M. Mustafa, H. Lin, U. Choe, and K. Sheng, "Anaerobic co-digestion of fish processing waste with a liquid fraction of hydrothermal carbonization of bamboo residue," *Bioresour. Technol.*, vol. 297, no. November 2019, p. 122542, 2020, doi: 10.1016/j.biortech.2019.122542.

Abstract

Li-ion batteries are the most suitable for energy storage technology, which makes them the most used in electronics and mobility. Yet, lithium availability on Earth is very limited in quantity and place. Sodium is abundant and presents a similar reactivity to lithium. Despite being similar in many points, their reactivity are still different: unlike lithium, the insertion of sodium ions between the graphite layers at the negative electrode is limited. Hard-carbon is used instead, however its price is three times higher and it is usually petro-based. To solve this problematic, it can be synthesized from waste biomass after high-temperature pyrolysis. Many studies report pyrolysis of dry matter, but few deal with wet biomass, which is an underestimate carbon resource because of its high moisture content (>60%). Moreover, to obtain a hard carbon with interesting performances, a low ash content is required, which limit even more the choice of the feedstock. It limits the suitable materials.

In order to open the possibility of biomass as the same time as reducing the cost and environmental impact, hydrothermal carbonisation (HTC) is performed before the pyrolysis. This thermal treatment takes place in a sealed vessel, in which the sample is directly immersed in water and hence doesn't require any drying step. With the temperature, the pressure autogenously increases: the water reach the subcritical state and directly react with the feedstock to provide a carbonaceous material called hydrochar. In addition, during the process the inorganics in the biomass leach in the liquid phase, preventing graphitisation and limiting the surface area development during the pyrolysis step, key parameter for hard carbon electrodes.

The objective of this thesis is to characterise the influence of the HTC pre-treatment on the resulting hard carbon, by investigated the reactions occurring depending on the operation conditions. A complete investigation on both the composition and structure of each starting, intermediate and final materials are performed, to conclude on the influence of each element on the resulting hard carbon. At last, both composition and structure are linked to the battery performance, offering a screening of the most suitable biomass as well of the best conditions to provide promising hard carbon for Na-ion batteries.

The HTC temperature was highlighted to impact greatly the reactions occurring, both regarding the biomass degradation and secondary reaction between the hydrochar and the liquid, particularly regarding the inorganics. Each behave differently: while alkali mainly leach and heavy metals remain no matter the conditions, Ca, Mg, P and Si behave differently depending on the chemical form they are in the biomass. Furthermore, even if they are first solubilised, the increase of the temperature favour their reprecipitation, leading them back in the hydrochar.

The volatilisation of these elements are limited during the high temperature pyrolysis, their quantity being mostly removed after the pre-treatment. Particularly K, Ca and Si have been linked to the resulting hard carbon properties. K and Ca, in addition to most of the heavy metal traces, tend to catalyse graphitisation. Moreover, K seems to favour its porosity. At last, all the hydrochars containing important Si contents, SiC whiskers have been observed in the resulting material, increasing the surface area in contact with the electrolyte and decreasing the cell performances.

Résumé

Les batteries Li-ion sont de nos jours représentent la technologie la plus adaptée au stockage d'énergie, qui en font la plus utilisées dans les appareils électroniques et portatifs. Cependant, la disponibilité du lithium sur Terre est limitée en quantité et localisation. Le sodium est abondant et sa réactivité est similaire au lithium, rendant les batteries Na-ion une alternative prometteuse. Bien que ces deux systèmes aient de nombreux points communs, une différence majeure s'impose : l'insertion du sodium entre les plans du graphite de l'électrode négative est très faible. A la place, du carbone dur est utilisé, cependant son coût est trois fois plus cher que le graphite et est souvent pétrosourcé. Pour répondre à cette problématique, il est possible de le synthétiser par pyrolyse à haute température de résidus de biomasse. Beaucoup d'études utilisent ce procédé sur des matières sèches, négligeant les biomasses humides, ressource sous-valorisée à cause de leur grand taux d'humidité (>60%). De plus, pour obtenir un carbone dur avec de bonnes performances électrochimiques, un faible taux de cendre est requis, limitant d'autant plus les possibilités de matière première.

Afin d'élargir les possibilités de biomasses tout en réduisant le coût et l'impact environnemental, une carbonisation hydrothermale (HTC) est effectuée en amont de la pyrolyse. Ce traitement thermique se déroule dans un réacteur scellé dans lequel le matériau est directement immergé dans l'eau et ainsi n'a pas besoin d'être séché préalablement. Avec la température, l'augmentation de la pression est autogénérée : l'eau atteint l'état subcritique et réagit directement avec le précurseur pour former un matériau riche en carbone appelé hydrochar. De plus, durant le procédé les inorganiques lixivient dans la phase liquide, évitant ainsi la graphitisation du matériau et limitant de développement de la surface spécifique pendant l'étape suivante de pyrolyse, facteur clé pour les électrodes de carbone dur.

L'objectif de ces travaux est de caractériser l'influence du prétraitement HTC sur le carbone dur final, en étudiant les réactions se produisant selon les différentes conditions expérimentales. Une analyse complète à la fois de la composition et de la structure des matériaux de départ, intermédiaires et finaux est présentée, pour conclure sur l'influence de chaque élément sur le carbone dur final. Enfin, chacun est lié aux performances de la batterie, offrant une perspective des matériaux les plus prometteurs ainsi que les meilleures conditions de synthèse pour obtenir le meilleur matériau pour batterie Na-ion.

Il a été démontré que la température de l'HTC impacte grandement les réactions, à la fois de dégradation de la biomasse, que les réactions secondaires entre l'hydrochar et le liquide, particulièrement concernant les inorganiques. Chacun a un comportement différent : alors que les alcalins vont principalement être solubilisés et les métaux lourds maintenu dans l'hydrochar quel que soit les conditions, Ca, Mg, P et Si vont avoir un comportement bien plus dépendant de la forme chimique dans laquelle ils sont présent dans la biomasse. De plus, bien qu'ils soient dans un premier temps libérés dans la phase liquide, l'augmentation de la température favorisera la reprécipitation de ces espèces, les intégrant à l'hydrochar.

La volatilisation de ces espèces est limitée pendant la pyrolyse à haute température, leur quantité étant déjà bien réduite suite à la première étape. En particulier, la présence de K, Ca et Si ont été associées aux propriétés du carbone dur. K et Ca, ainsi que les traces de métaux, vont avoir tendance à catalyser la graphitisation. De plus, il semble que K favorise la porosité du matériau. Enfin, dans tous les hydrochars contenant d'important taux de Si, des fils de SiC ont été observé dans le matériau final, augmentant grandement la surface accessible à l'électrolyte et diminuant ainsi les performances de la batterie.